UNIVERSITY OF
LIVERPOOL

Smart Base Station Antennas for MIMO and 5G Mobile Communications

By

Ahmed Alieldin

Thesis submitted in accordance with the requirements for the award of the degree of Doctor of Philosophy of the University of Liverpool

August 2019

To my dear wife, daughter, son and the soul of my parents.

Acknowledgements

First, I thank GOD ALMIGHTY who has given me the mental and physical strength and confidence to do this work. This thesis would have not seen the light without the support and guidance of many people who are acknowledged here. I would like to express my deep gratitude to my supervisor, Professor Yi Huang for offering me this opportunity. His kind support, fruitful advice, critical discussions and vast experience have motivated me during the whole time of my studies.

Special thanks to Mr. Mark Norman and Mr. Mark Burnley, who are technicians at electrical engineering workshop for their assistance in fabricating our designs.

Thanks to Rogers Corporation for providing us with free samples of PCB boards.

I would also like to thank Dr. Manoj Stanley at NPL, Dr. Jiafeng Zhou, Dr. Chaoyun Song, Dr. Stephen J. Boyes at DSTL, Dr. Qian Xu at Nanjing, Mr. Bahaa Al-Juboori and Mr. Sumin Joseph for their contributions and collaborations in editing the published papers of this research and for their friendly support. Special thanks to Dr Abed Poursohrab, Dr. Muaad Hussein and Dr. Ahmed Al-Tahmeesschi for their valuable advice and company during the PhD life. Thanks to all my friends and colleagues in the RF group for providing such a lovely and collaborative environment for research.

Finally, thanks to my beloved wife, my daughter and my son for their invaluable support. This journey would not have been possible without their love and prayers.

Table of Contents

Abstract

Because of the evolution of cellular communication technologies, base station antennas have developed a lot. This thesis focuses on the developing of base station antennas and addresses some of their challenges.

The challenges that face base station antenna designers for 3G, 4G and 5G mobile networks can be summarized as having a reconfigurable smart antenna that can operate in different roles, obtaining a MIMO antenna system with good diversity in multi-band, and constructing less conspicuous base station platforms. Of course, small size, low profile and less-cost antennas are preferable.

Based on the above discussions, this thesis offers *six* major contributions to address the stated problems and challenges. They can be summarized as follow:

- A novel design of reconfigurable base station antenna which can operate into two different roles across the band from 1.7 to 2.7 GHz.

- A new mathematical modelling for optimum partitioning of a phased-MIMO antenna array.

- A novel dual-band MIMO antenna system using overlapped subarrays based on the phased-MIMO technique to cover the bands from 0.7 to 0.96 GHz and from 1.7 to 2.7 GHz simultaneously. To the best of the author's knowledge, the phased-MIMO technique has been practically applied for the first time in this PhD work.

- A novel MIMO triple-broadband indoor base station antenna to serve 2G, 3G, 4G and 5G networks. The antenna performance supports MIMO system utilizing polarization diversity due to its co-located dual-polarized dipoles.

- A new MIMO antenna array for 5G mobile networks which can operate in broadcast or traffic communication topologies whenever required. The MIMO array uses a novel Pseudo Inverse Synthesis to produce concurrent dynamic multiple beams outperforming other multi-beam antenna array methods.

- A novel transparent antenna array for 5G pico-cell base stations is proposed. This transparency allows the antenna to be feasibly integrated with a street lamp to achieve visual camouflage.

List of Publications and Patents

Journal Articles

[1] **A. Alieldin**, Y. Huang and W. M. Saad, "Optimum Partitioning of a Phased-MIMO Radar Array Antenna," *IEEE Antennas and Wireless Prop. Letters*, vol. 16, pp. 2287-2290, 2017.

[2] **A. Alieldin**, Y. Huang, S. J. Boyes, M. Stanley, S. D. Joseph and B. Al-Juboori, "A Dual-Broadband Dual-Polarized Fylfot-Shaped Antenna for Mobile Base Stations Using MIMO Over-Lapped Antenna Subarrays," *IEEE Access*, vol. 6, pp. 50260-50271, 2018.

[3] **A. Alieldin**, Y. Huang, S. J. Boyes, M. Stanley, S. D. Joseph, Q. Hua and D. Lei, "A Triple-Band Dual-Polarized Indoor Base Station Antenna for 2G, 3G, 4G and Sub-6 GHz 5G Applications," *IEEE Access*, vol. 6, pp. 49209-49216, 2018.

[4] **A. Alieldin**, Y. Huang, M. Stanley, S. D. Joseph and D. Lei, "A 5G MIMO Antenna for Broadcast and Traffic Communication Topologies Based on Pseudo Inverse Synthesis," *IEEE Access*, vol. 6, pp. 65935-65944, 2018.

[5] **A. Alieldin**, Y. Huang, S. J. Boyes, and M. Stanley, "A Reconfigurable Broadband Dual-Mode Dual-Polarized Antenna for Sectoral/Omnidirectional Mobile Base Stations," *Progress In Electromagnetics Research*, Vol. 163, 1-13, 2018.

[6] M. Stanley, Y. Huang, H. Wang, H. Zhou, **A. Alieldin** and S. Joseph, "A Capacitive Coupled Patch Antenna Array with High Gain and Wide Coverage for 5G Smartphone Applications," *IEEE Access*, vol. 6, pp. 41942-41954, 2018.

[7] B. Al-Juboori, J. Zhou, Y. Huang, M. Hussein, **A. Alieldin**, W. Otter, D. Klugman and, S. Lucyszyn, "Lightweight and Low-Loss 3-D Printed Millimeter-Wave Bandpass Filter Based on Gap-Waveguide," *IEEE Access*, vol. 7, pp. 2624-2632, 2019.

[8] C. Song, E. L. Bennett, J. Xiao, **A. Alieldin**, K. Luk and Y. Huang, "Metasurfaced, Broadband, and Circularly Polarized Liquid Antennas Using a Simple Structure," *IEEE Transactions on Antennas and Propagation*, vol. 67, no. 7, pp. 4907-4913, July 2019.

Patent

[1] **A. Alieldin**, Y. Huang, "Road Lamp Antenna Array with Improved Invisibility", *China Patent*, CN201910695730.0, August 2019. (*Filed*).

Conference Papers

[1] **A. Alieldin** and Y. Huang, "Design of broadband dual-polarized oval-shaped base station antennas for mobile systems," *IEEE International Symposium on Antennas and Propagation & USNC/URSI National Radio Science Meeting*, San Diego, CA, 2017.

[2] **A. Alieldin**, Y. Huang and M. Stanley, "Design of Dual-Band Dual-Polarized Swastika-Shaped Antenna for Mobile Communication Base Stations", 12th *European Conference on Antennas and Propagation (EuCAP)*, London, 2018.

[3] **A. Alieldin**, Y. Huang, M. Stanley and S. Joseph, "A Circularly Polarized Circular Antenna Array for Satellite TV Reception," *15th European Radar Conference (EuRAD)*, Madrid, 2018, pp. 505-508. *2018.*

[4] **A. Alieldin**, Y. Huang, M. Stanley, S. Joseph, T. Jia, F. Elhouni, Q. Xu, "A Camouflage Antenna Array Integrated with a Street Lamp for 5G Pico-cell Base Stations" *The 13th European Microwave conference on Antenna and Propagation (EuCAP)*, Krakow, Poland, April 2019.

[5] M. Stanley, Y. Huang, H. Wang, H. Zhou, **A. Alieldin** and S. Joseph, "A novel mm-Wave phased array antenna with 360° coverage for 5G smartphone applications," *10th UK-Europe-China Workshop on Millimetre Waves and Terahertz Technologies (UCMMT)*, Liverpool, pp. 1-3, 2017.

[6] M. Stanley, Y. Huang, H. Wang, H. Zhou, **A. Alieldin** and Sumin Joseph "A Novel mm-Wave Phased Array for 180-degree coverage for 5G Smartphone Applications", *12th European Conference on Antennas and Propagation (EuCAP)*, London, 2018.

[7] M. Stanley, Y. Huang, H. Wang, H. Zhou, **A. Alieldin** and S. Joseph, "A Transparent Dual-Polarized Antenna Array for 5G Smartphone Applications," *IEEE International Symposium on Antennas and Propagation & USNC/URSI National Radio Science Meeting*, Boston, MA, 2018, pp. 635-636. *2018.*

[8] M. Stanley, Y. Huang, H. Wang, H. Zhou, **A. Alieldin**, S. Joseph, C. Song and, T. Jia, "A Dual-Band Dual-Polarized Stacked Patch Antenna for 28 GHz and 39 GHz 5G Millimetre-Wave Communication". *The 13th European Microwave conference on Antenna and Propagation (EuCAP)*, Krakow, Poland, April 2019.

[9] T. Elshikh, A. Sayed. A. Eid and **A. Alieldin**, "A Low-Cost Circular Polarized Antenna Array for GPS Receivers", *The 13th European Microwave conference on Antenna and Propagation (EuCAP)*, Krakow, Poland, April 2019.

[10] S. Joseph, Y. Huang, S. Hsu, M. Stanley, **A. Alieldin**, C. Li, "A Novel Miniaturized Broadband Yagi-Uda Antenna with Enhanced Gain", *The 13th European Microwave conference on Antenna and Propagation (EuCAP)*, Krakow, Poland, April 2019.

Acronyms

1G	First Generation
2G	Second Generation
3D	Three Dimensional
3G	Third Generation
4G	Fourth Generation
5G	Fifth Generation
ADC	Analogue to Digital Converter
BBU	Baseband Unit
BER	Bit Error Rate
BW	Bandwidth
CDF	Cumulative Distribution Function
CDMA	Code Division Multiple Access
CRAN	Cloud (or Centralized) Radio Access Network
DAC	Digital to Analogue Converter
dB	Decibel
dBi	Decibel relative to Isotropic
DC	Direct Current
DOA	Direction of Arrival
EC	European Commission
ECC	Envelope Correlation Coefficient
EDGE	Enhanced Data Rates in GSM

FBR	Front-to-Back Lobe Ratio
GPRS	General Packet Radio Service
GSM	Global System of Mobile
HPBW	Half Power Beam Width
HPMR-US	Hybrid Phased-MIMO system with Unequal Subarrays
INR	Interference-to-Noise Ratio
IoT	Internet of Things
IP	Internet Protocol
ITO	Indium Tin Oxide
LNA	Low Noise Amplifier
LTE	Long Term Evolution
MC	Micro-Cell
MIIT	Chinese Ministry of Industry and Information Technology
MIMO	Multiple Input Multiple Output
M-MIMO	Massive Multiple Input Multiple Output
OFDM	Orthogonal Frequency Division Multiplexing
OLAS	Overlapped Antenna Subarrays
OPPM	Optimum Partitioning of Phased-MIMO antenna array
P2MP	Point-to-Multipoint
PC	Pico-Cell
PCB	Printed Circuit Boards
PIM	Passive Intermodulation
PIS	Pseudo Inverse Synthesis

PSLL　　　　　Peak Side Lobe Level

RAT　　　　　Radio Access Technology

RF　　　　　Radio Frequency

RRH　　　　　Remote Radio Head

RRU　　　　　Remote Radio Unit

SINR　　　　　Signal to Interference plus Noise Ratio

SMS　　　　　Short Message Service

SNR　　　　　Signal-to-Noise Ratio

S-Parameters　Scattering Parameters

TCO　　　　　Transparent Conducting Oxide

UMTS　　　　Universal Mobile Telecommunications System

VNA　　　　　Vector Network Analyzer

VSWR　　　　Voltage Standing Wave Ratio

WiMAX　　　Worldwide Interoperability for Microwave Access

XPD　　　　　Cross Polarization Discrimination Ratio

List of Figures

List of Tables

Chapter 1. Introduction

Every story has a beginning, and the developments in mobile communications are not different. The use of mobile devices has been growing rapidly for the last few decades, and the same trend will continue in the near future, as the global number of mobile subscriptions is constantly increasing and applications are more and more data-intensive [1]–[4]. The constant evolution of mobile communications together with the emergence of multiple wireless communication systems fosters the antenna community to design new compact antenna systems capable of satisfying the market demands.

In this chapter, the evolution of mobile communication and base station design and its corresponding effect on the evolution of antenna designs are detailed. The various types of base station antennas are examined and their parameters corresponding to their usage are discussed. The problems and challenges of the existing base station antennas are identified; as a result, the development of new antennas for the base stations is selected as the research topic of the thesis.

1.1. Evolution of Mobile Communications

When mobile communications are described, they refer to the overall technology, speed, frequency and system in numeric generations such as 3G, 4G or 5G. Each generation has unique technologies that define it. The evolution of mobile communications is shown in Fig. 1.1.
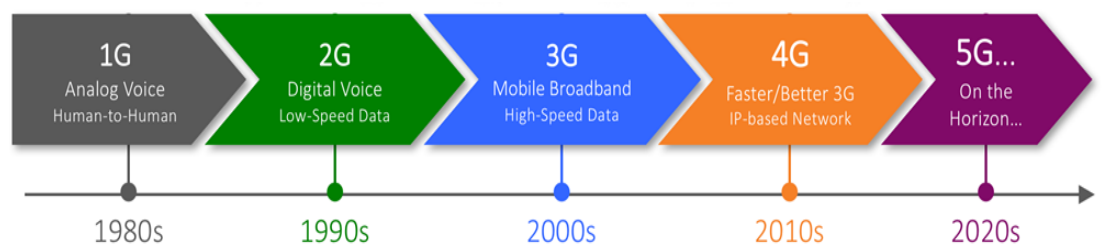
Fig. 1.1.   Evolution of mobile communication

The very first generation of a commercial cellular network was introduced in the late 70s with fully implemented standards being established throughout the 80s [4].

The radio signals used by 1G were analogue signals, meaning the voice of a call was modulated to a higher frequency rather than being encoded to digital signals. Analogue signals degrade over time and space meaning that voice data often lacked quality within a call. In comparison, for digital communications, a larger amount of data could be carried effectively.

The second generation saw the introduction of GSM (Global System for Mobile Communication) technologies as a standard in the early 90s. It allowed for digital voice and data to be sent across the network and allowed users to roam for the first time. It also used Signalling and Data Confidentially and Mobile Station Authentication to ensure improved security and privacy of telephone calls. The advance in technology from 1G to 2G introduced many of the fundamental services that are still used today, such as SMS, international roaming, conference calls, call hold and billing based on services e.g. charges based on long distance calls and real-time billing.

Between the year 2000 and 2003, an upgrade in technologies introduced the packet network, which provided high-speed data-transfer and Internet, and became known as 2.5G. The standards included GPRS (General Packet Radio Service) and EDGE (Enhanced Data Rates in GSM). GPRS supported flexible data transmission rates and provided a continuous connection with the network. It also allowed the service provider to charge for the quantity of data sent, rather than their connection time.

Introduced commercially in 2001, the goals set out for the third generation (3G) mobile communications were to facilitate greater voice and data capacity, support a wider range of applications and increase data transmission at a lower cost [5]. For the first time, this generation supported high-speed Internet access as well as fixed wireless Internet access and allowed for video calls, chatting and conferencing, mobile TV, video on demand services, navigational maps, email, mobile gaming, music and digital services such as movies. Significantly, greater security features were introduced within 3G, including Network Access, Domain Security and Application Security.

Initiated in 2010, 4G is an all IP based network system [6]. Its purpose was to provide high speed, high quality and high capacity to users while improving the security and lowering the cost of the voice and data services, multimedia and Internet over IP. One of the major benefits of an IP based network was that it was able to seamlessly handover, for voice and data to GSM, UMTS and CDMA2000 technologies from the previous different generation infrastructure. The fourth

generation introduced the LTE standard, which only supported packet switching and an all IP Network. There was a significant amount of infrastructure changes that had to be implemented by service providers in order to supply because voice calls in GSM, UMTS and CDMA were circuit-switched, so with the adoption of LTE, carriers had to re-engineer their voice call network. However, LTE could not fulfil the specifications, but its successor LTE-Advanced did [7]. The 4G networks used over 40 frequency bands around the world [5], [7] and provided 1 Gb/s peak data transmission by utilizing techniques such as MIMO and carrier aggregation [8].

The fifth generation (5G) is the next generation of commercial cellular network, set to increase Internet connection speeds significantly. Different estimations have been made for the date of commercial introduction of 5G networks, but they are generally around the year 2020. One of the main benefits of increased connectivity being plugged as the underlying selling point of 5G is the IoT (Internet of Things), which would make the most of the higher speed of connectivity to allow for seamless integration of devices on a scale never been achievable before. It will operate at new sub-6 GHz bands for massive MIMO (M-MIMO) operation as well as mm-wave frequency bands for increased data rate and higher capacity [9].

1.2. Evolution of the Base Station Antennas

As well as its obvious function of providing communication links between a base station and a mobile terminal, the base station antenna improves the channel capacity and the signal-to-noise ratio (SNR) [10]. Researchers have focused on the use of smart antenna technologies to construct base station antennas in which identical frequencies can be used in the same cell, increasing the maximum number of users in the cell without allocation of additional radio frequency bands.

In the mid of 1990s, the term *smart antenna* (also known as *intelligent antenna*) was introduced to describe antenna systems which have the capabilities of estimating the useful signal Direction of Arrival (DOA). Nowadays, the term has been broadened to include antenna systems which can control their parameters such as radiation patterns, frequency bands, geometries, .. etc. [11].

Antenna systems for base stations have evolved significantly since the early days of analogue and then digital mobile communications, which typically operated on a

single frequency, through to the 4th generation LTE systems, which support multiple radio spectrum bands and increasingly higher frequencies.

Table 1.1 includes the most major worldwide frequency bands. However, other frequency bands are allocated to mobile communication services in some countries [5]

Table 1.1.   Frequency bands

Frequency Band	Short reference
450 - 470 MHz	450 MHz
800 - 890 MHz	800 MHz
870 - 960 MHz	900 MHz
1710 - 1880 MHz	1800 MHz
1850 - 1990 MHz	1900 MHz
1900 - 2170 MHz	2100 MHz
2170 - 2710 MHz	2600 MHz
3300 - 3800 MHz	5G Sub-6 GHz (B1)
4800 - 5000 MHz	5G Sub-6 GHz (B2)
24-86 GHz	5G mm-Wave

Cellular radio engineering defines transmission from a base station to a mobile device as the downlink while the opposite direction, from the mobile device to the base station, is known as the uplink. The radio link budget for the downlink and uplink need to be calculated independently with the weakest ultimately limiting the cellular radio coverage. Mobile networks are typically uplink limited due to the lower transmit power of the mobile device when compared with the radio base station. Several techniques are available to enhance radio performance of the uplink and are typically visible in the configuration of the antenna systems in both base stations and mobile devices [12].

In this section, the evolution of the base station antenna systems are explored starting with the introduction of the digital cellular with the GSM. The GSM antenna systems are important to understand the evolution of 3G UMTS and 4G LTE systems, as there is much in common with later generations of technology. However, the level of functional integration means that many of these components are not necessarily exposed as stand-alone functions in modern systems.

GSM networks started to appear during the early 1990s, initially operating in the same 900 MHz-band as the analogue system enabling it to be combined in to the then

existing antennas. Given the increasing popularity of mobile phones, it was necessary for the operators to build denser networks of cell sites to manage capacity while also extending geographical coverage to satisfy the demand for service. This, along with the introduction of several new mobile network operators into the cellular market, led to a massive programme of cell site rollout and rapid evolution in the antenna systems [13]. Although GSM was initially specified to operate in the 900 MHz band, a higher frequency version, GSM1800, was introduced for the 1800 MHz band.

1.2.1. Antenna Systems for 2G GSM

Early GSM base station antenna systems operated with a technique known as space diversity, a system in which two receiving antennas are deployed at the base station to improve the uplink. These antennas are separated in space such that their fading is de-correlated, thereby reducing dropped calls. Fading occurs due to the combination of multipath components of the signal received from the mobile device, which arrives via multiple reflections rather than a direct line of sight [14].

The use of space diversity antennas is a key consideration in determining the size of the structure and mounting frame. Typically, a base station would require a separation of at least ten wavelengths between the two receiving antennas (i.e. 3.3 metres separation at 900 MHz and 1.67 metres at 1800 MHz). It was quite common for operators to deploy omnidirectional antennas in the early days of GSM rollout - effectively a single set of radio transceiver equipment providing coverage to 360°. Deploying a three-cell sector site would be more expensive as three sets of radio transceiver equipment would be required although this would offer greater capacity and, more importantly, in the early days of rollout, greater geographical coverage due to the higher antenna gain which can be achieved through a more focused radiofrequency beam (i.e. 120° rather than 360°) [15].

Fig. 1.2 illustrates a typical GSM1800 site configuration. In the case of space diversity omnidirectional antenna systems, this figure illustrates the complete RF deployment whilst, for a typical three cell sector site, this illustrates a single cell sector. To provide 360° coverage, two additional cell sectors would be constructed in the same way. Depending on the traffic capacity offered, more than one transceiver (consisting of one transmitter and two receivers along with associated processing capability) per cell sector may be deployed [13].
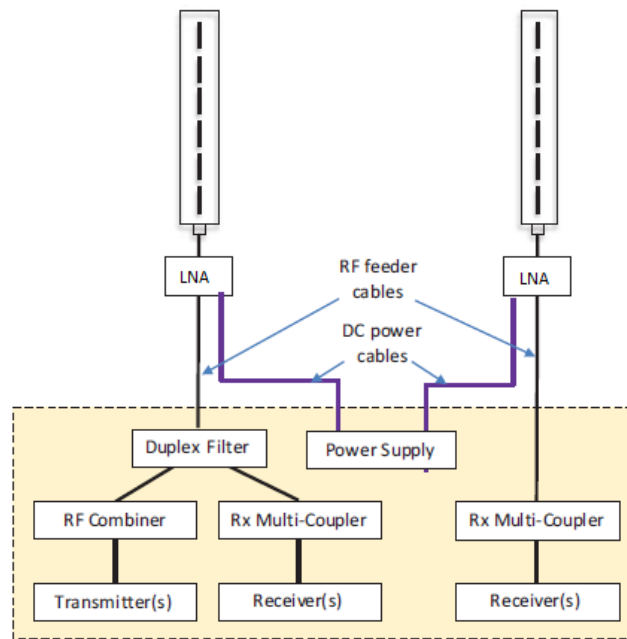
Fig. 1.2.   Typical RF and antenna system of an early GSM1800 base station [13]

Several transmitted signals are combined using an RF combiner to provide a single output containing multiple (if more than one transceiver) RF signals. The combined output forms an input to the duplex filter, which enables an antenna to transmit and receive at the same time. In this way, one antenna of the space diversity pair is a transmit/receive antenna while the other is receive-only in most common early implementations.

The antenna side of the duplex filter is extended to a tower-mounted Low Noise Amplifier (LNA) using a 50 Ω coaxial cable RF feeder. The LNA associated with the transmit/receive antenna contains two duplex filters, one either side of the receive amplifier, which splits the transmitted signal from receive and allows the transmitted signal to pass through the LNA without any active modification (albeit with slight attenuation) and is unaffected if the LNA loses its DC power source. A short coaxial cable connects the LNA to the antenna from which the transmitted signal is radiated. In the receive direction, the signal arrives at one or both antennas and is passed to the LNA in which the duplex filter directs the weak received signal to the amplifier which has a typical gain from 12 dB to 15 dB. After amplification, the duplex filter allows the received signal to travel down the main RF feeder to the base station-mounted duplex filter. The duplex filter directs the received signals to the primary and diversity receive multi-couplers (not required on the receive-only antenna). These are active RF

signal splitters which produce a number of copies of the received signal, one for each primary and one for each diversity receiver. The multi-coupler contains amplifiers to offset the losses incurred by splitting the signal. Digital signal processing algorithms within the base station determine whether the best-received signal is from one path or the other or, whether combining the two signals will improve the situation. Many of the RF components of an early GSM base station were subsequently integrated to form a single transceiver module [16].

The cable supplying DC power for the LNA was true of early LNAs (shown in Fig. 1.3) although, as these components evolved, use was made of a Bias-T device. The Bias-T device takes DC power from the base station and injects this in the main RF coaxial cable in a way that does not interfere with the higher frequency cellular radio transmissions. The Bias-T operation is reversed within the LNA to access the DC power required to operate the amplifier.
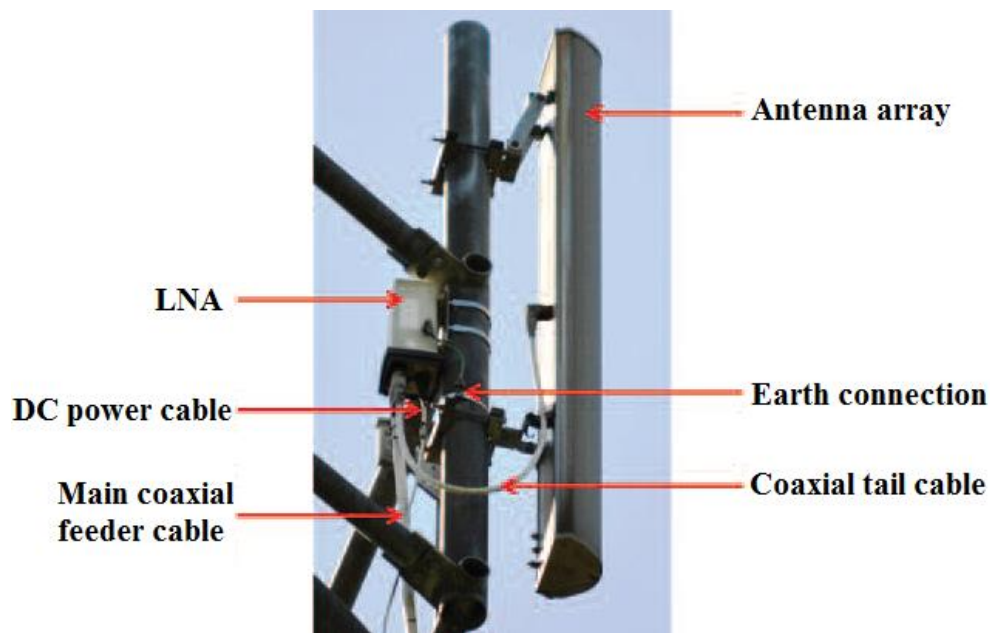
Fig. 1.3.   A vertical polarization antenna from a space diversity pair, with LNA [16]

During the late 1990s, there were significant developments into an alternative approach to uplink antenna diversity. This new design would use polarization diversity rather than space diversity. All radio wave transmissions operate at a defined polarization, the most common being either vertical or horizontal. A vertically polarized signal has an electric field, which is perpendicular to the surface of the Earth whereas the electric field of a horizontally polarized signal is parallel to the surface of

the Earth. Polarization diversity replaced two vertically polarized antennas with one antenna containing two ports (for two internal arrays), these being oriented at 45° clockwise of vertical and the other at 45° anti-clockwise. By removing the need for spatial separation, a new range of narrower towers and slim columns and lampposts could be used to support cellular antenna systems thereby reducing the visual impact and enabling new and innovative site designs [10].

Although spatial diversity performs slightly better than polarization diversity, this has to be set against the advantages of not needing to build the spatial diversity requirements into site and structure designs. Over time, polarization diversity became the solution of choice. Fig. 1.4 illustrates the concept of space diversity versus polarization diversity; each solution has two ports (antennas) for diversity.
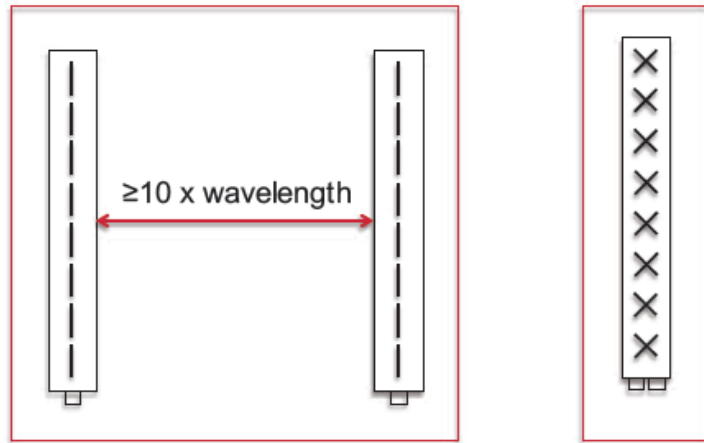
Fig. 1.4. **Vertically polarized space diversity antennas (left) compared to a polarization diversity antenna with ±45° slant polarization (right) [17]**

Additionally, as sites became ever closer in distance to support higher capacity in more densely populated areas, the slightly poorer performance of polarization diversity became less of an issue; the greater flexibility with site design is a real advantage. Likewise, in rural areas, once the new antenna performance figures were built into the propagation-modelling tool, they were automatically taken into consideration when selecting new site locations and parameters. As with all aspects of cellular radio engineering, base station antenna design is an evolving field; dual-band, dual-polarization antennas became common after the introduction of 3G UMTS systems followed by remote electrical tilts, which simplified the process of network optimization [17].

1.2.2. Rolling out 3G UMTS

The introduction of 3G UMTS in the 2100 MHz band drove the adoption of dual-band antenna systems, the majority using polarization diversity but with some space diversity systems. There are two approaches to supporting multiple frequency bands in an antenna system. Firstly, the antenna could be wideband and as such, the operating frequency bands of two or more radio systems are covered [18]. The second approach is to integrate multiple antenna arrays in a common housing/shroud such that there are two antennas per band [19]. The wideband antenna approach offers lower gain and is only practical for bands that are close to each other in frequency, i.e. 1800 MHz and 2100 MHz. The multi-antenna approach ensures maximum gain for a given operating band but requires a wider and more expensive antenna system (illustrated in Fig. 1.5).
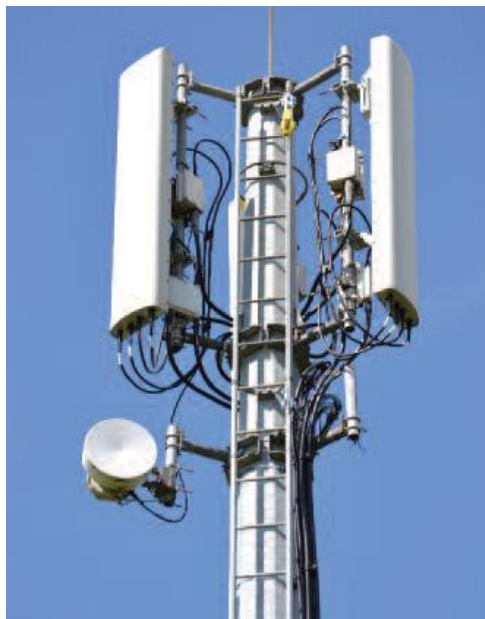
Fig. 1.5.   4-port, dual-band (1800 & 2100 MHz) passive antenna panels [19]

The radio network planning process and practical site design considerations determine which approach is adopted, often on a site-by-site basis. The significant growth of mobile data traffic has led to further densification of the 3G network using smaller base stations with limited geographical coverage deployed in hotspots to increase network capacity. These small cell sites often required small and discreet antennas.

The rollout of 3G networks was a catalyst for the introduction of network sharing; some operators sharing just passive infrastructure such as sites, power supplies, towers and antennas while others also sharing active equipment (i.e. 3G radio base stations). Antenna sharing often involves combining radio systems from different operators on to common RF feeder systems. Network sharing to varying extents is a trend, which continues today [12].

1.2.3. Moving to 4G LTE

EE launched its 4G network with the 1800 MHz spectrum, which was repurposed from GSM. This enabled a rapid rollout of 4G because it could reuse the entire antenna system that was in place to support GSM1800. The 4G spectrum auction released two new frequency bands for cellular use; these are 800 and 2600 MHz. The 800 MHz band provides greater coverage than the higher frequency band whilst the 2600 MHz band provides significantly more capacity.

The trade-off between coverage and capacity is nothing new in cellular radio engineering [19]-[20]. LTE introduced the concept of MIMO to the cellular radio interface. In its base configuration, this includes two transmitters and two receivers per radio unit (base station and user equipment), known as 2×2 MIMO. The use of MIMO increases the data rate and performance of the cellular radio interface. Higher-order MIMO modes such as 4×4 are increasingly being deployed to further enhance 4G LTE networks. A 4×4 system requires four antennas, typically 2 × cross-polarized arrays to support the base station transmission and four antennas in the mobile device [21].

The introduction of two new frequency bands had a dramatic effect on radio site design. Existing antenna systems did not support either band; therefore, a large programme of site upgrades was necessary to support the mass rollout of 4G from the operators. At the same time, a new concept for base station architecture was being adopted which involved a level of functional decomposition of the traditional rack-mounted base station into dedicated baseband capability and separate radio units. The radio transceiver could be a rack-mounted Radio Frequency Unit or Remote Radio Unit (RRU) (also known as Remote Radio Head (RRH). The split base station solution enabled the concept of Cloud (or Centralized) Radio Access Network (CRAN) as originally proposed by China Mobile Research Institute. In a CRAN architecture, the

Baseband Unit (BBU) would be centralized at a location, which connects to multiple cell sites, each cell site having multiple RRUs [13].

One of the advantages of a centralized BBU is the ability to coordinate scheduling and mitigate interference between adjacent cell sites thereby increasing overall network performance and, in particular, improving cell edge performance. The interface between the BBU and RRU is based on an industry standard known as Common Public Radio Interface, which, because of the split of functionality, has very exacting performance requirements in terms of high throughput and low latency.

Fig. 1.6 illustrates the level of complexity, which is common when multiple radio access technologies and/or frequency bands are deployed on a cell site. The diagram shows an 8-port antenna operating in four groups of two, each group of two having ±45 degrees polarizations.
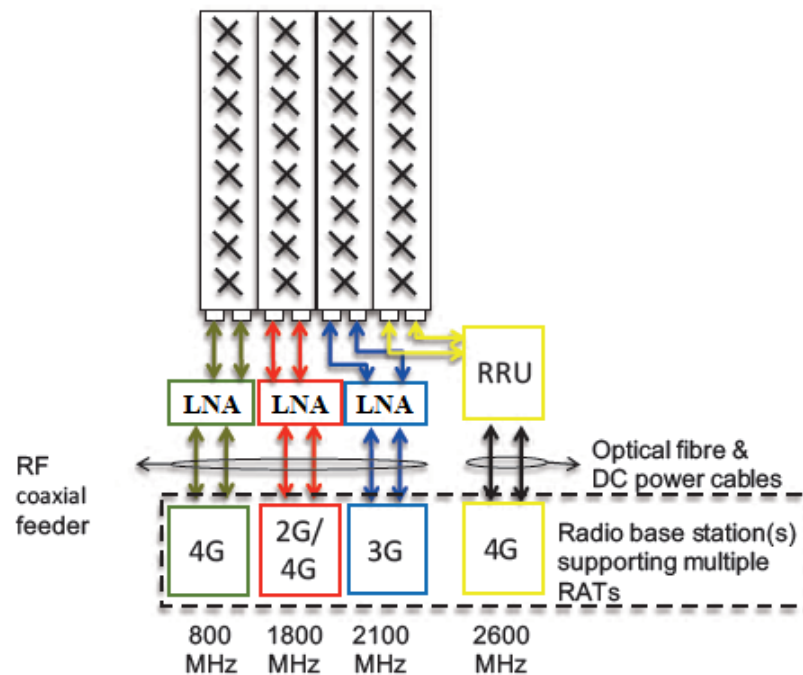
Fig. 1.6.   Multi-band antenna system supporting multiple RATs across a range of frequency bands [13]

The base station could be a single system supporting multiple Radio Access Technologies (RATs) across a range of frequency bands or could be several separate base stations contributing to the overall site build. Fig. 1.6 consists of a single base station supporting 2G in the 1800 MHz band and 4G in the 800, 1800 and 2600 MHz

bands along with a dedicated base station for 3G in the 2100 MHz band. The diagram is simplified as that the internal RF components are not illustrated, and the base station is represented as a single functional entity.

The 800, 1800 and 2100 MHz bands are all deployed with ground-mounted radio frequency units while the 2600 MHz system consists of ground-mounted baseband with tower-mounted RRU to optimize the radio interface. The attenuation of a coaxial feeder system increases with frequency and therefore the coverage at 2600 MHz can be improved by deploying the radio as close to the antenna as possible. Placing the RRU close to the antenna removes the need for an external LNA because its functionality is included in the RRU.

Fig. 1.7 shows an 8-port antenna system supporting 800, 1800, 2100 and 2600 MHz frequency bands. Each pair of ports having the same colour provides ±45° polarizations. RED ports cover the frequencies from 790 to 960 MHZ, WHITE ports cover the frequencies from 1710 to 1880 MHz, BLUE ports cover the frequencies from 1900 to 2170 MHz and YELLOW ports cover the frequencies from 2500 to 2690 MHz. Four indicators are used to indicate the beam tilting at each band [22].
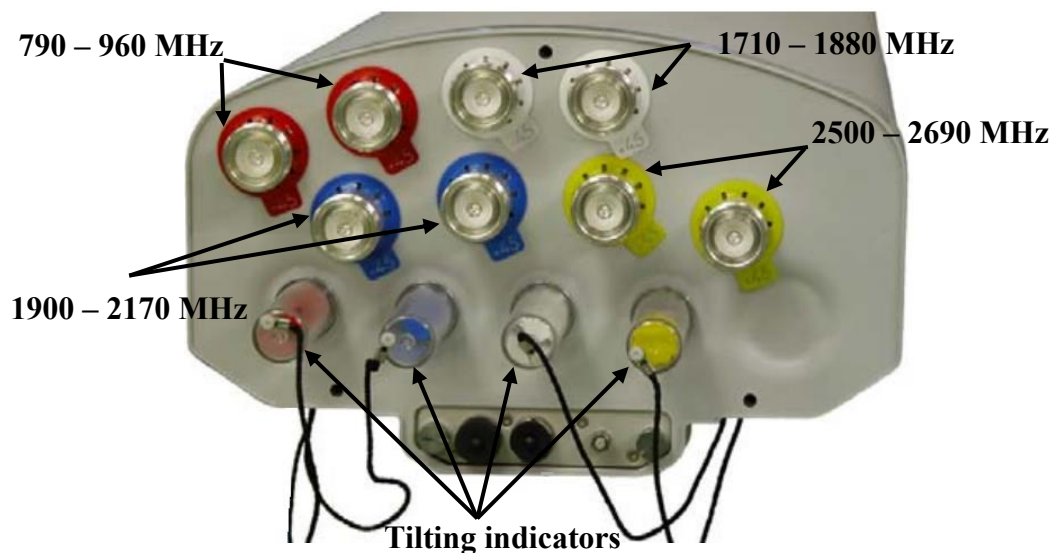
Fig. 1.7.   8-port antenna supporting 800, 1800, 2100 and 2600 MHz frequency bands [22]

1.3. Research Motivations

In recent years, mobile communications have evolved rapidly. This evolution induced a parallel development in the designing of both smartphone and base station antennas. Although many pieces of research have been conducted on the design of base station antennas, there is a continuous demand for finding new antenna solutions to meet the current and future wireless technology generations. As an example, the avenue of designing a compact reconfigurable smart antenna with tuned parameters (frequency band, radiation pattern, etc...) to meet the requirements of various cellular mobile networks in different urban areas. Moreover, the demand for offering high quality simultaneous mobile communication services (2G, 3G and 4G) with fewer numbers of antenna platforms and compact sizes. Despite a considerable amount of researches have already been done on the design of MIMO base station antennas, the design of small size, low cost, fewer elements and yet efficient and multi-standard (wideband or multi-band) diversity antennas for base stations still remains a challenging issue.

The transition from the current 4G mobile network to 5G is anticipated to occur within the near future. Realizing a superior mobile network when upgrading to higher frequencies is a big challenge, especially, for the indoor coverage where the effects of the path loss and multipath become more severe. For such cases, compact size indoor base station antennas covering multiple bands (rather than multiple narrowband antennas) are in high demand to cover multiple services (3G, 4G and 5G) simultaneously. Moreover, the limitation in the available space for the indoor application makes MIMO co-located antenna with polarization diversity a better option than MIMO widely separated antenna with spatial diversity.

The 5G wireless network is scheduled to be deployed in the early 2020s, and this commercialization process would be faster than the plan. Wireless speeds in a 5G world are expected to be remarkably fast with download rates of up to 10 Gb/s (10 times faster than current top-of-the-line Internet service) and the lag time between sending a message and its arrival should be reduced to almost nothing at less than one millisecond. Such speeds would allow a consumer to download a high-definition movie in less than a second. The 5G base station is expected to operate in two different roles. The first role is the broadcast topology where 5G offers similar services like 2G,

3G and 4G networks. Furthermore, the second role is to provide traffic topology where base station antenna allocates multiple beams for multiple users on what is called point-to-multipoint (P2MP) basis

Utilizing higher frequencies in 5G networks than their counterparts used in 4G networks arises the problem of suffering from higher path losses. This problem may be overcome by deploying more MC and/or PC base stations. To respond to the public pressure of less conspicuous base stations, the camouflage antenna is a good candidate. The challenge in this situation emerges from the trade-off between achieving good antenna performance and suitable camouflage.

Based on the above discussion, this thesis proposes several designs of smart base station antennas covering the 3G, 4G and sub-6 GHz 5G mobile networks. Each design has been validated by fabricating and measuring its prototype. Both the indoor and outdoor scenarios have been taken into consideration. Moreover, new algorithms are proposed to support the functionality of the smart base station antennas. The proposed designs and algorithms meet the shortcomings of the existing base station antenna designs.

1.4. Organization of the Thesis

The rest of the thesis is organized as follows:

Chapter 2 illustrates the main parameters and features of the base station antennas categorized according to their applications.

Chapter 3 discusses MIMO antenna systems and their design parameters. Then, it discusses the antenna diversity systems and their effects on MIMO performance. This chapter also studies the applications of MIMO systems in base station antennas.

Chapter 4 introduces a novel reconfigurable three-sector dual-mode dual-polarized antenna for use primarily in mobile communication base stations. The design offers the flexibility to be used as a sectoral (directive) or omnidirectional base station antenna whenever required.

Chapter 5 introduces and optimizes the concept of applying phased-MIMO OLAS for multi-band service where the antenna array is divided into multiple subarrays which are allowed to be overlapped. In this chapter, a mathematical formula for the

optimum partitioning scheme is derived to determine the optimum division of an array into subarrays and the number of elements in each subarray.

Chapter 6 applies the concept of using OLAS presented in Chapter 5, to a dual-broadband antenna array. Firstly, Chapter 6 proposes a novel design of a dual-broadband dual-polarized antenna for mobile communication base stations. Moreover, a new linear array is proposed and implemented. Unlike reported dual-band base station antenna arrays, the proposed array uses a novel technique of two MIMO OLAS with shared radiating antenna elements.

Chapter 7 introduces a new design of a triple-band dual-polarized indoor base station antenna for mobile communication systems serving the 2G, 3G, 4G and the new sub-6 GHz 5G applications simultaneously.

Chapter 8 introduces a new design of a dual-polarized base station antenna element for sub-6 GHz 5G communications. Furthermore, the antenna element is extended to form a planar MIMO antenna array to either perform in a broadcast or traffic communication topology whenever required. In the broadcast communication topology, the MIMO antenna array offers similar services like 2G, 3G and 4G networks. In traffic topology, the proposed MIMO antenna array can direct multiple beams to concurrent multiple users in a P2MP communication based on a novel PIS.

Chapter 9 focuses on PC base stations, which are more likely to be utilized in 5G mobile communication networks. It presents a novel transparent dual-polarized antenna array based on the element design proposed in Chapter 8. The antenna element has a transparent radiator printed on a transparent glass laminate, which gives the proposed design the advantage of being partially invisible. This low visibility allows the proposed antenna to be feasibly integrated with other daily suitable surrounding equipment to achieve visual camouflage. In Chapter 9, the street lamp is selected as an example of such surrounding equipment, which can be any other suitable one.

Chapter 10 draws the conclusions of this research work, the key contributions and, some thoughts for future work.

Chapter 2. Base Station Antenna Parameters and Applications

2.1. Outdoor Base Station Antenna

In this section, the general specifications for outdoor base station antennas are provided as well as their working principles.

In order to provide the required radiation pattern and gain, a base station antenna is typically formed of a vertical array of radiating elements. The design of each element provides the required azimuth radiation pattern characteristics, whereas the vertical extent of the array and the number of radiating elements in the array are chosen to provide the required gain.

2.1.1. Azimuth Radiation Pattern

The azimuth half power beamwidth (HPBW) of a base station antenna is chosen to suit the frequency reuse plan chosen for the network and the surrounding environment (suburban, flat rural terrain, etc.). Base stations typically support three cells spaced by 120° apart in azimuth as shown in Fig. 2.1 [5], although this plan is not universal especially where coverage may be limited by buildings or hills or where usage patterns are not uniform, as in the case of a base station alongside a major highway.
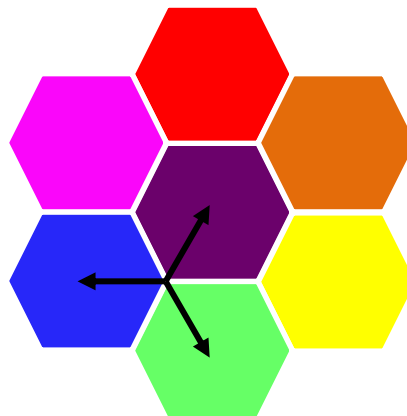
Fig. 2.1.   Hexagonal cells in a mobile communication system

Although three-sector cellular mobile networks are deployed by employing directional base station antennas, omnidirectional base station antennas are not less important. In case of severe shadowing, changing the location or height of the base station antenna may resolve the problem but may also cause an issue with the frequency re-use of the closest neighbour cell that uses the same frequency. This issue is well known as "co-channel interference". In this case, adding an omnidirectional base station antenna is a better option to cover the unserved spots.

To understand how the surrounding environment affects the HPBW of a base station antenna, let us consider cell plan as shown in Fig. 2.1. The objective is to provide equal signal strength on the border of the hexagonal cell. In this way, the SNR is constant for all mobile terminals on the edge of the cell, i.e. the location where communication with a base station is expected to be most difficult. Assuming that the received power at the mobile, P_{RX}, linked to the transmitted power at the base station, P_{TX}, is described by Friis' formula [23]:

$$P_{RX} = P_{TX} \left(\frac{\lambda}{4\pi}\right)^2 \left(\frac{1}{R}\right)^\gamma G_{RX} G_{TX}(\Phi) \tag{2.1}$$

where $G_{TX}(\Phi)$ and G_{RX} are the gains of the base station antenna and mobile (omnidirectional) terminal antenna respectively, λ is the wavelength, R is the distance and Φ is the azimuth angle measured from the boresight of base station antenna. The exponent γ has empirically been found to be in the range from 3 to 5 for propagation in typical mobile communication environments.

If the hexagon shape of the cell is approximated to a circle, the distance to a point on the cell border is approximately $R(\Phi) \approx 2r_0 \cos(\Phi)$ where r_0 is the length of the side of the hexagon. For a constant radiation intensity on the cell border, the following condition should be satisfied [24]:

$$\frac{G_{TX}(\Phi)}{R(\Phi)^\gamma} = \frac{G_{TX}(\Phi)}{\left(2r_0\cos(\Phi)\right)^\gamma} = constant \tag{2.2}$$

Thus, if $\gamma = 4$, which is a typical value for a suburban environment, the ideal radiation pattern should be $cos^4(\Phi)$. If this is translated to base station antennas, which are typically defined by their HPBW, we should look for a beamwidth of [24]

$$HPBW = 2cos^{-1}\left(0.5^{\frac{1}{\gamma}}\right) \tag{2.3}$$

In this case, the horizontal HPBW has been found to be 65°. If γ is assumed to be 2 instead, which could be the case for a very open flat rural terrain, the optimum HPBW is around 90° instead.

2.1.2. Elevation Radiation Pattern

To provide a maximum field strength to the intended covered area of a cell, the elevation HPBW and the elevation angle of the maximum radiation should be assigned properly. If the maximum radiation of a base station antenna is left-aligned in the horizontal plane without being down tilted in the elevation plane, mostly the maximum radiation over the surrounding area will pass over the heads of most users especially at a long distance where the curvature of the earth takes effect. By tilting the beam of the base station antenna slightly downward, the field strength toward the users in the covered area of service will increase. Consequently, the power radiated towards the neighbour cells will decrease which leads to a significant improvement in the carrier-to-interference ratio in neighbour cells, which share the same frequency. The situation can be compared to dipping the headlights of a car to avoid dazzling the approaching drivers [14].
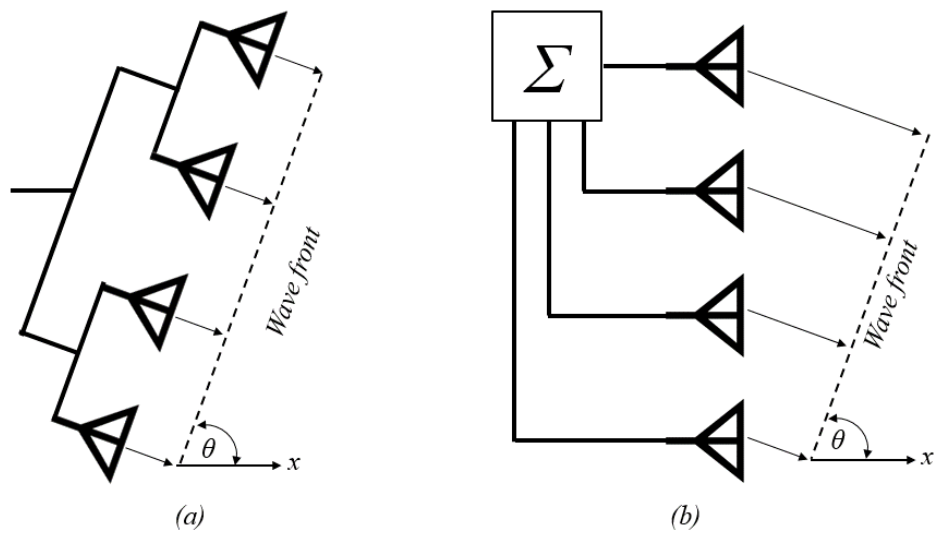
Fig. 2.2.   Illustration of the down-tilting in base station antennas

(a) mechanically (b) electronically [14]

The angle at which the maximum radiation in the elevation plane is placed below the horizontal plane is known as the beam tilt angle of the antenna. The beam tilt angle can be achieved by two means; mechanical tilting or electronic tilting. In mechanical tilting the base station antenna array is physically tilted downward meanwhile in the electrical tilting, phase shifters are used to control the feeding phase of each antenna element and hence steer the wavefront electronically downward while the array structure lies vertically to the platform as presented in Fig. 2.2 [14].

In mechanical tilting, while the main lobe is tilted downward, the back lobe is tilted upward which may cause severe interference with the neighbour cells using the same frequency. Moreover, beam squint is caused due to mechanical tilting which distorts the main lobe footprint. On the other hand, applying electronic tilting needs to utilize more antenna and phase shifter modules to avoid gain reduction due to beam steering. In most situations, both electrical and mechanical titling are used and the net titling is the sum of both.

2.1.3. Gain

The mobile communication networks are usually provided with antennas which have the highest gain economically possible. This reduces the number of stations needed and improves in-building penetration. The antenna gain is a function of both the azimuth HPBW and the vertical electrical length [25]. The maximum length of the base station antenna array is determined by the maximum physical length that may be accepted without being too conspicuous or by the minimum accepted vertical HPBW. The length and the attenuation of the internal feeding transmission lines increase as a consequence of increasing the array length. Thus, increasing the array length may increase its directivity but not the gain.

For uniform excitation of a base station antenna array, a number of minor lobes and nulls are formed above and below the main lobe. Nulls below the main lobe (especially the first null) may cause a poor (or even blind) spot at the area of coverage near the base station. Moreover, side lobes above the main lobe may interfere with neighbour cells if the radiation pattern is down tilted or if the terrain rises between a base station and another. So, elevation pattern shaping is widely used to fill the nulls below the main lobe (at least the first null) and suppress the side lobes level above the main lobe as shown in Fig. 2.3 [25].

Choosing the base station antenna location and height may resolve shadowing problems. On the other hand, very high base station antenna may cause a problem with frequency reuse [16]. In this case, adding micro-cell (MC) and/or pico-cell (PC) base stations are better options to cover the uncovered spots.
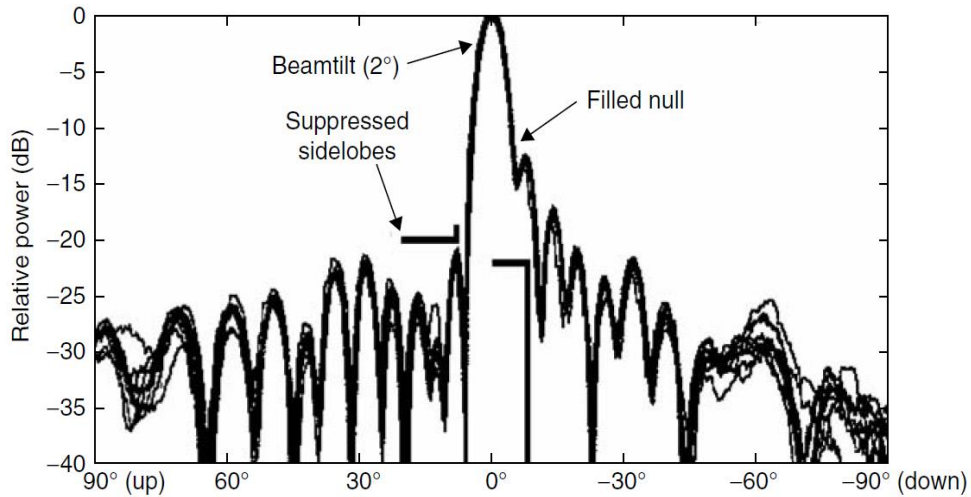
Fig. 2.3.   A typical beam pattern of a base station antenna in the elevation plane after applying elevation pattern shaping [21]

2.1.4. Diversity and Isolation

When a mobile user moves within a covered area, the received signal strength by the base station antenna fluctuates widely due to the multipath effect. A diversity system uses two (or more) antennas and combines their outputs in a manner that can utilize the uncorrelated fluctuated signals at each antenna terminals [26]-[27]. The main benefit of using a diversity system is to increase the availability of the received signal. For a given signal availability, this increase can be simply achieved by increasing the transmitted power. Therefore, diversity gain can be defined as the increase in the power required to achieve the stated availability [27].

The transmitted signal from a mobile terminal is strongly polarized in the direction of its long axis. In most cases, the handset is typically held between the user's mouth and ear radiating a linear polarized wave at around 45°. Thus, the diversity gain obtained from a pair of antennas with vertical and horizontal polarizations is exceeded by a pair of linear polarized antennas located at ±45° from the vertical axis. Moreover, the ±45° linear polarized antennas have identical effects due to multiple reflections rather than the different effects resulting from vertical and horizontal polarizations.

Therefore, dual ±45° polarization is applied almost universally for polarization diversity in base station antennas.
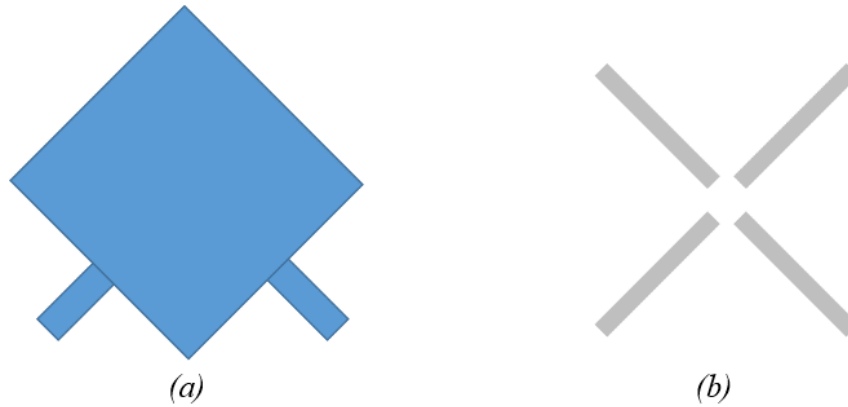
Fig. 2.4.   Dual-polarized radiating antennas (a) patch (b) crossed dipole

The Cross Polarization Discrimination Ratio (XPD) is an essential requirement in antennas, which utilize dual-polarization as a diversity system. The higher XPD, the purer received signal at the antenna port dedicated to its polarization [28]. This can be achieved easily on boresight of a dual-polarized antenna boresight. Unfortunately, achieving a constant polarization is not an easy task across a wide range of azimuth angles. Take an example of a diagonal patch or crossed dipole, which has ±45° dual-polarization as shown in Fig. 2.4. In the boresight direction, the transmitted signals are orthogonal at ±45°. Deviating from the boresight, the polarization angle tends towards 90° (vertical) simply because of the geometrical arrangement. The required XPD for a base station antenna on boresight is typically 23 dB meanwhile at the edges of a sector it is likely to drop to 10 dB [24].

During downlink communication, each antenna transmits half of the transmitted power. There should be at least 25 dB isolation between the antennas. In most cases, achieving 25 dB isolation between the two ports of a dual-polarized antenna is not an easy task. Significant coupling exists between the adjacent ±45° elements. To avoid this coupling, several decoupling methods may be applied to arrays [29].

2.1.5. Power Handling Capabilities

The average output power of a base station is typically not more than 20W. However, due to that several transmitters may be combined into each antenna and the fact that the peak power of the radio signal may be up to 10 times greater than the

average, the base station antenna is often required to withstand at least 500W input power. Sometimes even 1000W. If any part within the base station antenna structure including feeding ports, coaxial cables, power dividers, phase shifters and radiators will not be able to handle this level of power, catastrophic failures in the base station may happen [21] as in Fig. 2.5.

Fig. 2.5.   Failure of base station antennas which cannot handle high powers

2.2. Indoor Base Station Antennas

For indoor base station antennas, high gain is not of high importance as for outdoor base station antennas. However, because of the limited available spaces in indoor places such as shopping malls, parking garages and airports, it is favourable to have a single multi-band or broadband antenna element rather than multiple narrowband antenna elements to offer multiple services over a certain spot. Moreover, due to the dense uncorrelated multi-path reflections in indoor communications, MIMO antenna systems are desirable and efficient. In such cases, co-located antennas with polarization diversity are more favourable than widely separated antennas with spatial diversity for more space-saving. Typically, two scenarios are used to install an indoor base station antenna [21]:

   (a) Wall-mounted antenna: in this scenario, the radiation pattern of an antenna should be unidirectional with a wide horizontal HPBW to ensure wide coverage and an average gain of about 6 dBi. An example of such an antenna is presented in Fig. 2.6(a).

(b) Ceiling- mounted antenna: in this scenario, the antenna should have a conical radiation pattern, which may be obtained using a patch antenna for example. The antenna is mounted on the ceiling (as in Fig. 2.6(b)) and radiates downwards towards the users.
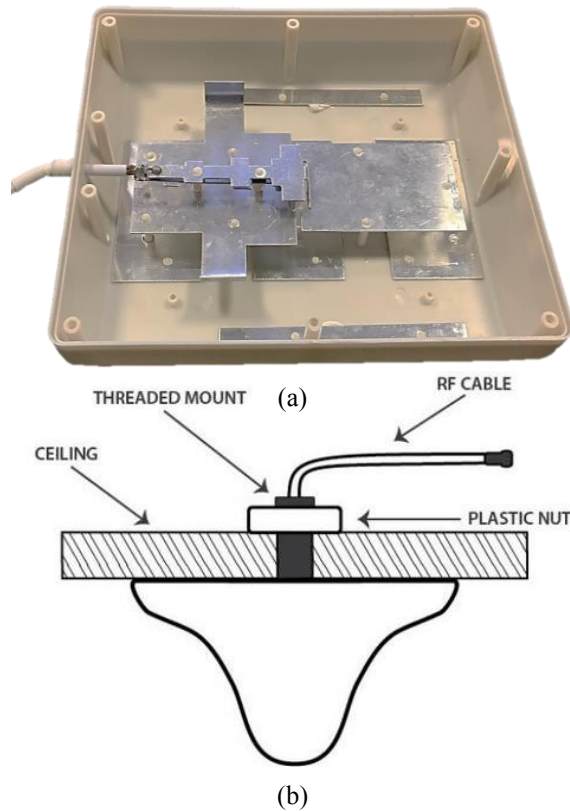
Fig. 2.6.   Indoor base station antennas
(a) Wall-mounted dual-band antenna (b) Ceiling-mounted antenna

2.3. Multiband Antenna Arrays

In most countries, users have access two or more mobile communication services (2G, 3G, 4G, etc...). These services operate across different frequency bands. To minimize the cost and platform space of base station installation, and to respond to public pressure for less conspicuous antenna systems, designers tend to produce base station antennas operate over several frequency bands simultaneously. Replacing the existing single band antenna array with a new multiband antenna array could be a challenge because of the array physical dimensions limitations, the grating lobes phenomena, the PIM products and many other issues. However, most solutions fall into one of the following categories:

2.3.1. Independent Antennas Mounted Side-by-Side under a Single Radome

This kind of arrays has several arrangements. Mostly the antennas comprise of two arrays with the same overall physical length and typically follows one of the following combinations:

Array 1	Array 2
850 and/or 900 MHz	1800 and/ or 1900 MHz
1800 and/ or 1900 MHz	1900-2170 MHz
1900-2170 MHz	2170-2700 MHz

Although both arrays have the same physical length, they have different azimuth HPBW, polarizations and, sometimes, different electrical elevation beam tilt [21].

A significant problem facing this arrangement of antennas is that the arrays operate on an asymmetrical reflector. Being mounted side-by-side, the reflector for each array extends farther on one side rather than the other. This leads to an asymmetrical azimuth pattern and the beam maximum squints off-axis [21].

2.3.2. Interleaved Arrays

As base station antenna arrays operate over different frequency bands, the spacing between the antenna elements at the higher band arrays is smaller than their equivalents at the lower band arrays, sometimes by a half. Thus, an array structure can be devised in which the high band and the low band antenna elements are co-located and interleaved with a spacing between the same band-elements slightly less than one wavelength as shown in Fig. 2.7. Mostly, the lower band antenna elements are formed as bowls and the higher band antenna elements are nested inside them [30].
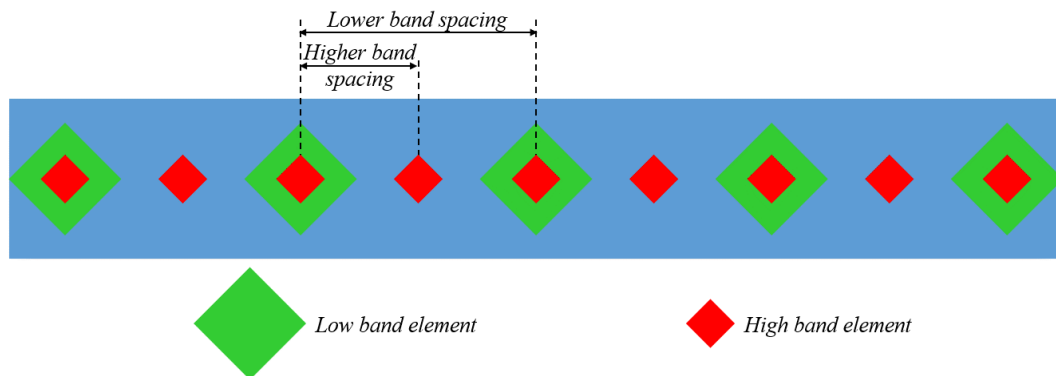
Fig. 2.7.   Example of an interleaved array

The overall physical and electrical specification of the interleaved array will be very similar to the lower band array in terms of dimensions, gain, azimuth and elevation HPBWs, etc. The interleaved dual-band antenna array typically consists of around 5 elements for the lower band and 10 elements for the higher band.

The required isolation between the lower band and the higher band arrays should be around 25 dB to avoid interactions between transmitters. This high level of isolation may not be easy to achieve because of the close proximity of the bowel and nested elements, hence, filters are commonly used to improve isolation [28].

2.3.3. Wideband Arrays

This type of arrays is based on wideband antenna elements. The feasibility of such an array is complicated and difficult. So, the use of wideband arrays is limited. The following discussion expresses the reasons. Dual-polarized wideband antenna elements with sufficient BW are quite large devices with complex mechanical features. To avoid grating lobes, the distance between two successive elements should not exceed one wavelength at the higher band when they are arranged to form an array. Meanwhile, the physical dimensions of the antenna module itself are around half wavelength at the lower band. Even if the antenna element can be compressed using miniaturization techniques, high mutual coupling between the elements at the lower band severely degrades the overall gain and affects the array input impedance [28].

2.4. 5G Base Station Antennas

As mobile communication systems are moving rapidly towards 5G services, which are going to be deployed in the near future, base station antennas have been evolved to meet the new requirements of the 5G services. The main challenge facing the 5G base station antenna designers is that 5G base stations are going to be involved in two different roles. The first role is that they are going to perform side-by-side with 3G and 4G base station antennas to provide signal broadcasting. Moreover, the second role is to provide multiple beams for multiple concurrent users on a Point-to-Multipoint (P2MP) basis [31]. M-MIMO system is considered as the key technology in 5G wireless communications. In addition to the considerations mentioned in the previous sections about the parameters of the conventional 3G and 4G base station antennas,

5G base station antennas are denoted to have more features to deploy the functionality of multiple beams. Fig. 2.8 illustrates multiple-beam M-MIMO base station antenna in 5G mobile communications.
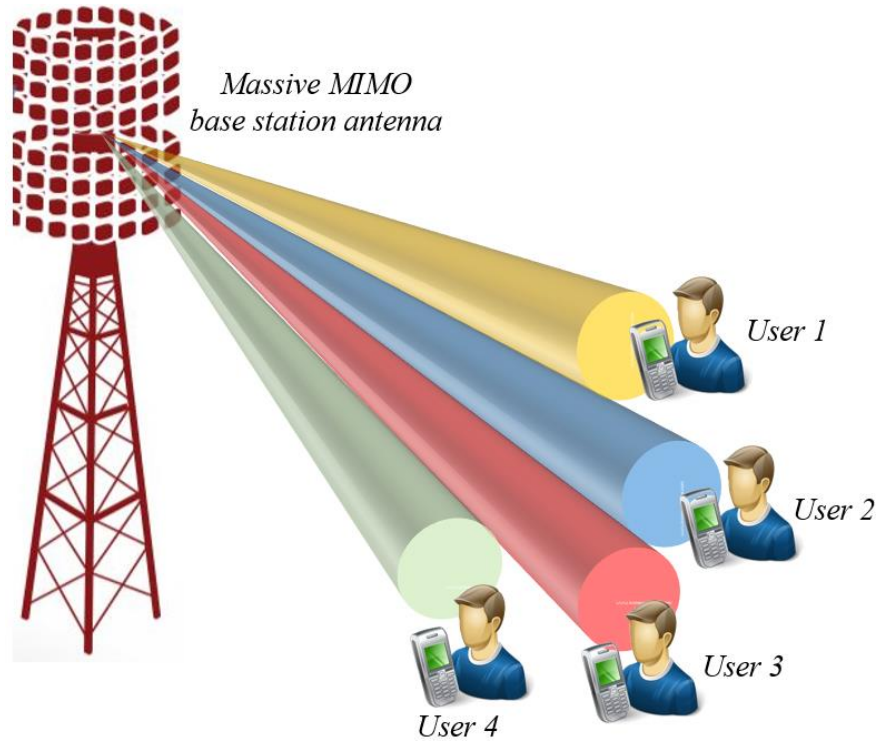
Fig. 2.8.   Multiple beam M-MIMO base station antenna

The multiple beam antennas are capable of generating a number of simultaneous and independent highly directive beams. The generation of multiple beams can be categorized into three major types: analogue static multi-beam antenna, analogue dynamic multi-beam antenna and digital dynamic multi-beam antenna [32].

2.4.1. Analogue Static Multi-beam Antenna

In analogue statistic multi-beam antennas, the beamforming is achieved in the RF domain without utilizing any active components. Generally, this technique uses a finite number of ports which of each is backed by a transceiver and controls a single narrow beam pointing toward a pre-defined direction. This technique is usually of low cost. Orthogonal beamforming network as Butler matrix (shown in Fig. 2.9) and Blass matrix are very common in this technique [23]. Other methods based on quasi-optical components including Rotman lens, Luneburg lens and reflector may also be used [32].
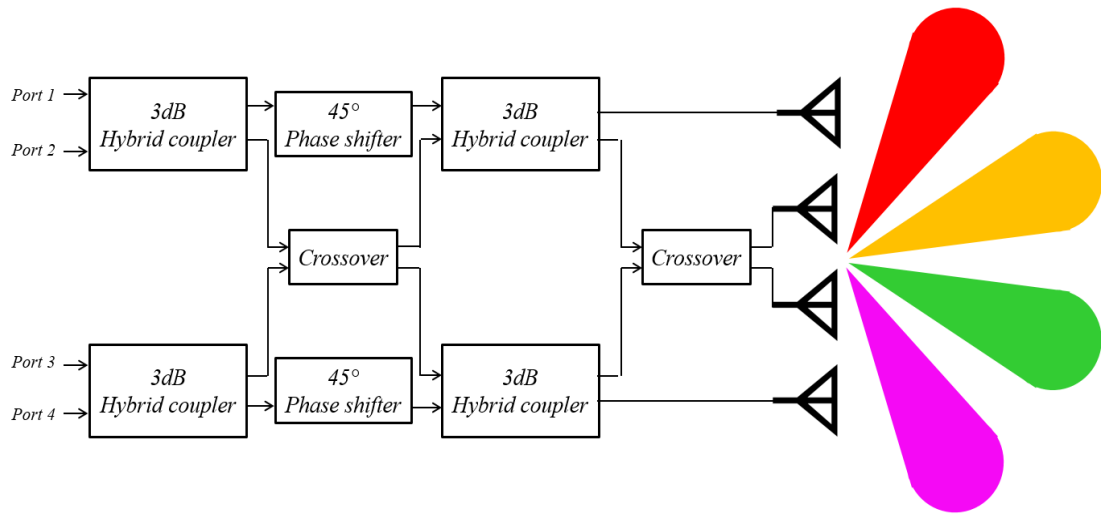
Fig. 2.9. **A 4 × 4 Butler matrix used in analogue static multi-beam antenna**

2.4.2. Analogue Dynamic Multi-beam Antenna

Generating multiple concurrent beams using a phased antenna array has been developed a lot over the last few decades. RF phase shifters and adaptive amplifiers are considered as the most important parts in analogue dynamic antenna arrays as they play an essential role in forming multi-beam radiation. Therefore, these RF modules should be of low insertion loss, broad BW, high precision, low cost, fast response and easy integration facilities to meet the requirements of the 5G network. These requirements make the design of an analogue dynamic multi-beam antenna a big challenge for base station antenna designers [31]. The block diagram of this technique is shown in Fig. 2.10.
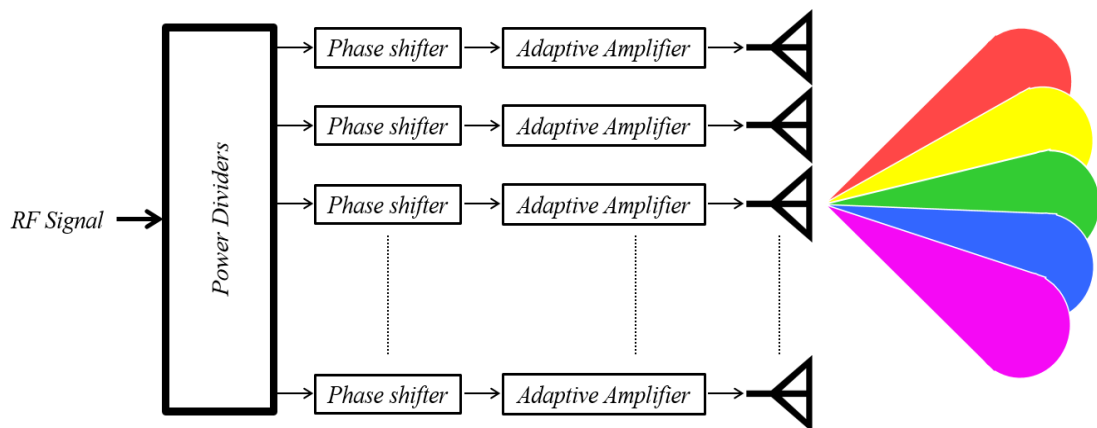
Fig. 2.10. **Analogue dynamic multi-beam base station antenna**

2.4.3. Digital Dynamic Multi-Beam Antenna

Performing the beamforming in the digital domain at the baseband is a flexible approach. This type enjoys high robustness against any failure of a few antenna elements. Therefore, it is considered as the ultimate target of beamforming. Each antenna element has its own amplifier without any phase shifter or attenuator. As a result, the antenna part consists of antenna elements only with a good radiation phase consistency. Since the beamforming is processed in the digital domain, a large number of analogue-to-digital (ADC) and digital-to-analogue (DAC) converters are needed. In addition, the transmission loss, heat dissipation and the overall cost would be issues [31]. The block diagram of the digital dynamic multi-beam antenna is illustrated in Fig. 2.11.
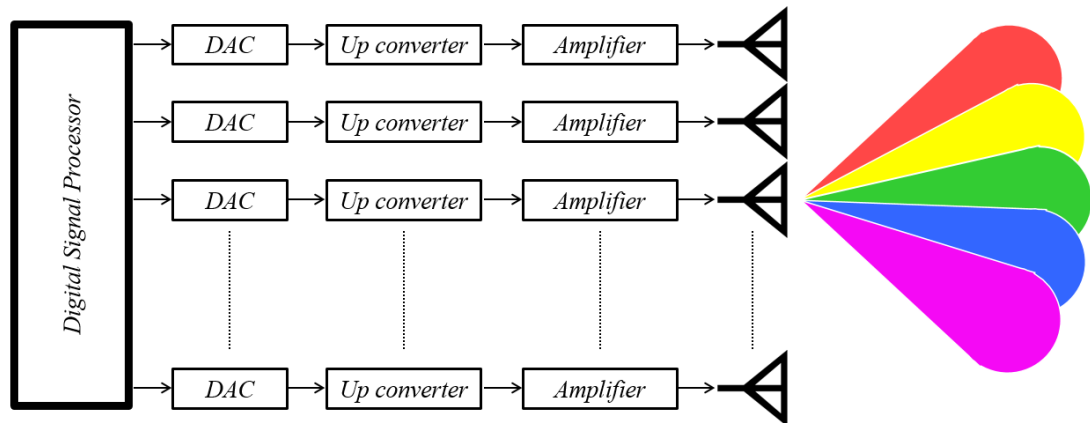
Fig. 2.11.   Digital dynamic multi-beam base station antenna

The pros and cons of the analogue and digital beamforming solutions can be summarized and tabulated in Table 2.1. Therefore, hybrid digital and analogue multi-beam systems have recently attracted researchers' interest as a trade-off between analogue and digital techniques.

Table 2.1.   Advantages and Disadvantages of Beamforming Approaches

Technique	Advantages	Disadvantages
Analogue beamforming	• Few transceiver chains meaning low power consumption due to the limited number of ADC and DAC for many antennas.	• Less flexible than digital beamforming. • Implies users are separated in time thus puts constraints on implementation. • Difficult to get channel estimates if at RF.
Digital beamforming	• Null steering/ zero forcing possible since channel responses are known at the baseband. • A higher degree of freedom.	• Significant power consumption and cost due to high-speed ADC and DAC required in each transceiver.

2.5. Summary

Although base station antennas share some common challenges, they have different parameters according to their applications. These parameters can be achieved by utilizing different technologies. In this chapter, an overview about base station antenna features and parameters have been discussed for different applications and across different mobile communication services.

Chapter 3. MIMO Antenna Systems

Advanced wireless technologies like LTE have introduced MIMO [33] as one of the key steps to achieve high data rates without the need for more spectrum or higher transmit power. MIMO employs more than one antenna at both the transmitter and the receiver in a scattering environment to create multiple uncorrelated channels between them. This can be used to provide higher data rates, higher received SNR and increased robustness to interference [34].

For base station antennas, although applying MIMO using spatial diversity performs slightly better than MIMO based on polarization diversity, this has to be set against the advantages of not needing to build the spatial diversity requirements into site and structure designs. Over time, the MIMO system based on polarization diversity became the solution of choice [35].

In this chapter, the various antenna diversity techniques and the key parameters of MIMO antennas are discussed. In addition, a discussion of MIMO techniques in base station antennas is also included.

3.1. MIMO System
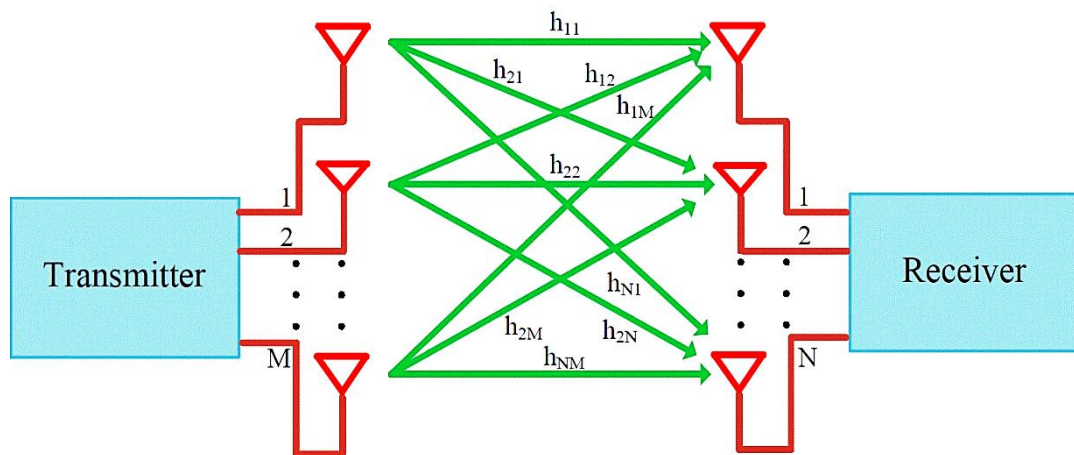
Fig. 3.1.   **MIMO system [36]**

The MIMO concept as a technique to increase wireless system capacity was first investigated in the 1990s [36]-[37]. Since then, it has been under research worldwide [38]-[44]. Fig. 3.1 gives an illustrative diagram of a generic MIMO system. Different from a conventional single antenna system, a MIMO system has multiple transmitting M and multiple receiving antennas N. Each receiving antenna can receive signals from all the transmitting antennas, creating $M \times N$ signal transmission paths.

A MIMO system is not the first time when multiple antennas have been used in wireless communication. Early on, multiple antennas (e.g. antenna array) were used to enhance system SNR through beamforming by concentrating antenna radiation energy to a specific direction. Later on, multi-antennas were used to provide spatial diversity, countering the multipath fading effects. With multiple receiving antennas at a certain distance in between, signals from different propagation paths can be picked up independently by the multiple antennas and then added together constructively. Since the chance of all the signal paths suffering from strong multipath fading is much lower, the system bit error rate (BER) is significantly reduced in this way. However, spatial diversity from multiple antennas has limited benefits. What makes multiple antenna systems powerful and appealing is the extra spatial multiplexing it offers. With multiple independent signal propagation paths between the multiple transmitting and multiple receiving antennas, multiple independent data streams can be transmitted through those independent paths. Take the example in Fig. 3.1. Assuming no signal and noise correlation at both transmitter and receiver sides, the capacity of the MIMO system increases linearly with respect to the minimum number of transmitting/receiving antennas (*min {M, N}*) [36]-[37], at no more cost on either power or spectrum resources. Due to this significant advantage in spectral efficiency over conventional single-antenna systems, MIMO has become an essential element in many wireless communication standards, such as 4G LTE, WiMAX and 5G.

3.2. Antenna Diversity Techniques

To reduce the spatial correlation between antennas and to generate replicas of a signal for diversity purposes, frequency diversity, time diversity and antenna diversity are used widely. As this thesis is concerned with antenna diversity, this section only discusses antenna diversity techniques like spatial diversity, polarization diversity and

pattern diversity as shown in Fig. 3.2. All multi-element antennas combine these diversity techniques in order to achieve high performance when employed in MIMO systems [36]-[37].

(a)   (b)

(c)
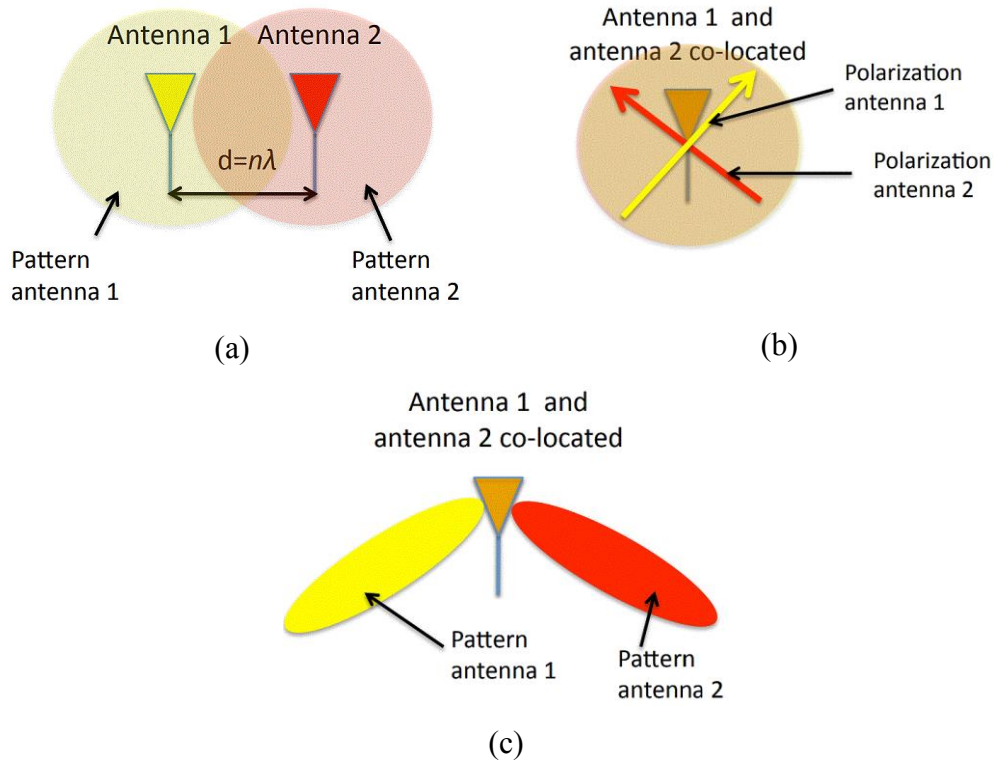
Fig. 3.2.   Three different antenna diversity techniques:
(a) spatial diversity, (b) polarization diversity and (c) pattern diversity [36]

3.2.1. Spatial Diversity

The simplest and most common form of diversity in wireless communications is spatial diversity [45]-[46] as depicted in Fig. 3.2(a). By having antennas at two separate points in space, the phase delay between them can allow the fading signal in the second antenna to be uncorrelated with the first antenna. In order to achieve sufficient decorrelation, the antennas must have a minimum spacing depending upon the surrounding environment and in particular upon the width of the multipath angle of arrival. It has been shown in [45] that a spacing greater than 10λ is required in an urban area to have complete decorrelation, while in an indoor environment with rich scattering, a minimum spacing of only 0.5λ is necessary [46]. Fig. 3.3 shows an example of two base station antennas that utilize spatial diversity.
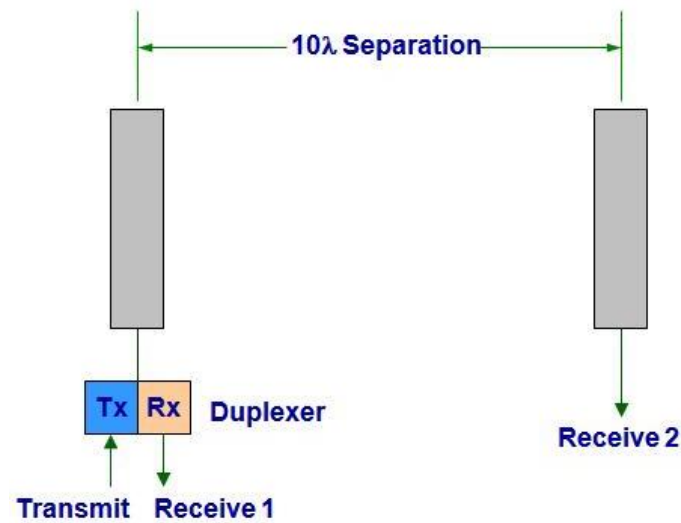
Fig. 3.3. **Spatial diversity [45]**

3.2.2. Polarization Diversity

Unlike spatial diversity, the benefits of polarization diversity include the ability to locate the antennas in the same place. The impact of polarization diversity on sub-channel decorrelation and channel capacity in MIMO systems have been studied through simulation and measurements mainly employing dual-polarized antennas [47]-[50]. It has been shown that by employing a dual-polarized system of co-located antennas, it is possible to achieve almost the same channel capacity achieved through spatial diversity [47].

Fig. 3.4. **Polarization diversity [49]**

While previously it was thought that only two different polarizations (vertical and horizontal) could be used to de-correlate the communication sub-channels, it has been demonstrated in 2001 that it is possible to use all three electric field components and all three magnetic fields components, as in Fig. 3.4, to drastically increase the capacity of a MIMO communication link [49]. The design of novel antennas that can propagate waves to cause independent fluctuations in all six electric and magnetic field components has attracted a lot of attention [49].

3.2.3. Pattern Diversity

The diversity gain can be large if multiple antennas have different patterns. In pattern diversity, the antenna system consists of two or more co-located antennas with different radiation patterns. This type of diversity makes use of directional antennas that are usually physically separated by some (often short) distance. Collectively they are capable of discriminating a large portion of angle space and can provide a higher gain versus a single omnidirectional radiator [51].

This kind of diversity can guarantee the reception of different sets of multipath waves [51]-[53]. Pattern diversity has been used at base stations [54], [55] and a similar performance to that of spatial diversity was achieved, especially, in dense urban areas. Fig. 3.5 shows an example of a 5G base station system that utilizes pattern diversity.
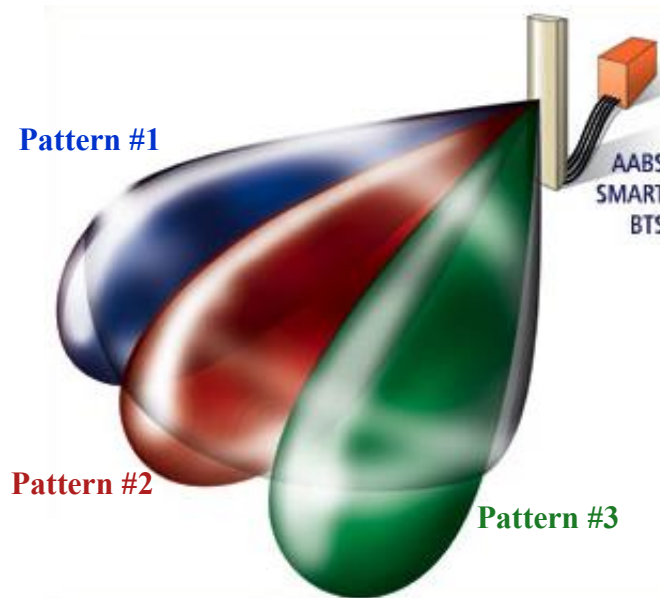
Fig. 3.5.   Pattern diversity [54].

3.3. MIMO Antennas and Key Parameters

By the introduction of MIMO technology, the design of multiple antennas at both the base station and the mobile terminal has received great research attention. In addition to the new design challenges that are brought by implementing multiple antennas in compact sizes, this new technology created more performance parameters than those of a conventional single antenna system. While single antenna metrics such as total radiation efficiency, radiation patterns, reflection coefficient and operating BW are required to characterize MIMO antennas [56], new metrics are added such as mutual coupling, Envelope Correlation Coefficient (ECC) and diversity gain [57].

3.3.1. Mutual Coupling

The presence of multiple antennas near each other creates an interaction among them known as mutual coupling [58]. This coupling is due to an induced current flowing in one antenna element from the excitation of the other antenna element. This alters the input impedance of each antenna element in which the input impedance was defined by both self-impedance and mutual impedance. This change produces an impedance matrix which contains both the self-impedances (Z_{ii}) and the mutual impedances (Z_{ij}) as shown in equation (3.1).

$$Z = \begin{bmatrix} Z_{11} & \cdots & Z_{1N} \\ \vdots & \ddots & \vdots \\ Z_{N1} & \cdots & Z_{NN} \end{bmatrix} \qquad (3.1\ )$$

As an inevitable result of the creation of the impedance matrix, antenna BW is no longer depends only on the reflection coefficient but on both reflection and transmission coefficients as shown in the S-parameter matrix in equation (3.2).

$$S = \begin{bmatrix} S_{11} & \cdots & S_{1N} \\ \vdots & \ddots & \vdots \\ S_{N1} & \cdots & S_{NN} \end{bmatrix} \qquad (3.2\ )$$

S_{ii} is the ratio of the reflected wave voltage to the incident one at the port of the ith element when all other elements are terminated with matched loads. While S_{ij} represents the ratio of the transferred voltage from the jth element port to the ith element port to the incident voltage at the jth element port, S_{ij} is also known as the mutual coupling coefficient. Typically, a mutual coupling from -20 to -25 dB is acceptable for base station antenna [56].

3.3.2. Envelope Correlation Coefficient (ECC)

Up to this point, it has been mentioned many times that in order to achieve a good MIMO and diversity performance, the received signals at the receiver of the diversity system should be independent of each other. This independence can be measured and quantified using the correlation coefficients [57], [59]-[61].

Experimentally, the calculation of correlation coefficients can be done using the pattern approach [59], which is time-consuming, as it needs a 3D radiation pattern. Therefore, the correlation coefficients can be defined in another form which is the ECC. This can be done using S-parameters approach [62] as shown in the following equations:

$$ECC = \frac{\left|S_{ii}^* S_{ij} + S_{ji}^* S_{jj}\right|^2}{(1 - |S_{ii}|^2 - \left|S_{ji}\right|^2)(1 - \left|S_{jj}\right|^2 - \left|S_{ij}\right|^2)} , i \neq j \qquad (3.3)$$

Although the S-parameters approach in [62] is very simple and fast, it is only accurate for the case of loss-free antennas. Therefore, the S-parameter method has been modified in which the effect of the radiation efficiency has been taken into account [63]. Equation (3.4) represents this new method, which is used widely in the calculation of the ECC [64], [65]:

$$ECC = \left|\frac{\left|S_{ii}^* S_{ij} + S_{ji}^* S_{jj}\right|}{\left|(1 - |S_{ii}|^2 - \left|S_{ji}\right|^2)(1 - \left|S_{jj}\right|^2 - \left|S_{ij}\right|^2)\eta_{radi}\eta_{radj}\right|^{0.5}}\right|^2 , i \neq j \qquad (3.4)$$

where η_{radi} and η_{radj} represent radiation efficiencies of the antennas i and j respectively. For a good diversity gain, the ECC among received signals should satisfy the condition [59], [60] as follows:

$$ECC \leq 0.3 \qquad (3.5)$$

3.3.3. Diversity Gain

The spatial diversity combats multipath fading via sending multiple versions of the same transmitted signal to the receiver through the multipath channel. Therefore, if one of the diversity combining techniques is deployed at the receiver, the receiver can

have more freedom in choosing the best-received signal (best SNR), which will improve the reliability of the wireless system. This improvement is called the diversity gain, which is the improvement in the received SNR at the output of the diversity combiner relative to the SNR resulting from a reference single antenna at a certain level of performance criterion such as cumulative distribution function (CDF) [64], [65]. CDF is plotted in Fig. 3.6 and a diversity gain of 10 dB can be seen when the number of diversity branches is increased from 1 to 2 at 1% probability.
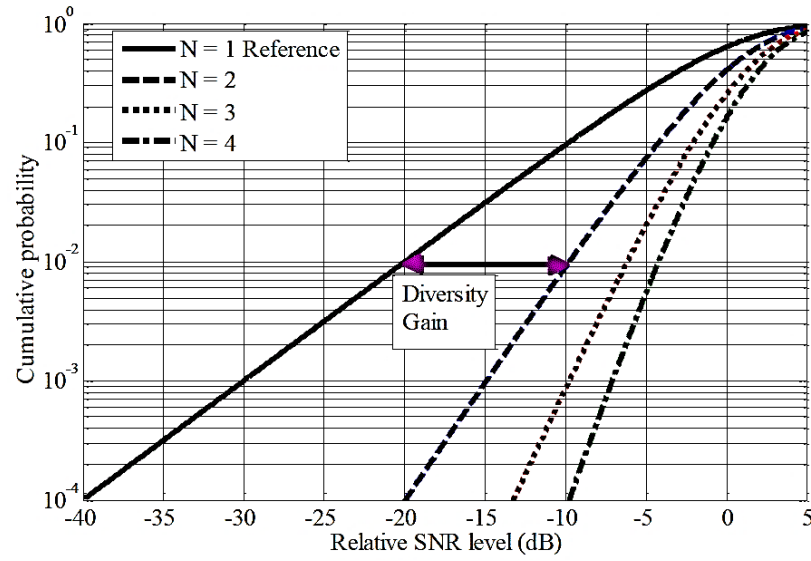
Fig. 3.6.   CDF of relative SNR threshold for N different diversity branches [64]

Although the diversity gain is easily predictable from the measured and calculated CDF, some information such as the frequency range is lost during the post-processing and the generation of the CDFs. In many cases, it is important to know how the diversity gain varies as a function of frequency. To do this, the ECC between measured samples from each diversity branch is calculated using equation (3.4) and used for the calculation of the diversity gain as in equation (3.6) [66].

$$Divesity\ Gain = 10.48\sqrt{1 - ECC}$$

(3.6)

3.4. MIMO Antenna for Base Stations

Currently, base stations use multiple antennas for reasons of diversity. The obtained diversity gain increases as the spatial correlation between signals reduces. In a MIMO system, the relationship between spatial correlation and performance is more complex

[67]. For example, at the edge of the cell where signal strength is low, it is preferable to use diversity-based single-stream transmission strategies that require one of the spatial channels to be significantly stronger than the others. This is possible when the spatial correlation between signals received at the antenna elements is high. In contrast, when the signal strength is high (near the base station), it is beneficial to use spatial multiplexing strategies to increase the capacity. In this situation, spatial correlation among received signals lowers the capacity gains obtained. Thus, the spatial correlation has different implications in diversity-based and MIMO systems. This is the primary reason for the difference in design principles for diversity-based and MIMO antenna arrays. Spatial correlation might arise due to the antenna arrays employed at the transmitter and receiver (small inter-element spacing, mutual coupling etc.) or due to the channel characteristics [68]. If the wireless propagation environment has sufficient multipath, the channel spatial correlation is generally low. In contrast, when the channel does not have rich multipath or when a strong line of sight exists between the transmitter and receiver, the channel spatial correlation is considerably higher. The impact of high channel spatial correlation can be lowered using effective MIMO antenna design techniques. For example, using antenna arrays where the elements have orthogonal polarizations or patterns, the spatial correlation of the signals received at the antenna array can be significantly reduced, even when channel spatial correlation is high.

By spacing antenna elements far apart, or by using elements that have orthogonal radiation patterns or polarizations, it can be ensured that signals received at these antenna elements have undergone independent scattering in the propagation environment and hence, have low correlation. Effective antenna designs can improve MIMO performance by utilizing the following three antenna diversity effects:

(a) Spatial diversity - spacing antenna elements far apart

(b) Pattern diversity - using antenna elements with orthogonal radiation patterns

(c) Polarization diversity - using antenna elements with different (orthogonal) polarizations, typically at $\pm 45°$.

Scattering effects might cause a transmitted signal to suffer a (small) change in its polarization. As MIMO takes advantage of multipath, antenna design at the MIMO front end must be capable of handling these changes in polarization. Further, mobile terminals might be held or placed at different orientations. MIMO antenna designs at

the base station must be able to effectively tolerate random orientation effects and still provide good data rates at the receiver. The prohibitive costs of leasing tower space require that base station antennas not to occupy too much space. Further, knowledge of the optimum values of parameters like cross-pol and port-to-port isolation enables antenna designers to reduce the time and effort needed to meet (possibly) unnecessarily high specifications of these parameters.

To summarize, the requirements of an effective MIMO base station antenna design are that it should:

(a) exploit the additional spatial dimension by incorporating combinations of the three antenna diversity effects in the design,

(b) have a structure such that it can cope with random orientation effects at the receive side,

(c) be able to cope with slight changes in the polarization of the received signals (in the uplink case),

(d) offer a fair balance between tower space occupied and performance obtained (due to the high costs associated with leasing tower space) and

(e) present a trade-off between design specifications and performance obtained (especially for parameters like cross-pol isolation and port-to-port isolation).

3.5. Summary

MIMO systems are capable of increasing channel capacity and reliability of wireless systems without increasing system BW and transmitter power. In this chapter, an overview of various antenna diversity schemes along with the key parameters of a MIMO system have been described. Moreover, the requirements of an effective MIMO base station antenna design have been stated.

Chapter 4. Reconfigurable Dual-Mode Antenna for Base Stations

This chapter proposes a new design of a reconfigurable three-sector dual-mode dual-polarized antenna for use primarily in mobile communication base stations. The design offers the flexibility of being used as a sectoral (directive) or omnidirectional base station antenna whenever required. The two radiating modes (omnidirectional and sectoral) depend only on the excitation scenario. The design is based on a basic structure of two orthogonal oval-shaped crossed dipoles. The proposed antenna has the advantages of offering broadband, stable radiation pattern and high XPD within the desired frequency band, and a simple feeding structure with compact size (less than 800 cm^3) and a low profile. The achieved fractional BW is 55.3% (1.7-3 GHz). A prototype antenna was constructed and tested with the two modes of operation. Results have demonstrated the principle of the design and show how the design may be packaged in a compact size to offer excellent omnidirectional or sectoral performance, which makes this new design an ideal candidate for reconfigurable dual-mode mobile base stations.

4.1. Introduction

Dual-polarized antennas with a broad BW have become necessary requirements for mobile communication systems because of the rapid development of communication technologies [69]. Many attempts have been made in 2G, 3G and 4G frequency bands to meet their requirements. In [70] and [71], two antennas have been proposed for such applications, but the BW is insufficient to meet requirements. In [72], despite the achievement of a high XPD, the BW (1920- 2200 MHz) of the designed antenna limits its usage for mobile systems. In [73], a multiband array design with a compact structure was introduced using an optimal array scheme but the BW was still limited. In [74], the XPD was improved by adding parasitic elements at the expense of the antenna size. In [75], a 3D printed cross-dipole structure was employed, but the design showed some

drawbacks as it lacks simplicity and ease of fabrication. In [76], the high capacitive structure at the feeding point limited the power handling capability of the design. Furthermore, in [77], although oval-shaped crossed dipoles were used to improve the BW, the XPD is not high enough to meet base station antenna requirements. In [77]-[82] crossed dipoles were widely used as dual-polarized radiators printed on one side of a dielectric substrate with some limitations in size, BW, radiation pattern stability and XPD.

Omnidirectional base station antennas are primarily used to fill the uncovered spots resulted from shadowing effects. In such cases, the antenna should radiate approximately a constant power density in the azimuth plane [83]-[84]. In [85]-[86], four dipoles were used with 90° rotating positions but the BW was limited. The BW was improved in [87] by adding parasitic elements to two back-to-back dipoles. Dual-polarization in omnidirectional base station antennas has been achieved with broadband designs [88]. In [88], two separate structures were used with two separate feeds (one for the horizontal polarization and the other for the vertical polarization).

This chapter proposes a design of reconfigurable broadband dual-mode dual-polarized three-sector crossed dipoles for mobile stations covering the frequency band from 1.7 to 2.7 GHz. The basic element of the antenna is oval-shaped cross-dipole. Oval-shaped geometry enhances the size reduction with a wider BW. As a further development, a novel design of a three-sector dual-polarized antenna is introduced based on the antenna element and a detailed discussion of the antenna element operation principles is presented. The three-sector antenna can operate as a sectoral or omnidirectional base station antenna. If the antennas in the three sectors are fed simultaneously with the same in-phase signal, a uniform omnidirectional radiation pattern can be obtained, while if they are fed independently with different frequency signals, a directive radiation pattern in each sector is achieved. This can offer mobile operators the desired flexibility in some cases. Section 4.2 describes the antenna element and its working principles; Section 4.3 discusses the three-sector antenna in the two modes (omnidirectional and sectoral), its principle of operations, results and, its performance. Section 4.4 illustrates the parametric studies. Finally, a summary is drawn in Section 4.5.

4.2. Dual-Polarized Antenna Element

4.2.1. Antenna Element Design

In this section, a novel broadband dual-polarized antenna element covering the frequencies from 1.7 GHz to 2.7 GHz is illustrated and applied as the radiating element in the proposed three-sector reconfigurable antenna. Fig. 4.1 illustrates the geometry of the antenna element.
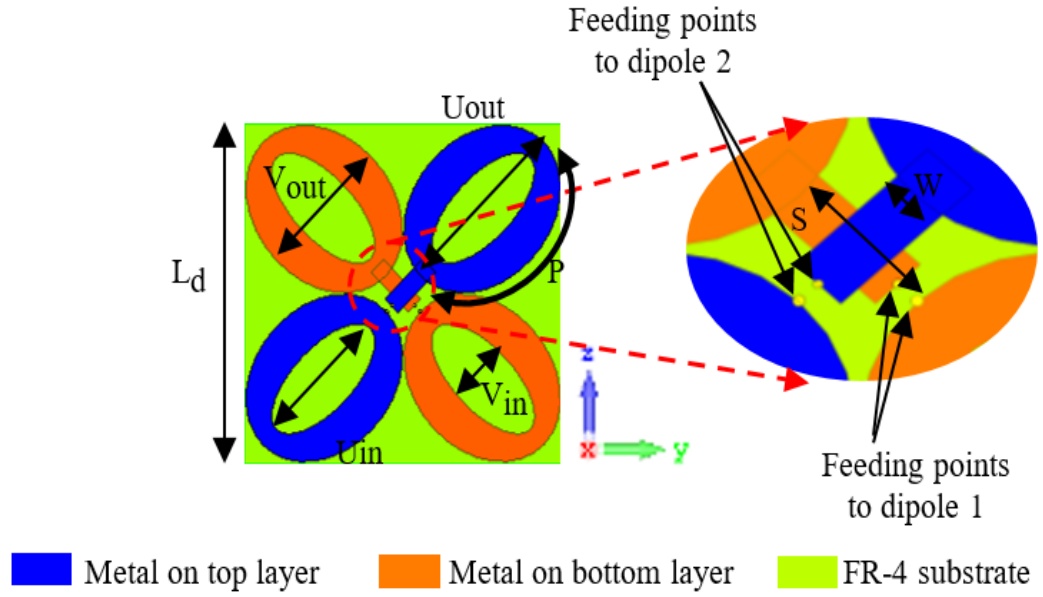
Fig. 4.1.   The geometry of the radiating antenna element

Generally, the geometry can be described as two orthogonal half-wavelength dipoles, placed on ±45° with respect to the Y-axis respectively in order to provide a polarization diversity capability. The dipole radiating elements are printed on the opposite sides of a double-sided FR-4 substrate with relative permittivity ε_r =4.3, loss tangent of 0.025 and, thickness Hd = 1.6 mm. Each dipole consists of two slotted ellipses linked to a feeding strip and a connector to excite the dipole. The substrate and dipoles are oriented in the YZ plane. The optimized dimensions are determined as follows (in mm): Uin = 19, $Uout$ = 30, Vin = 7, $Vout$ = 21, S = 8, W = 3, Ld = 52 and P = 40.

4.2.2. Methodology and Principle of Operation

The design is based on constructing a half wavelength dipole then widening its BW by creating two inductive loops at its terminals [77].

Two reference designs (antenna Ref1 and antenna Ref2) can be employed to understand the working principle of the antenna element as shown in Fig. 4.2. Initially, the dipole length is set to $0.5\lambda_0$ (antenna Ref1) (where λ_0 is the free space wavelength at the central frequency 2.2 GHz). In this case, the BW observed is narrow. The design is amended to be elliptical-shaped dipole instead of the traditional dipole as the elliptical radiator dipole has a wider BW (antenna Ref2) [77]. Initially, the ellipse major and minor axes (*Uout* and *Vout*) are selected such that the shortest current path length from the feeding point to the endpoint of the ellipse (*Uout*) equals to $0.25\lambda_{min}$ while the longest current path length from the feeding point to the endpoint of the ellipse (*P*) equals to $0.25\lambda_{max}$ (where λ_{min} and λ_{max} are the free-space wavelength at the highest and lowest frequencies of the desired band at 2.7 and 1.7 GHz respectively and *P* is half of the ellipse circumference). *P* is related to the axes length as:

$$P = \pi \sqrt{\frac{\left(\frac{Uout}{2}\right)^2 + \left(\frac{Vout}{2}\right)^2}{2}} = \frac{\lambda_{max}}{4} \qquad (4.1)$$

It is worth noting that all current path lengths from the feeding point to the ellipse endpoint ranging from the shortest path *Uout* to the longest path *P* are equal to a quarter of the wavelengths ranging from λ_{min} to λ_{max} respectively. Thus, the dipole length may be considered as a half-wavelength for all the frequencies within the desired band. In antenna Ref2, the BW observed is wider but is still not satisfactory.

Antenna Ref1   **Antenna Ref2**   **Proposed Antenna**
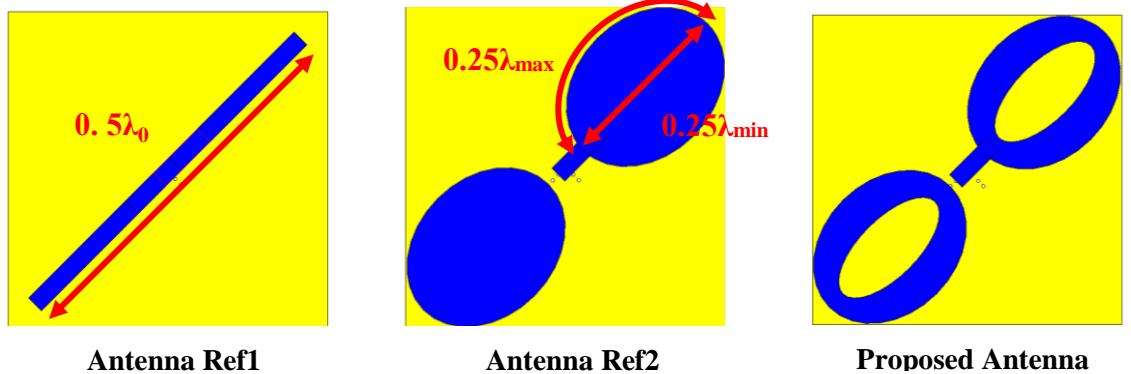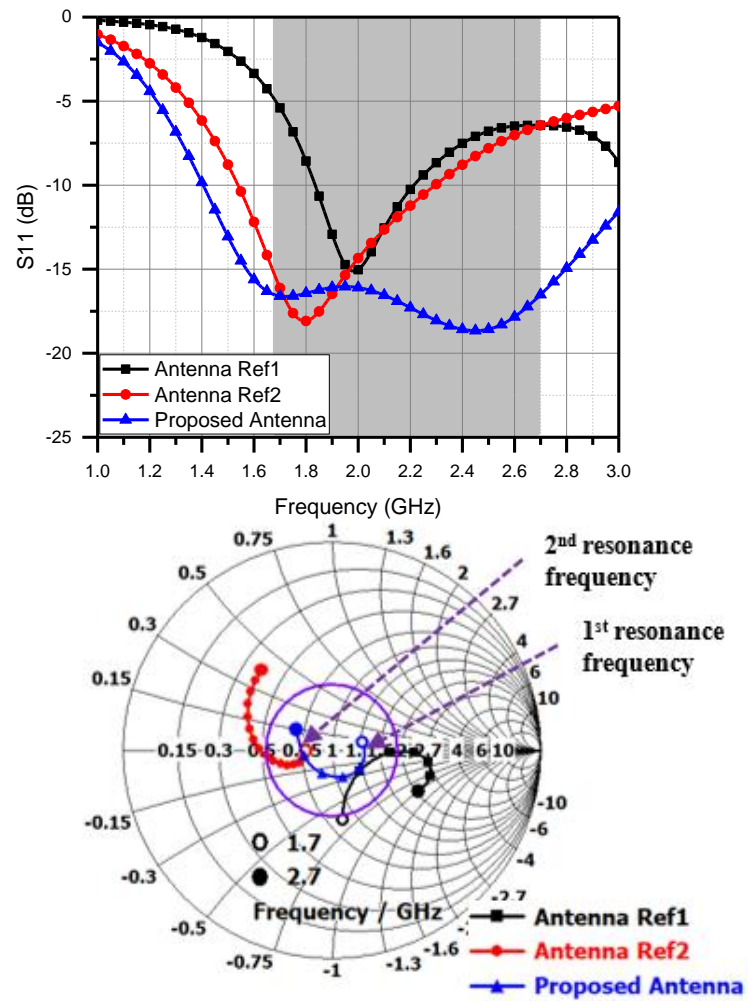
Fig. 4.2.   References and the proposed antenna element designs

This can be improved by further matching the dipole input impedance to the characteristic impedance Z_0 (50 Ω in our case) by cutting an elliptical slot in each arm (proposed antenna element). The major and minor axes of the slot are *Uin* and *Vin* respectively which are optimized to achieve minimum reflection coefficient across the desired band.

From the Smith chart in Fig. 4.2, it is evident that the proposed antenna has two resonant frequencies (where the plot intersects the horizontal line of the Smith chart) at 1.9 and 2.4 GHz, respectively. Fig. 4.3 shows the surface current distributions of the radiating dipole at the two resonant frequencies. At the first resonant frequency, the surface current is observed to flow over the dipole surface from the feeding point to the endpoint. At the second resonant, the current flow at the edges of the ellipses and the slots forming another resonator.
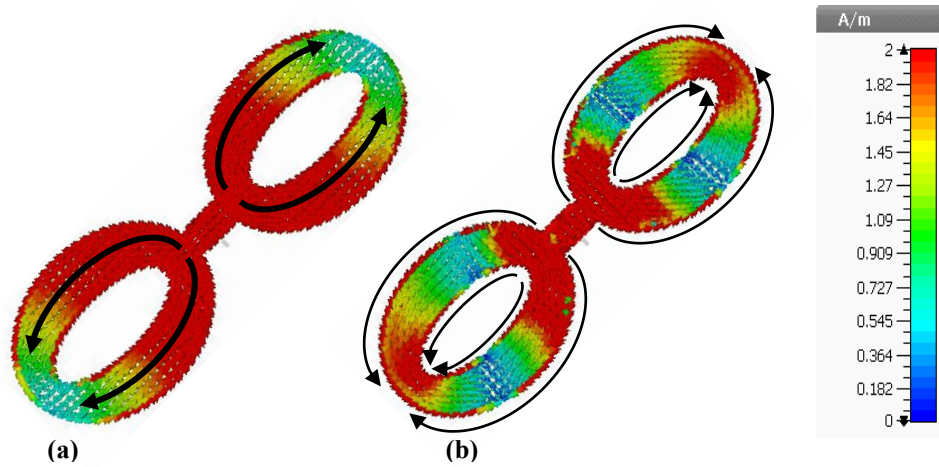
Fig. 4.3.   **Current distributions at the resonant frequencies (a) 1.9 GHz (b) 2.4 GHz**

4.3. Three-Sector Antenna

In this section, a novel three-sector reconfigurable dual-polarized antenna based on the antenna element presented section 4.2 is designed to operate in one of two different modes; (mode1: omnidirectional radiation and mode 2: sectoral radiation). This flexibility in operation offers the advantage that the same antenna may be used for different applications.
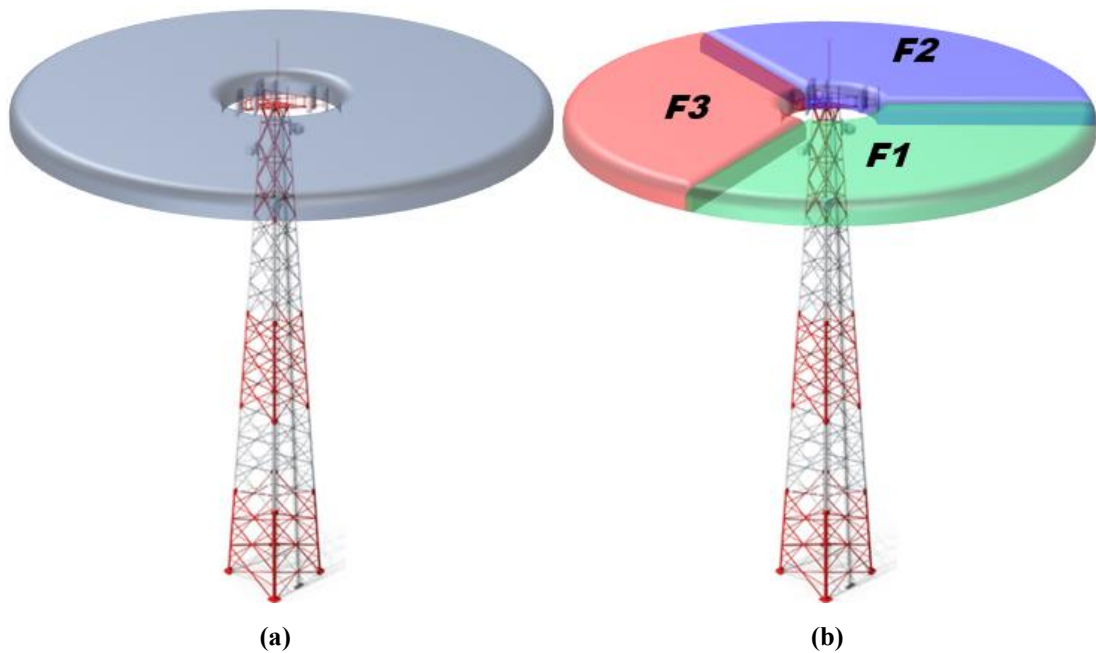
Fig. 4.4.   **Three-sector antenna modes of operation (a) omnidirectional (b) sectoral**

The mode of operation for the three-sector antennas (sectoral or omnidirectional) depends only on the excitation mechanism. If the three-sector antennas are fed simultaneously with the same signal (of the same amplitude and phase), an omnidirectional radiation pattern is obtained. Alternatively, if the three sectors are fed with different frequency signals independently, a directive radiation pattern in each sector is achieved. This type of varying behaviour can be desirable as a single antenna design could be able to be deployed into two different roles if so desired. Fig. 4.4 shows the two mode-of-operation scenarios of the proposed three-sector antenna.

The key points of achieving such a design are:

(a) Optimizing the design of the radiating antenna elements to achieve the optimum impedance matching and port-to-port isolations.

(b) Constructing a three-sector antenna structure by placing three antenna elements around an equilateral triangular-shaped metallic reflector with a rotating angle of 120° between each pair and as close to each other as possible with accepted degradations in reflection coefficients and isolations.

(c) Chamfering the metallic reflector edges L_C with 30° at each side to get suitable radiation patterns in both modes.

■ (blue)	**Metal on substrate top layer**	■ (yellow) **FR-4 substrate**
■ (red)	**Metal on substrate bottom layer**	■ (green) **Metallic reflector**
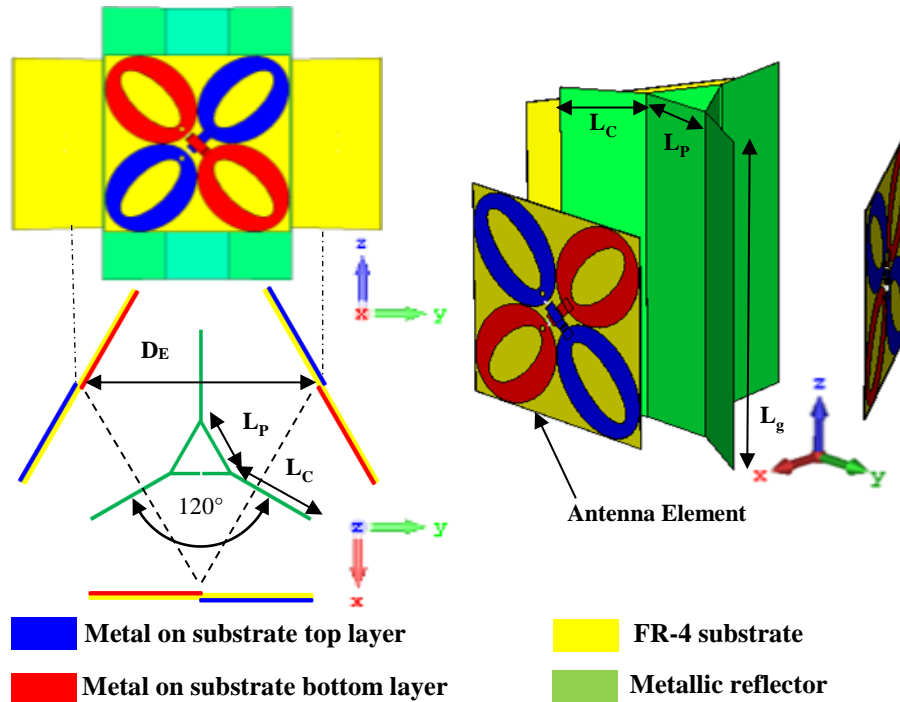
Fig. 4.5.   **The geometry of the proposed three-sector antenna**

The structure is shown in Fig. 4.5 and detailed dimensions are illustrated in Table 4.1. The two modes of operation are described in details as follows

Table 4.1.   Dimensional Parameters of the Proposed Three-Sector Antennas

Dimension	Value (mm)
D_E	60
L_C	24
L_P	10
L_g	80

4.3.1. Mode 1: Omnidirectional Radiation Mode

The element-to-element separation D_E has a major effect on forming the omnidirectional radiation pattern. For a better understanding of the effect of D_E, let us approximate the equilateral triangular antenna array with a side length of D_E to a circular array with three elements and a radius a as shown in Fig. 4.6(a) where $a = D_E \tan(30)$. The array factor in XY plane, in this case, equals to [89]:

$$AF(\emptyset) = \sum_{m=1}^{3} W_m e^{-j(ka\cos(\emptyset))} = \sum_{m=1}^{3} W_m e^{-j(kD_E\tan(30)\cos(\emptyset))} \qquad (4.2)$$

where W_m is the complex weight of the element number m, $k = 2\pi/\lambda$ is the angular wavenumber, λ is the wavelength and, ϕ is the horizontal angle in XY plane. Conventional weights of equal magnitude and phase signals are applied to the six ports.

(a)
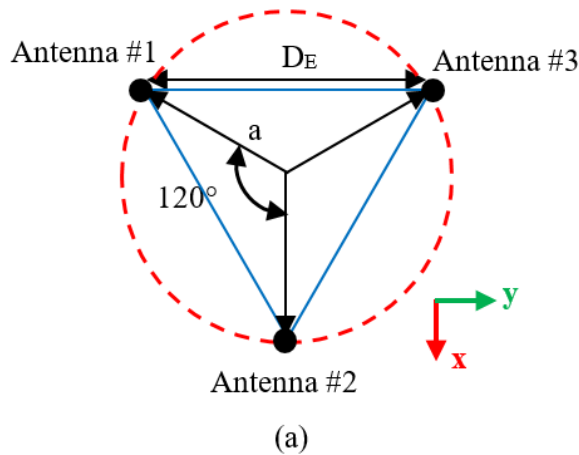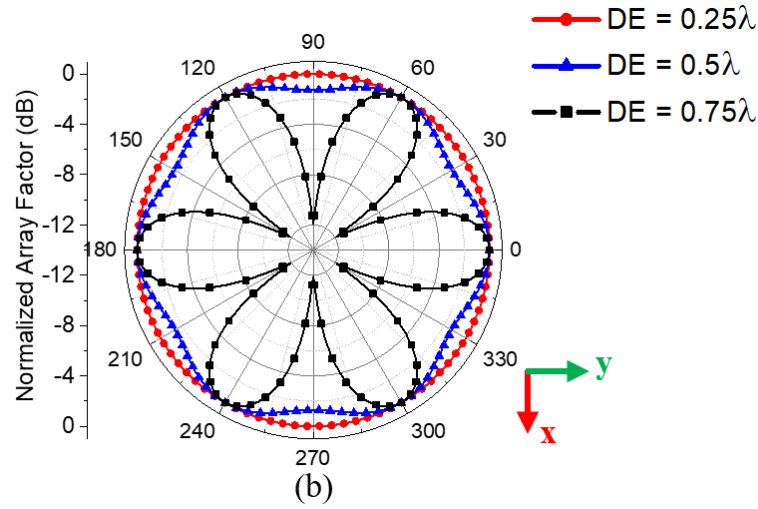
Fig. 4.6.   Three-element circular array (a) structure (b) array factor

Fig. 4.6(b) illustrates the array factor as a function of ϕ at different values of D_E in terms of the wavelength. It is clear that the larger D_E is, the higher the difference between peaks and troughs. For a 3dB-beamwidth of 360° in the horizontal plane, the radiation pattern at any horizontal angle should not exceed 3 dB below the peak value.

Fig. 4.7 illustrates the difference D between peaks and troughs against D_E where:

$$D = \max\big(AF(\emptyset)\big) - \min\big(AF(\emptyset)\big) \tag{4.3}$$

From Fig. 4.7, we can see that D_E should not be larger than *0.54λ_{min}* to ensure the difference D is less than 3 dB. Of course, the smaller D_E, the more uniform radiation pattern in azimuth. On the other hand, if D_E is too small, the performance will suffer from high reflection coefficients because the radiating antenna elements may become too close to each other and to the common metallic reflector. So, D_E should be chosen carefully as a trade-off between uniform radiation pattern and good reflection coefficients. Another critical parameter in the proposed three-sector antenna design is the chamfered metallic reflector width L_C. If L_C is small, a uniform radiation pattern in azimuth is easily obtained but on the other hand, the HPBW in sectoral mode would be larger than the desired. If L_C is large, a disturbance in the electric field in the azimuth plane may occur and result in a non-uniform radiation pattern. Thus, again the selection of L_C is a trade-off between omnidirectional and sectoral radiation patterns.
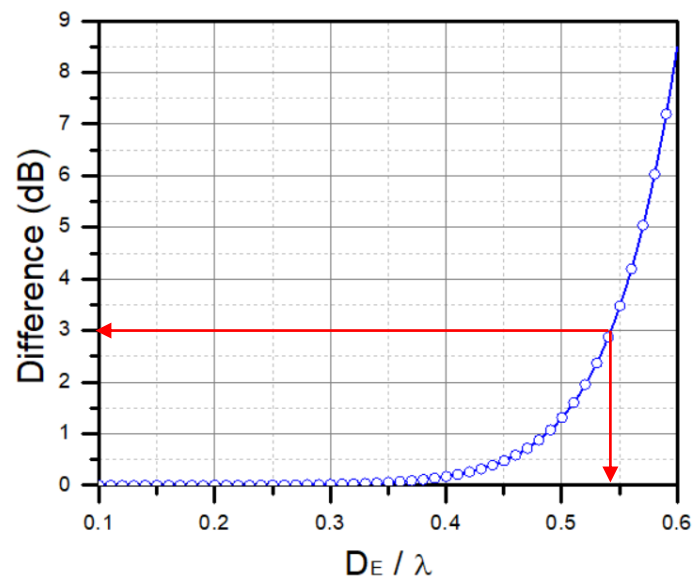
Fig. 4.7.   **Variation in difference D against D_E**
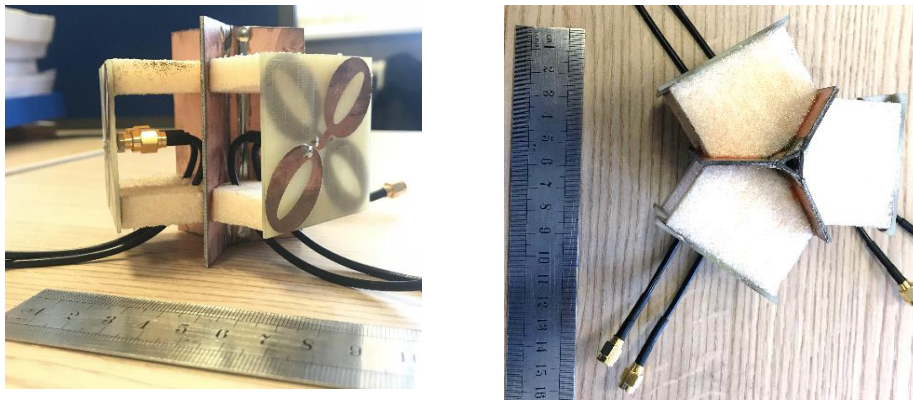
(a)
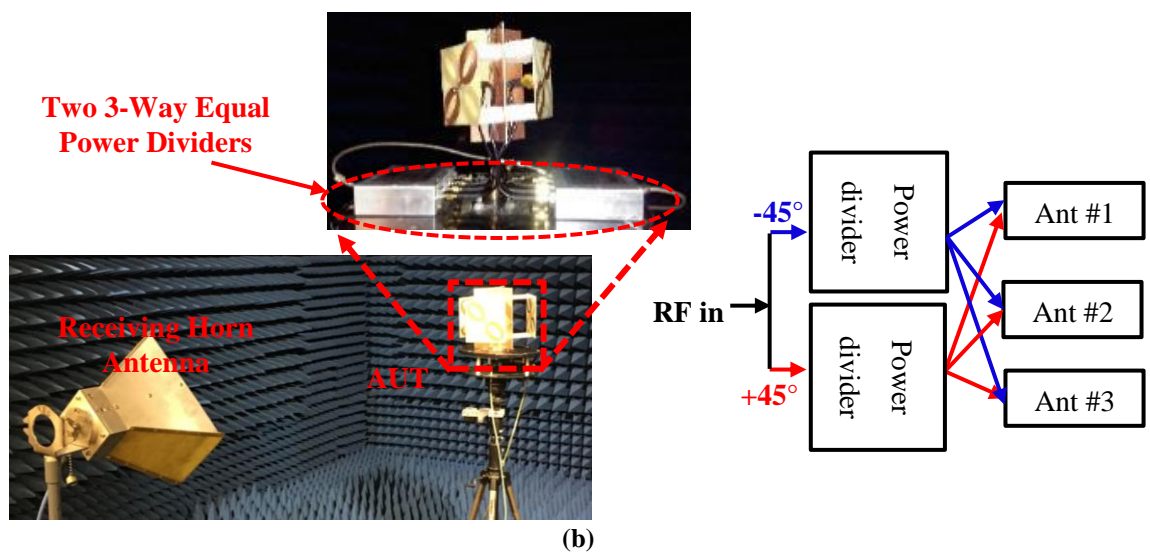
(b)

Fig. 4.8.   **Dual-polarized three-sector antenna (a) prototype (b) in omnidirectional mode**

To validate the design, a prototype of the dual-polarized three-sector antenna element has been manufactured and tested as shown in Fig. 4.8. To excite the omnidirectional mode, a 6-way equal power divider (typically a 3-way power divider for each polarization) is used to feed the antenna ports as shown in Fig. 4.8(b).

Reflection coefficient and isolation between the six ports are measured. For simplicity, Fig. 4.9 illustrates the reflection coefficients, the worst and the best cases of isolation between any pair of ports. All other isolation values are in-between the values shown in Fig. 4.9. There is a good agreement between simulated and measured reflection coefficients of the proposed antenna. A BW of 55.3% (1.7-3 GHz) is achieved for $S_{11} \leq -10$ dB. The isolation between any pair of ports is better than 18 dB.
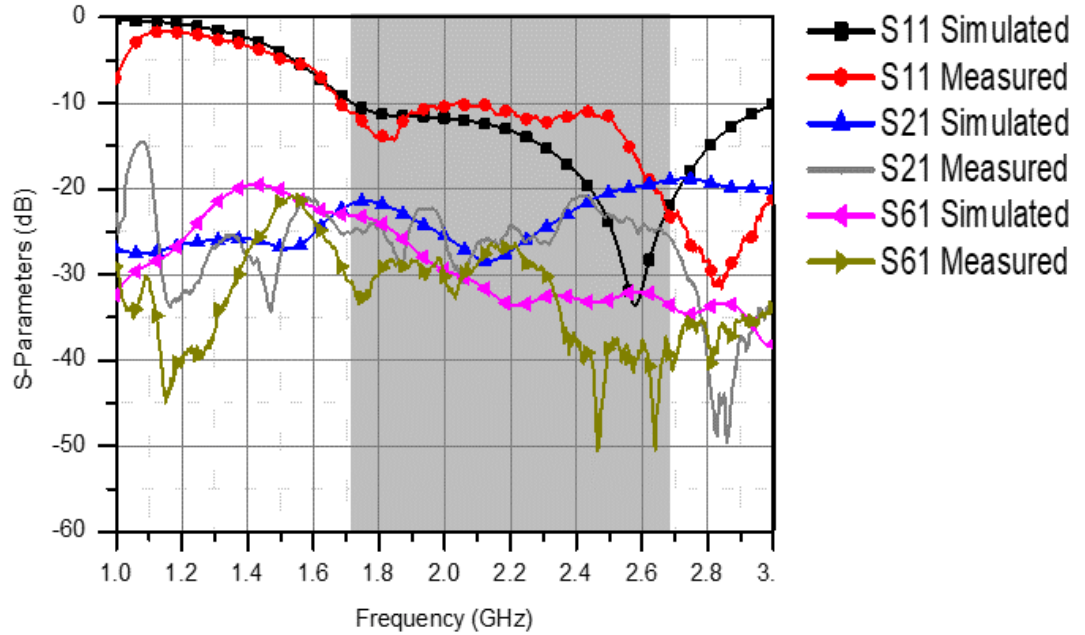
Fig. 4.9.   Simulated and measured S-parameter of the three-sector antenna

The simulated and measured radiation patterns in the H-plane (XY plane) and V-plane (XZ plane) for the proposed three-sector antenna in the omnidirectional mode for co- and cross-polarization at frequencies 1.7, 2.2, and 2.7 GHz are plotted in Fig. 4.10. It is evident that the radiation pattern in the H-plane is approximately uniform with a difference between peaks and troughs ≤ 3 dB and XPD better than 20 dB. The HPBWs in the V-plane is 60 ± 2.5º.
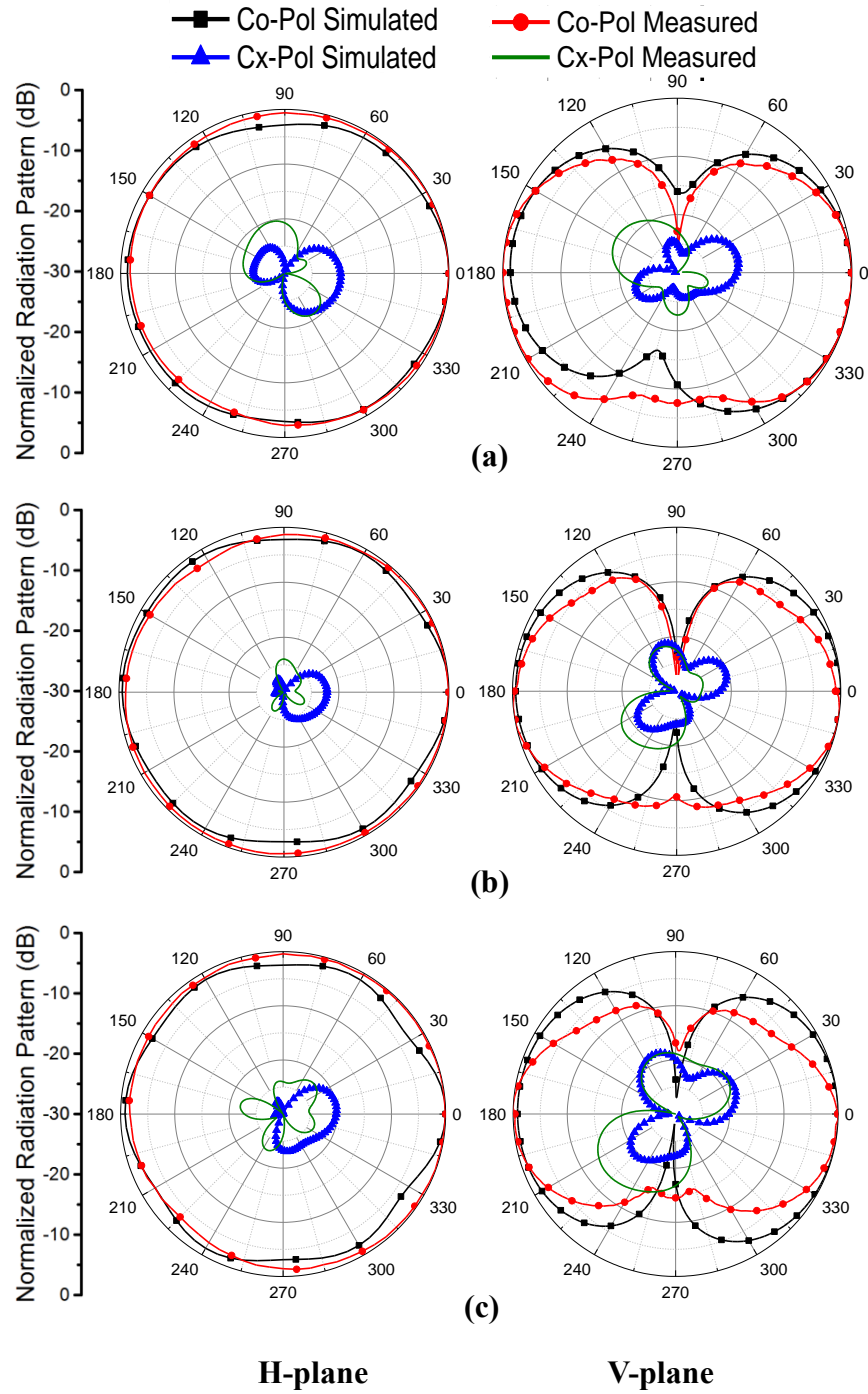
Fig. 4.10.   The radiation pattern of the proposed three-sector antenna in omnidirectional mode at (a) 1.7 GHz (b) 2.2 GHz (c) 2.7 GHz

Table 4.2 compares the proposed three-sector antenna in the omnidirectional mode with other reported designs. These designs have a similar frequency band. For a fair comparison, the BWs are chosen with VSWR ≤ 2. It is clear that the proposed design has the widest BW and the smallest size with a relatively high XPD. Moreover, it has

a dual-polarization of ±45° which is typically used in base station antennas rather than the vertical-horizontal (V-H) dual-polarization used in the reference antennas.

Table 4.2.   Comparison with reported omnidirectional base station antennas

Ref.	BW (GHz)	Size (cm³) (L×πr²)	Polarization	XPD (dB)
[85]	1.7-2.2 (25.6%)	814.3	Single (45°)	15
[87]	1.7-3 (55.3%)	1271	Dual (V- H)	22
[88]	1.7-2.7 (45.5%)	942.5	Dual (V- H)	10
This Work	1.7-3 (55.3%)	760	Dual (±45°)	20

The simulated and measured realized gains are presented in Fig. 4.11. The proposed antenna has a stable gain of 2.5±0.15 dBi throughout the desired frequency band.
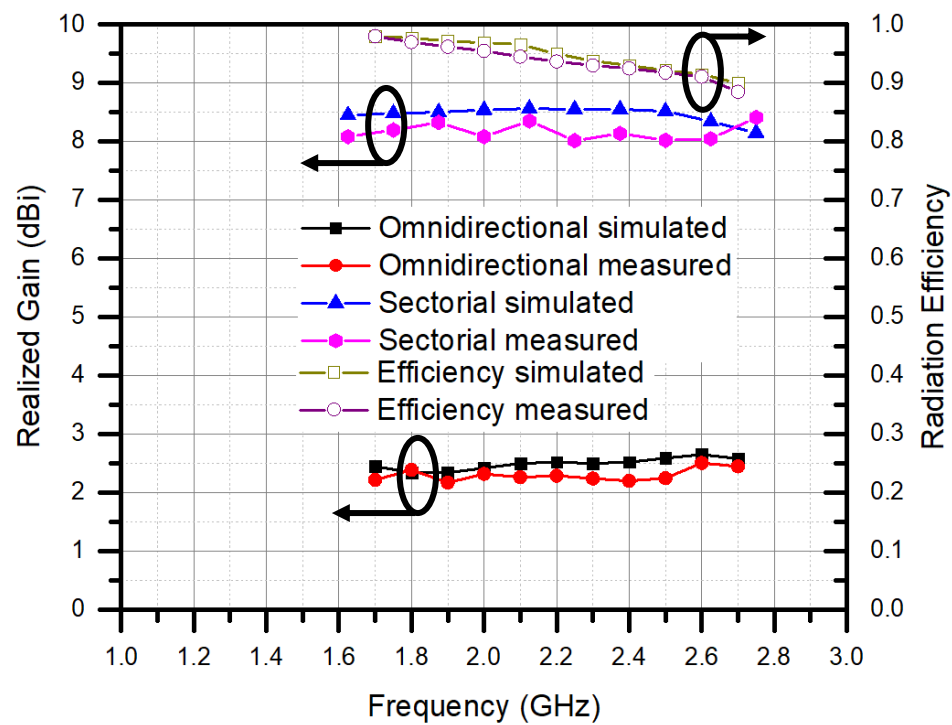
Fig. 4.11.   Simulated and measured radiation efficiencies and gains of the proposed antenna in the omnidirectional and sectoral modes

4.3.2. Mode 2: Sectoral Radiation Mode

In this mode, each pair of orthogonal dipoles in a sector is excited individually by a signal with a different frequency from the other two pairs. Thus, each pair radiates in a specific sector without interfering with the other two pairs in the other sectors.
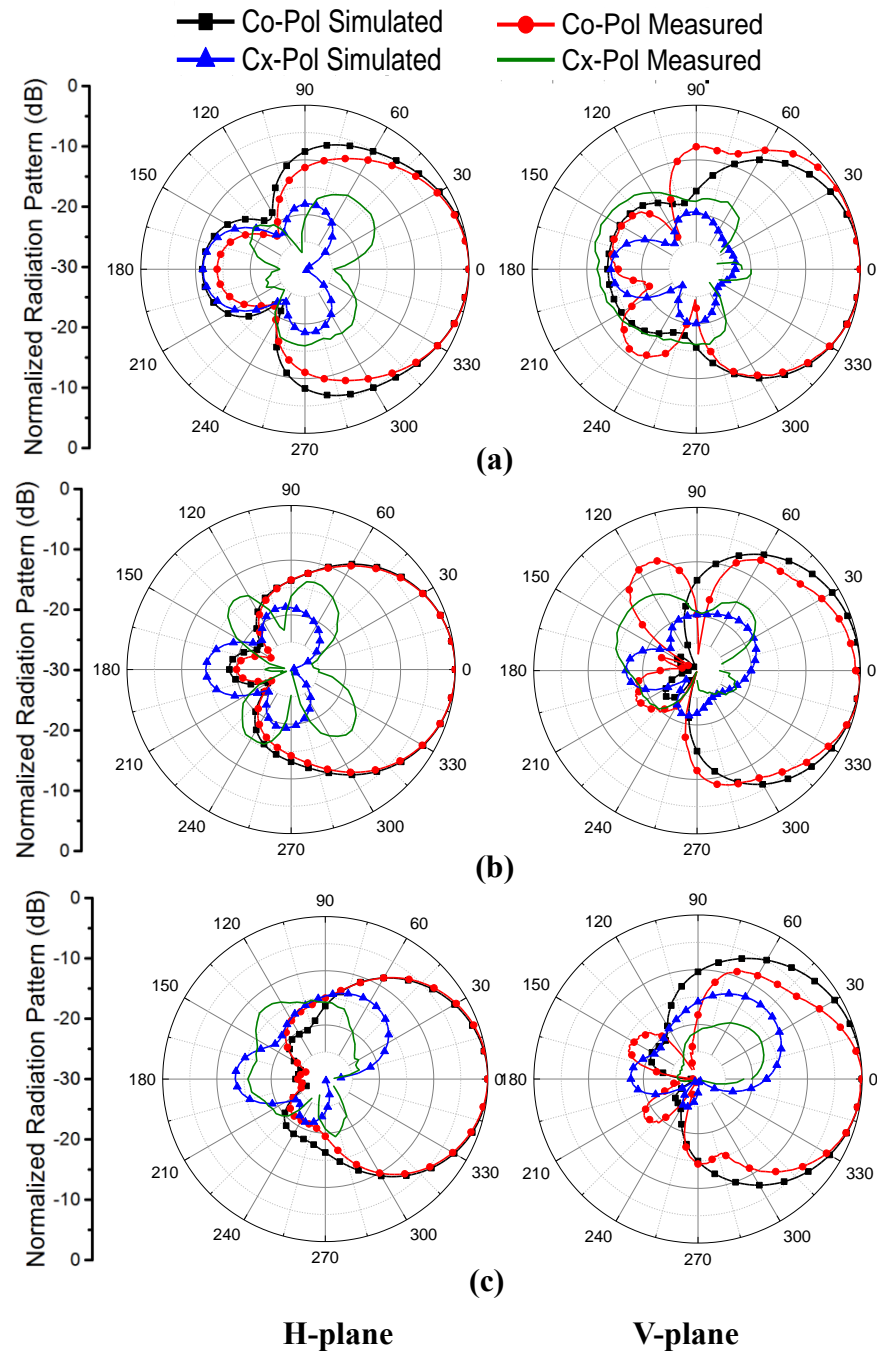
Fig. 4.12.   The radiation pattern of the proposed three-sector antenna in sectoral mode at (a) 1.7 GHz (b) 2.2 GHz (c) 2.7 GHz.

The simulated and measured radiation patterns in H-plane and V-plane for co- and cross-polarization at frequencies 1.7, 2.2, and 2.7 GHz for the proposed three-sector antenna in sectoral mode are plotted in Fig. 4.12. The HPBWs for the proposed antenna in the sectoral mode are 68±3° and 60±2.5° in the H-plane and V-plane respectively. As noticed in Fig. 4.12, the HPBW in the H-plane slightly decreases as the frequency increases. Therefore, the antenna directivity increases. Fig. 4.11 shows the proposed antenna radiation efficiency, which reaches 98% at 1.7 GHz and slightly decreases as the frequency increases until it reaches 90% at 2.7 GHz due to using a lossy FR-4 substrate. This slight reduction in efficiency compensates the increase in the antenna directivity and hence the realized gain remains almost constant throughout the frequency band. The XPD is better than 24 dB at boresight and better than 8 dB within a sector of ±65°. The simulated and measured realized gains of the proposed antenna are plotted in Fig. 4.11. It is clear that each radiating dipole has a stable gain of 8.5±0.3 dBi across the desired frequency band in the sectoral mode.

It can noticed from the antenna results that the proposed design meets the standard requirements for both omnidirectional and sectoral base station antennas in terms of BW, isolation between ports, HPBWs and gains. Therefore, the proposed design can swap between these two modes just only be adjusting its feeding scenario.

Table 4.3 displays a comparison of antennas in the reference with the proposed sectoral antenna. These antennas have a similar frequency band, working principle and manufacturing process (PCB). The impedance BWs are chosen with VSWR ≤ 2. It can be seen that the proposed antenna has the smallest size and the highest XPD at boresight with a relatively high gain and a wide BW as compared to the antennas in [77]-[82].

Table 4.3.   Comparison with reported directive base station antennas

Ref	BW	Size (mm³)	Gain (dBi)	XPD (dB)	
				At boresight	Within ±65°
[77]	67%	165×165×76	8.2	13	5
[78]	55%	150×150×32	7.8	20	10
[79]	60%	150×150×31	8.2	20	8
[80]	45%	140×140×34	8.2	22	8
[81]	70%	150×150×35	8.8	22	4
[82]	58%	145×145×35	8.5	18	NA
This Work	55.3%	100×80×37	8.5	24	8

4.4. Parametric Studies

4.4.1. Effect of the Elliptical Slotted Dipoles

A very important parameter in the design is the separation S (see Fig. 4.1) between the ellipses. As shown in Fig. 4.13(a), when S increases, the dipole is seen to be more inductive especially at higher frequencies. $S = 8$ mm is found to be the optimum value for VSWR ≤ 2 (the circle in the middle of the Smith chart) within the frequency band.

The second parameter studied is the elliptical slot axis Uin. When this parameter changes, the slot area changes and consequently the impedance matching changes. It is noticeable that the change in Uin affects the shorter current path lengths close to the ellipse major axis ($Uout$) rather than the longer current path lengths close to the ellipse edges (P). Thus, the higher frequencies are more sensitive than the lower frequencies to Uin as shown in the Smith chart in Fig. 4.13(b). Uin is chosen to be 19 mm for optimum impedance matching for VSWR ≤ 2.
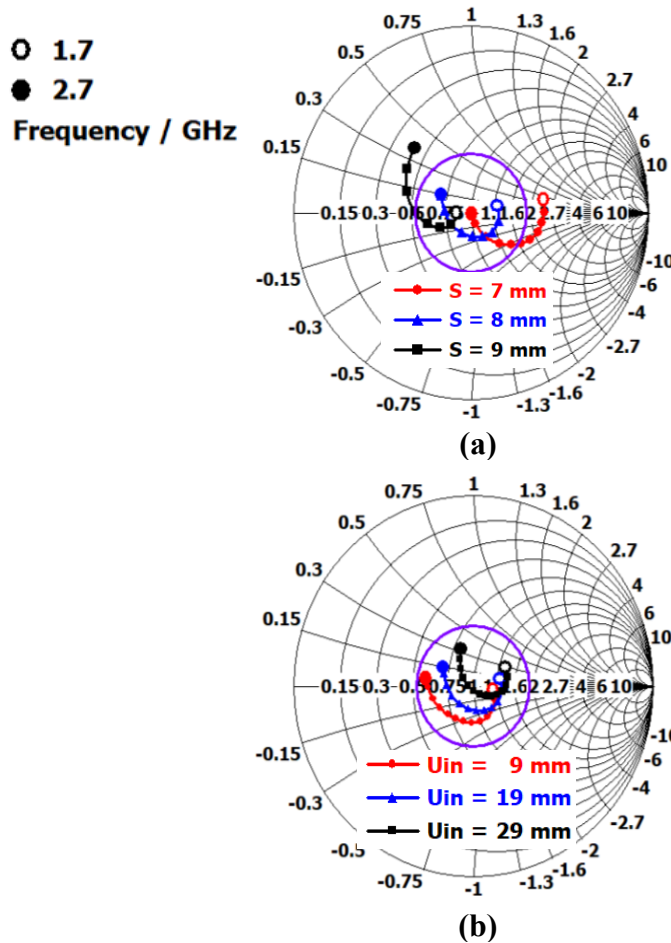
Fig. 4.13.   **Effect of (a) *S* (b) *Uin* on the impedance matching.**

4.4.2. Effect of the Triangular-Shaped Metallic Reflector

As mentioned in section 4.3, D_E has a major effect on forming the uniform radiation pattern in omnidirectional mode. Fig. 4.14 shows the effect of D_E on both reflection coefficient and omnidirectional radiation pattern at the central frequency 2.2 GHz. It is clear that when $D_E = 50$ mm, although the variation in the radiation pattern is less than 3 dB, the reflection coefficient is not sufficient to cover the desired frequency band because the radiating elements are too close to the metallic reflector. On the other hand, when $D_E = 70$ mm, the reflection coefficient is improved but the variation in the radiation pattern is larger than 3 dB at some horizontal angles in the H-plane. Thus, $D_E = 60$ mm has been found to be the optimum value to achieve a good reflection coefficient and uniform radiation pattern as well.

(a)

(b)
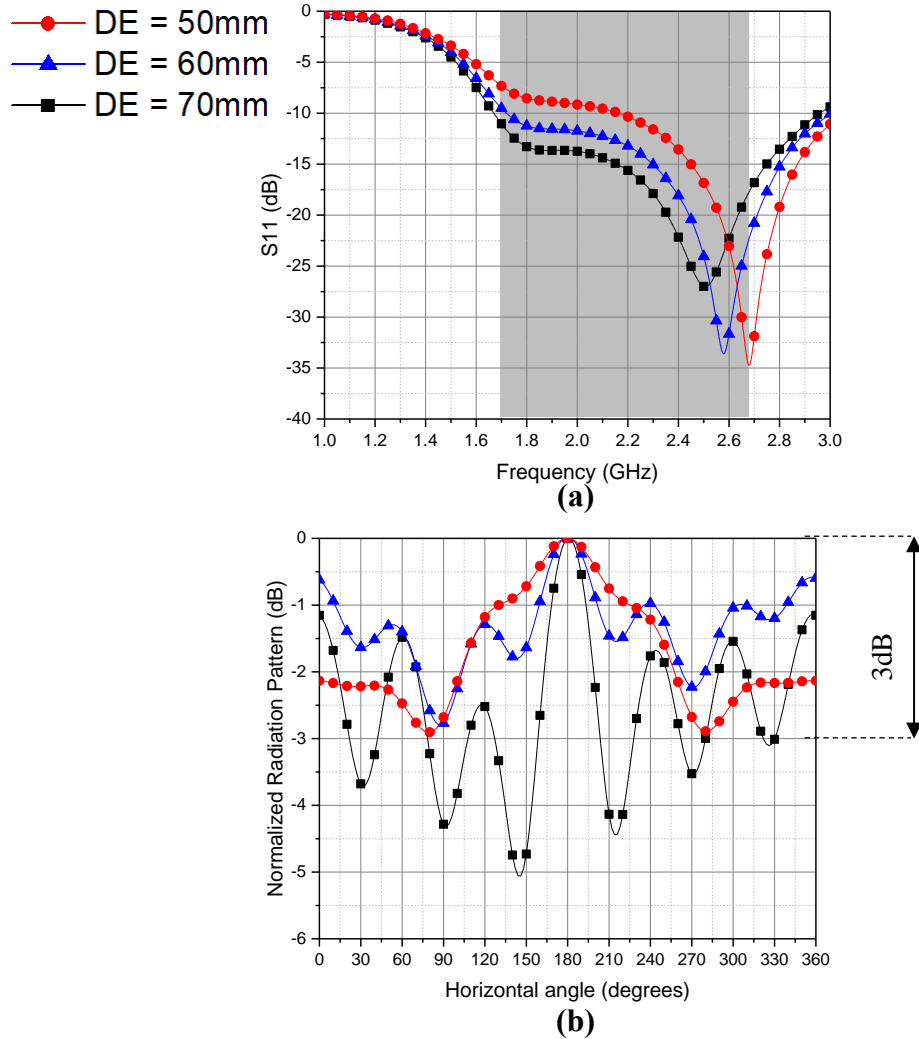
Fig. 4.14.　　Effect of D_E on the (a) reflection coefficient (b) radiation pattern in omnidirectional mode at 2.2 GHz

The second parameter studied is the reflector-chamfered edge L_C. Fig. 4.15 presents the effect of L_C on both the HPBW in sectoral mode and the radiation pattern in omnidirectional mode at the central frequency 2.2 GHz. When $L_C = 20$ mm, the radiation pattern in omnidirectional mode is uniform with spatial variation less than 3 dB between peaks and troughs. Nevertheless, unfortunately, the HPBW in the sectoral mode is too wide to be employed for directive base station antenna (HPBW >> 65°). On the other hand, if $L_C = 28$ mm, the HPBW in sectoral mode is suitable for directive base station antenna but a disturbance in the electric field in omnidirectional mode occurs causing a non-uniform radiation pattern in the H-plane. Thus, L_C was set to 24 mm as an optimum value to achieve suitable HPBW in sectoral mode and a uniform radiation pattern in omnidirectional mode.

(a)

(b)
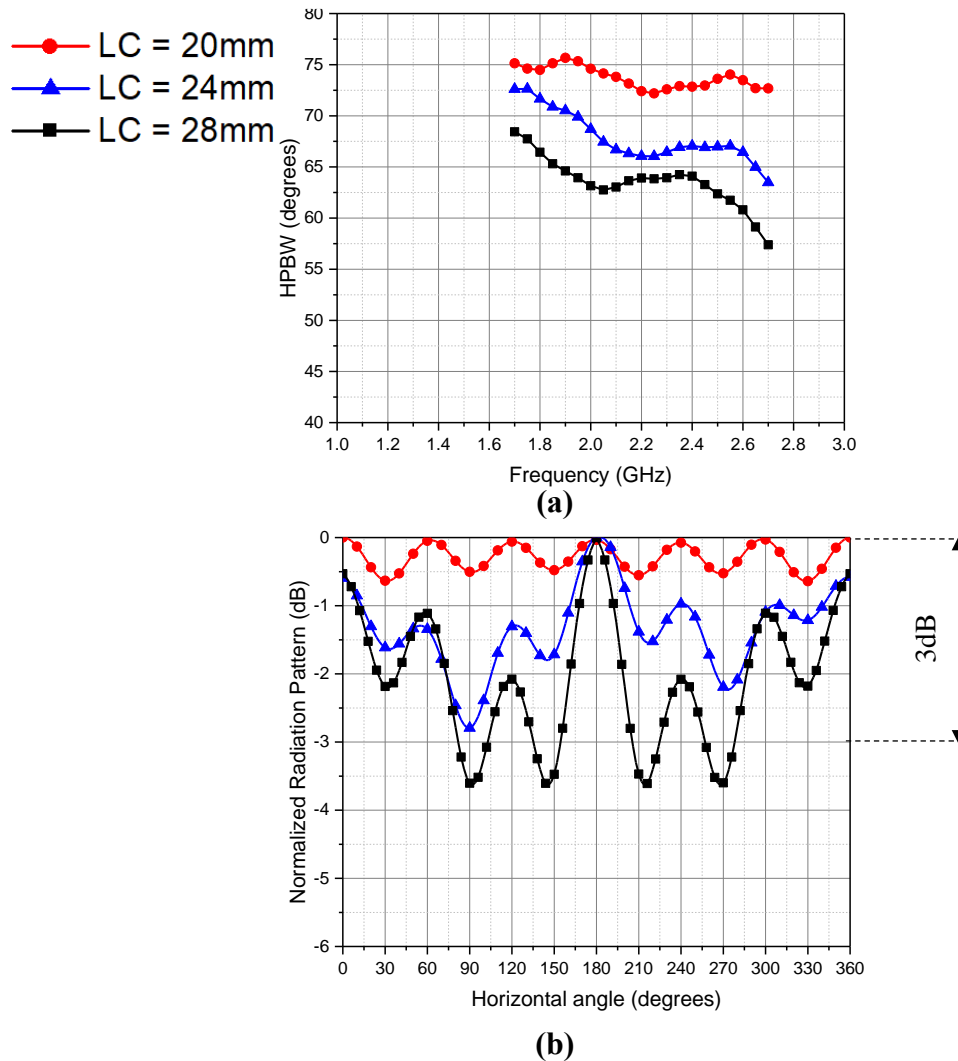
Fig. 4.15.   **Effect of L_C on the (a) HPBW in sectoral mode (b) radiation pattern in omnidirectional mode at 2.2 GHz.**

4.5. Summary

A novel reconfigurable dual-mode three-sector broadband dual-polarized antenna has been designed, optimized, fabricated and measured for mobile communication systems to cover the frequency band from 1.7 to 2.7 GHz. The flexibility of the design has the ability to switch between two different radiation modes (omnidirectional or sectoral) by changing the feeding. The proposed design has been found to have a small size (less than 800 cm^3), high XPD, wide BW and, stable radiation pattern. The proposed antenna radiation pattern features fulfil the base station antenna requirements at both modes in terms of gains, XPD and, HPBWs. Thus, a single structure of antenna can be employed to operate at one of the two different radiating modes by changing only its excitation mechanism whenever required. The proposed antenna is, therefore, an excellent candidate for reconfigurable dual-mode mobile base stations. The frequency range may be further extended for 2G/4G applications covering the frequency band from 0.7 to 0.96 GHz.

An expected limitation of the proposed design can be noticed at the feeding of the antenna element. A Balun may be required to be designed to improve the antenna design.

Chapter 5. Optimum Partitioning of a Phased –MIMO Antenna Array

The previous chapter focused on the base station antenna that covers a single band. In practice, double or multi-band antenna arrays are required to serve 2G, 3G and 4G mobile communication systems. Therefore, the concept of applying MIMO Overlapped Antenna Subarrays (OLAS) is adopted and optimized in this chapter for multi-band services. This concept has been introduced recently in 2010 and is well known as a "*phased-MIMO antenna array*". In a phased-MIMO system, the antenna array is divided into multiple subarrays that are allowed to be overlapped. In this chapter, a mathematical formula for optimum partitioning scheme is derived to determine the optimum division of an array into subarrays and the number of the elements in each subarray. The main concept of this new scheme is to place the nulls of the transmit beam pattern against the peak side lobes of the diversity beam pattern and place the nulls of the diversity beam pattern against the peak side lobes of the transmit beam pattern. It is shown that the main advantage of this optimum partitioning scheme is the improvement of the main-to-side lobe levels without any reduction in beam pattern directivity. In addition, the SNR is improved using this optimum partitioning scheme.

5.1. Introduction

5.1.1. What is Phased-MIMO System?

Previous developments in wireless communication systems were based on the idea that the signal can be processed coherently at the transmit/receive antenna arrays if the signal coherency is preserved. The corresponding technique is well known under the name phased antenna array [90]. In the last few decades, the development of a new wireless communication system paradigm that is best known under the title MIMO system has become the focus of intensive research [91]. Two types of MIMO systems are being investigated: MIMO systems with widely separated antennas and MIMO

systems with co-located antennas. Both have many unique advantages, but also face many challenges [92]-[93]. The enabling concept for MIMO system, e.g., the transmission of multiple orthogonal waveforms from different antennas, is usually referred to as waveform diversity.

Recently, some attempts to exploit jointly the benefits of phased array and MIMO antennas have been also reported [94]-[98]. In [94], a general antenna configuration is considered where several well-separated subarrays are used to form a MIMO system with each subarray operating in phased array mode. In [95], the idea of dividing the aperture of the transmit array with co-located antennas into multiple disjoint sub-apertures has been introduced. Utilizing the same partitioning structure, the authors of [96]-[98] have developed closed-form expressions for MIMO signal sets to achieve wide transmit beam pattern. In particular, it is shown that the height and width of a rectangular beam pattern can be controlled by adjusting the level of correlation between the MIMO signals. Later on, the authors of [99] developed a new technique, which combines the advantages of a MIMO antenna (such as waveform diversity) with the advantages of a phased antenna array (such as coherent processing). In order to enable such integration, they partitioned the transmit array into a number of subarrays that are allowed to overlap. Then, each subarray was used to coherently transmit a waveform that is orthogonal to the waveforms transmitted by other subarrays. Coherent processing gain can be achieved by designing the weight vector of each subarray to form a beam towards a certain direction in space (the same direction for all subarrays). In parallel, the subarrays are combined jointly to form a MIMO system. The advantage of this system, which is called phased-MIMO system, over the phased array and MIMO systems, is that it enjoys the advantages of the MIMO systems without losing the benefits of phased arrays. Moreover, it offers a virtual antenna aperture larger than the actual antenna aperture. Fig. 5.1 represents the main concept of the phased-MIMO array as a trade-off between the phased array and MIMO. However, the main question is how to divide the array elements into subarrays to achieve optimum performance. Unfortunately, the authors in [99] neglected the effect of partitioning the antenna elements on beam pattern parameters.
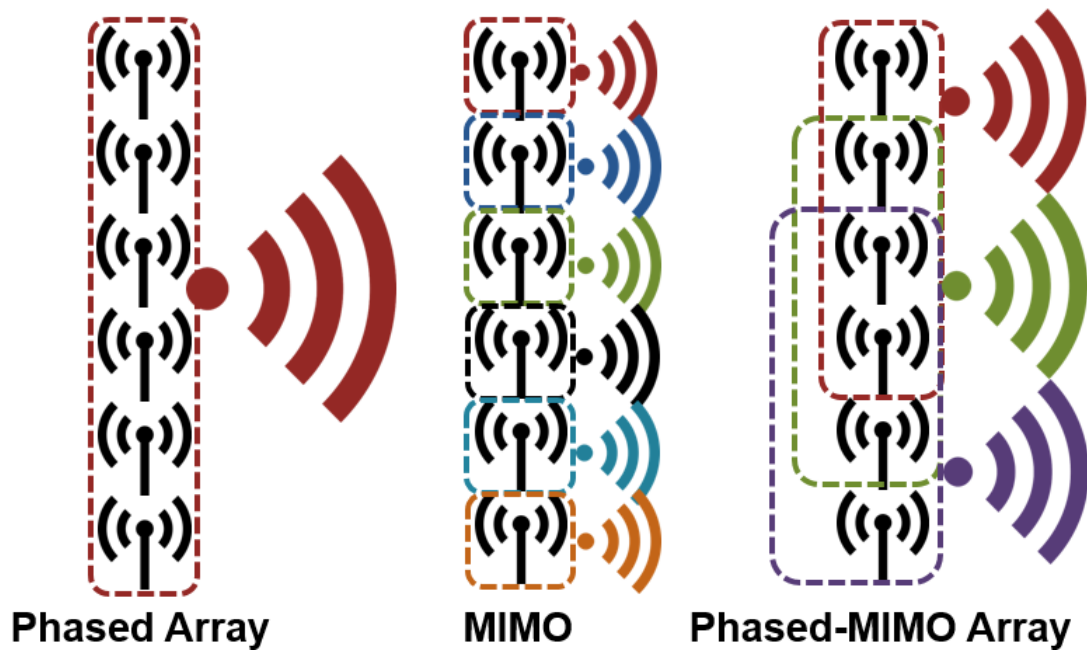
Fig. 5.1.   Phased-MIMO array: a trade-off between phased array and MIMO

5.1.2. Partitioning of Phased-MIMO Antenna Array

How to improve the antenna performance by investigating different partitioning schemes of phased-MIMO antenna arrays has attracted researchers' interest. In [100], a partitioning scheme for phased-MIMO antenna array was investigated but it is valid for an array that consists of an even number of elements ranging from 12 to 24, i.e. it is not a general formula. Furthermore, [101] gave a new partitioning scheme for a Hybrid Phased-MIMO system with Unequal Subarrays (HPMR-US) but with a complicated feeding structure.

In this chapter, a new mathematical formula is proposed which optimizes the antenna elements partitioning in a phased-MIMO array. This algorithm can determine the optimum number of subarrays within the antenna array and the number of the elements in each subarray. The proposed algorithm provides an optimum antenna element partitioning solution for the phased-MIMO array to achieve the minimum peak side lobes level (PSLL) without any reduction in antenna directivity. Also, high output signal to interference plus noise ratio SINR is achieved.

A beam can be formed by each subarray in a certain direction. The beamforming weight vector can be properly designed to maximize the coherent transmit processing gain. At the same time, different waveforms are transmitted by each subarray. Each

subarray has a waveform Φ_k orthogonal to other subarray waveforms. This orthogonality offers a waveform diversity gain. Coherent transmit gain can be expressed as [99]:

$$C(\theta) = [W_1^H B_1, \ldots\ldots, W_K^H B_K]^T \tag{5.1}$$

where $B_K(\theta) = [b_1(\theta), b_2(\theta), \ldots\ldots, b_{M_K}(\theta)]^T$ is the transmit steering vector with a size of $M_K \times 1$, $W_K(\theta) = [w_1(\theta), w_2(\theta), \ldots\ldots, w_{M_K}(\theta)]^T$ is the $M_K \times 1$ beamforming vector which contains only elements corresponding to the active antennas of the kth subarray, $b_{m_k}(\theta) = e^{-j\frac{2\pi}{\lambda}d(m_k-1)sin(\theta)}$ is the phase shift between the signals at the 1st antenna and the $m_k{}^{th}$ antenna for each subarray due to spatial displacement, θ is the aspect angle measured from the array boresight, w_{mk} is the complex weight of the $m_k{}^{th}$ antenna, d is the displacement between two successive antennas and λ is the signal wavelength. On the other hand, diversity gain can be expressed as [99]

$$D(\theta) = [a_1(\theta), a_2(\theta), \ldots\ldots, a_K(\theta)]^T \tag{5.2}$$

where $a_k(\theta) = e^{-j\frac{2\pi}{\lambda}d(k-1)sin(\theta)}$ is the phase shift between the signal at the 1st antenna of the array and the 1st antenna of the kth subarray due to spatial displacement. Both coherent transmit gain and diversity gain form the normalized overall gain as follows [99]:

$$U(\theta) = \big(C(\theta) \odot D(\theta)\big) \otimes R(\theta) \tag{5.3}$$

where $\odot$ is the Hadamard product (element-wise product), $\otimes$ is the Kronecker product and $R(\theta)$ is $S \times 1$ received steering vector and S is the number of receivers. It is clear that $U(\theta)$ is $KS \times 1$ virtual steering vector. Coherent, diversity and overall received gains depend on the number of subarrays K, and the number of elements in each subarray M_K. Although dividing an antenna array with M elements into overlapping *(M/2)-1* subarrays with *(M/2)+2* elements in each subarray provides, virtually, the maximum number of elements as mentioned in [100], this partitioning will not give the optimum beam pattern parameters. Hence, it is important to figure out the optimum partitioning values of K and M_K.

5.2. A New Formula for Optimum Partitioning of a Phased-MIMO Array

In this section, a transmit array of M elements is divided into K subarrays which can be disjointed or overlapped as shown in Fig. 5.2.
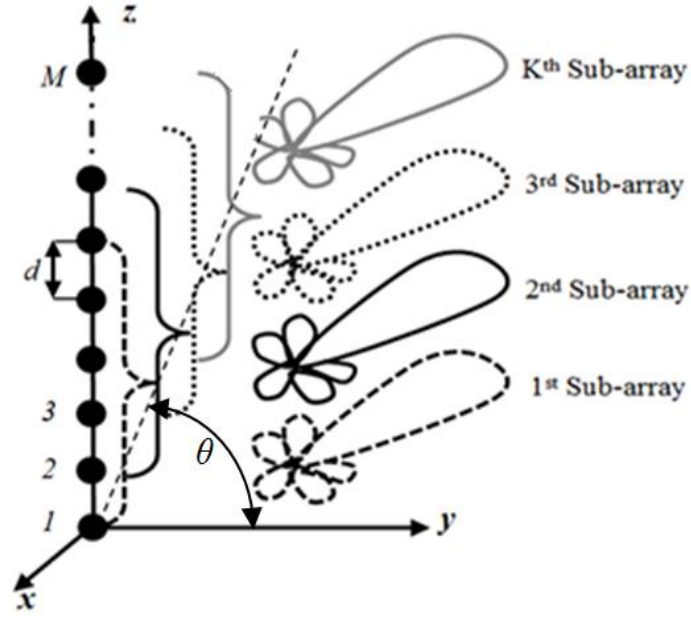
Fig. 5.2.   Illustration of a phased-MIMO array

Every transmit subarray can be composed of any number of elements ranging from 1 to M. However, unlike the general phased-MIMO array discussed in the literature, in this work we will partition the array into K subarrays with overlapping elements V, non-overlapping elements N in the first and last subarrays and non-overlapping elements N_I in the intermediate subarrays. The total number of the elements per subarray is

$$M_K = \begin{cases} N + V & \text{\textit{the first and last subarrays}} \\ N_I + 2V & \text{\textit{the intermediate subarrays}} \end{cases} \qquad (5.4\ )$$

where $N_I = N - V$

Now let us consider an array with M elements and K subarrays each contains N (or N_I depending on its position) non-overlapping and V overlapping elements. V can vary from 0; i.e. no overlapping between subarrays which gives totally disjointed ones ($M_K = N = N_I = M/K$), to M that gives a single antenna array ($M_K = M$; $K = 1$).

K also can vary from M which indicates the whole array as one MIMO antenna array ($M_K = N = N_I = 1$; $V = 0$) to 1 which refers to a single phased antenna array.

For a better understanding of all the possible partitioning schemes for an array into K subarrays with equal M_K elements, M can be classified into $2N$ (in both the 1st and last subarrays), $(K-2)N_I$ (in the intermediate subarrays) and $V(K-1)$ (total number of overlapped elements). Simply M can be expressed as:

$$M = 2N + (K - 2)N_I + V(K - 1) \tag{5.5}$$

Substituting N_I in equation (5.5) with N-V, the possible partitioning values of K subarrays can be deduced as

$$K = \frac{M - V}{N} \qquad K\ is\ an\ Integer \tag{5.6}$$

Therefore, there are a limited number of feasible partitioning schemes, which can satisfy the condition of getting an integer value of K. These partitioning schemes will be expressed in the form of (N, K, M_K). For example, if $M = 20$, the disjoint subarrays with $V = 0$ overlapping elements can be expressed as (1, 20, 1), (2, 10, 2), (4, 5, 4), (5, 4, 5,), (10, 2, 10) or (20, 1, 20). Note that the first case indicates a MIMO antenna array while the last case indicates a phased antenna array. For $V = 2$, the antenna array can be divided in the form of (1, 18, 3), (2, 9, 4), (3, 6, 5), (6, 3, 8), (9, 2, 11), (18, 1, 20). Since then, we are eager to select the optimum partitioning scheme, which gives optimum beam pattern parameters.

We now consider an antenna array with $M = 72$. Every two successive elements are separated by a distance of $\lambda/2$. Using equations (5.3) and (5.6), Fig. 5.3 shows all possible partitioning values against PSLL. The infeasible partitioning schemes (which do not satisfy an integer value of K in equation (5.6)) are assumed to have 0 dB side lobes level. From Fig. 5.3, it is obvious that the minimum value of PSLL occurs when

$$M_K = M - K + 1 \tag{5.7}$$

It is also clear that equation (5.7) offers a feasible physical partitioning scheme for any value of M. Substituting equations (5.7) and (5.4) into (5.6), we have
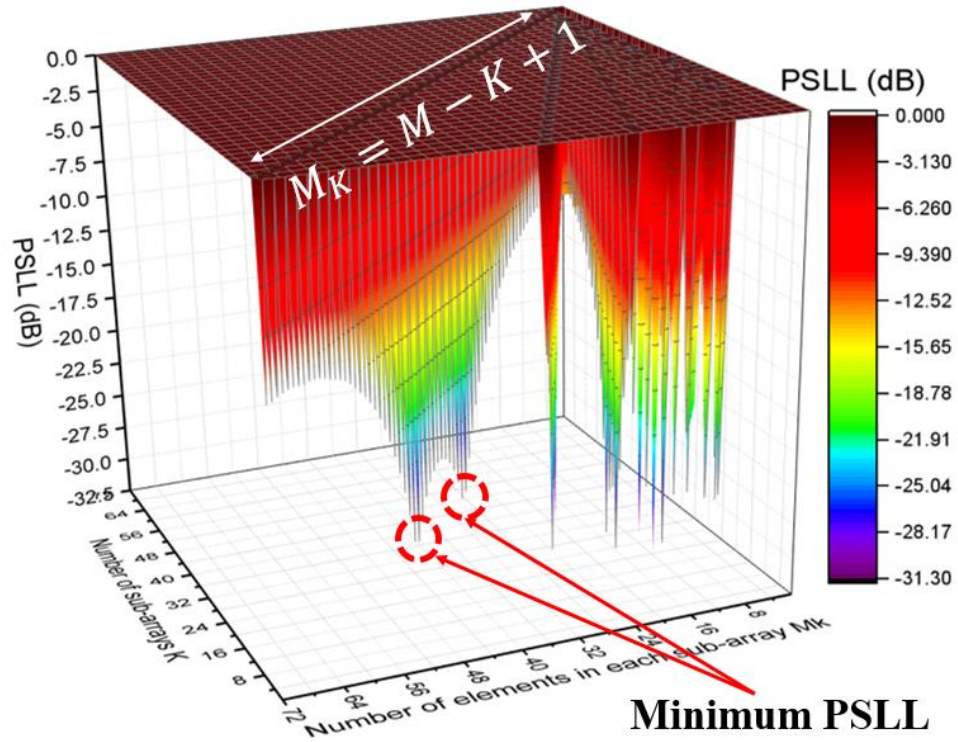
Fig. 5.3.   PSLL for all possible partitioning schemes of $M = 72$ phased-MIMO array

$$\frac{M - V}{N}(N - 1) = N - 1 \qquad\qquad (5.8\ )$$

From equation (5.8), there are 3 solutions corresponding to the cases of optimum division.

(a) Case (1): $N = 1$; i.e. there is only one non-overlapping element between any two adjacent subarrays ($V = M_K$ - 1).

(b) Case (2): $M = V + N = M_K$, $K = 1$; i.e. phased antenna array mode.

(c) Case (3) $V = 0$, $M = N = M_K$; i.e. MIMO antenna array mode.

Case (2) and Case (3) are neglected, as they do not satisfy the phased-MIMO mode conditions so we are interested in Case (1) only.

Fig. 5.4 illustrates the PSLL (in dB) against the number of subarrays at $N = 1$ (Case (1)). Note that Fig. 5.4 is a section of Fig. 5.3 at the line that satisfies equation (5.7). Minimum PSLL (which equals to -31.22 dB) occurs at $K = 31$ and $K = 42$. Thus, the optimum partitioning can be written in (N, K, M_K) form as (1, 31, 42) or (1, 42, 31). Note that PSLL at $K = 1$ and $K = M$ is -13.3 dB which is the PSLL for conventional phased array and MIMO antenna array, respectively.
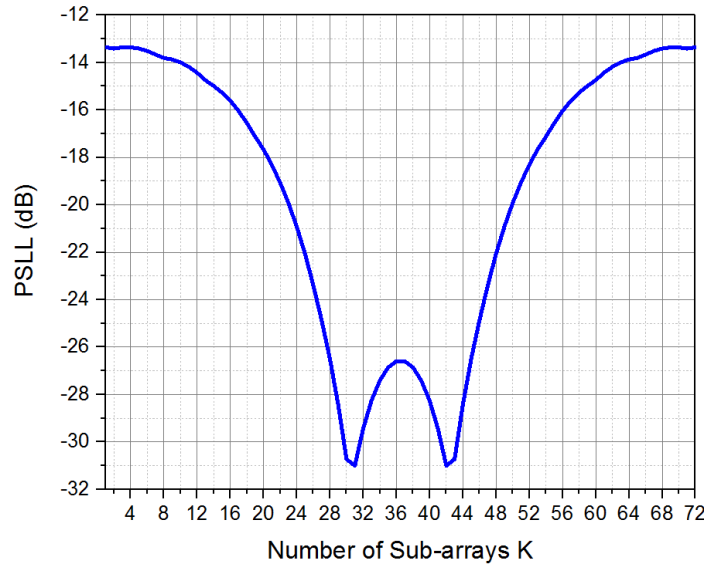
Fig. 5.4.   PSLL against the number of subarrays for *M* = 72

Fig. 5.5 illustrates different values of *M* as odd, even and multiple of 12. It can be estimated that the lowest PSLL occurs at (1, 27, 37) and (1, 37, 27) when *M* = 63 and it occurs at (1, 26, 37) and (1, 37, 26) when *M* = 62. Finally, the lowest PSLL occurs at (1, 26, 35) and (1, 35, 26) when *M* = 60. Note that *K* and M_K are reciprocal.

A general formula for Optimum Partitioning of Phased-MIMO antenna array (OPPM) can be expressed as:

$$ K = \left\lceil \frac{M}{2} - \left\lfloor \frac{M-1}{12} \right\rfloor \right\rceil \qquad (5.9\ ) $$
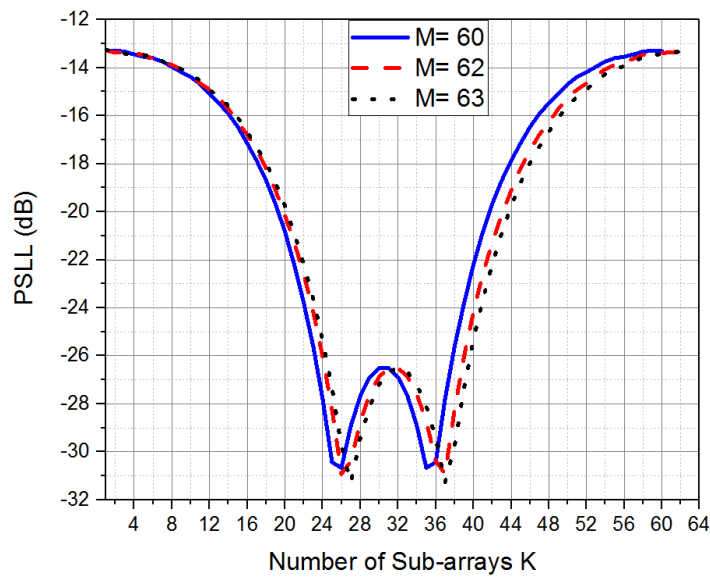
Fig. 5.5.   PSLL against the number of subarrays at different values of *M*

where $\lceil X \rceil$ (ceiling X) gets the closest upper integer value to X and $\lfloor X \rfloor$ (floor of X) gets the closest lower integer value to X for any real value of X.

OPPM formula given in equation (5.9) can be simplified for even values of M. Using properties of ceiling and floor functions, a simplified OPPM formula can be expressed as

$$K = \left\lceil \frac{5M + 1}{12} \right\rceil \qquad M\text{: even integer} \qquad (5.10\ )$$

Substituting equation (5.10) into equation (5.7), simplified OPPM formula can be obtained as

$$M_K = \left\lfloor \frac{7M + 11}{12} \right\rfloor \qquad M\text{: even integer} \qquad (5.11\ )$$

Note that as K and M_K are reciprocal, their values can be switched. Therefore, equation (5.10) can represent the value of K when equation (5.11) gives the value of M_K and vice versa.
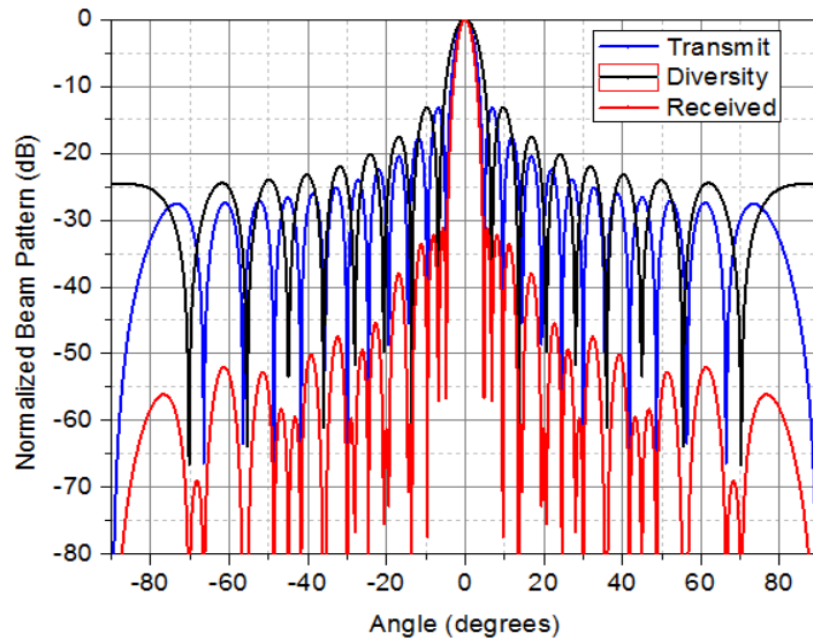
Fig. 5.6.   **Transmitted, Diversity and Received beam pattern at OPPM partitioning schemes ($M = 40$)**

For a better understanding of why equation (5.9) can express the OPPM, we will consider an array with $M = 40$. According to equation (5.9), OPPM are (1, 17, 24) and (1, 24, 17). Fig. 5.6 shows coherent, diversity and overall received beam patterns with the aid of equations (5.1), (5.2) and (5.3). It is clear that there are nulls in the coherent transmit beam pattern at the angles where the diversity beam pattern has its peak side lobes and there are nulls in the diversity beam pattern at the angle where the coherent transmit beam pattern has its first side lobes. Placing nulls against side lobes by this way reduces the overall received beam pattern PSLL which is different from other partitioning scenarios.

For simplicity, we use the conventional transmitted/ received beamforming technique and analyse the performance of the proposed OPPM in comparison to other schemes in [100] and [101]. Again using the previous example with $M = 40$, Fig. 5.7 shows the received Phased-MIMO beam patterns for such an array at *(M/2)-1* partitioning scheme in [100], HPMR-US in [101] and proposed OPPM. It is indisputable that OPPM has the lowest PSLL without any reduction in the HPBW (antenna directivity is kept at the same level). Table 5.1 shows a comparison between [100], [101] and proposed OPPM in terms of PSLL and Directivity. It is clear that OPPM achieves the lowest PSLL without a reduction in array directivity.
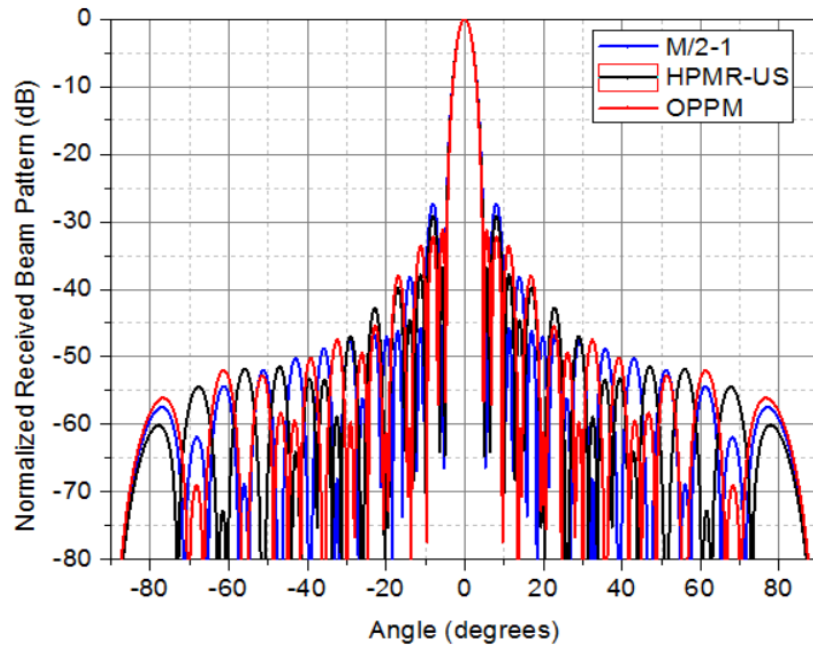
Fig. 5.7.   Received Phased-MIMO beam patterns using *(M/2)-1*, HPMR-US and OPPM partitioning schemes (*M* = 40)

Table 5.1.   Comparison between Reference Partitioning Schemes and Proposed OPPM in PSLL and Directivity

M	PSLL (dB)			Directivity (dB)		
	[100]	[101]	OPPM	[100]	[101]	OPPM
10	-23.1	-26.0	-26.0	9.45	9.32	9.32
20	-29.9	-29.9	-29.9	12.2	12.2	12.2
30	-28.0	-30.5	-31.4	13.9	13.9	13.9
40	-27.3	-29.3	-31.2	15.0	15.1	15.1
50	-27.0	-30.1	-30.8	16.0	16.0	16.1
60	-26.9	-29.2	-30.7	16.8	16.8	16.9
70	-26.8	-28.3	-31.2	17.5	17.5	17.5
80	-26.8	-28.8	-31.6	18.0	18.1	18.1
90	-26.7	-29.2	-31.9	18.5	18.6	18.7
100	-26.7	-28.8	-31.8	19.0	19.0	19.1

Generally, the received signal is accompanied by interference signals I and noise n. The SINR can be expressed as follows [100]:

$$SINR = \frac{\left(\frac{M}{K}\right)\sigma_s^2(M-K+1)^2K^2S^2}{\sum_{i=1}^{I}\left(\frac{M}{K}\right)\sigma_i^2|U^H(\theta_s)U(\theta_i)|^2 + \sigma_n^2(M-K+1)KS} \qquad (5.12)$$

where σ_s, σ_i and σ_n are the variances of the signal, i^{th} interference and noise respectively. θ_s and θ_i are the signal and the ith interfere angle respectively.

Fig. 4.8 shows the output SINR against interference-to-noise ratio (INR). It is clear that OPPM has slightly higher output SINR than other partitioning schemes used in [100] and [101] when the interference signal level is lower than or comparable to the noise signal level. However, when the INR goes higher, i.e. interference signal dominates; OPPM introduces much higher output SINR rather than other schemes.
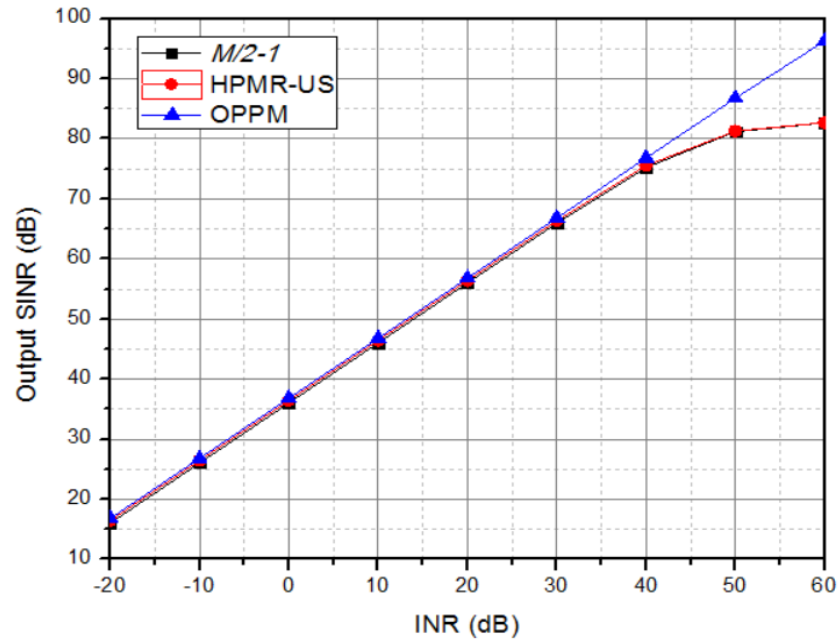
Fig. 5.8.   Output SINR against INR at different partitioning schemes

5.3. Summary

This chapter has proposed an optimum scheme for partitioning an array into a number of subarrays that are allowed to be overlapped. Then, some illustrative values of antenna elements for Phased-MIMO antenna array have been introduced and OPPM formula is deduced to get an optimum partitioning scheme for any number of antenna elements. This optimum scheme improves the PSLL without sacrificing the directivity comparing to other division techniques as it places the nulls of the transmit radiation beam pattern against the peak side lobes of the diversity beam pattern and vice versa. It also improves the output SINR as a result of improving the PSLL.

As the optimized formula is based on observations rather than derivations, more studies should be conducted to generalize it for a larger number of antenna elements.

Chapter 6. A Dual-Broadband MIMO Overlapped Antenna Subarrays

In the previous chapter, phased-MIMO antenna array using OLAS (Overlapped Antenna Subarrays) was illustrated and optimized. In this chapter, the concept of using OLAS is applied to a dual-broadband antenna array. First, this chapter proposes a novel design of a dual-broadband dual-polarized antenna for mobile communication base stations. The proposed antenna is Fylfot-shaped and covers the frequencies from 0.7 GHz to 0.96 GHz (B1) and from 1.7 GHz to 2.7 GHz (B2) simultaneously (with $S_{11} \leq$ -10 dB) which are the two common frequency bands for mobile communication systems. Three resonant frequencies are produced in the proposed design where two of them are independently controlled to achieve the dual-broadband performance. A prototype of the proposed antenna has been developed and tested. The results demonstrate that the proposed antenna has high isolation between its ports, high XPD and stable radiation patterns across both frequency bands. Moreover, a new linear array is proposed and implemented. Unlike the reported dual-band base station antenna arrays, the proposed array uses a novel technique of two MIMO OLAS with shared radiating antenna elements. The OLAS has excellent frequency diversity performance with low ECC. The array has been found to have the same performance as a standard conventional base station antenna but with 25% less number of antenna elements, which leads to a smaller size and lower cost. The simple antenna structure and the novel smart MIMO OLAS technique give the design the privilege to be an ideal candidate for a low-cost directive base station antenna.

6.1. Introduction

The evolution of smartphone technology has resulted in the development of base station antennas for mobile communication systems from single-polarized to dual-polarized and from single band to dual or multi-bands [102]. The most common frequency bands used for mobile communication systems are band B1 (from 0.7 to 0.96 GHz) and band B2 (from 1.7 to 2.7 GHz). To increase the data rate and channel capacity and reduce the signal fading in a multipath environment, space diversity and/or polarization diversity are commonly used [103]. Many successful designs have been introduced in the literature to meet these specifications for a single band antenna (either band B1 or B2) using planar cross dipoles [104] or 3D-printed dipoles [105][106].

The most challenging task is to get a compact design which covers dual or multi-bands. There are quite a few published designs. A dual-broadband antenna was reported in [107] but its single-polarization characteristic limits its use as a base station antenna. In [108], a dual-polarized dual-band antenna array was designed using two different co-located elements to cover the two bands, an arc-probe-fed ring antenna for B1 and a printed microstrip dipole antenna for B2. Moreover, in [109] - [111], two 3D pairs of cross-dipoles are used to widen the BW (one pair for each band). Again, they are co-located to reduce the antenna size. Later on, multi-band arrays have been achieved using three or more different frequency band elements with embedded scheme [112] or optimal array structure [113]. For more size reduction in dual-band base station antenna arrays, elements at B2 are embedded inside the 3D octagonal-shaped elements at B1which are formed as bowls [114]. Although high isolation between the two co-located elements is achieved, the BW is insufficient to cover the whole B1 and B2. In [115], the BW has been improved using a similar embedded array structure as in [114] but the radiation pattern HPBW at B2 is 90° which is not suitable to be employed in densely populated urban areas (typically $65 \pm 5°$) [116] in addition to the antenna large size.

Generally, most of the designs presented in the literature use different element designs for different frequency bands. In [117]-[120], the approach of covering both bands (B1 and B2) by a single antenna element was adopted but with some limitations in the BWs which were insufficient to cover all the desired frequencies. Also, the large

antennas size obligates the spacing between the elements to be larger than one wavelength when they are arranged to form linear antenna arrays at B2. Thus, undesirable grating lobes may be formed. Moreover, some of these dual-band elements have complicated multilayer structures [117] [118] while others provide a single polarization [119] [120].

In this chapter, a novel Fylfot-shaped antenna design is introduced to cover both B1 and B2 simultaneously with a dual-polarization. The antenna enjoys good impedance matching and high XPD with a low cost and a compact size. The design is extended to form a linear antenna array using the MIMO OLAS technique. Although two subarrays are overlapped and share some radiating antenna elements, they have an excellent frequency diversity performance with low ECC.

This chapter is organized as follows: Section 6.2 describes the dual-band antenna design, its principle of operation, initial results and its performance. Section 6.3 presents the development of MIMO OLAS base station. Finally, a summary is drawn in Section 6.4.

6.2. Fylfot-Shaped Antenna Element

6.2.1. Antenna Structure

Fig. 6.1 presents the proposed antenna element geometry while Table 6.1 illustrates its dimensional parameters. Generally, the antenna element can be described as two orthogonal slotted elliptical-shaped cross dipoles printed on opposite sides of an FR-4 substrate with relative permittivity ε_r= 4.3, tangential loss of 0.025, thickness Hd= 1.6 mm and side length Ld (which is to be determined). The dipoles are placed at ±45° with respect to the Y-axis in order to provide polarization diversity. Each dipole consists of two elliptical-shaped elements linked by a feeding strip and an RF connector. The endpoints of each slotted elliptical-shaped dipole are extended to form a bowtie dipole, which is placed orthogonal to the ellipse major axis forming a Fylfot shape. Thus, again the bowtie dipoles on both sides of the substrate are placed on ±45° with respect to Y-axis. The substrate and dipoles are oriented in the XY plane. The substrate is placed above two square metallic ground reflectors to enable directional radiation; a small reflector and a large reflector are used for the beam radiations at B2 and B1 respectively. The small reflector is placed at a height $H1$ and has a side length

Lg1 while the large reflector is placed at a height *H2*, with side length *Lg2* and four sidewalls of a height *Hw*.

The four sidewalls work as four parasitic elements located at ± 45º with respect to the radiating dipoles to improve the XPD [104]. The substrate and the two metallic reflectors are concentric, and their edges are parallel to X and Y-axes. The antenna is fed through two coaxial cables. The outer of the coaxial cable is connected to one of the elliptical elements of the antenna while the inner is connected to the stripline.
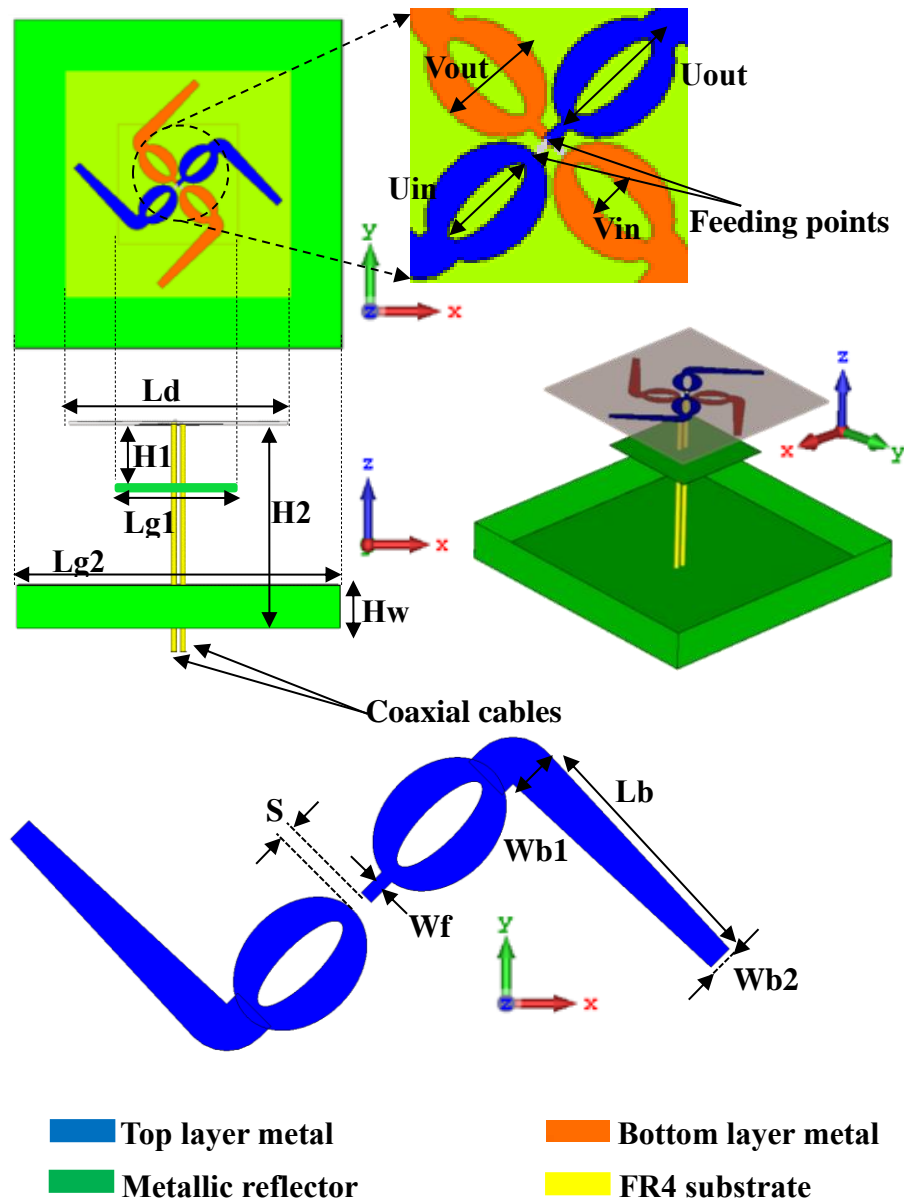
Fig. 6.1.   The geometry of the proposed antenna element

Table 6.1.   Parameters of the Proposed Antenna

Parameter	Value (mm)	Parameter	Value (mm)	Parameter	Value (mm)
Vout	22	Wb1	9	Lg1	80
Uout	29	Wb2	5	Lg2	220
Vin	7	Wf	3	H1	30
Uin	19	S	4	H2	100
Lb	52	Ld	150	Hw	23

6.2.2. Methodology and Principles of Operation

The antenna design is based on creating dual-band coverage based on constructing two combined radiators.

The proposed antenna can be considered as two different types of dipoles printed on each side of the substrate and connected together, a slotted elliptical-shaped dipole and a bowtie dipole. To understand the working principle of the proposed antenna, two reference designs (antenna REF1 and antenna REF2) are used as shown in Fig. 6.2. Initially, the design was based on the antenna element, which has been presented and illustrated in Chapter 4 (antenna REF1). The slotted elliptical-shaped dipole length (*2Uout*) equals to *$0.5\lambda_{0B2}$* (where λ_{0B2} is the free space wavelength of the central frequency of B2, 2.2 GHz). It is observed that antenna REF1 has two resonant frequencies at B2, one is due to the long current path from the feeding points to the ellipse endpoints along the ellipse edges and the other is due to the short current path from the feeding points to the ellipse endpoints along the elliptical slot edges. Antenna REF1 covers B2 only as shown in Fig. 6.2.

The design is amended by adding a bowtie dipole with a length of (*2Lb*) to the slotted elliptical-shaped dipole. Each pole of the bowtie dipole is connected to one of the endpoints of the slotted elliptical-shaped dipole and forming 90° with respect to the ellipse major axis (antenna REF2). Thus, the bowtie dipoles on both sides are

orthogonal and placed on ±45° with respect to Y-axis. The dimension *Lb* was initially selected such that the dipoles total length (*2Uout+2Lb*) equals to *0.5λ0B1* (where *λ0B1* is the free space wavelength of the central frequency of B1, 0.83 GHz). It is evident that a third resonant frequency has been created at B1 as shown in Fig. 6.2 but unfortunately, the BW at B2 has been shrunk.
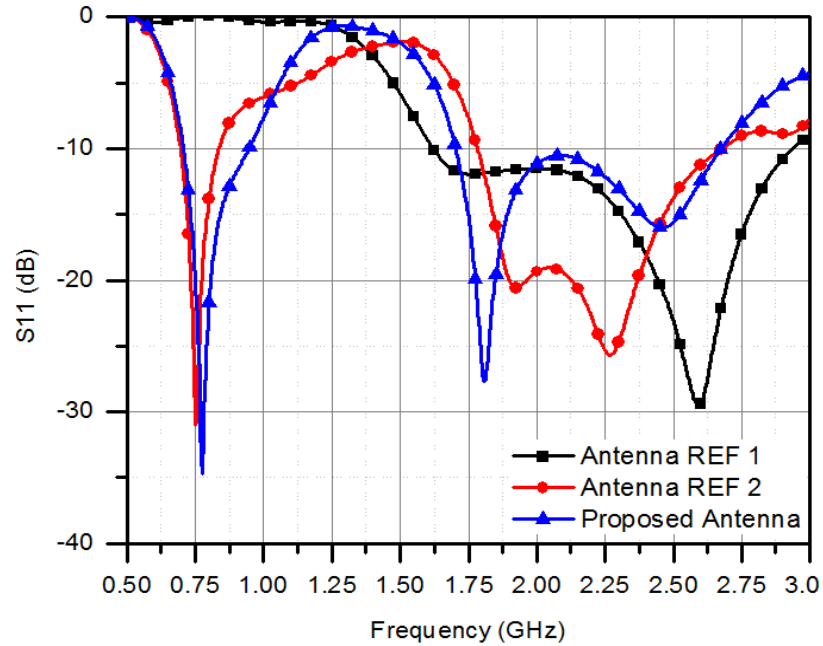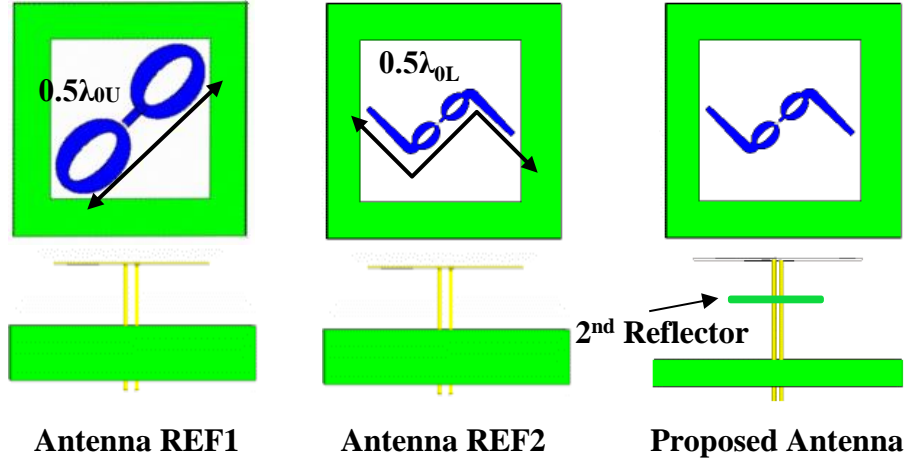
Fig. 6.2.   References and the proposed antennas

A second small metallic reflector is placed at a height *H1* with respect to the substrate (proposed antenna). This second reflector has two functions; the first one is to improve the impedance matching across B2 as will be discussed in detail in section

6.2.4. The second function is to enable directional radiation for the signals at B2. The dimensions $H1$ and $H2$ were initially selected to be $0.25\lambda_{0U}$ and $0.25\ \lambda_{0L}$ respectively.

The input impedance (Z_{in}) of the proposed antenna in correlation to the reflection coefficient is presented in Fig. 6.3. The three resonant frequencies (Fr1 at B1 and Fr2, Fr3 at B2) are located at the points where the imaginary part of Z_{in} (Im (Z_{in})) equals to zero. Fr1, Fr2 and, Fr3 are 0.77, 1.84 and 2.5 GHz respectively. One of the advantages of this design is that Fr1 and Fr3 can be controlled independently of one another and of Fr2, as going to be discussed in detail in section 6.2.3. Therefore, once Fr2 is obtained, Fr1 and Fr3 can be independently tuned and dual-broadband can be achieved. Note that the values of the real part of Z_{in} (Re (Z_{in})) around these resonant frequencies satisfy VSWR $\leq$ 2 ($Z_0/2 \leq Re$ (Z_{in}) $\leq 2Z_0$) where Z_0 is the characteristic impedance (50Ω in our case).
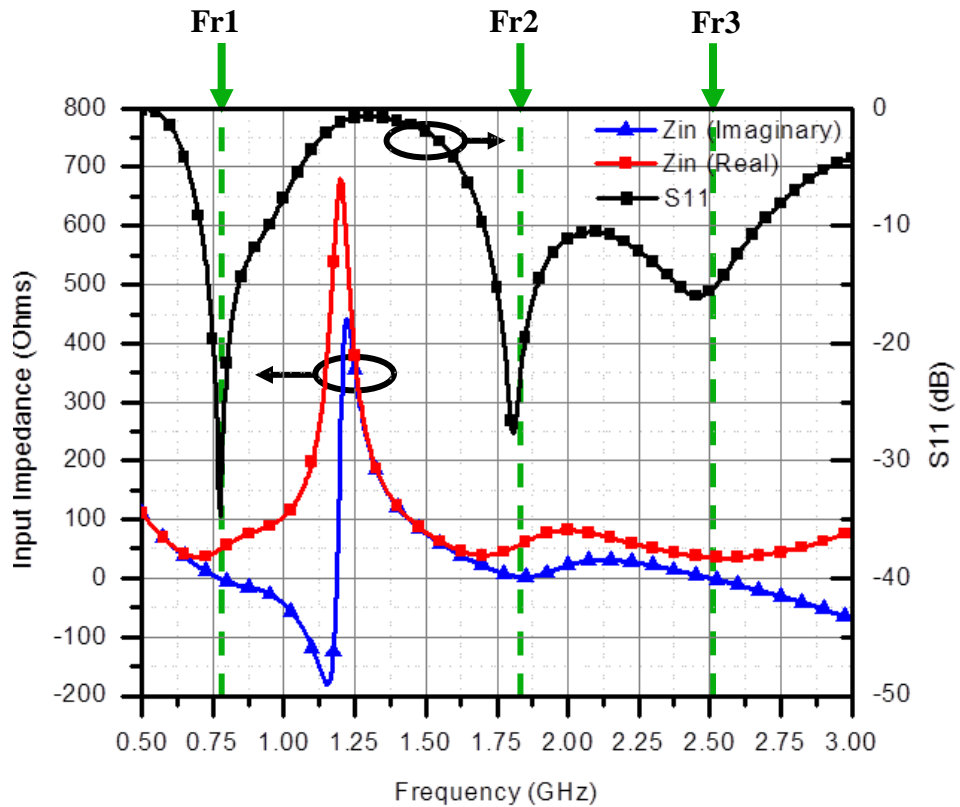
Fig. 6.3.   The input impedance of the proposed antenna correlated to S_{11}

The current distributions across the radiating dipoles at the three resonant frequencies are shown in Fig. 6.4. It can be seen that at Fr1, the current flows from the feeding point to the terminal points through both dipoles (slotted elliptical-shaped and

bowtie dipoles) uniformly. This means that both dipoles contribute to forming impedance matching across B1. On the other hand, the current distributions at Fr2 and Fr3 are highly dense around the slotted elliptical-shaped dipole while there is a light current density across the bowtie dipole. Therefore, we can conclude that the elliptical-shaped dipole contributes to creating impedance matching across both bands while bowtie dipole mainly affects B1 only.

(a)

(b)

(c)
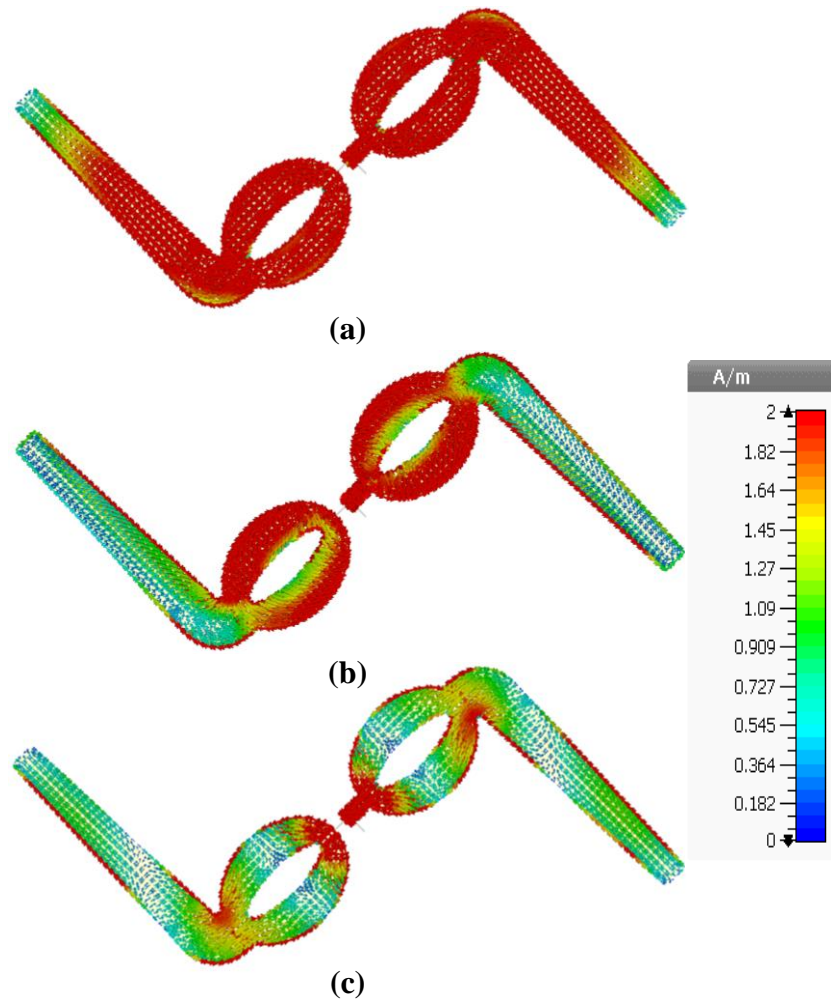
Fig. 6.4.   The current distributions at (a) Fr1 (b) Fr2 (c) Fr3

By adjusting the dimensions of the feeding lines, the elliptical-shaped dipoles, the elliptical slot, and the bowtie dipoles, it is possible to achieve good impedance matching. By appropriately designing the reflectors and adjusting their height from the substrate, a stable radiation pattern with high gain and suitable HPBW for base station antenna can be achieved.

To validate the proposed design, a prototype was fabricated and tested as shown in Fig. 6.5. The PCB and the small reflector are fixed above the large reflector using foam layers. It is favourable to use pillars to fix the antenna pieces altogether to make it more rigid mechanically in case of industrial usage.
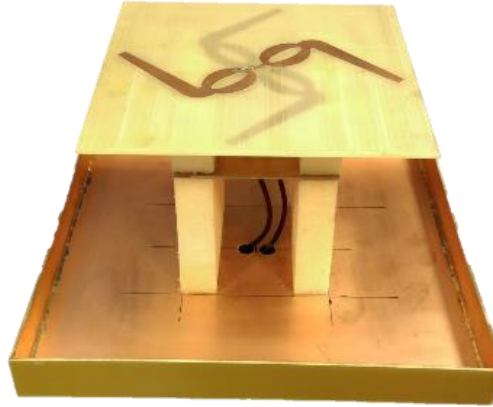
Fig. 6.5.   A prototype of the proposed antenna element

Fig. 6.6 shows a good agreement between the simulated and measured reflection coefficients. For $S_{11} \leq$ -10 dB, the measured fractional BWs are 40% (0.7-1.05 GHz) and 60% (1.6 -3 GHz) for B1 and B2 respectively.
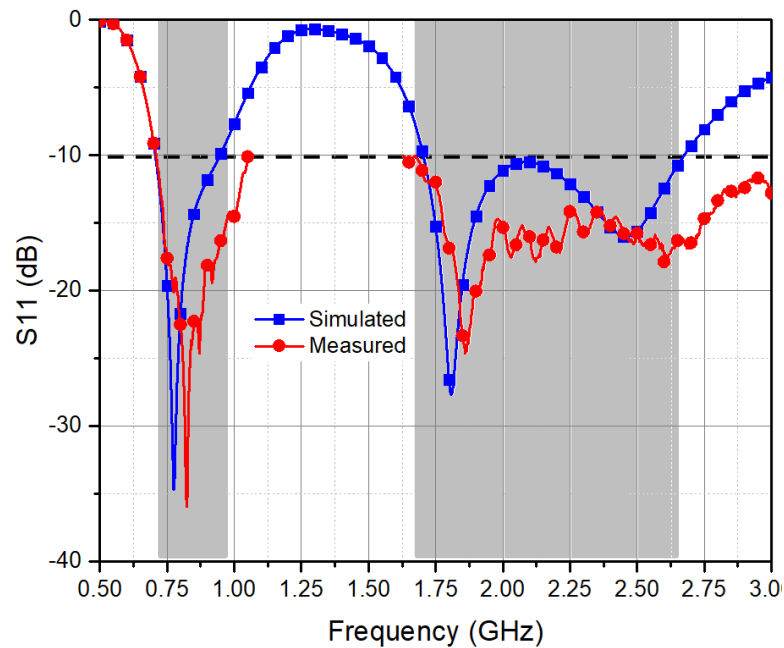
Fig. 6.6.   Simulated and measured reflection coefficients

Fig. 6.7 shows that the measured port-to-port isolation is better than 30 dB for B1 and better than 20 dB for B2. The isolation across B2 is less than the isolation across B1 because of the high surface current density at B2 formed at the feed point of the antenna (see Fig. 6.4), which can couple to the other orthogonal dipole. The deviation between the simulated and the measured port-to-port isolations may be due to fabrication tolerance.
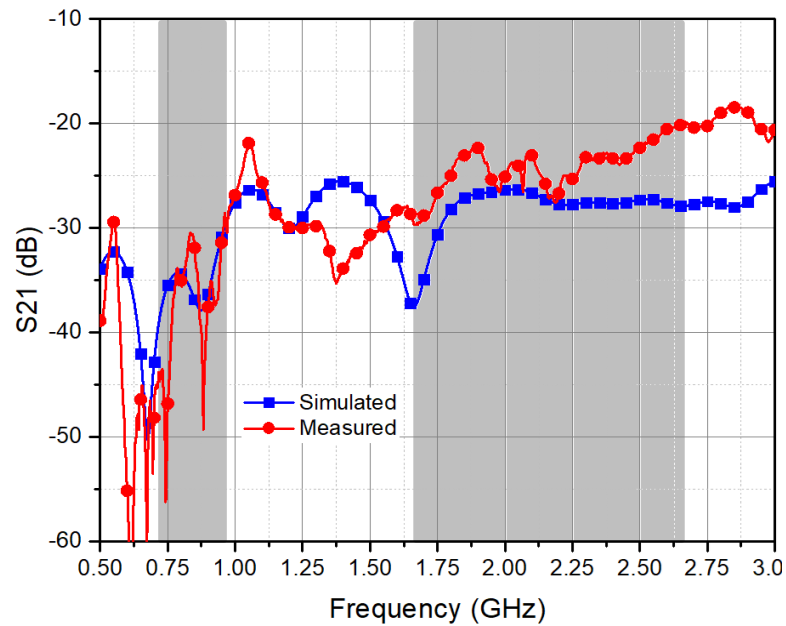
Fig. 6.7.   Simulated and measured port-to-port isolation

The simulated and measured co- and cross-polarized radiation patterns at the start, central and end frequencies of each band in H-plane (XZ plane) and V-plane (YZ plane) are shown in Fig. 6.8. It is apparent that the proposed antenna has a good agreement in the radiation patterns between the simulation and the measurement results. The HPBWs in the H-plane are $73\pm2°$ and $65\pm5°$ at B1 and B2 while the HPBWs in the V-plane are $90\pm5°$ and $72\pm8°$ at B1 and B2 respectively.

The XPD at boresight is better than 20 dB at B1 and better than 18 dB for B2. The detailed values of XPD are illustrated in Table 6.2.

Fig. 6.9 presents the simulated and measured realized gains of the proposed antenna across B1 and B2, which are 6 ± 1 dBi and 6.7 ± 2 dBi respectively.
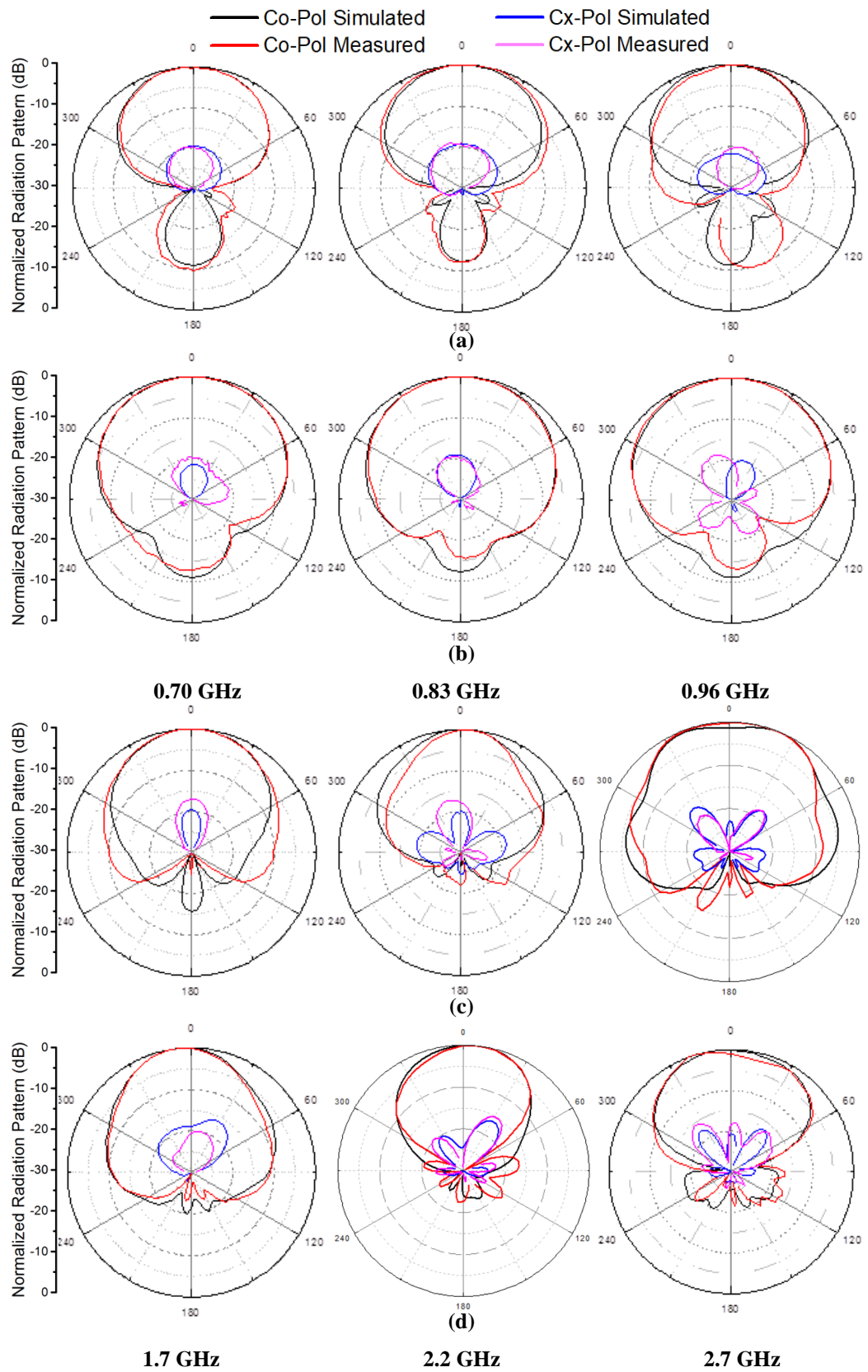
Fig. 6.8.   **Simulated and measured co- and cross-polarized radiation patterns for**
(a) B1 in H-plane (b) B1 in V-plane (c) B2 in H-plane (d) B2 in V-plane

Table 6.2.   XPD at Boresight of the Proposed Antenna Element

Frequency Band	Frequency (GHz)	XPD (dB)
	0.7	20.8
B1	0.83	20.5
	0.96	20.3
	1.7	18
B2	2.2	19.6
	2.7	18.3
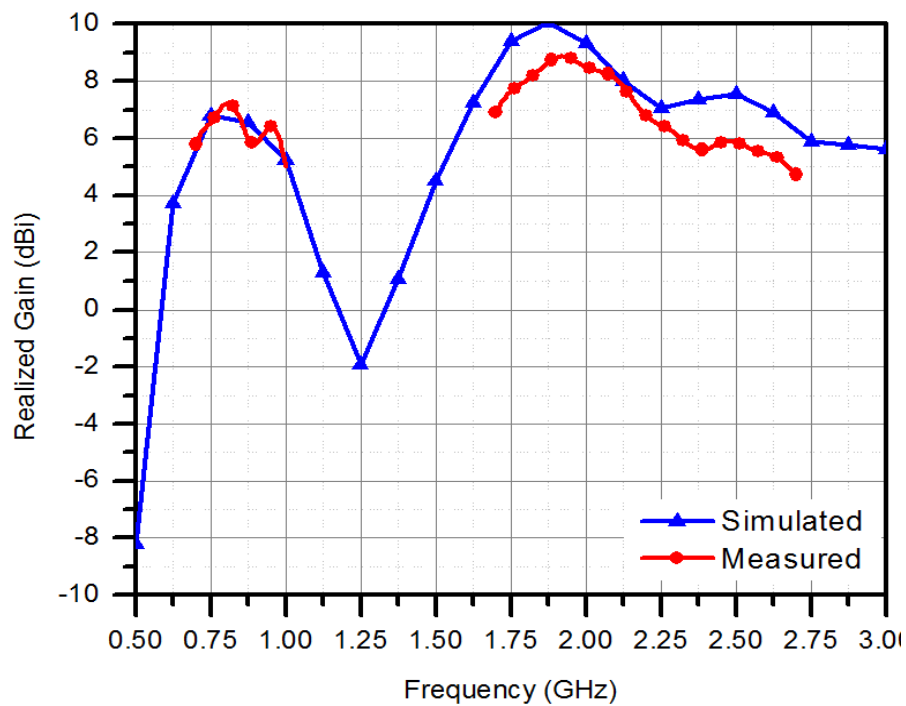
Fig. 6.9.   Simulated and measured realized gains of the proposed antenna

Table 6.3 displays a comparison between the state-of-the-art dual-band dual-polarized base station antenna elements performance and the proposed antenna. It is apparent that the proposed antenna is an optimum design, which has a relatively wide BW, suitable HPBWs for base station antennas employed in densely populated urban areas and, a small size. In addition, it has a simple manufacturing process using PCB instead of the 3D printing used in [110], [111], [114] and [115]. The most important feature in the proposed antenna is that it covers both bands simultaneously which gives it the privilege to be used as a shared element between subarrays at B1 and B2 at the same time in a base station antenna as will be discussed in detail in section 6.3.

Table 6.3.   Comparison of Several Dual-Band Dual-Polarized Antennas

Ref	Band (GHz)		BW (%)		HPBW (°)		Gain (dBi)		Size (mm³)		Manufacturing Process	Number of Elements
	B1	B2	B1	B2	B1	B2	B1	B2	Without reflectors	With reflectors		
[110]	0.79 - 1	1.64 – 2.76	23.5	51	69	73	8.6	8.8	135×135×75	140×140×75	3D printing	1 for B1 + 1 for B2
[111]	0.79 – 0.96	1.71 – 2.17	19.4	23.7	64.5	66	9.3	9	152×152×71	255×255×71	3D printing	1 for B1 + 1 for B2
[114]	0.79 – 0.96	1.71 – 2.17	19.4	23.7	65	65	9.5	9	166×166×68	255×255×130	3D printing	1 for B1 + 2 for B2
[115]	0.7 – 1.18	1.67 – 2.73	51	48	61.5	90	8.4	8.7	152×152×100	290×290×100	3D printing	1 for B1 + 1 for B2
[119]	0.78 – 1.02	2.04 – 3.13	26.6	42.2	60	50	8.4	8	125×125×16	244×244×50	PCB	1 for B1 + 1 for B2
Proposed Antenna	0.7 – 1.05	1.6 - 3	40	60	73	65	6	6.7	150×150×1.6	220×220×100	PCB	1 for both bands

To optimize the proposed antenna design, it is necessary to understand how the design parameters affect the proposed antenna performance. Therefore, some important parameters and their effects are studied through simulations. When one parameter is studied, all other parameters are kept constant.

6.2.3. Effect of Dipole Dimensions

Controlling the two resonant frequencies (Fr1 and Fr3) independently is the key-point of achieving dual-broadband operation. Therefore, in this section, we are going to present these controlling dimensional parameters.

The first parameter to be studied is the bowtie dipole length (Lb). As the working principles of the antenna have been discussed in section 6.2.2, the bowtie dipoles contribute to the impedance matching across B1 only with a very slight effect on B2. Thus, Fr1 can be controlled independently of Fr2 and Fr3 by changing the length Lb. As noticed in Fig. 6.10, when the length Lb increases, the overall length of the dipole ($2Lb+2Uout$) increases while the length of the elliptical dipole ($2Uout$) remains constant. Thus, B1 is shifted to lower frequencies while B2 has almost no changes. The optimum value of Lb is 52 mm to cover the whole B1with VSWR ≤ 2.

The second parameter to be studied is the elliptical-slot major axis Uin. Changing Uin does not result in any changes in the two dipole lengths. Thus, it has almost no effect on the first and second resonant frequencies (Fr1 and Fr2). The third resonant frequency Fr3 can be tuned by changing the dimension Uin as shown in Fig. 6.11. The optimum value of Uin is found to be 19 mm to fully cover B2.
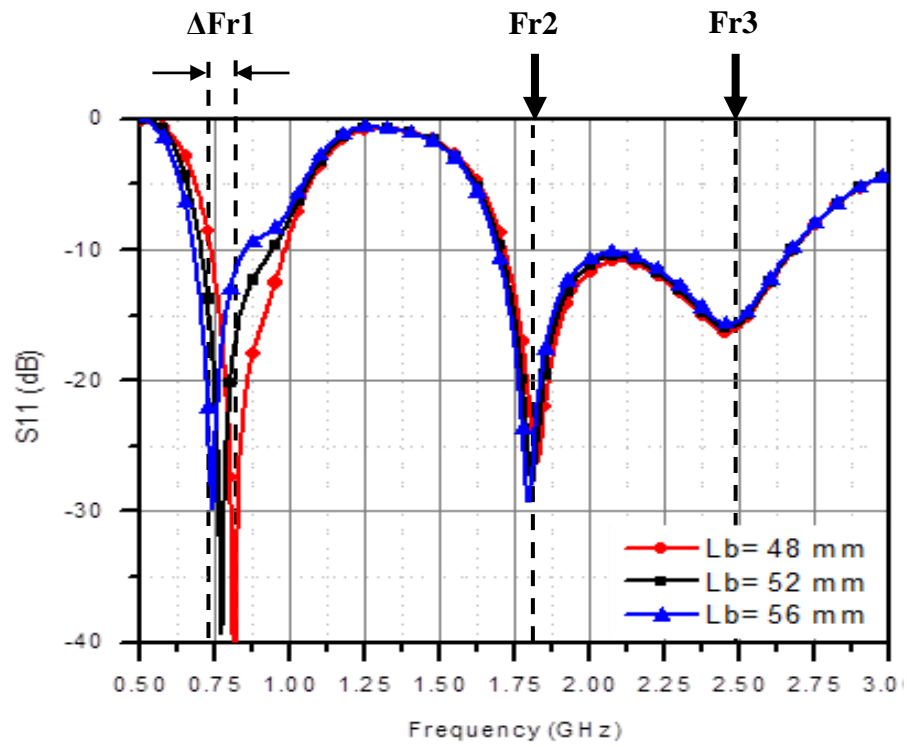
(a)
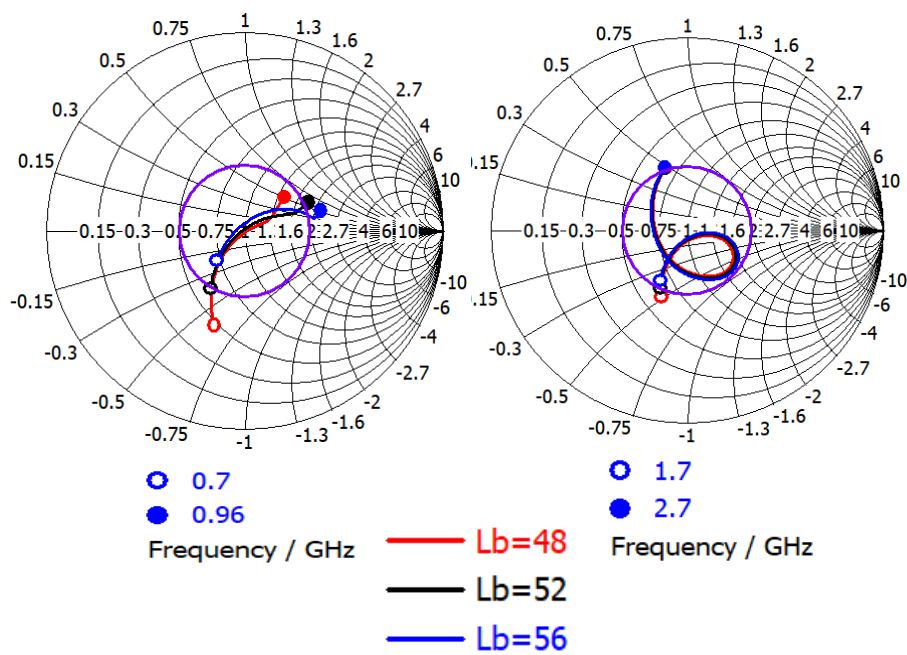
(b)

Fig. 6.10.   **The effect of *Lb* on the impedance matching illustrated by**

(a) reflection coefficient (b) Smith charts
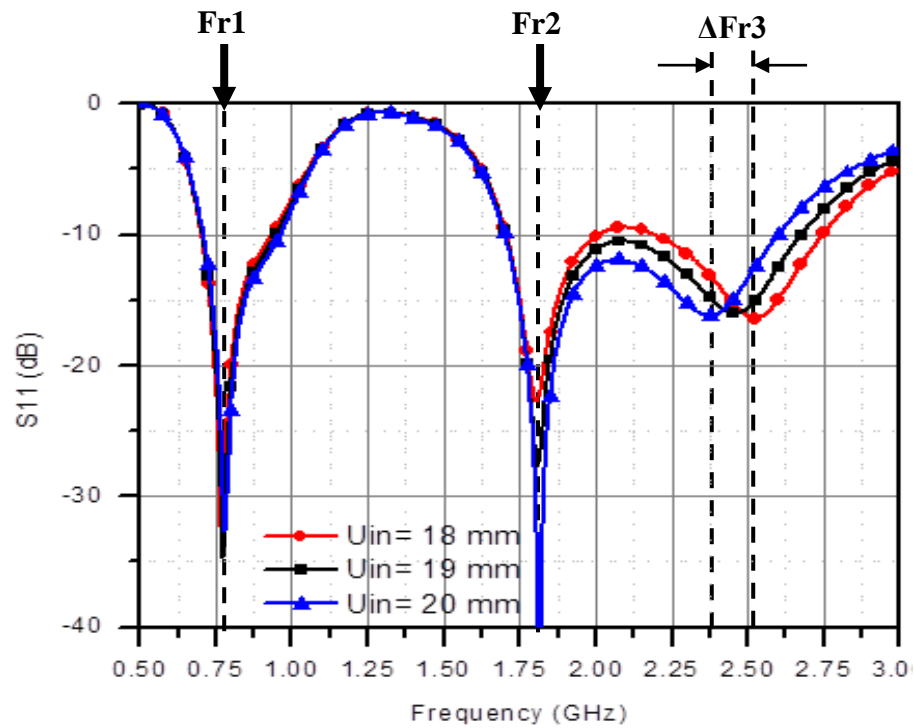
(a)
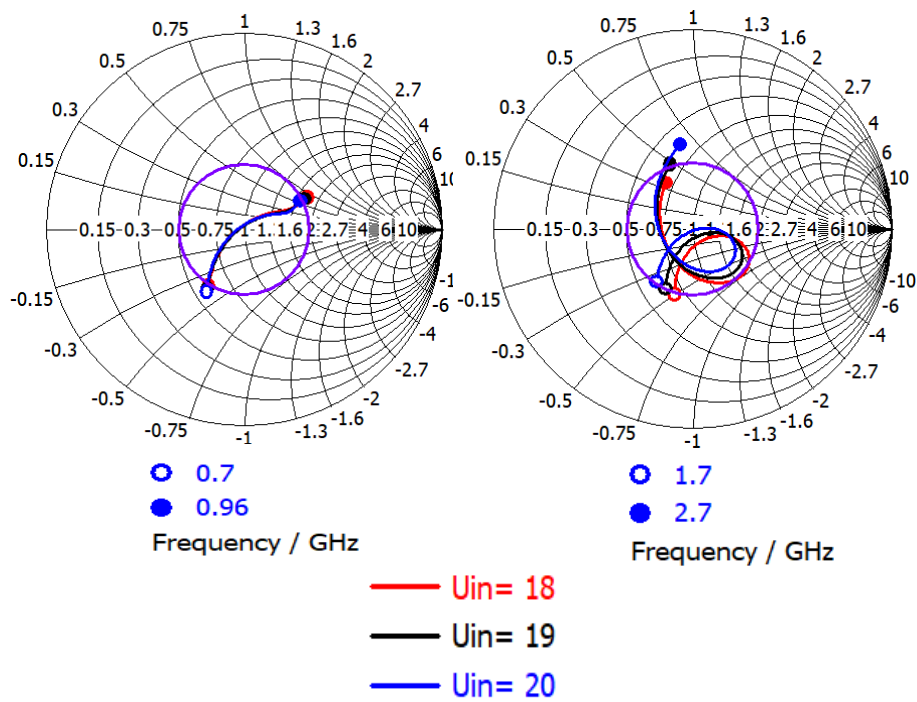
(b)

Fig. 6.11.   The effect of *Uin* on the impedance matching illustrated by (a) reflection coefficient (b) Smith charts

6.2.4. Effect of the Small Metallic Reflector

(a)

(b)
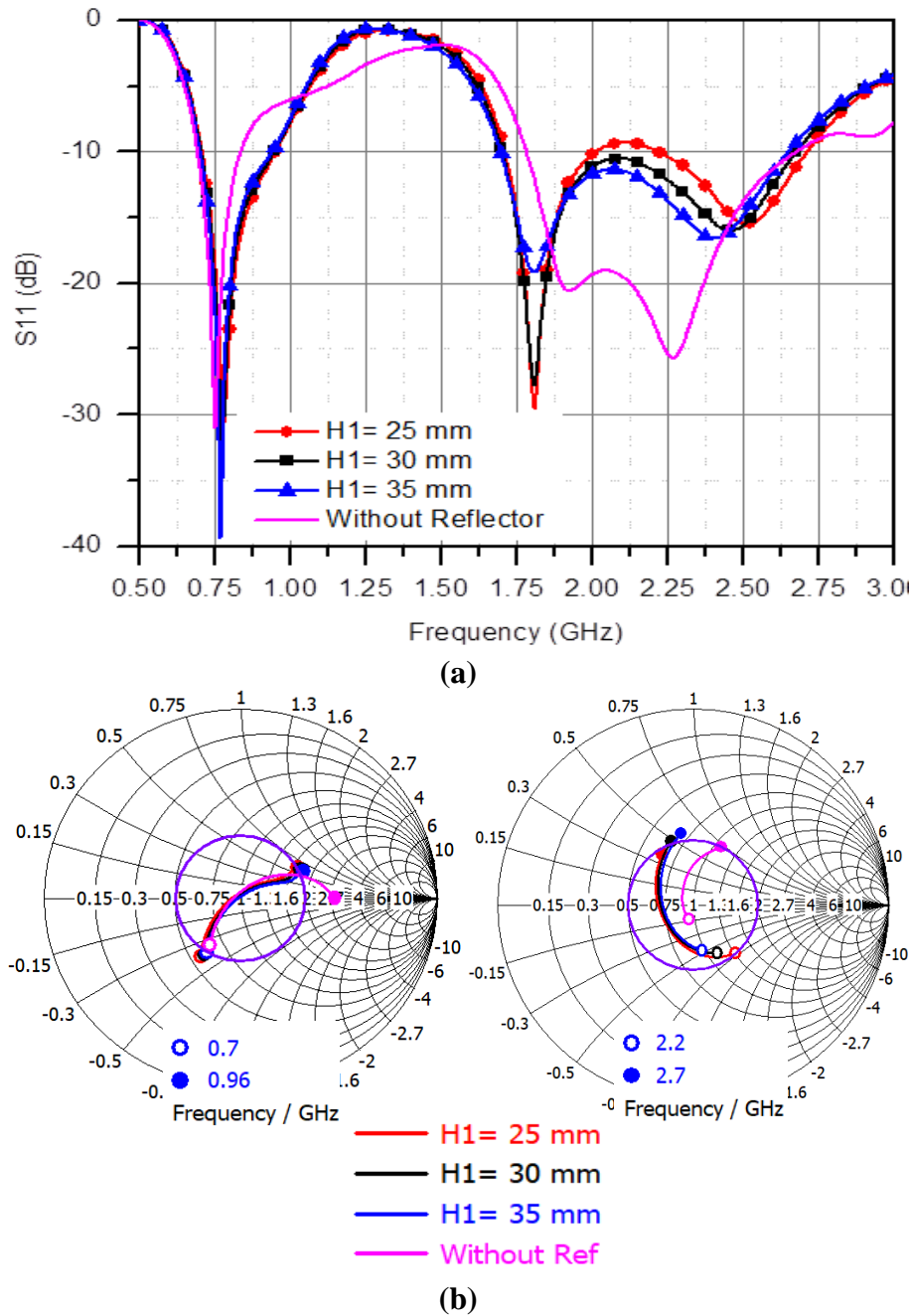
Fig. 6.12.   The effect of the small reflector on the impedance matching by
(a) reflection coefficient (b) Smith charts

The small reflector has two functions in the antenna performance enhancement. The first function is improving the antenna BW across B2. Although there are two independent resonant frequencies at B2, it is not possible to achieve full coverage across the whole B2 without the small reflector as shown in Fig. 6.12.

From Fig. 6.12(a), the height *H1* affects only Fr3 with almost no effect on Fr1 and Fr2. By investigating the effect of changing *H1* on the dipole input impedance around Fr3 (2.2-2.7 GHz), we notice from the Smith chart in Fig. 6.12(b) that the small reflector adds a capacitive loading to the radiating dipoles at Fr3. Thus, when the height *H1* increases, the capacitive loading decreases and the plot goes inductive at Fr3. The optimum height *H1* is 30 mm to get the best achievable impedance matching. Note that there is almost no significant change in the impedance matching across B1.

The second function is improving the antenna gain stability of the radiated signals across B2 as it enables the unidirectional radiation by reflecting most of the back radiation at this band as illustrated in Fig. 6.13. It is noticeable that the small reflector has no effect on the antenna gain at B1.
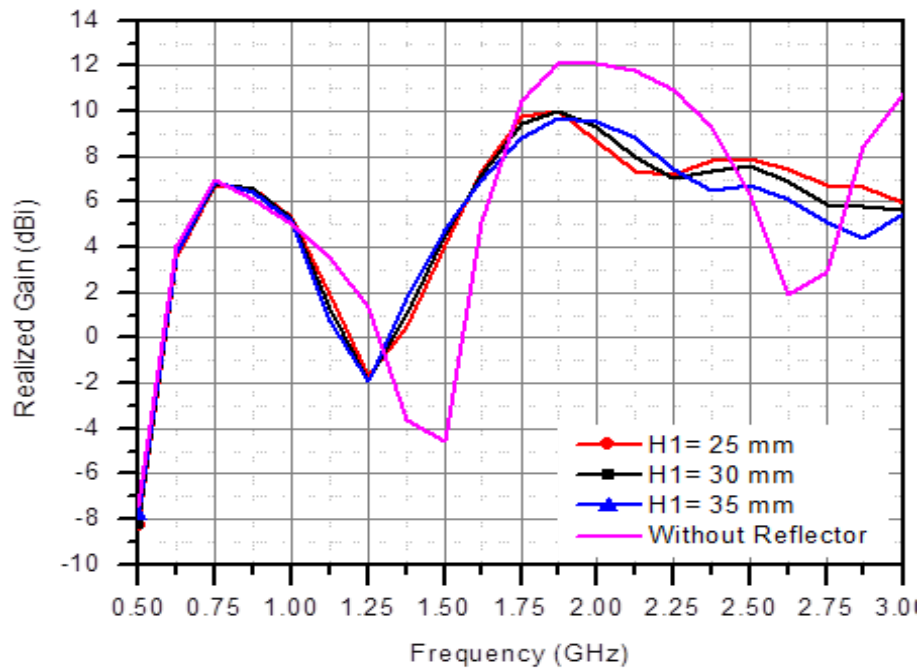
Fig. 6.13.   The effect of the small reflector on the realized gain

6.3. MIMO Overlapped Antenna Subarrays

Directive base station antennas are formed in linear arrays with high gains typically 12-14 and 15-17 dBi at B1 and B2 respectively [121]. The conventional base station antenna array diagram is presented in Fig. 6.14(a). It consists of two linear arrays, typically one array for each band. These arrays may be totally disjointed but mostly they are co-located in the same radome/ housing to reduce the antenna size. However,

in all cases, each array uses its own antenna element structure and a separate feeding network.
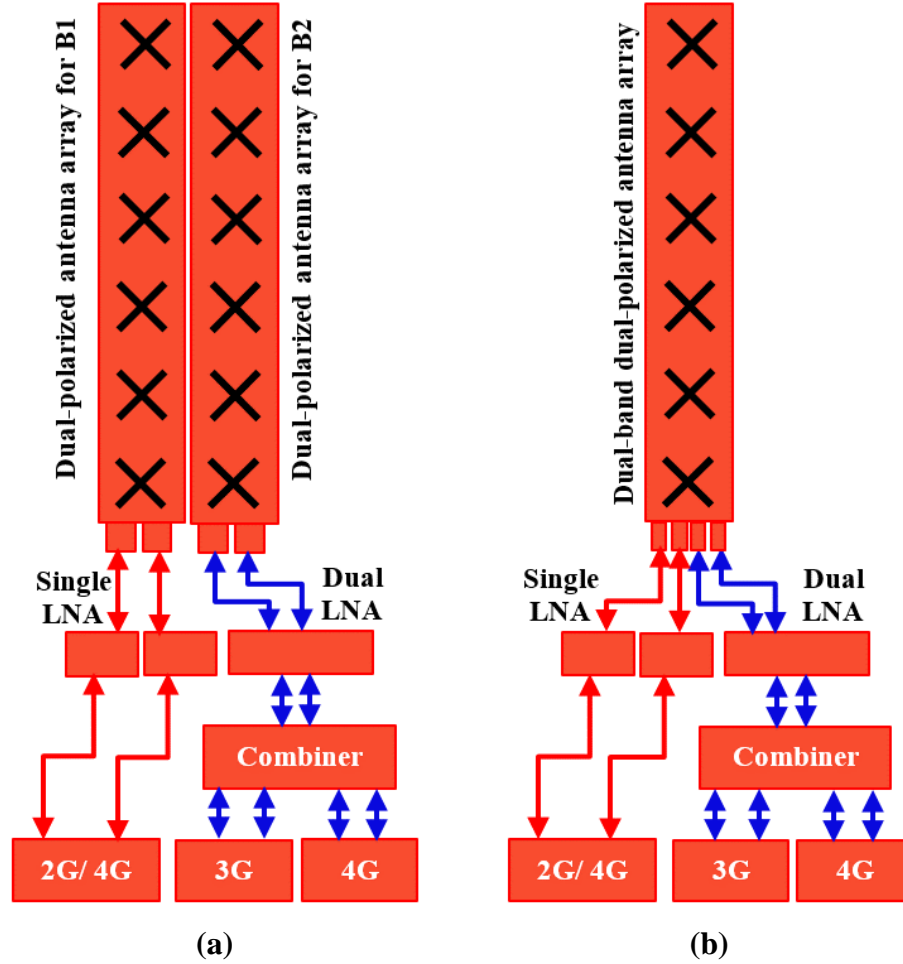
Fig. 6.14.   Illustrative diagrams of the
(a) conventional (b) proposed MIMO OLAS base station

In this section, a proposed single linear array is constructed using two MIMO OLAS, with a subarray for each band. Unlike the base station antenna arrays reported in the literature, these two MIMO OLAS shared some of their radiating elements (i.e. some antenna elements contribute to forming the radiation patterns of both subarrays simultaneously). Therefore, the proposed antenna array can take the role of both B1- and B2-arrays in the conventional base station antenna with fewer elements as shown in Fig. 6.14(b). The proposed array consists of two subarrays: B1-subarray and B2-subarray. Thus, the subarrays have frequency diversity. The number of the elements N in each subarray may be found by [122]:

$$N = \frac{D\lambda_0}{2d} \qquad (6.1\ )$$

where D is the subarray directivity and d is the distance between two successive elements in the subarray. To avoid high coupling between elements and grating lobes, d is selected as $0.5\lambda_{max} < d < \lambda_{min}$ [122] where λ_{max} is the free space wavelength at the start frequency of the desired band (0.7 GHz for B1 and 1.7 GHz for B2) and λ_{min} is the free space wavelength for the end frequency of the desired band (0.96 GHz for B1 and 2.7 GHz for B2). Therefore, d is chosen to be 285 mm for B1-subarray and 95 mm for B2-subarray. Note that for practical implementation, d in B1-subarray is three times d in B2-subarray. From equation (6.1), the number of the elements in each subarray is five and seven elements for B1- and B2-subarrays respectively.

To build such subarrays, a 9-element antenna array is constructed with elements distributed as shown in Fig. 6.15. B2-subarray consists of the middle elements numbering from 2 to 8 with a total number of seven elements while B1-subarray consists of five elements numbered 1, 2, 5, 8, and 9. Note that element number 2, 5 and 8 are shared between the two subarrays. Therefore, virtually, the total number of elements in both subarrays are twelve (five elements for B1-subarray and seven elements for B2-subarray) while the actual number of elements is nine. This means a 25% reduction in elements capacity, which leads to a reduction in antenna size and cost. Each one of the shared antenna elements numbered 2, 5 and 8 is fed through a frequency duplexer. The input port of the frequency duplexer is connected to the antenna element while its output ports are connected to B1 and B2 power dividers respectively. In the receiving mode, signals at B1 and B2 propagate from the antenna to the input port of the duplexer which in turns directs each signal to the corresponding output port and hence to the corresponding power divider. In the transmitting mode, this process is reversed. Each subarray is fed through two ports for two orthogonal polarizations (*P1* and *P2* for ±45° of B1-subarray and *P3* and *P4* for ±45° of B2-subarray respectively). The Feeding network including the power dividers, the frequency duplexers and feeding ports is presented in Fig. 6.15.
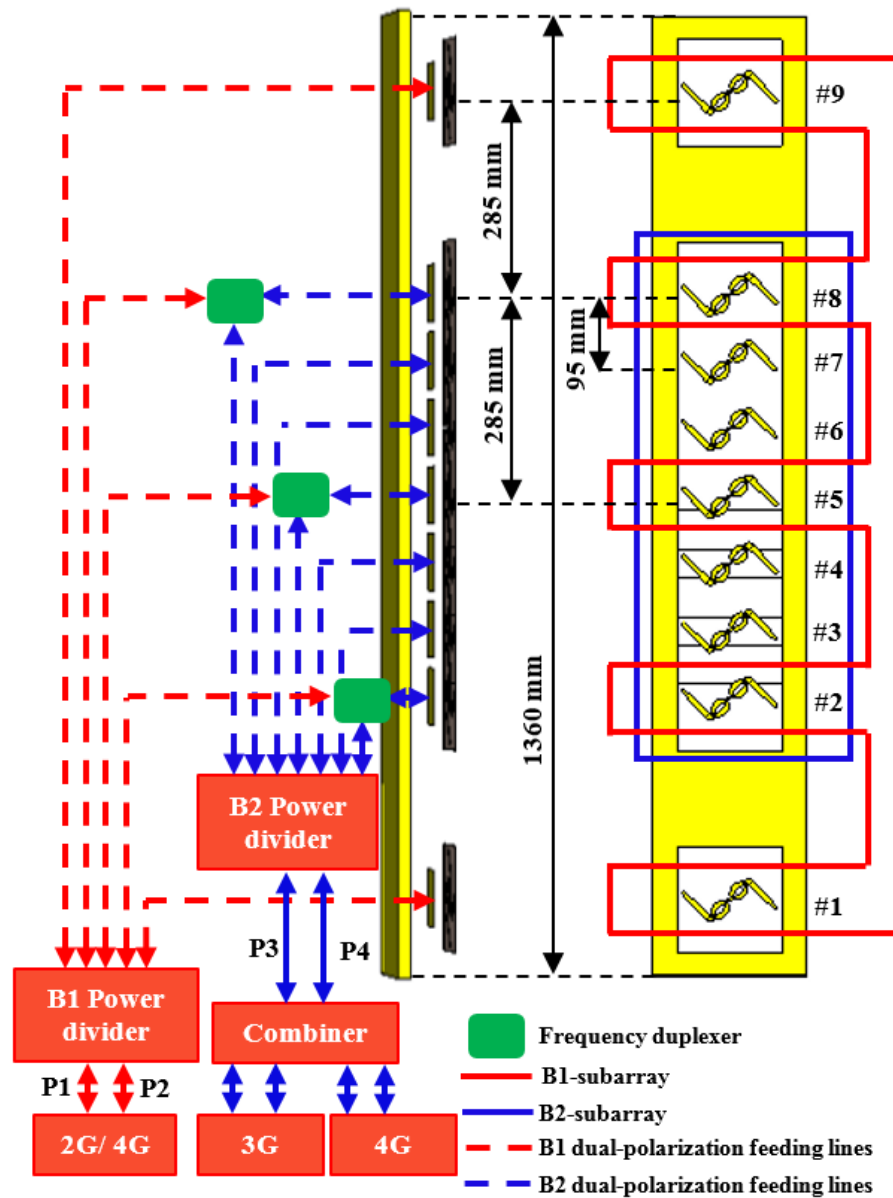
Fig. 6.15.   The proposed 9-element MIMO OLAS base station

Two different types of diversity are used in the proposed MIMO OLAS to enhance the communication performance: polarization diversity between the dipoles in each antenna element and frequency diversity between the subarrays. The overall array height is 1360 mm which is smaller than the conventional base station antenna array height (typically 1500 mm) [121].

Fig. 6.16 shows the simulated 3D radiation patterns and gains of the proposed antenna array at the start, middle and stop frequencies of each band. It is seen that the gains are 13.5 and 17.6 dBi across B1 and B2 respectively.
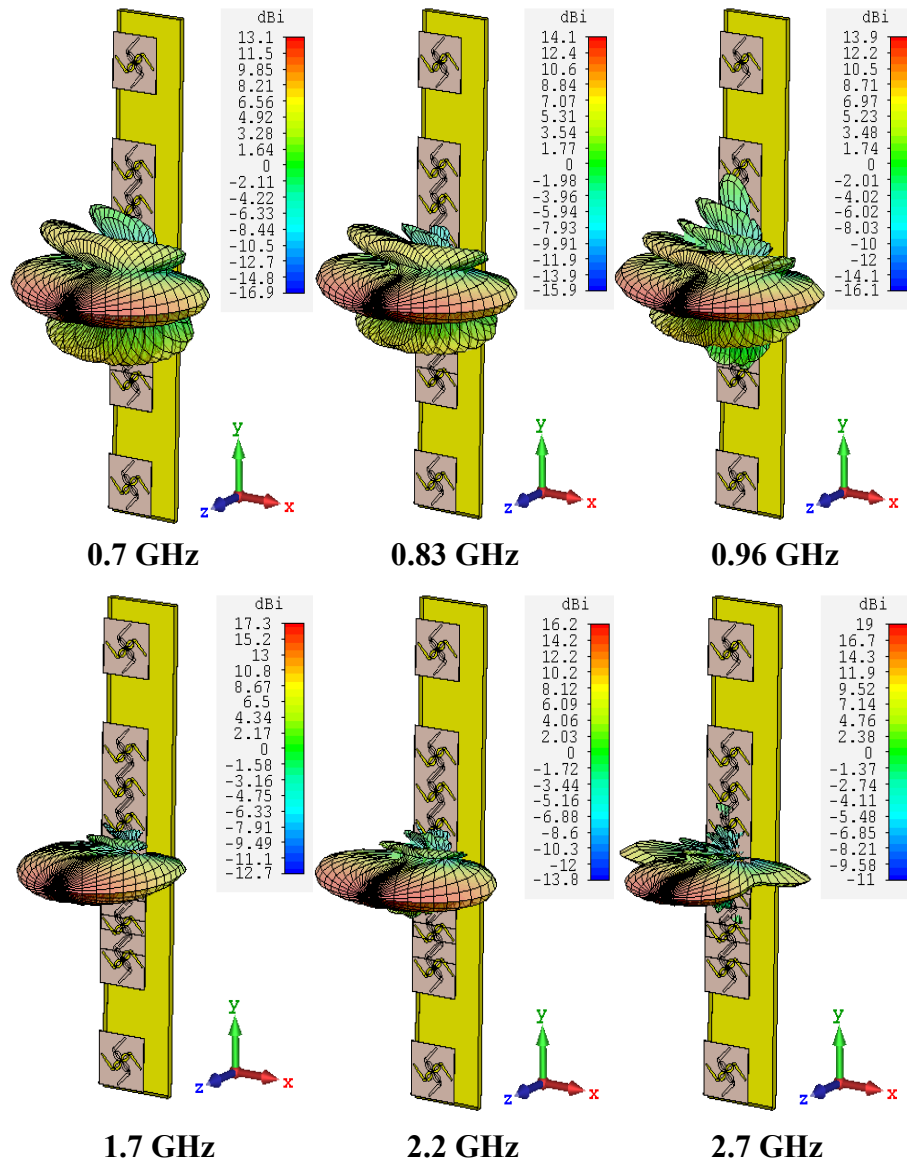
Fig. 6.16.   **Simulated 3D radiation patterns of the OLAS base station**

The proposed MIMO OLAS is compared to the standard base station antenna and the state-of-the-art array presented in [114] and the comparison is tabulated in Table 6.4. From the comparison, we notice that although the electrical specifications (front-to-back lobe ratios (FBR) and realized gains) for both arrays are comparable to each other and meet the specifications of the standard base station antenna, the proposed antenna array has remarkable better mechanical specifications (a fewer number of elements, a smaller size and, a simpler manufacturing technique). Also, the array in [114] uses three different types of elements to cover B1 and B2 (one for B1 and two for B2) while the proposed array uses the same antenna element for both bands.

Table 6.4.   Comparison of Standard and Several Dual-Band Base Station Antenna Arrays

Ref		Standard base station antenna [121]	[114]	Proposed Antenna
Total Number of Elements		The fewer, the better	15	**9**
Number of Element Types		The fewer, the better	3	**1**
Overall Size (mm³)		The smaller, the better	$1420 \times 260 \times 130$	**$1360 \times 220 \times 100$**
Realized Gain (dBi)	**B1**	12-14	15	**13.5**
	B2	15-17	17.3	**17.6**
FBR (dB)	**B1**	≥ 25	25	**27**
	B2	≥ 25	25	**29**

To validate the MIMO OLAS design, a small-scale prototype was fabricated. The prototype array consists of six elements and has two subarrays (a subarray for each band). By applying the optimum partitioning scheme from equation (5.11) where $K = 2$ and $M = 6$, the number of elements in each subarray $M_K = 4$. Therefore, virtually the total number of elements is eight elements while actually, the array consists of six elements as shown in Fig. 6.17. Again, the actual number of elements is less than the virtual number by 25%. B2-subarray consists of the middle elements numbering from 2 to 5 while B1-subarray consists of the elements number 1, 2, 5 and 6. Thus, the elements number 2 and 5 are shared elements.
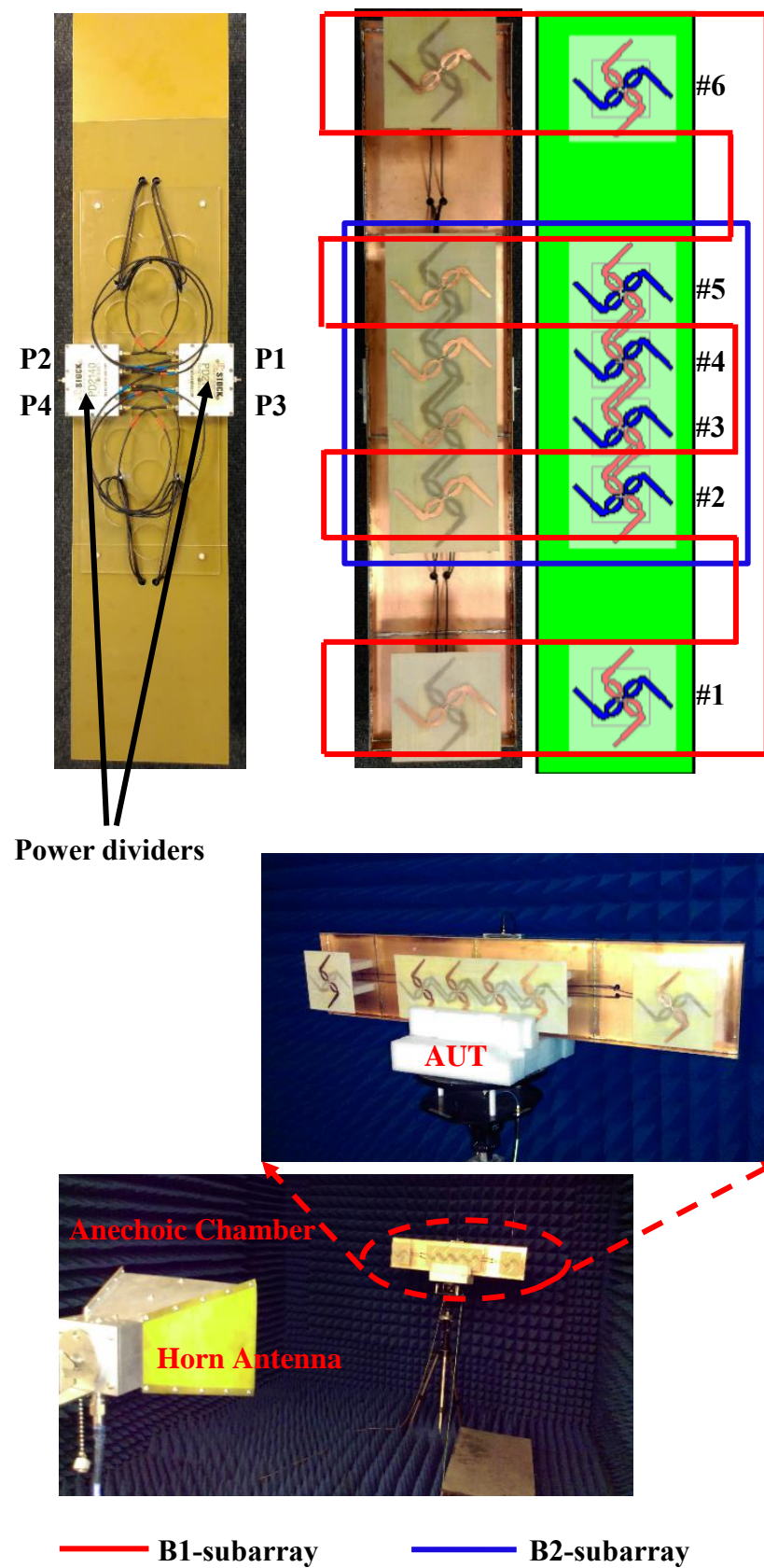
Fig. 6.17.   A Prototype of the proposed MIMO OLAS base station

To evaluate the diversity performance of the proposed MIMO system, the ECC should be obtained, which is calculated as in equation (3.4) for the four feeding ports *P1*, *P2*, *P3* and *P4* across the dual-band. In this case, each of i and j represents one of the feeding ports *P1*, *P2*, *P3* or *P4* and $i \neq j$. the polarization diversity is represented as the ECC of *P1-P2* and *P3-P4* while the frequency diversity is represented as the ECC of *P1-P3* and *P2-P4*. It worth noting that each pair of these ECC is reciprocal because of the array symmetrical feeding structure.

The calculated ECC based on the measurements is plotted in Fig. 6.18. For simplicity, only the ECC of *P1-P2*, *P1-P3* and *P1-P4* are plotted. Results show that the proposed MIMO OLAS offer very low ECC due to the polarization and frequency diversities. The maximum ECC is less than 0.008 across B1 and less than 0.001 across B2, far less than the general criteria of ECC < 0.3 [123].
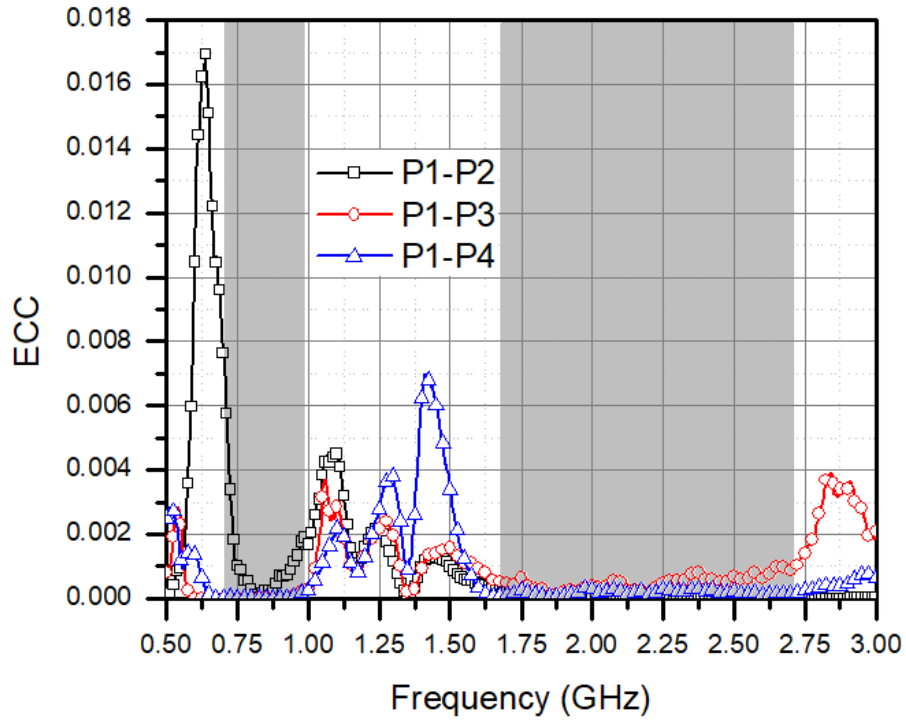
Fig. 6.18.   Measured ECC of the ports of the proposed MIMO OLAS

The isolation between the dipoles of two adjacent elements (we take elements numbers 2 and 3 in Fig. 6.17 as an example) is measured and presented in Fig. 6.19. The isolation between the two crossed dipoles (dipoles 1 and 2) is similar to the isolation measured and presented in Fig. 6.7 for a single antenna element. For dipoles 1 and 3, the isolation across B1 is less than the isolation across B2 because the bowtie

dipoles (which contribute to forming the radiation at B1) are parallel and close to each other. That causes an electric field coupling between these two dipoles. However, the worst case of isolation at B1 is close to 20 dB but it is better than 30 dB throughout B2. For dipoles 1 and 4, isolation is better than 30 dB for both bands
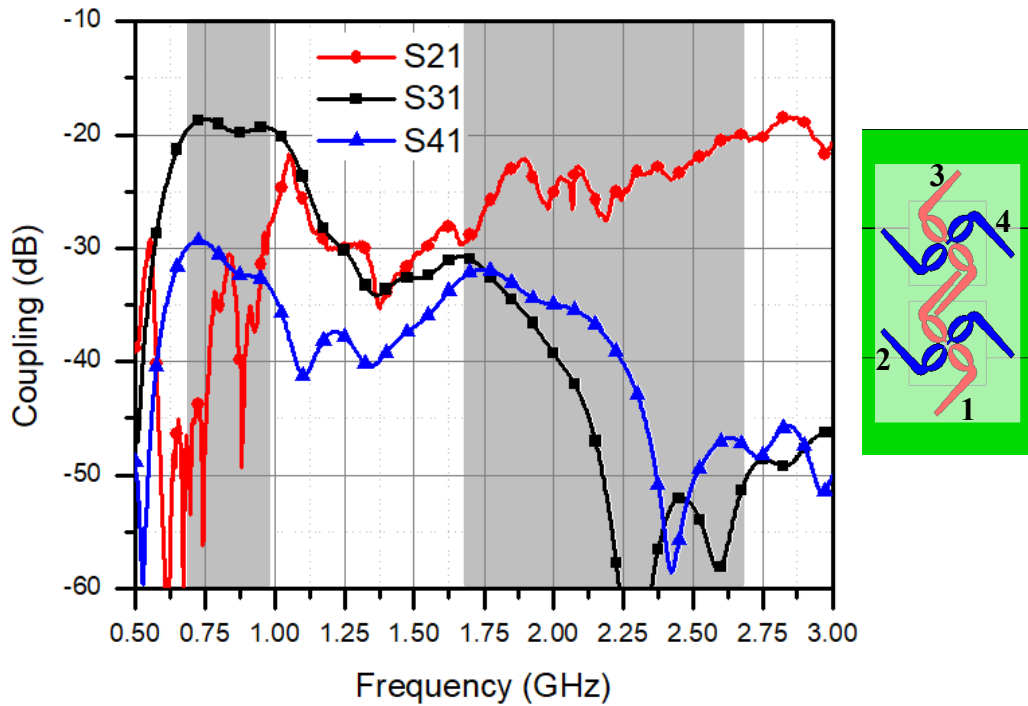
Fig. 6.19.   Measured isolation between two adjacent elements in the MIMO OLAS

The prototype array radiation patterns and gains are measured using a Vector Network Analyzer (VNA) and an anechoic chamber. A good agreement between the simulated and the measured radiation patterns can be noticed in Fig. 6.20.

The simulated and measured realized gains across both bands are presented in Fig. 6.21. The array measured parameters can be concluded in Table 6.5. The normalized 3D measured radiation patterns for the prototype MIMO OLAS base station at the two bands are shown in Fig. 6.22, which demonstrate that both subarrays have stable radiation patterns across the bands of interest.
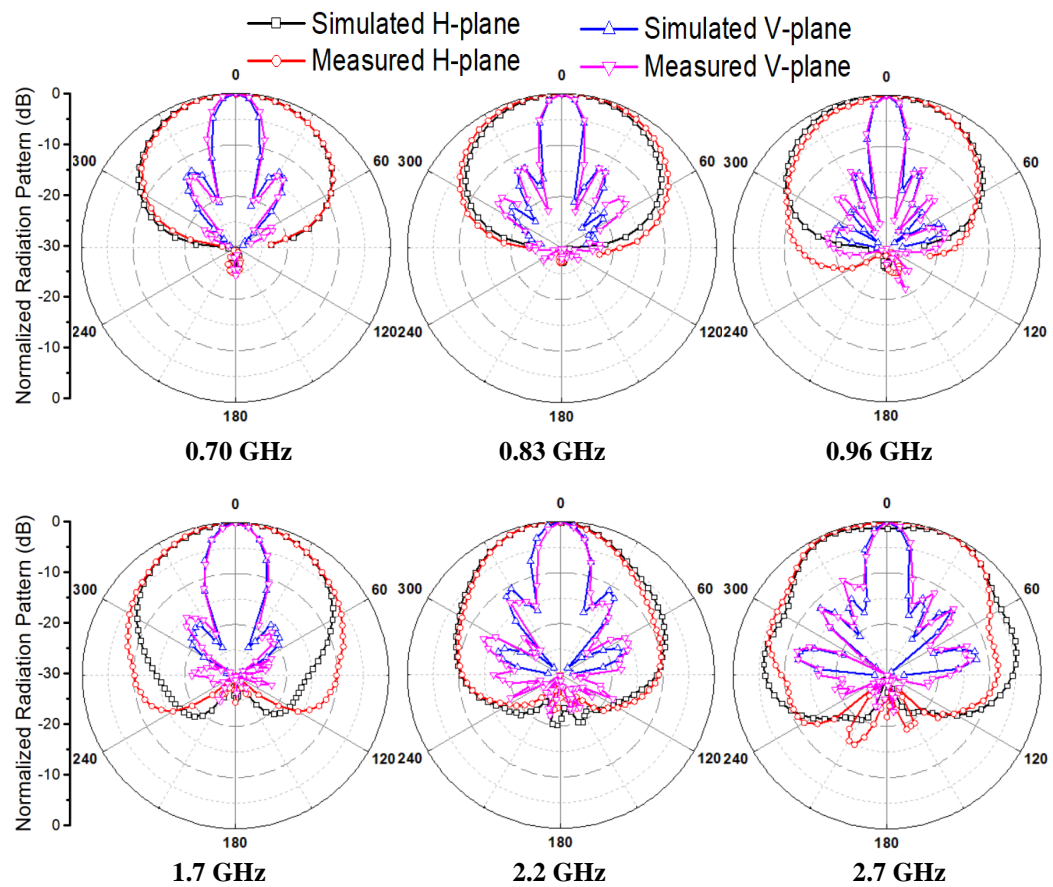
Fig. 6.20.   Simulated and measured radiation patterns of the MIMO OLAS base station
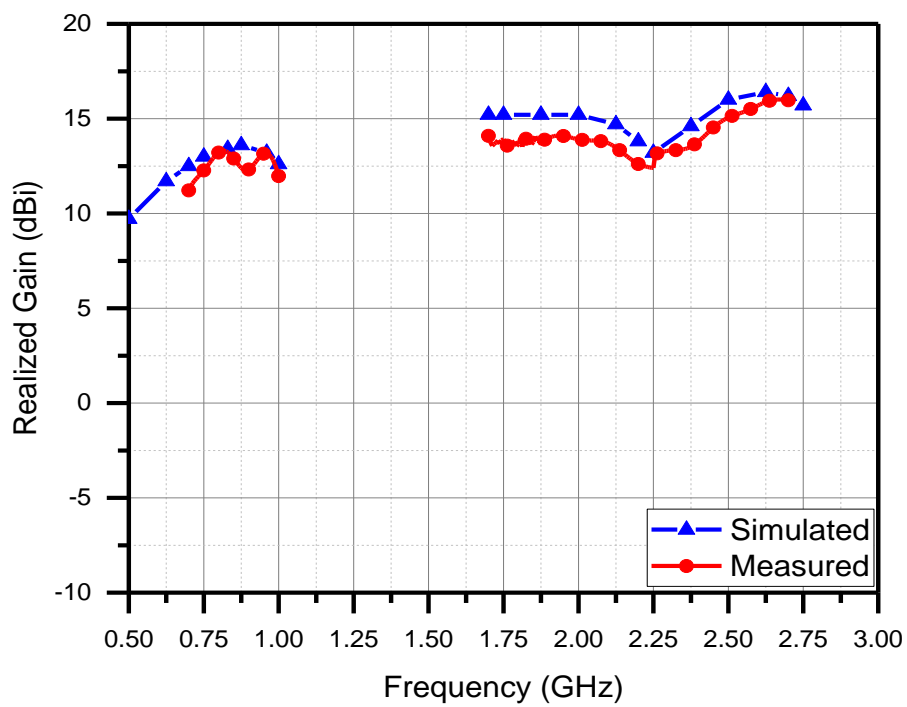
Fig. 6.21.   Simulated and measured realized gains of the MIMO OLAS base station

Table 6.5.   Measured Parameters of the Prototype MIMO OLAS Base Station

Frequency Band	B1	B2
V-plane HPBW (°)	18 ± 1	17 ± 3
Realized Gain (dBi)	12.6 ± 1.4	14 ± 1.6
FBR (dB)	27	29
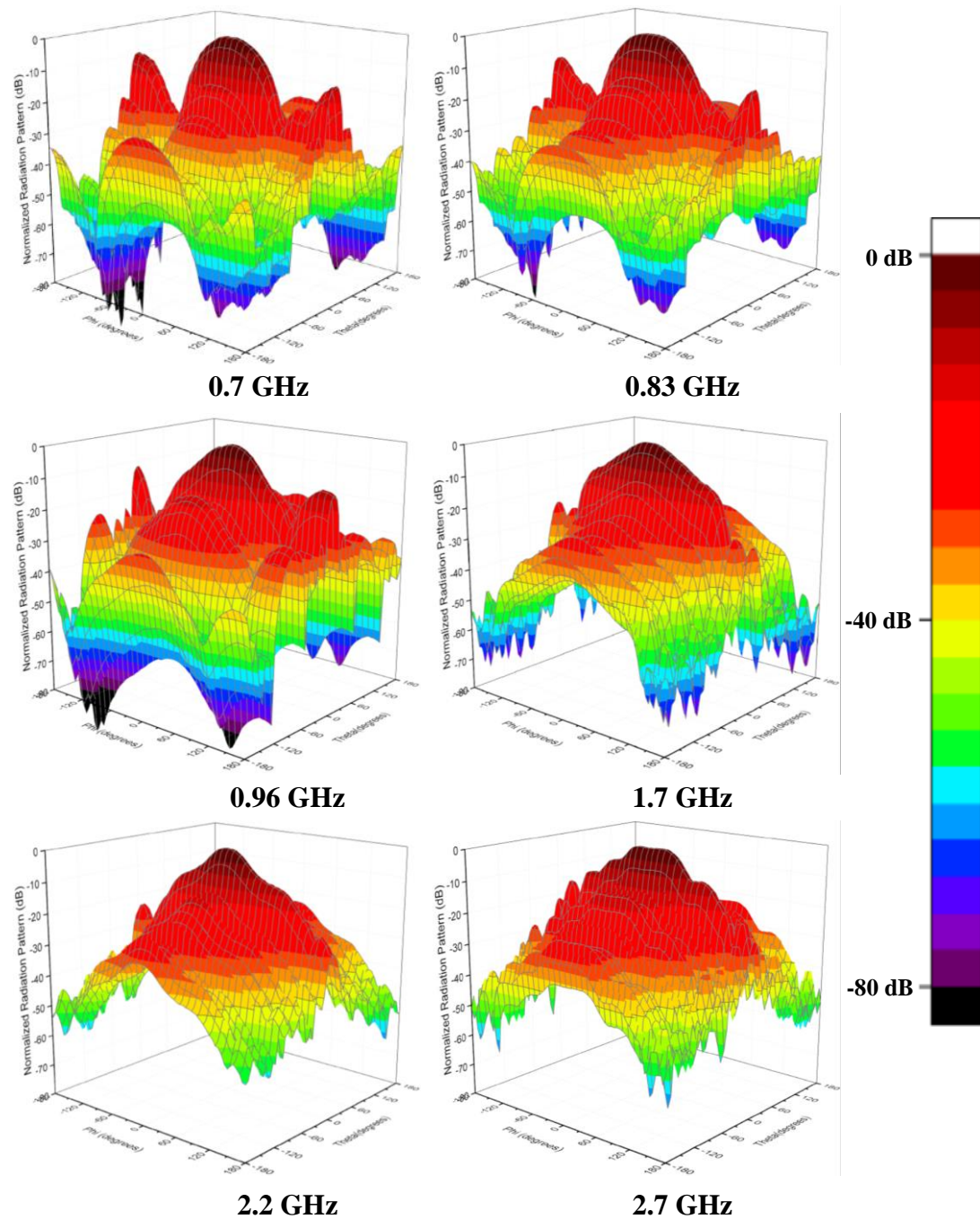
Fig. 6.22.   Normalized measured 3D radiation patterns of the MIMO OLAS base station

6.4. Summary

A novel dual-broadband dual-polarized Fylfot-shaped antenna has been designed, optimized, fabricated and tested to cover two different bands 0.7 - 0.96 GHz (B1) and 1.7 - 2.7 GHz (B2) simultaneously for mobile communication systems. The proposed antenna has a high XPD with a good impedance matching performance for both bands. In comparison with reference designs, the proposed design is much simpler as it uses a single element to cover both bands instead of two elements for two bands. In addition, the proposed antenna uses PCB manufacturing technology, which is easier than 3D printing used in reference designs.

A novel MIMO OLAS technique has been applied to form a dual-band linear array base station antenna with similar electrical performance as a conventional base station antenna but with 25% fewer number of elements and remarkable smaller size, which makes the proposed design a good candidate for a low-cost and efficient directive base station antenna.

The limitation of the antenna element can be noticed at the dipole feeding points where a Balun should be designed for balance feeding. This has been overcome during the measurements by using a ferromagnetic RF choke around the feeding coaxial cables.

Chapter 7. A Triple-Band Indoor Base Station Antenna

In the previous chapter, a dual-band base station antenna was proposed to serve the 2G, 3G and 4G mobile communication systems. For the future mobile communication systems, 5G is going to be deployed side-by-side to the 2G, 3G, and 4G services. This leads to the need of extending the operating frequency bands of base station antennas to cover the new sub-6 GHz 5G band (from 3.3 to 3.8 GHz) in addition to the exciting frequency bands of 2G, 3G and 4G applications. Therefore, this chapter proposes a new design of a triple-band dual-polarized indoor base station antenna for mobile communication systems serving the 2G, 3G, 4G and the new sub-6 GHz 5G applications simultaneously. The design consists of two orthogonal dipole antennas to provide dual polarization. Each dipole consists of three different radiator types: elliptical dipole, bowtie dipole and, cat-ear shaped arms for different bands. The proposed antenna offers three broad bands with the fractional BWs of 31.3% (0.7-0.96 GHz), 55.3% (1.7-3 GHz) and, 14% (3.3-3.8 GHz) which can be controlled independently. The design also offers a stable radiation pattern within the desired frequency bands, high XPD and, a simple feeding structure with a compact size and low profile which make this new design an ideal candidate for indoor mobile base stations serving the 2G, 3G, 4G and the new sub-6 GHz 5G applications.

7.1. Introduction

As telecommunication vendors look to introduce 5G mobile communication systems from 2019, base station and mobile antennas need to evolve to fulfil the new sub-6 GHz 5G frequency bands in addition to the existing 2G, 3G and 4G bands (0.7-0.96 GHz and 1.7-2.7 GHz). For indoor base stations, where the available spaces to install antennas are limited, it is favourable to have a single antenna element covering the frequency bands of interest rather than multiple antennas for multiple bands. Furthermore, due to the increase of the uncorrelated multi-path reflections in the

indoor communications, MIMO antenna systems are vital and efficient. In such cases, co-located antennas with polarization diversity are a better option than widely separated antennas with spatial diversity to save the spaces occupied by the antenna platforms.

Many attempts have been done to satisfy the 2G, 3G and 4G applications by a single antenna covering the frequency bands from 0.7 to 0.96 GHz (B1) and from 1.7 to 2.7 GHz (B2). In [124], the dual-polarized performance was achieved for both bands (B1 and B2) but the impedance BWs were insufficient (0.86 – 096 GHz for B1 and 1.7-1.9 for B2). In [125], the BWs were improved but only a single polarization was provided which makes the design not suitable for base station applications. There are many other designs. For example, in [126]-[128], BWs were much improved either by using irregular shorted patches as in [126] or dual-band dipoles as in [127] and [128]. Unfortunately, these reported designs again are single polarization. In [129], a dual-band dual-polarized antenna was presented but the BWs are not wide enough for 2G, 3G and, 4G communication systems. Due to the introduction of 5G, single-polarized dual-band indoor base station antennas were reported to cover B2 and the new sub-6 GHz 5G frequency band from 3.3 to 3.8 GHz (B3). In [130], a single-polarized dual-band folded dipole antenna was designed to operate across 2.3-2.5 GHz and 3.1-4.2 GHz. In [131] and [132], single antennas were produced to cover most of the frequencies in B2 and B3 simultaneously, from 1.8 to 3.77 GHz in [131] and from 2.4 to 3.6 GHz in [132]. Recently, an E-shaped triple-band patch antenna was presented in [133] to cover B1, B2 and B3 simultaneously. The main drawbacks of this design are that the BWs are not sufficient (0.92-0.96 GHz, 1.9-2.2 GHz and, 3.4-3.8 GHz) and it is single polarization.

This chapter proposes a novel design of a dual-polarized triple-band antenna for 2G, 3G, 4G and, sub-6 GHz 5G indoor base stations covering B1, B2 and, B3 simultaneously. The design consists of two cross dipoles. Each dipole may be considered as a combination of three different types of radiators (typically one type for each band); elliptical dipole (type 1), bowtie dipole (type 2) and cat-ear shaped arms (type 3). As each radiator parameter can be controlled individually, the three bands (B1, B2 and, B3) can be tuned independently to achieve triple broad performance.

This chapter is organized as follows: Section 7.2 describes the proposed antenna configuration and its principle of operations, Section 7.3 discusses its performance and a sensitive study of its parameters and finally, a summary is presented in Section 7.4.

7.2. The Proposed Antenna Design

7.2.1. Antenna Configuration

Fig. 7.1 illustrates the geometry of the proposed antenna. Generally, we can describe the geometry as a pair of two orthogonal crossed dipoles: dipole *A* and dipole *B*. Dipole *A* consists of an elliptical-shaped dipole (type 1) placed on 45º with respect to Y-axis. The two elliptical arms of dipole *A* are printed on opposite sides of an FR-4 substrate with a relative permittivity $\varepsilon_r = 4.3$, a loss tangent of 0.025, a thickness of 1.6 mm and a side length *Ld*. The two arms are fed through a strip (printed on the substrate top layer) and a 50 Ω coaxial cable. For practical implementation, a hole in the bottom arm is drilled to insert the 50 Ω coaxial feed. The endpoints of the elliptical dipole are extended to form a bowtie dipole (type 2) which is placed orthogonally to the ellipse major axis. Furthermore, a pair of cat-ears (type 3) is added to each elliptical arm such that the major axes of the two cat-ears are intersecting at the ellipse centre and forming angles of ±45º with the ellipse major axis respectively. Therefore, in summary, we can describe dipole *A* as a combination of three different types of radiators; type 1: elliptical dipole, type 2: bowtie dipole and, type 3: cat-ear arms.

The second crossed dipole (dipole *B*) is a rotated replica of dipole *A* with a relative angle of 90º around Z-axis. There are two major differences between dipoles *A* and *B*. The first difference is that the feeding strip of dipole *B* is modified. One part of the strip is printed on the bottom layer of the substrate, and then is connected to the top parts through two vias to avoid intersecting with the feeding strip of dipole *A*. Each via is fabricated by first drilling a hole through the FR-4 substrate, then drawing a copper wire through the hole, and finally by soldering the copper wire to the stripline on both sides of the substrate. The second major difference is that one of the cat-ears in the bottom layer is shifted to the top layer to add a capacitive loading to the input impedance (*Zin*) of dipole *B* to compensate the inductive effect introduced by the vias as will be discussed in detail in the next section. Thus, the distribution of the cat-ears

at dipole *B* is asymmetric (three on the top layer and one on the bottom layer) unlike their symmetric distribution at dipole *A* (two on each side).
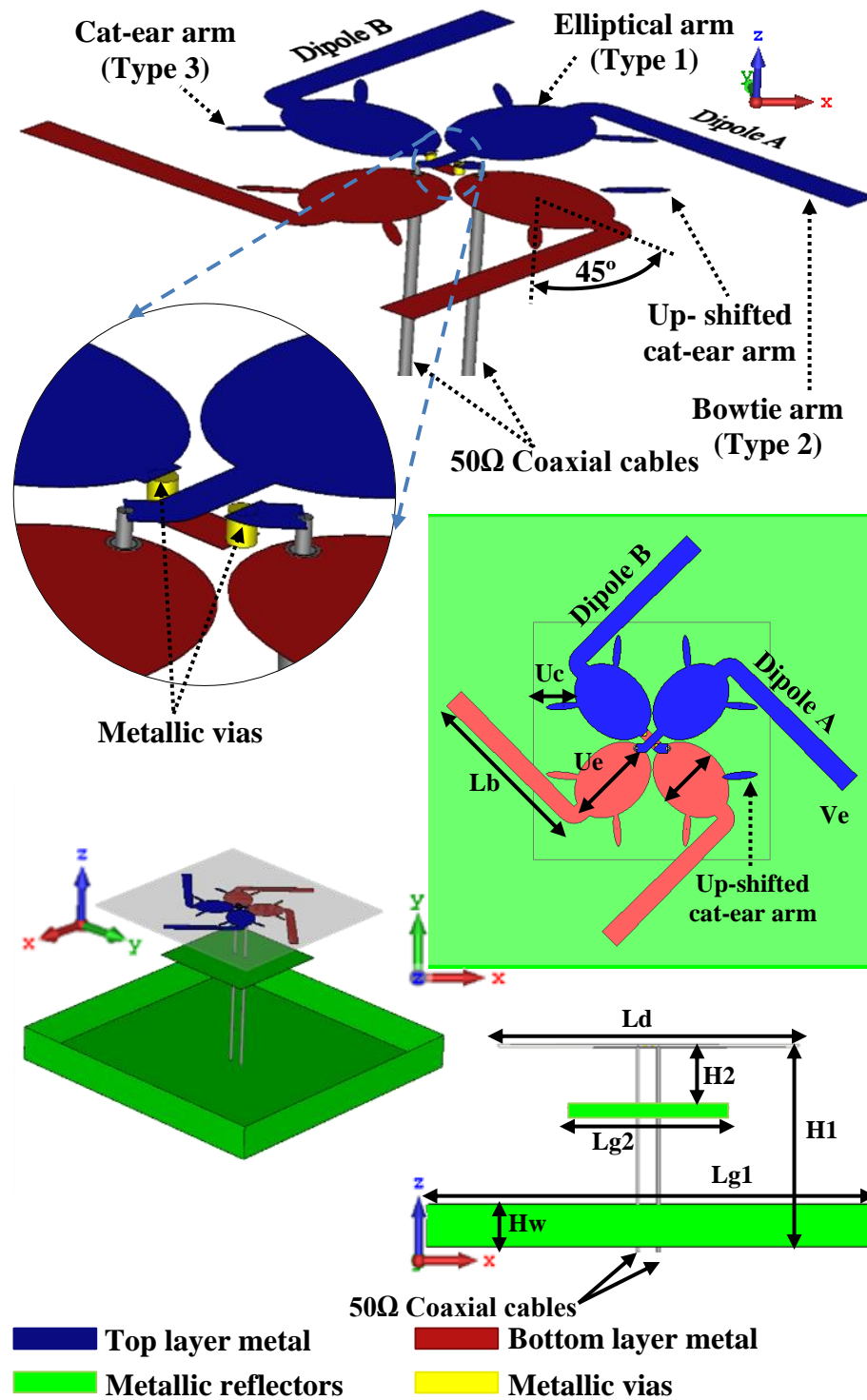
Fig. 7.1.   The geometry of the proposed antenna

The substrate and dipoles are oriented in the XY plane as shown in Fig. 7.1. The substrate is placed above two square metallic ground reflectors to enable directional radiation, a large reflector for the lower frequencies band B1 and a small reflector for the higher frequencies bands B2 and B3. The large reflector is placed at a height of *H1* from the substrate, with a side length *Lg1* and four sidewalls of a height of *Hw* while the small reflector is placed at a height of *H2* from the substrate and has a side length *Lg2*. The substrate and the two metallic reflectors are concentric and their edges are parallel to X and Y-axes. The optimized dimensions are determined as follows (in mm): *Ue* = 29, *Ve* = 21.4, *Lb* = 54, *Uc* = 11.6, *Ld* =150, *H1* = 100, *H2* = 30; *Hw* = 23, *Lg1* = 220 and, *Lg2* = 80.

7.2.2. Methodology and Principles of Operation

The antenna design is based on creating triple-band coverage based on constructing three combined radiators with independent designing parameters.

Two reference designs (antenna Ref 1 and antenna Ref 2) can be employed to understand the working principle of the proposed design as shown in Fig. 7.2. Initially, antenna Ref 1 was designed based on the elliptical dipole (type 1) discussed in Chapter 4 to cover B2 as it has the widest BW among the three desired bands. The ellipse major and minor axes (*Ue* and *Ve*) are selected such that the shortest current path length from the feeding point to the endpoint of the ellipse (*Ue*) equals to $0.25\lambda_{B2H}$ while the longest current path length from the feeding point to the endpoint of the ellipse (*P*) equals to $0.25\lambda_{B2L}$ (where λ_{B2H} and λ_{B2L} are the free-space wavelengths at the highest and lowest frequencies of B2 respectively and *P* is half of the ellipse circumference). *P* is related to the axes lengths as:

$$P = \pi \sqrt{\frac{\left(\frac{Ue}{2}\right)^2 + \left(\frac{Ve}{2}\right)^2}{2}} = \frac{\lambda_{B2L}}{4} \tag{7.1}$$

It is worth noting that all current path lengths from the feeding point to the ellipse endpoint ranging from the shortest path *Ue* to the longest path *P* are equal to a quarter of the wavelengths ranging from λ_{B2H} to λ_{B2L} respectively. Thus, the dipole length may be considered as a half wavelength for all the frequencies within B2.

In antenna Ref 2, a bowtie dipole with a total length of *2Lb* (type 2) is combined with the elliptical dipole. Each arm of the bowtie dipole is connected to one of the

endpoints of the elliptical dipole and forming 90° with respect to the ellipse major axis. The dimension *Lb* was initially selected such that the dipoles total length (2*Ue*+2*Lb*) equals to 0.5λ_{0B1} (where λ_{0B1} is the free space wavelength of the central frequency of B1, 0.83 GHz). Thus, B1 and B2 are fully covered by a combinational design of type 1 and type 2.
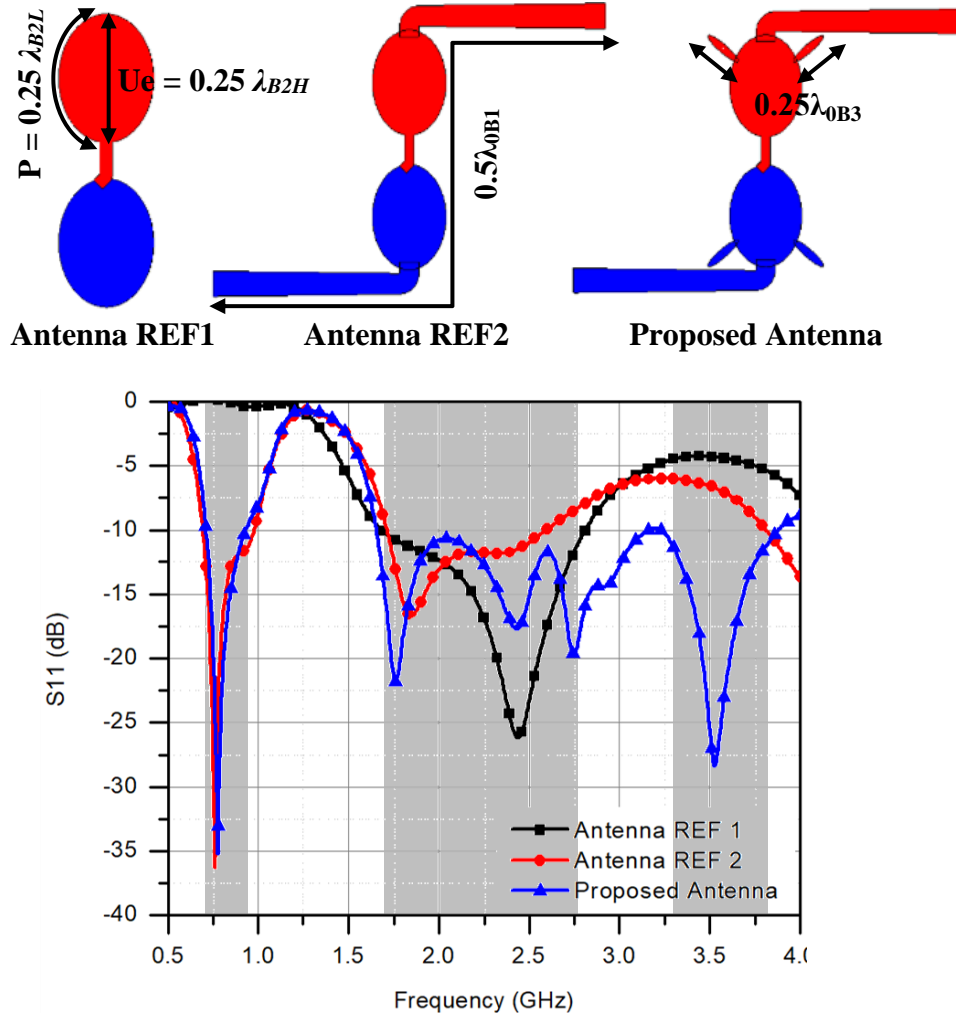
Fig. 7.2.   References and the proposed antenna designs

Furthermore, in the proposed design, the cat-ear arms (type 3) are combined to the antenna Ref 2. The major axes of the cat-ear arms form angles of ±45° with the ellipse major axis respectively. Thus, each pair lies on one of two perpendicular axes (X-axis and Y-axis). The dimension *Uc* was initially selected such that the total length of each pair of cat-ear arms (2*Uc*) is 0.25λ_{0B3} (where λ_{0B3} is the free space wavelength of the central frequency of B3, 3.55 GHz). So, triple-band performance is achieved.

As mentioned in the previous section, in dipole *B* (which has two vias through the feeding strip), one of the cat-ear arms should be shifted from the bottom layer to the top layer to create a capacitive loading and compensate the inductive effect of the vias. For a better understanding of this matter, Fig. 7.3 shows three cases of different positions of the cat-ear arms at dipole *B*. Case (1) is the initial case where both cat-ear arms are in the bottom layer of the substrate. Therefore, B3 is not fully covered with VSWR ≤ 2 (the fully complete purple circle in the middle of the Smith chart) due to the inductive effect of the vias especially at the stop frequency of B3 (note that the higher the frequency, the more sensitive Z_{in} to any inductance change). In case (2), both cat-ear arms are shifted to the top layer of the substrate to add two parallel capacitive loadings between them and the elliptical arm. Thus, Z_{in} across B3 becomes too capacitive especially at the start frequency of B3 (note that the lower the frequency, the more sensitive Z_{in} to any capacitive change). Case (3) is the proposed design where one of the cat-ear arms is printed on the bottom layer while the other is shifted to the top layer. In this case, B3 is fully covered with VSWR ≤ 2. It is worth noting that the vias do not have any significant effect on the impedance matching across B1 and B2 as their reactance is too small at these bands.
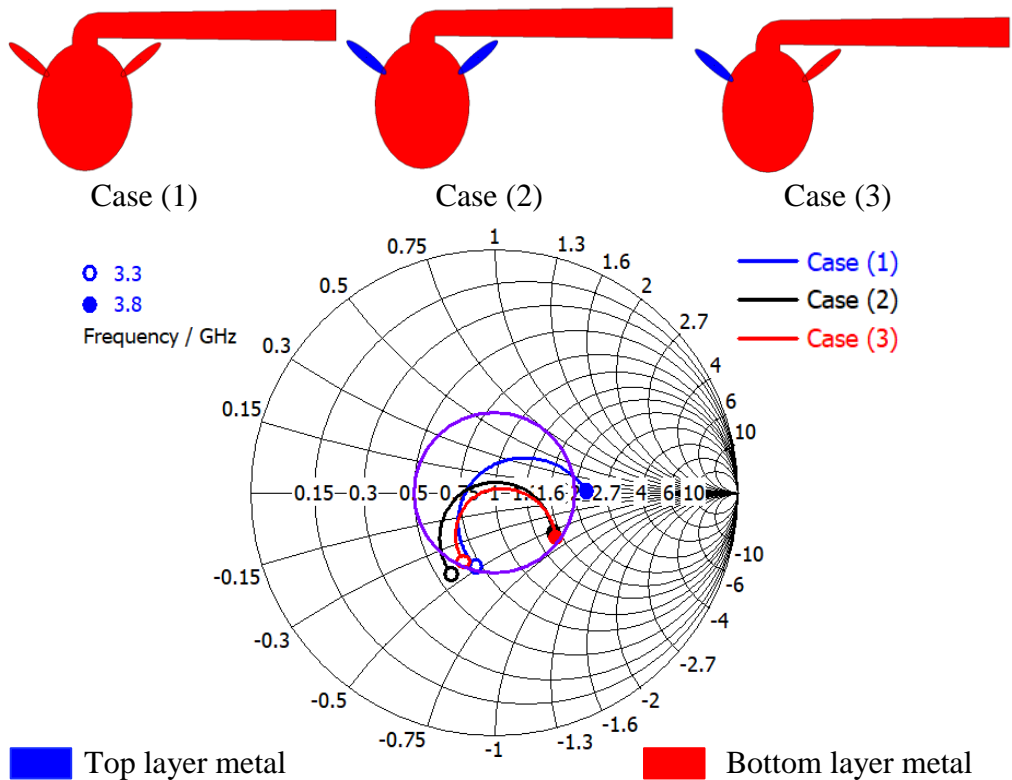
Fig. 7.3.   Effect of the cat-ear arm position on *Zin* of dipole B across B3

Fig. 7.4 shows the current distribution across the dipole at the central frequency of each band. It can be seen that at B1, the current flows from the feeding point to the terminal points through bowtie and elliptical dipoles, which indicates that these two radiator types (1 and 2) are the radiators across B1. On the other hand, the current distribution at B2 is highly dense around the elliptical dipole while there is a small current density across the bowtie and cat-ears. Furthermore, at B3, the current density is high at the cat-ears with small current density across the elliptical and bowtie dipoles.
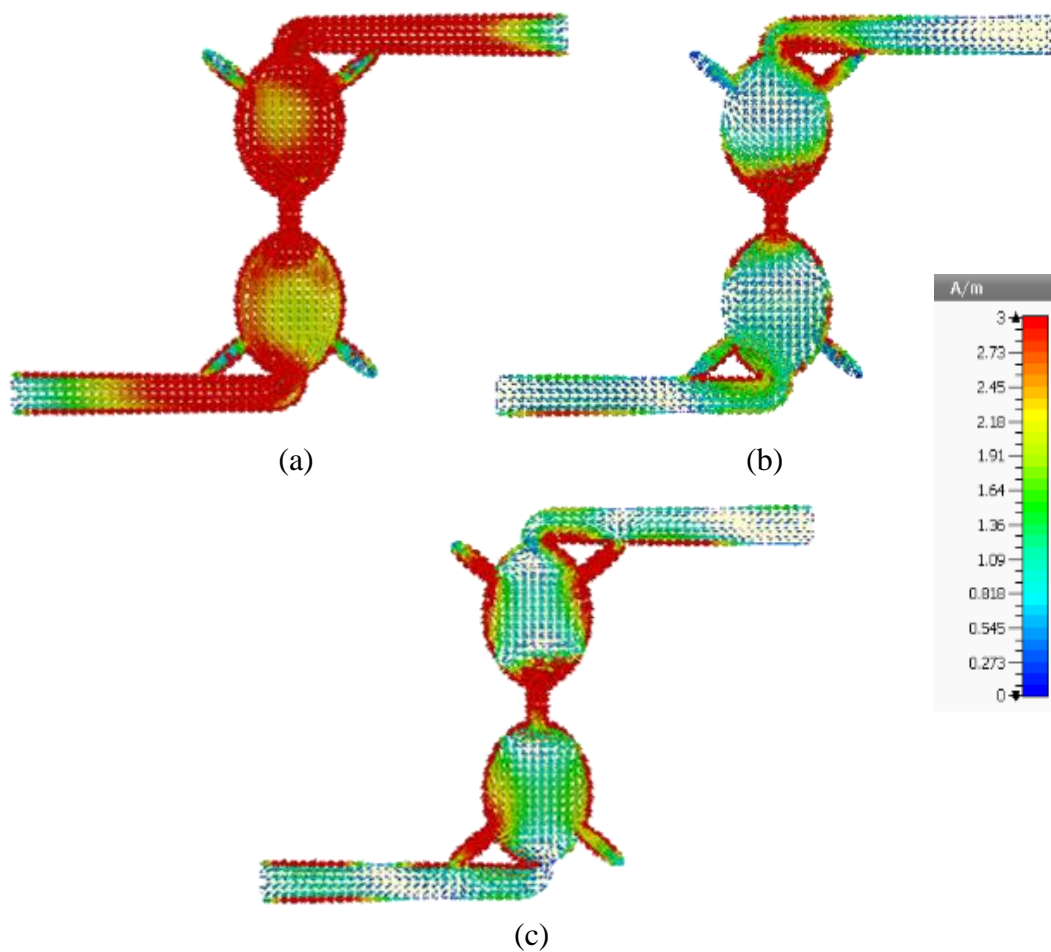
Fig. 7.4.   **The current distributions at the central frequency of (a) B1 (b) B2 (c) B3**

Table 7.1 summarises the contributions of each type of the three radiator types to the radiation across each band. It is evident from Table 7.1 that B1 and B3 can be tuned independently by controlling the dimensions of the bowtie and cat-ears respectively. More illustrations will be presented in the next section.

Table 7.1.   Contributions of the Three Radiator Types to the Radiation

Frequency Band	Radiator Type		
	Type 1 (Elliptical)	Type 2 (Bowtie)	Type 3 (Cat-ears)
B1	✓	✓	
B2	✓		
B3			✓

7.3. The Proposed Antenna Results

To validate the proposed design, a prototype was fabricated and tested as shown in Fig. 7.5. The simulation was accomplished by using CST Microwave studio. Measured results of S-parameters, gain, and radiation patterns were obtained by using a VNA and an anechoic chamber.

(a)   (b)

(c)
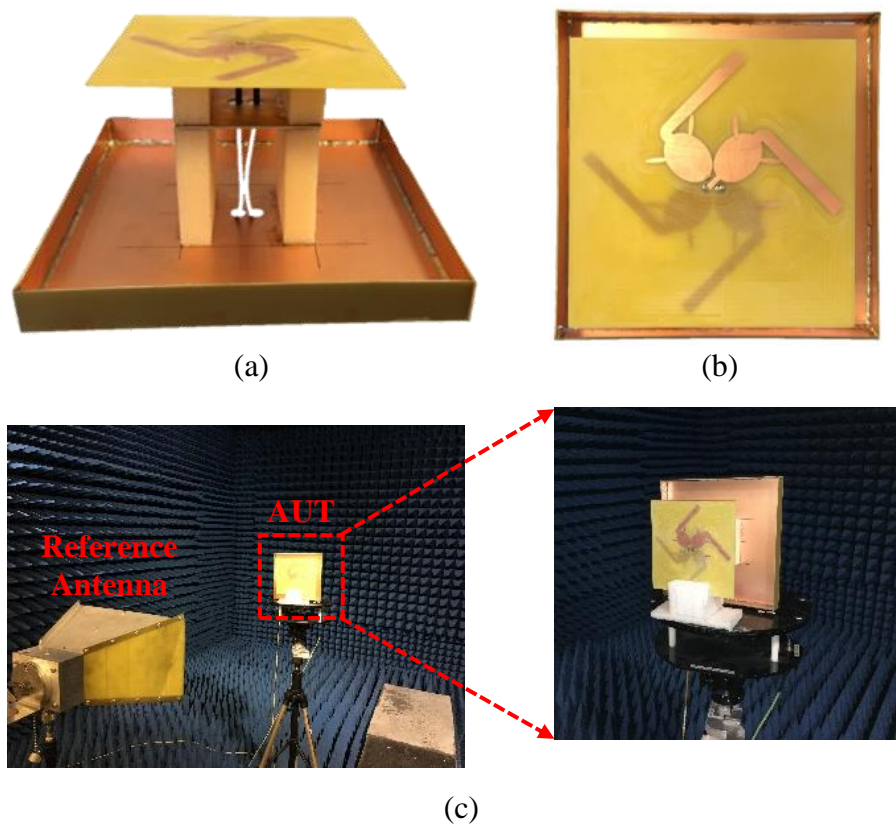
Fig. 7.5.   A prototype of the proposed antenna (a) side view (b) top view (c) during measurements

Fig. 7.6 shows a good agreement between the simulated and measured reflection coefficients for both ports. For VSWR $\leq$ 2, the fractional BWs are 31.3% (0.7-0.96 GHz), 55.3% (1.7 -3 GHz) and, 14% (3.3-3.8 GHz) for B1, B2 and, B3 respectively. Fig. 7.7 shows that the measured port-to-port isolation is better than 27 dB for B1 and better than 20 dB for B2 and B3.
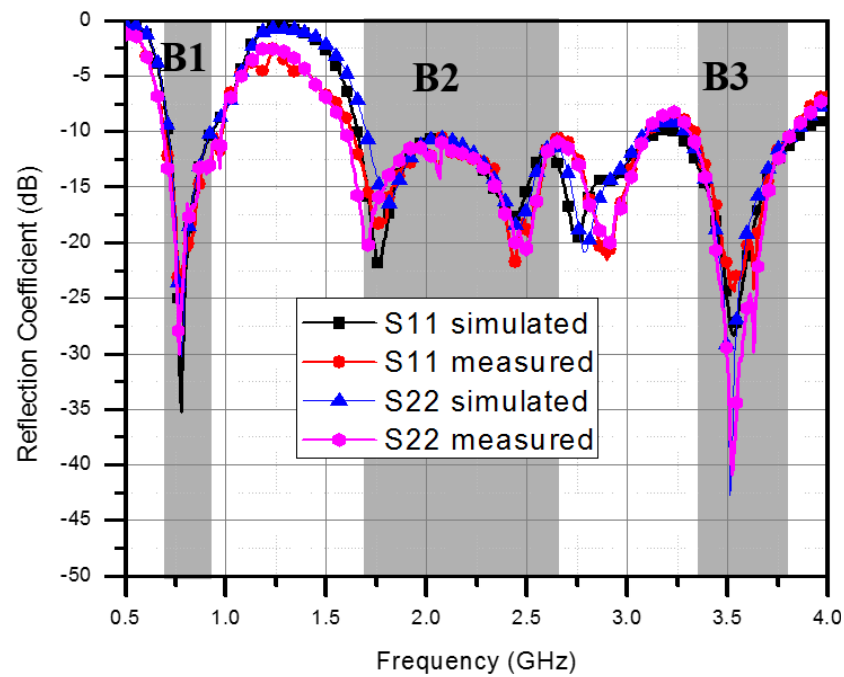
Fig. 7.6.   Simulated and measured reflection coefficients
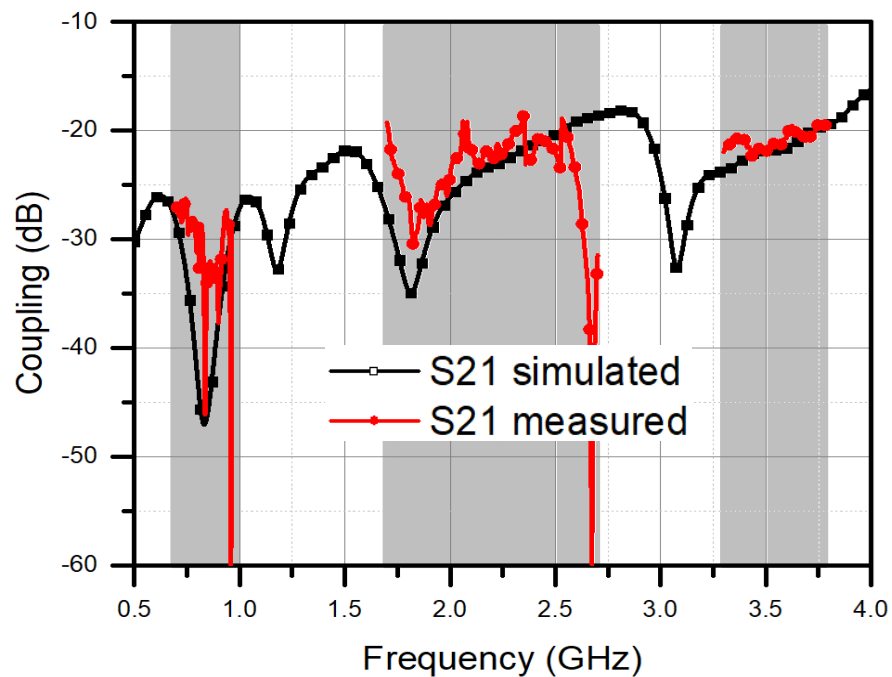
Fig. 7.7.   Simulated and measured port-to-port isolations
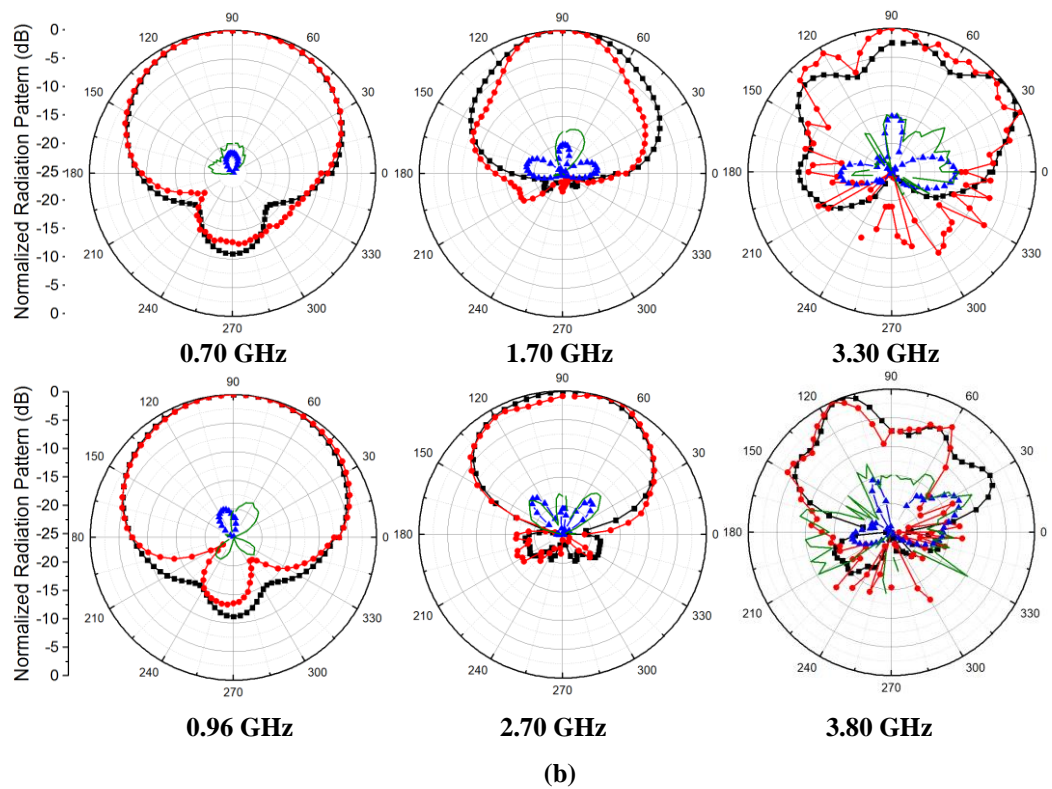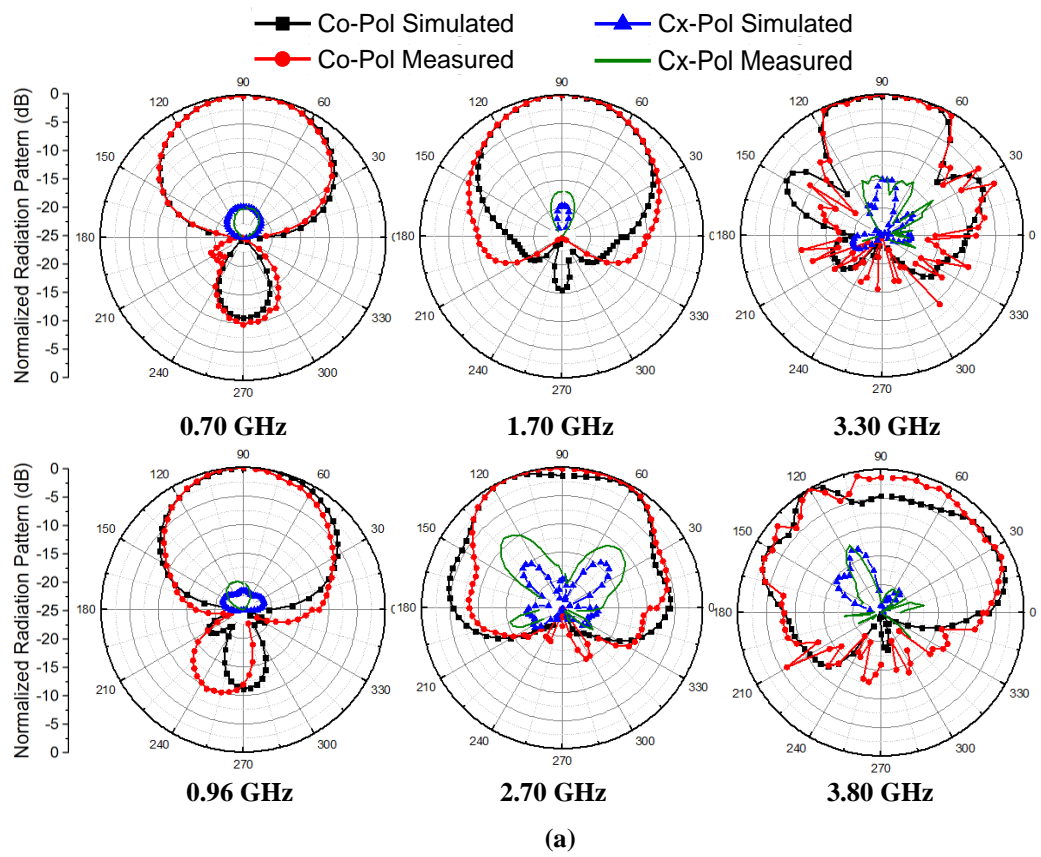
Fig. 7.8. **Simulated and measured co- and cross-polarized radiation patterns in (a) H-plane (b) V-plane (B1, B2 and B3 from left to right)**

The simulated and measured co- and cross-polarized radiation patterns at the start and stop frequencies of each band in H-plane (XZ plane) and V-plane (YZ plane) are shown in Fig. 7.8. It is apparent that the proposed antenna has a good agreement in radiation pattern between the simulations and the measurements. The radiation patterns may have some distortions at B3. These distortions are due to the large substrate aperture in terms of λ_{0B3} ($2\lambda_{0B3} \times 2\lambda_{0B3}$). Nevertheless, radiation patterns are still applicable to indoor base station antenna usage across the three bands. The HPBWs and the XPD are illustrated in Table 7.2. Fig. 7.9 presents the realized gains at B1, B2 and, B3 in simulation and measurements. The antenna has a stable gain across the entire bands. The average realized gains are tabulated in Table 7.2.

Table 7.2.   The HPBWs, XPD and Gains of the Proposed Antenna

Frequency Band	HPBW (º)		XPD (dB)	Average Gain (dBi)
	H-Plane	V-Plane		
B1	73±2	100±5	≥ 20	5.5
B2	65±5	72±8	≥ 18	8
B3	80±6	70±8	≥ 15	5.5
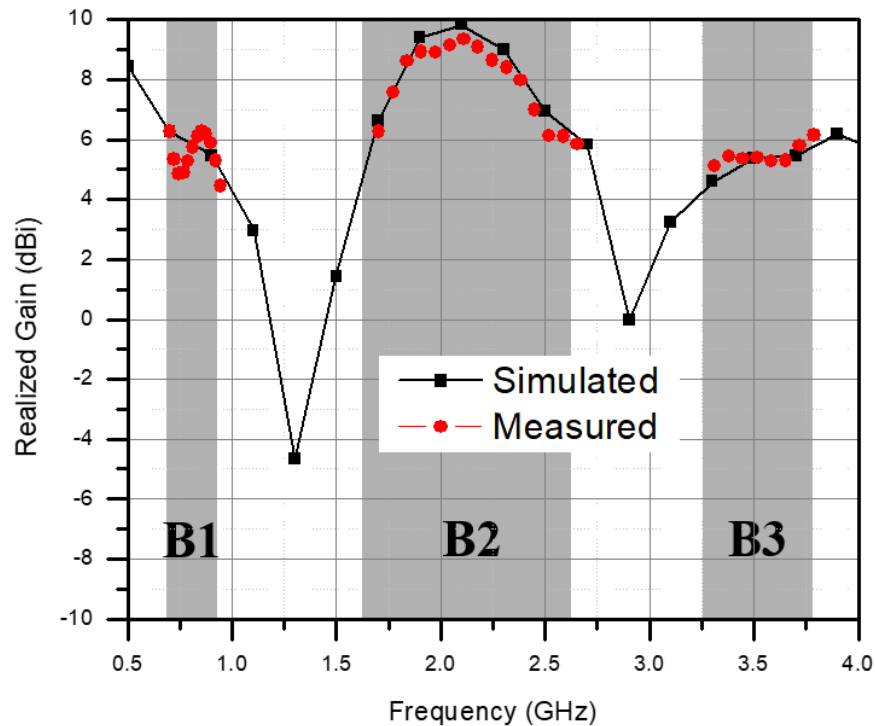
Fig. 7.9.   The proposed antenna simulated and measured realized gains

Table 7.3. Comparison of Several Multi-Band Antennas to the Proposed Antennas

Ref		[124]	[125]	[126]	[127]	[128]	[129]	[130]	[131]	[132]	[133]	Proposed
Fractional BW (%)	B1	11	26.7	34	17.5	28.6	14.1	-	-	-	4.3	31.3
	B2	11.1	44	35.4	21.2 - 33	11.1	24.7	8.3	36.1	11	14.6	55.3
	B3	-	-	-	-	-	-	29	36.1	11	11.1	14.1
HPBW (°)	B1	NA	60	103	360	80	63	-	-	-	40	73
	B2	NA	40	57	360	60	85	60	360	66	60	65
	B3	-	-	-	-	-	-	60	360	49	120	80
Average Gain (dBi)	B1	6.5	8.4	7	2	6	11.8	-	-	-	NA	5.5
	B2	7.3	8	8	2	9	7	9	2.9	9.2	NA	8
	B3	-	-	-	-	-	-	9	5.5	7	NA	5.5
XPD (dB)	B1	18	12	26	NA	NA	NA	-	-	-	NA	20
	B2	30	15	28	NA	NA	NA	40	NA	19	NA	18
	B3	-	-	-	-	-	-	29	NA	19	NA	15
FBR (dB)	B1	NA	18	18	NA	12	21.2	-	-	-	NA	10
	B2	NA	18	20	NA	18	4.1	22	NA	14	NA	15
	B3	-	-	-	-	-	-	22	NA	14	NA	18
Polarization		Dual	Single	Single	Single	Single	Dual	Single	Single	Single	Single	Dual
Antenna Size (λL)		0.3×0.3 ×0.04	0.33×0.33 ×0.2	0.48×0.28 ×0.12	0.3×0.04 ×0.005	0.6×0.6 ×0.15	0.68×0.51 ×0.06	0.6×0.4 ×0.25	0.6×0.3 ×0.005	0.5×0.25 ×0.1	0.3×0.2 ×0.03	0.35×0.35 ×0.23

Table 7.3 displays a comparison between multi-band indoor base station antennas performance and the proposed antenna. For a fair comparison, the size of each antenna is normalized to λ_L (where λ_L is the wavelength at the lowest operating frequency). It is apparent that the proposed antenna is the only candidate that can operate across the three bands simultaneously with broad BWs and dual-polarized performance. It also has a relatively small size. Note that the reported omnidirectional base station antennas in [127] and [131] have low profiles as they do not have reflectors.

As mentioned in the previous section, B1 and B3 can be tuned independently by controlling the parameters of the bowtie and cat-ear radiators (types 2 and 3) respectively. Therefore, to optimize the proposed antenna BW, it is necessary to understand how these parameters affect the antenna performance. Their effects are studied through simulations.

7.3.1. Effect of the Bowtie Dipole Length (Type 2)

The first parameter to be studied is the bowtie arm length (Lb). As has been stated in Table 7.1, the bowtie dipoles contribute to the radiation across B1 only with a very slight effect on B2 and B3. Thus, B1 can be controlled independently from B2 and B3 by changing the length Lb. As noticed in Fig. 7.10, when the length Lb increases, B1 is shifted to lower frequencies while B2 has almost no changes. There are slight changes in B3 due to the coupling between the bowtie arm and the closest cat-ear arm. However, there is almost no change in the BW across B3 due to this coupling. The optimum value of Lb is found to be 54 mm to cover the whole B1 with VSWR ≤ 2.
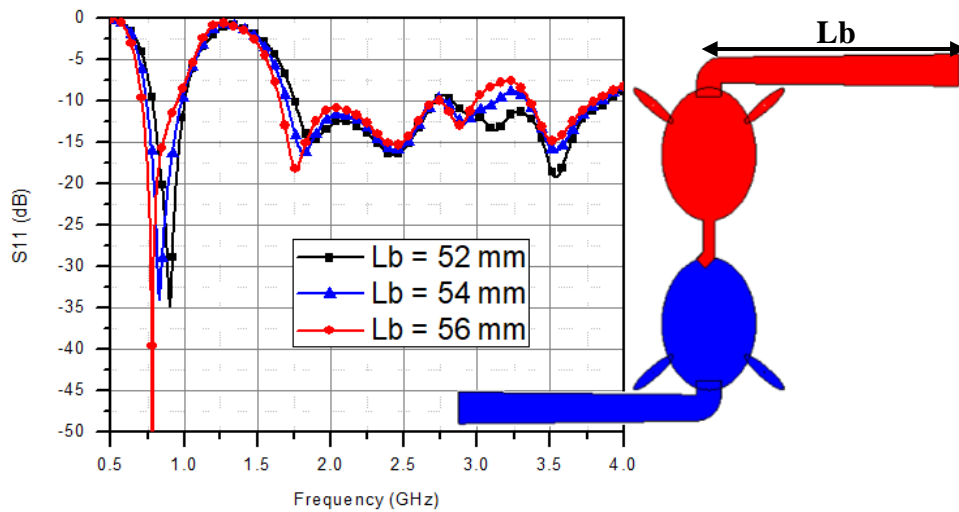
Fig. 7.10.   Effect of *Lb* on the reflection coefficient

7.3.2. Effect of the Cat-Ear Arm Length (Type 3)

The second parameter to be studied is the cat-ear arm length Uc. Changing Uc does not result in any changes in B1 and B2. Thus, B3 can be tuned by changing the dimension Uc as shown in Fig. 7.11. The optimum value of Uc is found to be 11.6 mm to fully cover B3.
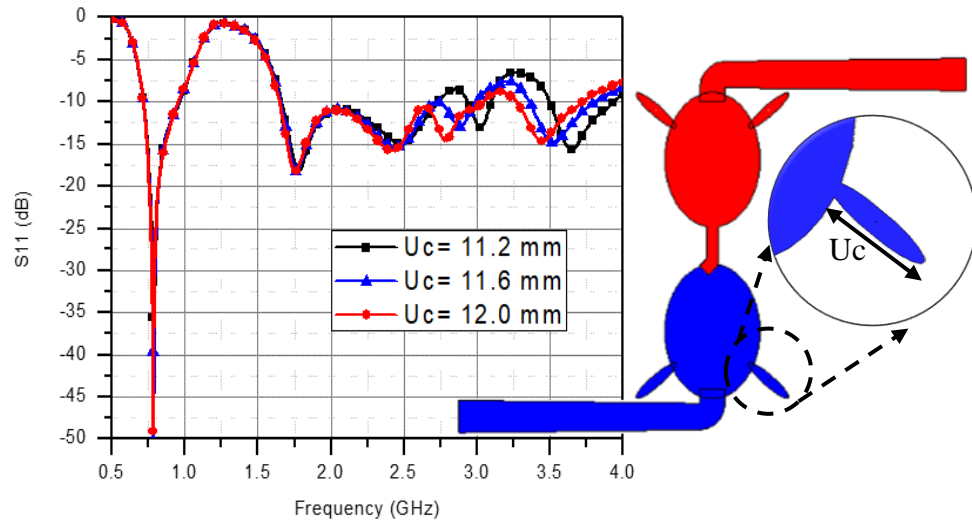
Fig. 7.11.   Effect of *Uc* on the reflection coefficient

7.4. Summary

A novel triple-band dual-polarized antenna for the indoor base station has been designed, optimized, fabricated and measured. It covers the frequency bands from 0.7 to 0.96 GHz, from 1.7 to 3 GHz and, from 3.3 to 3.8 GHz simultaneously with high XPD. The proposed antenna consists of a combination of three different types of radiators: one type for each band. The multi-band performance is achieved by optimizing each type which is dedicated to each band independently. Because of its multiband performance, its dual-polarization capabilities and small size, the proposed antenna is an excellent candidate for the indoor base station, which operates over the new sub-6 GHz 5G band as well as the exciting 2G, 3G and, 4G bands.

The limitation of the antenna element can be noticed at the dipole feeding points where a Balun should be designed for balance feeding. This has been overcome during the measurements by using an RF choke around the feeding coaxial cables.

Chapter 8. A 5G MIMO Antenna for Broadcast and Traffic Communications

In the previous chapter, 2G, 3G, 4G and sub-6 GHz 5G frequency bands were covered by a single antenna for indoor applications. When it comes to outdoor scenarios, 5G is expected to operate in two different roles. The first role is the broadcast topology where 5G offers similar services like 2G, 3G and 4G networks. Furthermore, the second role is to provide traffic topology where the base station antenna allocates multiple beams for multiple users.

Therefore, this chapter proposes a new design of a dual-polarized base station antenna for sub-6 GHz 5G communications covering the band from 3.3 GHz to 3.8 GHz. The proposed antenna element offers a good impedance matching across the desired frequency band with VSWR ≤ 1.5, a stable radiation pattern with a HPBW of 65 ± 5 ° and high isolation between the ports with a small size and a low profile. The antenna element is extended to form a planar MIMO antenna array with low ECC between its elements to either perform in a broadcast or traffic communication topology whenever required. In the broadcast communication topology, the proposed MIMO antenna array covers a sector of 65º in the horizontal plane with three different down-tilted beam directions at 0º, 10º and 20º in the vertical plane as conventional base station antennas used for 2G, 3G and 4G. In traffic topology, the proposed MIMO antenna array can direct multiple beams to concurrent multiple users in a Point-to-Multipoint (P2MP) communication based on a novel Pseudo Inverse Synthesis (PIS). The novel PIS is proved to be better than the other approaches which use frequency or pattern diversity as it possesses the advantage of the pattern diversity (by using a single frequency for multi-user coverage) and the advantages of the frequency diversity (by offering good steering capability and high directivity for each user). It is capable of radiating dynamic multiple beams simultaneously with excellent flexibility and steering capability in real-time processing and outperforming other multi-beam antenna array methods. Thus, this new design is an ideal candidate for the new 5G mobile base stations.

8.1. Introduction

Future wireless access will extend beyond people, supporting connectivity for any device that may benefit from being connected. One of the key motivators for 5G is to provide ubiquitous, high-speed, high-quality wireless broadband coverage to meet societal and industrial needs beyond 2020. Outdoors 5G base station antennas should maintain the same feature as 2G, 3G and 4G base station antennas (in terms of good impedance matching, dual-polarization, stable radiation pattern and high XPD) in addition to their ability to allocate multiple beams for multiple simultaneous users.

Many successful designs have been introduced for the 2G, 3G and 4G base stations using planar cross dipoles [133] or 3D printed cross dipoles [135]. Furthermore, quite a few designs have been recently introduced for the sub-6 GHz 5G applications. In [136], stacked patch antenna was used to operate at a single frequency of 3.7 GHz. In [137], an antenna based on vector synthetic mechanism was introduced with a small size and an industrial impedance matching (VSWR $\leq$ 1.5) but its BW is insufficient (3.3-3.6 GHz). In [138], the BW was improved at the expense of the antenna size to meet the non-industrial impedance matching requirement (VSWR $\leq$ 2). In [139], a 2×2 antenna subarray was used to provide a high gain covering the frequency band from 3.45 GHz to 3.55 GHz. Later on, a metamaterial was used to design multiband antennas as in [140] and [141] but their single-polarization limits their applications in mobile communications.

MIMO is considered as a key technology for deploying the 5G network at both Sub-6 GHz and mm-wave bands. For the next few years, the Sub-6 GHz for the 5G network will be in service side-by-side with the 3G and 4G networks to provide broadcast wireless mobile communications. Furthermore, 5G is expected to provide traffic communications on a P2MP basis [142]. Many approaches have been adopted to achieve traffic communication topology. The most commonly used approach is applying frequency or pattern diversity to a MIMO antenna array. In pattern diversity, the MIMO array is divided into small subarrays each of which is fed and controlled independently to direct its beam to a user [143]. For frequency diversity, different frequencies within the 5G frequency band (with a separation of 40 MHz at least between two successive frequencies) are employed to generate different radiation patterns directed to concurrent users on a one-to-one basis [144]. The main drawbacks

of the pattern diversity approach are the low directivity (user-selectivity) and the limited steering capability of the radiation pattern due to the limited subarrays apertures. On the other hand, although the frequency diversity approach affords high directive beams with good steering capabilities, the narrow BW limits the number of users to 10-12 at any moment per base station [145].

Another approach to achieve traffic communication topology is using multi-beam antenna arrays to generate a number of simultaneous or switchable but independent directive beams with a high gain [142]-[143]. A multi-beam antenna array may use a Butler matrix [146]-[148] or multi-feeding ports [149], to generate concurrent but static multiple beams or digital [150] and hybrid beamforming [151] to generate dynamic but switched multiple beams. To get the advantages of having concurrent and dynamic multi-beam radiation pattern simultaneously by a single antenna array, array syntheses are applied using different optimization algorithms [152]-[157]. These algorithms need a long processing time which limits their usages in the real-time 5G applications.

Based on the above discussion, a novel dual-polarized antenna element for sub-6 GHz 5G applications is proposed in this chapter. The proposed antenna element covers the frequency band from 3.3 GHz to 3.8 GHz with VSWR ≤ 1.5 and good isolation between its ports (better than 25 dB). It offers a high XPD and a stable radiation pattern within its frequency band with a HPBW of 65 ± 5º in addition to its small size and low profile in comparison to the reported antennas in the literature.

Another major contribution in this chapter is that a 5G MMO antenna array based on the new antenna element is proposed. The proposed MIMO array offers a good diversity performance with very low ECC between its antenna elements. It offers the freedom to operate in broadcast or traffic topology. In broadcast topology, the MIMO array covers a spatial sector of 65º and 30º in horizontal and vertical planes respectively. In traffic topology, a novel PIS is applied which has been found to enjoy the advantages of the frequency diversity approach (high directivity and good steering capability of the radiation pattern) without scarifying the advantage of the pattern diversity approach (using a single frequency for multi-user coverage). Furthermore, PIS outperforms the reported approaches in multi-beam antenna arrays as it offers simultaneous dynamic multiple beams with excellent flexibility and steering capability in real-time processing.

The chapter is organized as follows: Section 8.2 describes the proposed antenna element, its working principles, its results and some parametrical studies; Section 8.3 discusses the proposed MIMO antenna array in the two sub-6 GHz 5G communication topologies (broadcast and traffic) with a detailed discussion on the proposed PIS and a comparison to other reported approaches. Finally, a summary is drawn in Section 8.4.

8.2. Dual-Polarized Antenna Element

8.2.1. Antenna Element Design

In this section, a novel dual-polarized antenna element covering the band from 3.3 GHz to 3.8 GHz is illustrated. Fig. 8.1 shows the exploded geometry of the proposed design: the antenna consists of three stacked layers. Layer I (the feeding layer) is a Rogers RT5880 laminate with thickness $Hd = 1.6$ mm, relative permittivity $\varepsilon_{r1} = 2.2$ and a loss tangent of 0.0009. A square feeding patch is printed on the top of Layer I with two orthogonal 50 Ω feed lines for dual-polarization, which are excited by two feeding ports. A ground plane is printed on the bottom side of Layer I to provide unidirectional radiation. Layer II is a foam layer with thickness $H = 9$ mm and relative permittivity $\varepsilon_{r2} \approx 1$. Layer III (the radiating layer) is a Rogers RT5880 laminate, which has the same characteristics as Layer I. A radiating square patch, with the same dimensions as the feeding patch, is printed on the bottom side of Layer III while a parasitic copper patch is printed on the top side. Two orthogonal symmetrical rectangular slots are cut in the radiating patch. The three layers are oriented in the XY plane. The three layers, the three patches (feeding, radiating and parasitic patches) and the slots are concentric. For base station antennas, $\pm 45°$ dual-polarization is required. Therefore, the side lengths of the layers, patches, feed lines and slots form angles of $\pm45°$ with the X and Y-axes respectively.

The optimized dimensions (in mm) are determined as follows: $WP1 = WP2 = 27$, $WP3 = 20$, $WS1 = 71$, $WS2 = 30$, $L\_Slot = 9$, $W\_Slot = 3$, and $H = 9$.
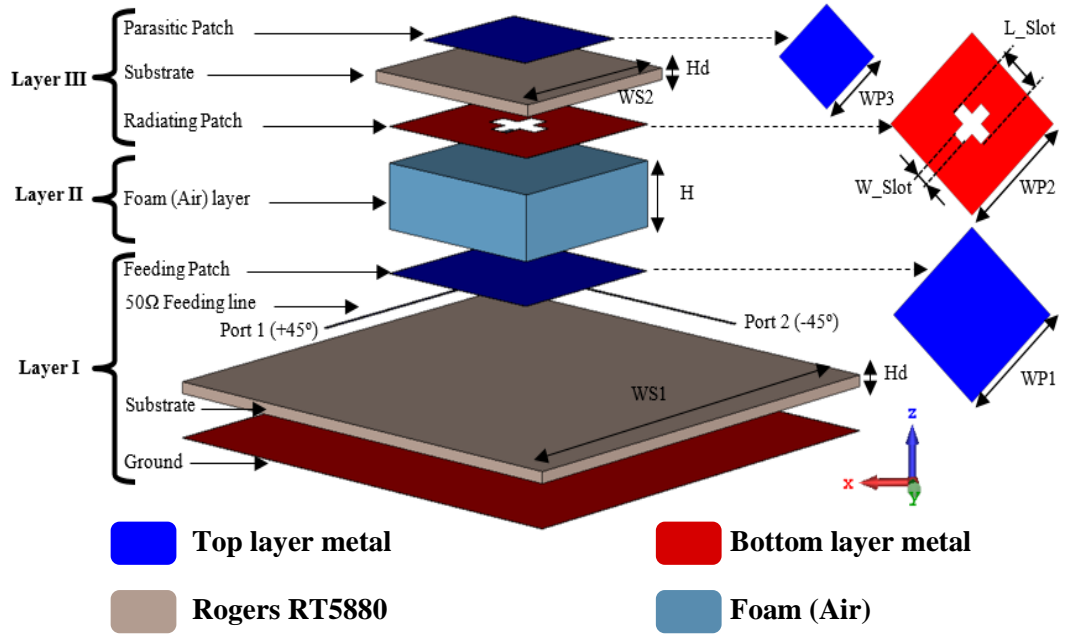
Fig. 8.1.   Exploded geometry of the radiating antenna element

8.2.2. Methodology and Principle of Operation

The design is based on creating a broadband antenna using capacitive coupling between multiple layers.

Two reference designs (antenna REF1 and antenna REF2) are employed to understand the working principle of the proposed antenna element as shown in Fig. 8.2. Initially, a single substrate (Layer I) with a square patch of $0.5\lambda_g$ in length was designed with dual orthogonal feed lines (where λ_g is the guided wavelength at the central frequency 3.55 GHz) (antenna REF1). In this case, the BW observed is narrow. The design is amended by adding Layer II and Layer III (without the parasitic patch) above Layer I with radiating patch printed on the bottom side of Layer III. The radiating patch, in this case, is fed by the electric field coupling from Layer I. Furthermore, two rectangular slots are cut in the radiating patch to improve the impedance matching across the desired frequency band (antenna REF2). So, the BW is observed to be wider but still not satisfactory. The BW can be further improved by printing a parasitic patch on the top side of Layer III (proposed design). The parasitic patch can improve the BW by adding a capacitive loading to the antenna input impedance and hence cover the frequency band from 3.3 GHz to 3.8 GHz with a reflection coefficient ≤ -15 dB (VSWR ≤ 1.5) as shown in Fig. 8.2.

Fig. 8.3 shows the current distributions across the radiating patch at the central frequency (3.55 GHz) feeding on port 1 (+ 45º) and port 2 (- 45º). It is evident that the two current distributions are symmetrically inverted which indicates good isolation between the ports and high XPD between co- and cross-polarized radiation patterns.
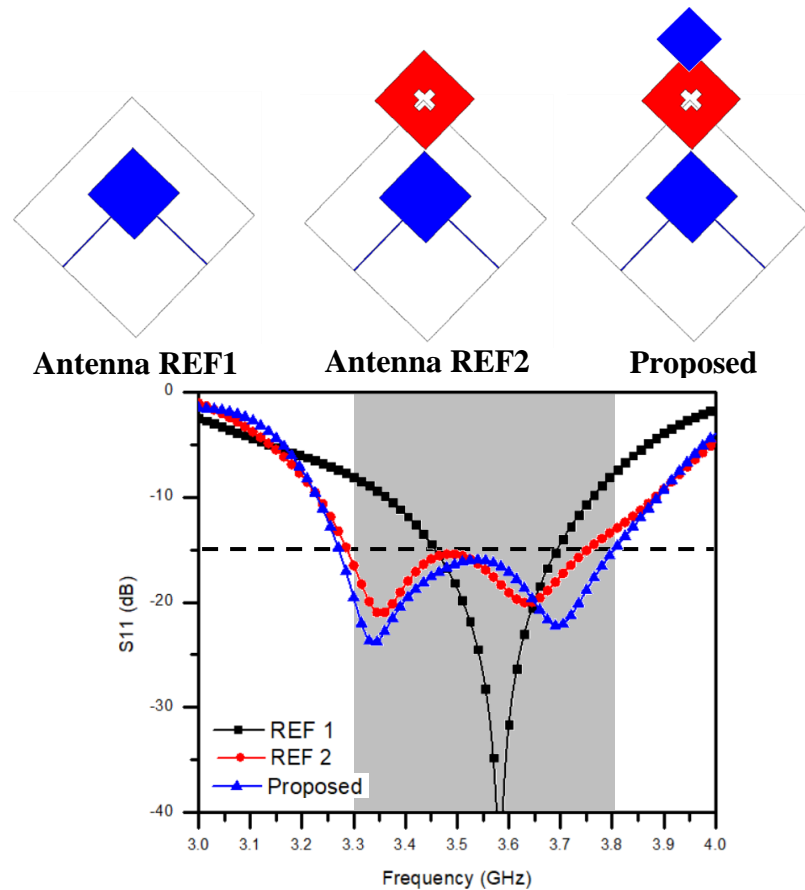
Fig. 8.2.   References and the proposed antenna element designs
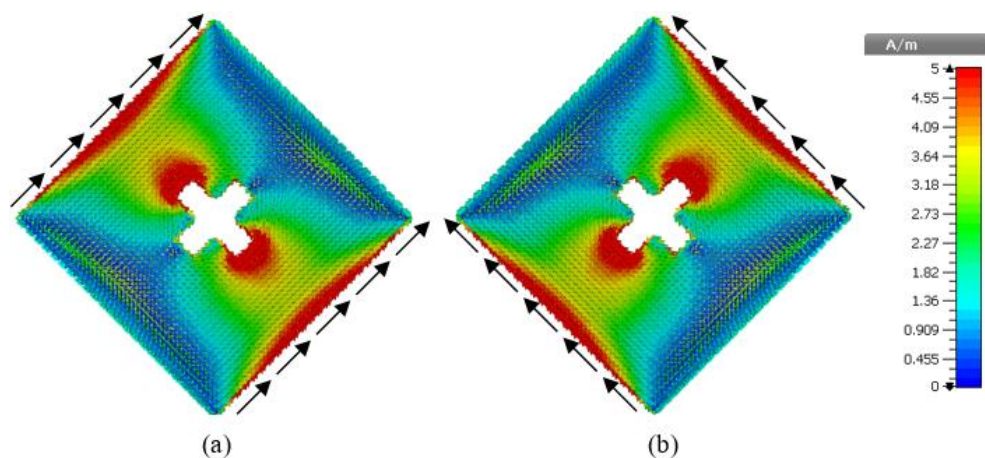
Fig. 8.3.   The current distributions across the radiating patch at the central frequency feeding from (a) port 1 (b) port 2

8.2.3. Antenna Element Results

To validate the proposed design, a prototype was fabricated as shown in Fig. 8.4 and then measured. The simulation was accomplished using CST Microwave studio. Measured results for S-parameters, gain, and radiation patterns were obtained by using a VNA and an anechoic chamber.
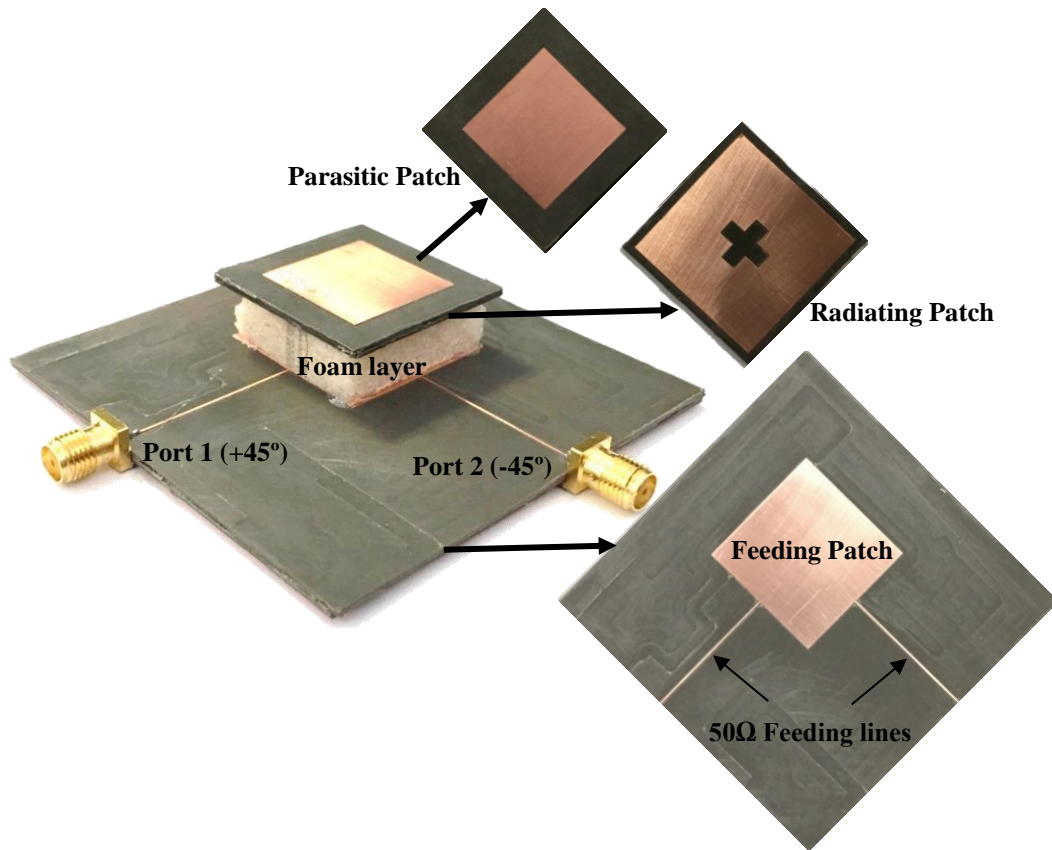
Fig. 8.4.   A prototype of the proposed antenna element

Fig. 8.5 shows a good agreement between the simulated and measured reflection coefficients, isolations between the ports and realized gains. A fractional BW of 14% is achieved (3.3-3.8 GHz) with VSWR $\leq$ 1.5 to meet the standard industrial requirement. For simplicity, reflection coefficients in Fig. 8.5 can represent either port 1 or port 2 because of the symmetrical feeding structure of the antenna element. The measured port-to-port isolation is better than 25 dB across the operating frequency band. It is apparent also that the proposed antenna has a stable realized gain of 8.5 $\pm$ 0.5 dBi across the frequency band of interest.
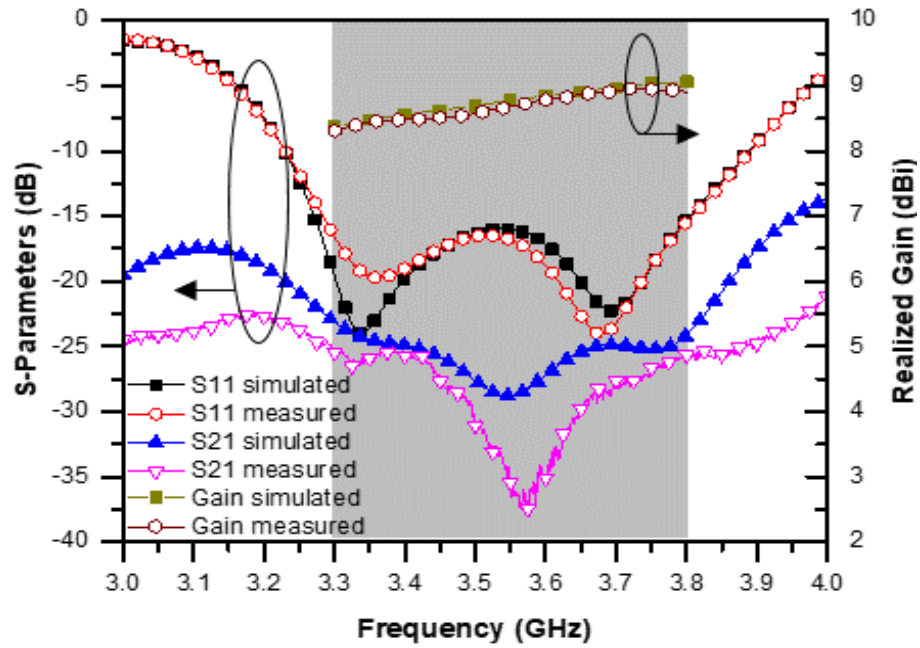
Fig. 8.5.   Simulated and measured reflection coefficients, isolations between the ports and realized gains

The measured co-and cross-polarized radiation patterns at the start, central and stop frequencies in H-plane (XZ plane) and V-plane (YZ plane) are shown in Fig. 8.6. Because the antenna structure is almost symmetrical around the X and Y-axes, the HPBWs in H-plane and V-plane are about $65 \pm 5°$ across the frequency band. The XPD is better than 22 dB at boresight and better than 8 dB within a sector of $\pm 65°$.
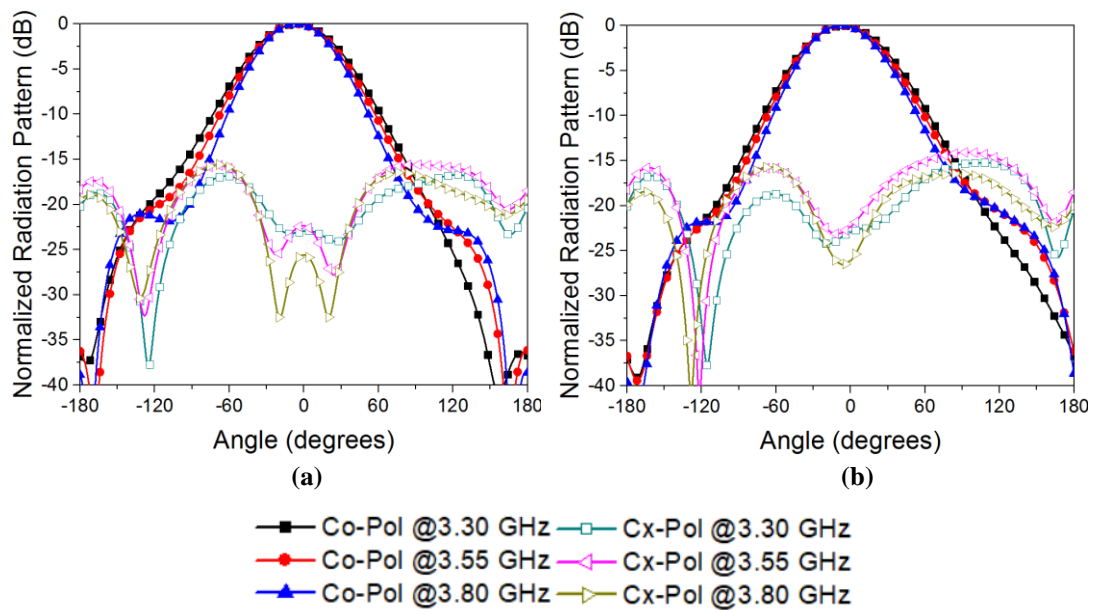
Fig. 8.6.   Normalized measured radiation patterns in (a) H-plane (b) V-plane

A comparison between the state-of-the-art sub-6 GHz 5G antennas reported in the literature and the proposed antenna is tabulated in Table 8.1. It is apparent that the proposed antenna design has the widest BW with the industrial standard VSWR ≤ 1.5, a small size, a high gain with good isolation between its ports and a high XPD.

Table 8.1.   Comparison of Reported Sub-6 GHz 5G Base Station Antennas to the Proposed Antenna

Ref.	[136]	[137]	[139]	Proposed
Frequency (GHz)	3.65-3.81	3.3-3.6	3.45-3.55	3.3-3.8
Size (mm³)	$86 \times 81 \times 3$	$72 \times 72 \times 18.8$	$74 \times 74 \times 1.5$	$71 \times 71 \times 12.2$
Isolation (dB)	31	28.8	15	25
Average gain (dBi)	10	8.2	8	8.8
Polarization	Dual	Dual	Single	Dual
XPD (dB)	23	24	NA	22

8.2.4. Parametric Study

An important parameter in the design is the height of the gap *H* between the feeding and the radiating layers, which determines the coupling between these two layers and hence affects the input impedance of the antenna.

(a)

(b)
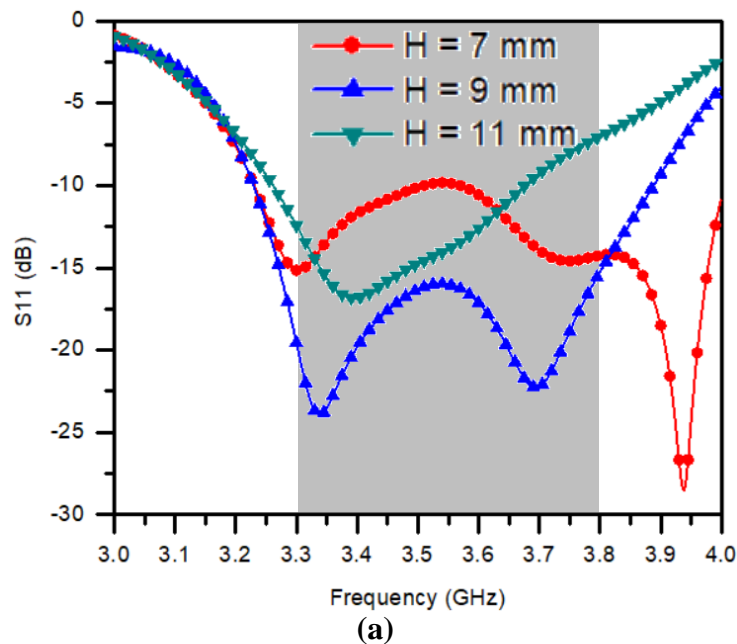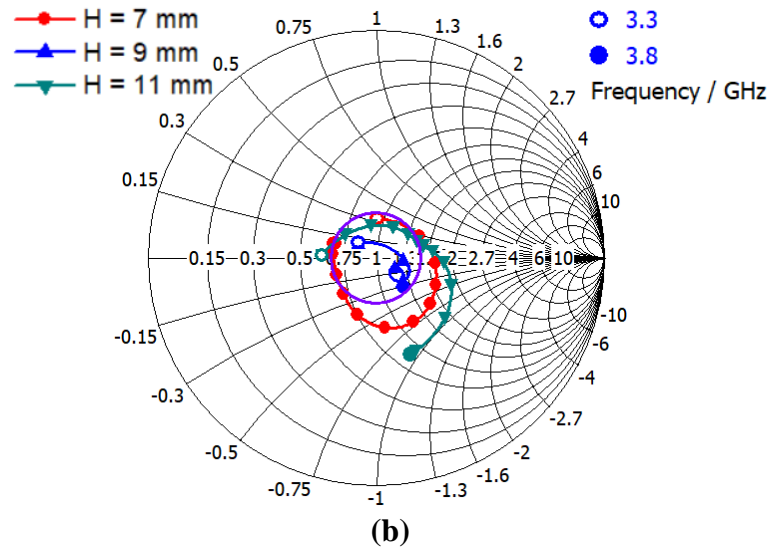
Fig. 8.7.   Effect of *H* on the reflection coefficient illustrated by
(a) S-parameters (b) Smith chart

When *H* is smaller, the feeding layer gets closer to the radiating layer and the input impedance becomes more capacitive and vice versa as shown in the Smith chart in Fig. 8.7(b). For optimum impedance matching, *H* should be 9 mm to achieve VSWR ≤ 1.5 (the purple circle at the middle of the Smith chart) within the desired frequency band.

The second parameter studied was the length of the slots *L_Slot* in the radiating patch. It controls the input impedance of the radiating patch seen from the feeding points. *L_Slot* is optimized and set to be 9 mm to cover the frequency band from 3.3 GHz to 3.8 GHz with a reflection coefficient better than -15 dB as shown in Fig. 8.8.
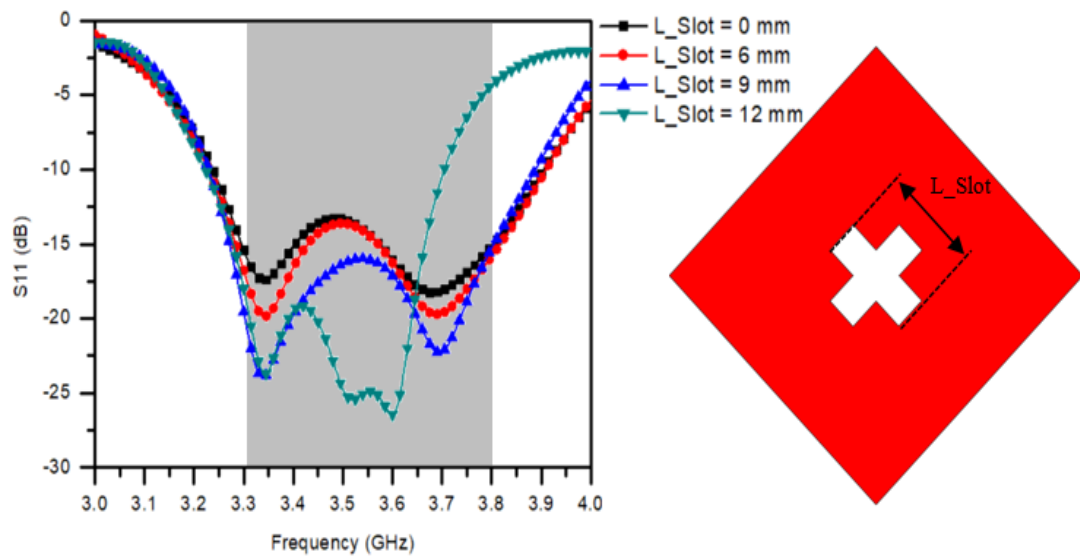
Fig. 8.8.   Effect of *L_Slot* on the reflection coefficient

The third parameter studied was the side length of the parasitic patch *WP3*. It affects the amount of the capacitive loading added to the antenna input impedance. The larger the parasitic patch, the higher the capacitive loading is added. *WP3* is set to 20 mm for optimum impedance matching across the desired frequency band as presented in Fig. 8.9.
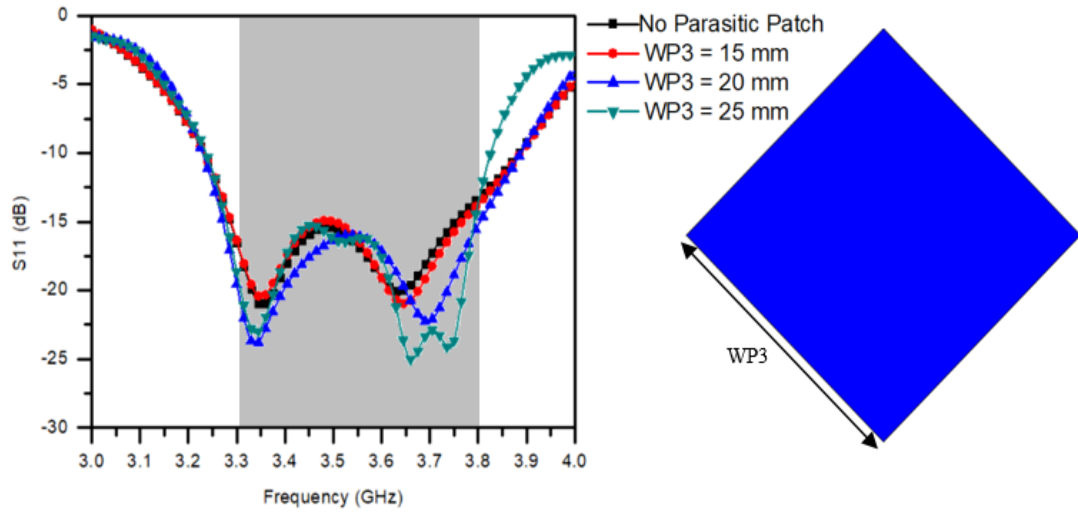
Fig. 8.9.   Effect of *WP3* on the reflection coefficient

8.3. MIMO Antenna Array

In this section, a dual-polarized MIMO antenna array based on the antenna element presented in Section 8.2 is designed to operate in one of the two different communication topologies used in 5G mobile communications (broadcast and traffic).

In the broadcast topology, the 5G base station antenna array is required to perform as conventional directive 2G, 3G and 4G base station antennas covering a sector in a hexagonal cellular mobile network with a horizontal HBPW of 65° and a vertical down tilting from 0° to 20°.

On the other hand, in the traffic topology, the 5G base station antenna is required to communicate with concurrent users in a P2MP communication by assigning multiple beams with narrow HPBWs to multiple users (typically one beam for each user). Switching between these two topologies (broadcast and traffic) depends on the excitation scenarios of the antenna elements in the MIMO array.

Fig. 8.10 presents the proposed MIMO antenna array structure. It consists of 27 elements (3 columns and 9 rows). The spacing between two successive columns is set

to 65 mm ($0.8\lambda_0$) while the spacing between two successive rows is set to 50 mm ($0.6\lambda_0$) (where λ_0 is the free space wavelength at the central frequency 3.55 GHz). To identify the location of an antenna element in the array easily, the columns are numbered as *C1*, *C2* and *C3* from left to right while the rows are numbered as *R1* to *R9* from up to down as shown in Fig. 8.10.
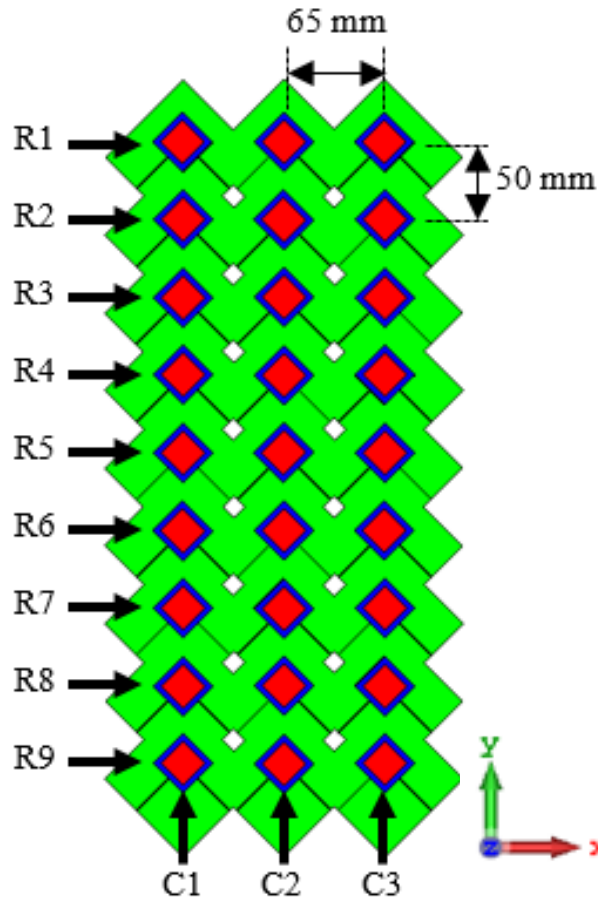
Fig. 8.10.   The structure of the proposed MIMO antenna array

To evaluate the diversity performance of the proposed MIMO array, the ECC can be obtained using equation (3.4). ECC is calculated and plotted in Fig. 8.11. Results show that the proposed MIMO array offer very low ECC. The maximum ECC is less than 0.004 across the operating frequency band, far less than the general criteria of ECC < 0.3. The two communication topologies are described in details as follows.
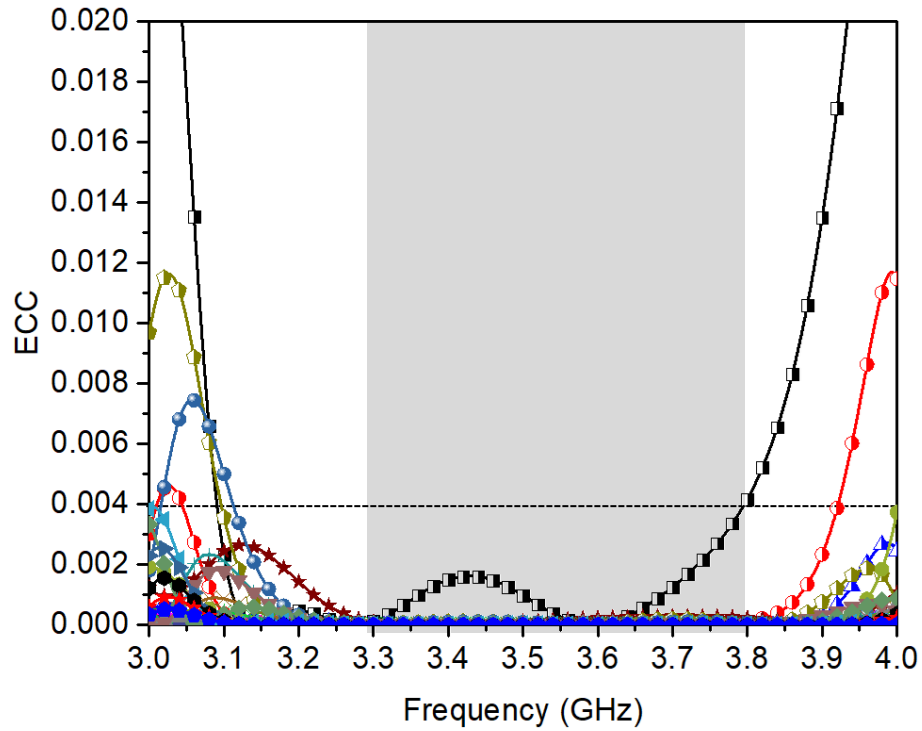
Fig. 8.11.   ECC of the ports of the proposed MIMO antenna array

8.3.1. Broadcast Communication Topology

In the broadcast communication topology, the MIMO antenna array is divided horizontally into three vertical linear subarrays; *C1*, *C2* and, *C3* as shown in Fig. 8.12(a). Each linear subarray consists of 9 antenna elements. The excitation signals for each subarray are set such that the radiated main lobes are directed to 0º (boresight), -10º and -20º for *C1*, *C2* and *C3* respectively. The negative sign at each angle indicates that the main lobe is tilted downwards. Each subarray has a vertical HPBW of 10º. Therefore, the three main lobes cover a vertical sector from +5º to -25º contiguously without overlapping or gaps (from +5º to -5º by *C1*, from -5º to -15º by *C2* and from -15º to -25º by *C3*) as shown in Fig. 8.12(b). It worth noting that the horizontal HPBW of each radiation pattern is almost the same as the single antenna element. Because the three main lobes are contiguous in the V-plane without overlapping, they almost do not interfere in the H-plane. Therefore, the combined radiation pattern also has the same horizontal HPBW as the single antenna element. The combined radiation pattern of the three subarrays covers a solid sector with horizontal and vertical HPBWs of 65º and 30º respectively.

(a)

(b)
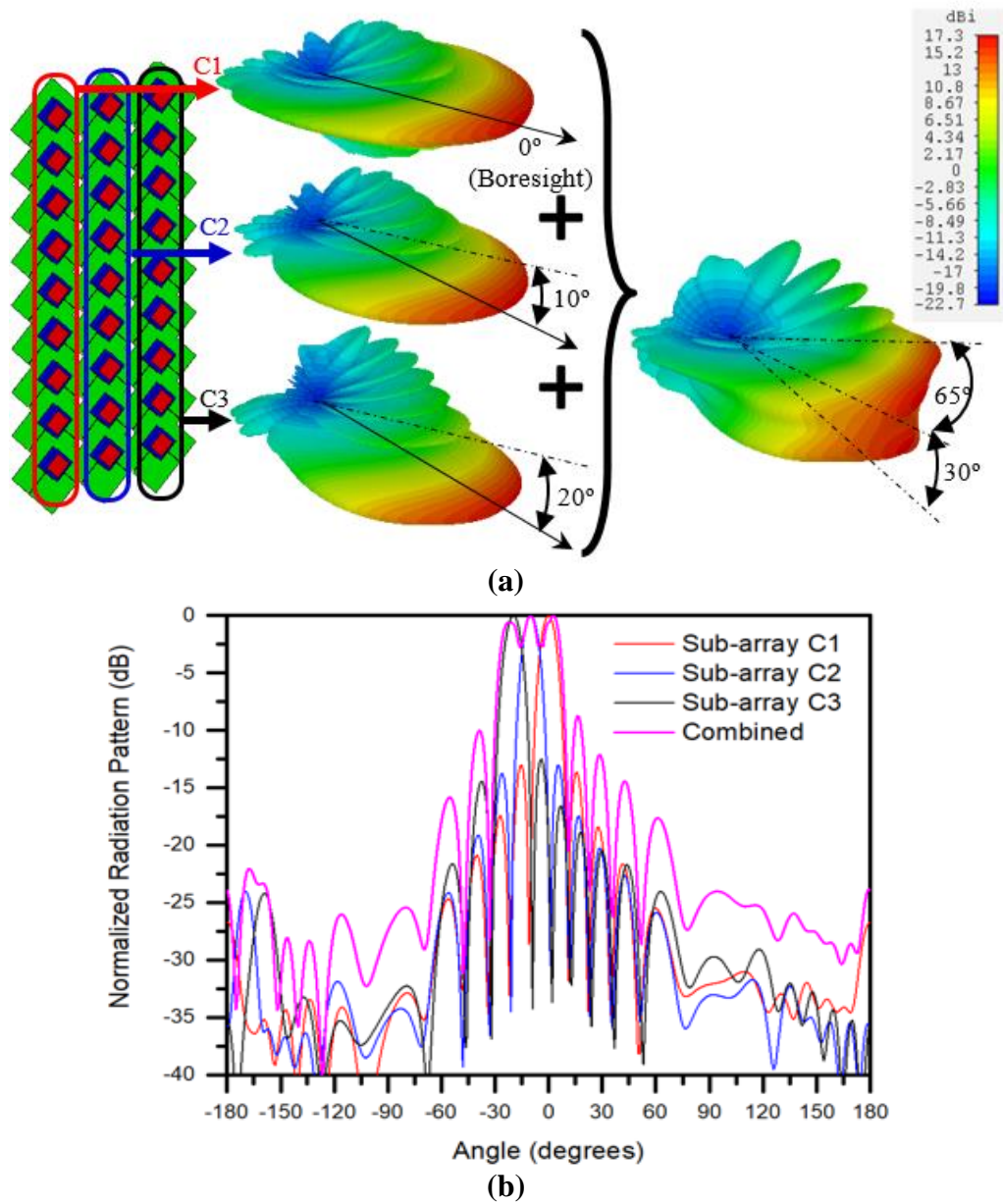
Fig. 8.12.   The broadcast communication topology illustrated by
(a) 3D radiation patterns (b) V-plane

8.3.2. Traffic Communication Topology

Generally, in traffic communication topology, pattern or frequency diversity approach is commonly used. The approach of using a multi-beam array is also applied. In this section, a multi-beam antenna array based on PIS is proposed. The pattern and frequency diversities for the same MIMO antenna array structure are illustrated to show how the proposed PIS can overcome the drawbacks of pattern and frequency diversities.
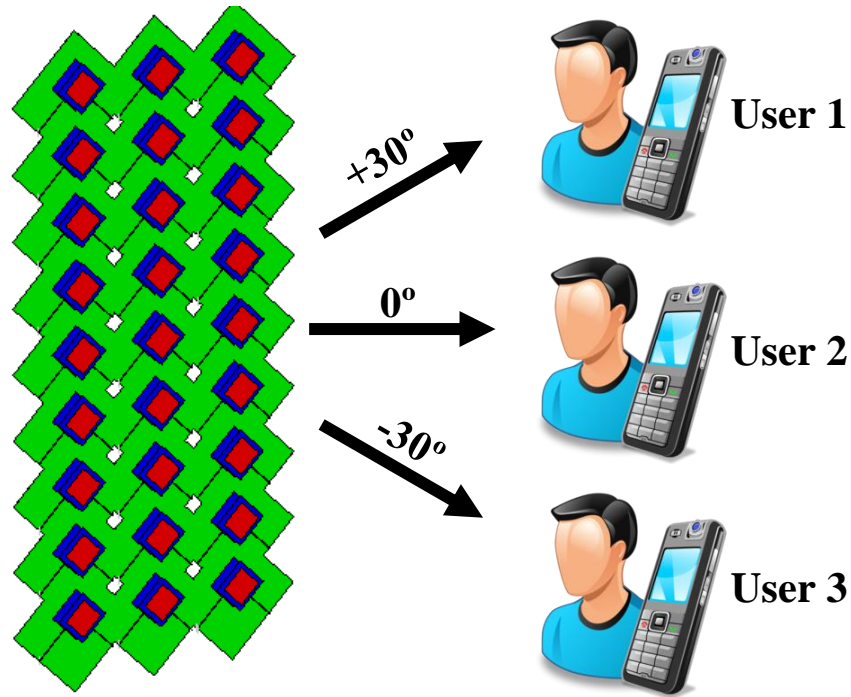
Fig. 8.13.   A P2MP communication scenario for three users

A P2MP communication scenario is assumed in this chapter where three users are located at three different angles (+30º, 0º and -30º respectively) as shown in Fig. 8.13. For the pattern diversity approach, the MIMO array is divided vertically into three planar 3×3 subarrays. Subarray I (consists of *R1*, *R2* and *R3*), subarray II (consists of *R4*, *R5* and *R6*) and subarray III (consists of *R7*, *R8* and *R9*) as shown in Fig. 8.14(a). The three subarrays operate at the same frequency and the excitation signals of each subarray are set independently to direct its main lobe to one of the users on a one-to-one basis. From the combined radiation pattern shown in Fig. 8.14(a), we can see that there are two main drawbacks in the pattern diversity approach. The first drawback is that the combined radiation pattern has overlapped the main lobes due to their low directivity (selectivity) toward the users because the subarrays aperture is limited. The second drawback is the limited capability of beam steering of each subarray due to the limitation in the subarray aperture.

For the frequency diversity approach, the whole MIMO antenna array is excited by signals at three different frequencies (3.3GHz, 3.5GHz and 3.8 GHz) as shown in Fig. 8.14(b). First, the phases of the signal at each frequency are adjusted to direct the main lobe of the radiation pattern at this frequency to one of the users in a one-to-one basis then the three signals are superimposed and fed to the MIMO array.
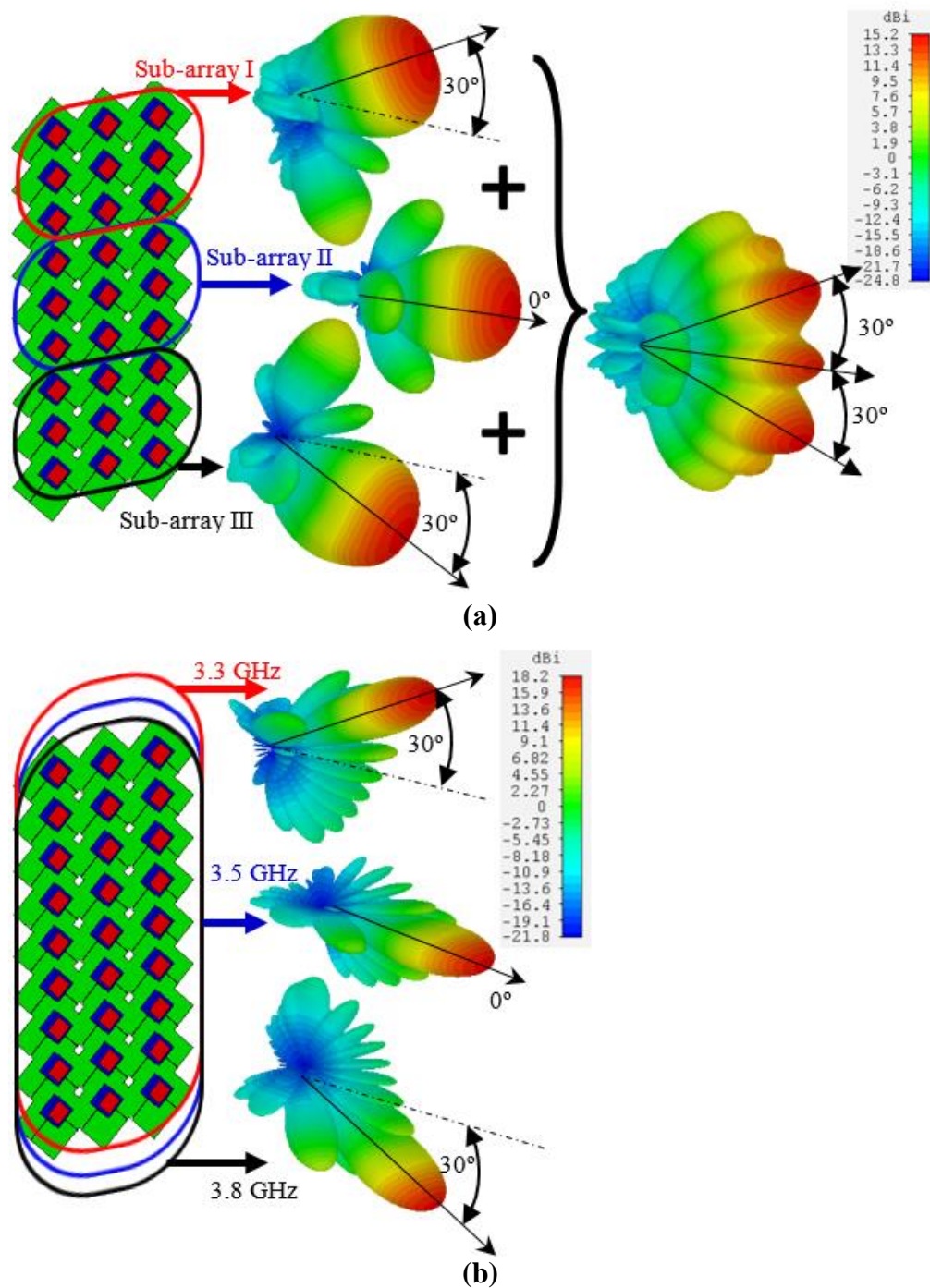
Fig. 8.14.   The traffic communication topology using
(a) pattern diversity (b) frequency diversity

From the radiation patterns shown in Fig. 8.14(b) we notice that the frequency diversity approach overcomes the drawbacks of the pattern diversity approach as it offers high directivity and good steering capability because it uses the whole array aperture. On the other hand, the disadvantage of the frequency diversity approach

is using a single frequency for each user instead of using a single frequency for multiple users, which is considered as an advantage in the pattern diversity approach. The separation between the frequencies should be 40 MHz at least [144]. This limits the number of users served by the base station antenna due to the limited spectrum of the 5G (typically 10-12 users).

Multi-beam antenna arrays may also be used to serve multiple users in the traffic communication topology. One of the methods used in multi-beam antenna arrays is the simultaneous static multi-beam approach using a Butler matrix or multiple feeding ports. The drawbacks of this method are the limited steering capability of the static multi-beam, which does not meet the requirements for 5G mobile applications and that the more beams are required, the more complicated feeding network is needed. Another method used in multi-beam arrays is utilizing digital, analogue or hybrid beamforming technique, which allows dynamic but switchable (not simultaneous) multiple beams. In this case, time-division coverage among the users is applied which highly limits the data streaming rate. Another method used in multi-beam antenna arrays is utilizing optimization algorithms to synthesize multi-beam radiation patterns. Although the radiation pattern, in this case, may have simultaneous and dynamic multiple beams, it needs a long processing time, which is not applicable for real-time 5G applications.

To understand how the proposed PIS works, we first study the general formula of the radiation pattern formed by a planar antenna array oriented in the XY plane. The 3D radiation pattern $P(\theta,\phi)$ can be found by multiplying the ($MN\times1$) complex weight vector Wmn by the ($MN\times LP$) steering matrix $A(\theta, \phi)$ [158]:

$$P(\theta, \emptyset) = W_{mn}^{H} \times A(\theta, \emptyset) \tag{8.1}$$

where

$$W_{mn} = [w_{11}, w_{21}, \dots, w_{M1}, w_{12}, \dots, w_{MN}]^{T} \tag{8.2}$$

$$A(\theta, \emptyset) = [a_{11}(\theta, \emptyset), a_{21}(\theta, \emptyset), \dots, a_{M1}(\theta, \emptyset), a_{12}(\theta, \emptyset), \dots, a_{MN}(\theta, \emptyset)]^{T} \tag{8.3}$$

$$
\begin{aligned}
a_{mn}(\theta, \emptyset) = & [e^{-iksin(\theta_1)[(m-1)d_x \cos(\emptyset_1)+(n-1)d_y \sin(\emptyset_1)]}, \dots, \\
& e^{-iksin(\theta_L)[(m-1)d_x \cos(\emptyset_1)+(n-1)d_y \sin(\emptyset_1)]}, \dots, \\
& e^{-iksin(\theta_L)[(m-1)d_x \cos(\emptyset_P)+(n-1)d_y \sin(\emptyset_P)]}]
\end{aligned} \tag{8.4}
$$

$(\cdot)^T$ and $(\cdot)^H$ stand for the transpose and Hermitian transpose, M and N are the total numbers of the array rows and columns, θ and ϕ are the aspect angles in the XZ and YZ planes measured from the antenna array boresight, L and P are the numbers of the defined aspect angles θ and ϕ, dx and dy are the separations between two successive antenna elements in the X-axis and Y-axis respectively, w_{mn} is the complex weight of the antenna element number mn, k is the angular wavenumber which equals to $2\pi/\lambda$ and λ is the free-space wavelength.

If we consider $P_d(\theta,\phi)$ as a pre-defined 3D radiation pattern at each value of θ and ϕ, the corresponding synthesized complex weight vector W_{mns} can be found by substituting in equation (8.1) to yield

$$W_{mns}^H = P_d(\theta, \emptyset) \times [A(\theta, \emptyset)]^{-1} \tag{8.5}$$

To obtain the inverse of the steering matrix $A(\theta,\phi)$ using classical mathematics, $A(\theta,\phi)$ should be a non-singular square matrix (i.e. $MN = LP$). Therefore, we have two cases.

(a) Case (1): the number of the array elements MN should be as large as the number of the defined aspect angles LP, which will result in an extremely large array (not practical).

(b) Case (2): the number of the defined aspect angles LP is as limited as the number of the array elements MN, which results in a radiation pattern with a poor resolution.

To solve this problem, pseudo Moore–Penrose inverse matrix is used to obtain the inverse of $A(\theta,\phi)$. Thus, from equation (8.5), PIS is defined as

$$W_{mns}^H = P_d(\theta, \emptyset) \times \left[A^H(\theta, \emptyset) \times \left(A(\theta, \emptyset) \times A^H(\theta, \emptyset) \right)^{-1} \right] \tag{8.6}$$

By applying PIS in equation (8.6) to a pre-defined radiation pattern $P_d(\theta,\phi)$ with three narrow main lobes at -30°, 0° and 30° to match the requirements of the P2MP communication scenario presented in Fig. 8.13, the corresponding synthesized complex weight vector W_{mns} can be determined as shown in Table 8.2. The weight vector tabulated in Table 8.2 is applied to the proposed MIMO antenna array and the simulated 3D radiation pattern is presented in Fig. 8.15(a).

Table 8.2.   Synthesized Complex Weight Vector *Wmns* Using PIS

Antenna Elements		R1	R2	R3	R4	R5	R6	R7	R8	R9
Complex weight	Attenuation (dB)	0	16	13	1.5	4.3	10	7	0.6	19
	Phase (º)	0	0	180	0	0	180	0	0	180

(a)

(b)
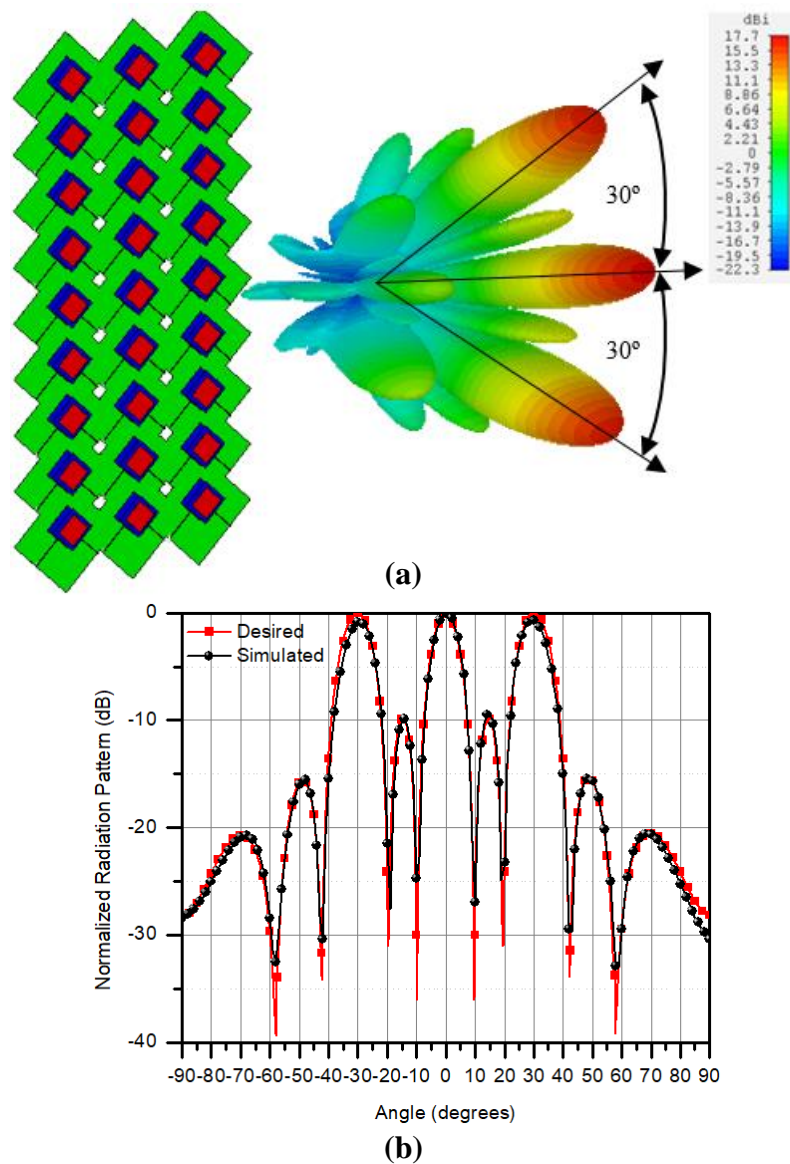
Fig. 8.15.   The traffic communication topology using the PIS illustrated by

(a) 3D radiation patterns (b) V-plane

It is clear that PIS has overcome the disadvantages of both the frequency and pattern diversity approaches as it can cover the three users simultaneously at a single frequency with a high directivity (a narrow beamwidth) and good steering capability. It can also generate a radiation pattern with simultaneous and dynamic multiple beams in real-time processing. From Fig. 8.15(b), it is evident that the pre-defined and the simulated radiation patterns have a good agreement, which indicates how accurate the PIS is.

For more validating of the proposed PIS, unlike the first scenario, another scenario with an asymmetric distribution of three users is assumed at +30º, -5º and -20º respectively. Again, the PIS could accurately direct multiple beams for multiple users on a one-to-one basis as shown in Fig. 8.16
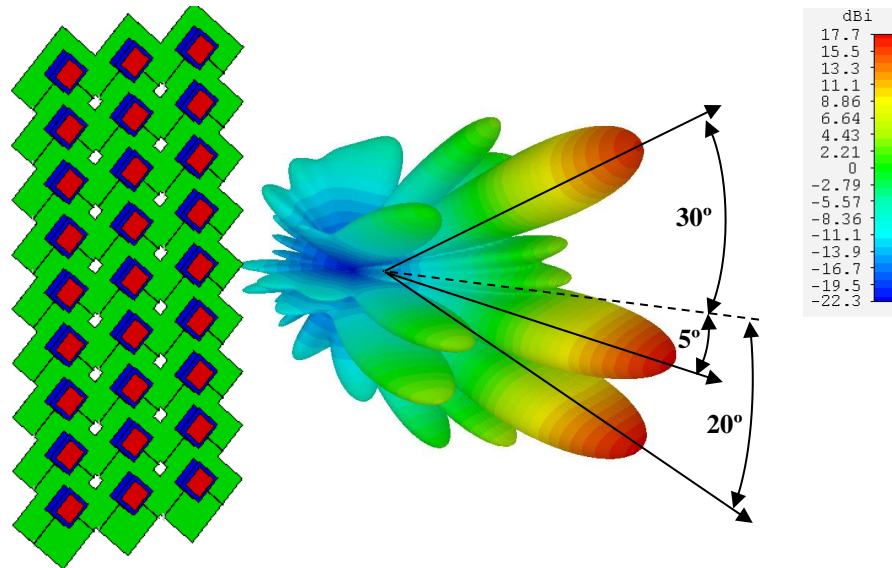
Fig. 8.16.   The traffic communication topology using the proposed PIS for asymmetric users distribution

Table 8.3 compares the different approaches used in the literature with the proposed PIS. It is clear that the proposed PIS overcomes the drawbacks found in other approaches as PIS can generate a simultaneous dynamic multi-beam radiation pattern with high directivity and a good steering capability at a single frequency in a real-time processing outperforming other multi-beam antenna array methods (while the frequency diversity approach uses multiple frequencies). Furthermore, the number of users served by the MIMO 5G base station can be increased by applying PIS at multiple frequencies.

Table 8.3.   Comparison of the Proposed PIS to Other Reported Approaches

Method	Frequency	Directivity	Steering Capability	Simultaneousness	Real-time
Pattern Diversity	Single	Low	Low	Yes	Yes
Frequency Diversity	Multiple	High	High	Yes	Yes
Simultaneous Multi-beam [146]-[147]-[148]-[149]	Single	High	Static	Yes	Yes
Switchable Multi-beam [150]-[151]	Single	High	High	No	Yes
Optimized Multi-beam [154]-[155]-[156]-[157]	Single	High	High	Yes	No
PIS	Single	High	High	Yes	Yes

8.4. Summary

A new dual-polarized base station antenna has been designed, optimized, fabricated and measured for the sub-6 GHz 5G applications. The proposed design covers the frequency band from 3.3 GHz to 3.8 GHz with industrial impedance matching specification (VSWR ≤ 1.5) and good isolation between its ports. It also has a stable radiation pattern within the desired frequency band with a small size and low profile in comparison to other reported designs. A MIMO antenna array based on the antenna element has been proposed to perform in one of the two 5G communication topologies (broadcast and traffic). A novel PIS has been illustrated and applied to the proposed MIMO array for the traffic topology. It has been shown that PIS offers the advantages of both the frequency and pattern diversity approaches as it uses a single frequency to generate multiple beams with high directivity and good steering capability. PIS has also been shown outperforming other multi-beam antenna array methods as it is

capable of radiating simultaneous dynamic multiple beams in real-time which makes the proposed design an ideal antenna candidate for the sub-6 GHz 5G base stations.

The only drawback of the PIS can be noticed when two or more users are very close to each other. In this case, time division multiplexing should be applied between these users which limits the data rate.

Chapter 9. A Camouflage Antenna for 5G Pico-Cell Base Stations

In the previous chapter, a MIMO base station antenna array was proposed to serve 5G applications in hexagonal cell networks. However, in this chapter, we focus on the PC base stations, which are more likely to be utilized in 5G mobile communication networks.

This chapter proposes a new design of a camouflage dual-polarized antenna for 5G PC base stations. The antenna covers the frequency band from 3.3 GHz to 3.8 GHz with VSWR ≤ 1.5. The antenna enjoys good isolation between its ports (≥ 23 dB) and a low profile. The proposed antenna consists of two layers (a radiating layer and a feeding layer) separated by an air gap. The radiating layer uses a Transparent Conducting Oxide (TCO) to form two patches (a radiating patch and a parasitic patch) printed on the opposite sides of a glass laminate. The radiating layer has visual transparency of 77%, which makes it possible to be integrated with the glass cover of the head of a street lamp while the feeding layer is embedded inside the head for camouflage. A 2×2 antenna array is formed to achieve a realized gain of 13.2 dBi and a 3-dB solid angle of 33º $\times$ 33º, which makes the proposed design an excellent candidate for the 5G PC base stations.

9.1. Introduction

To deliver that high-speed connectivity, the next generation of cellular networks (5G) will use new types or airwaves that do not travel far. Meaning carriers will need to build dense webs of small cell towers on the side of buildings, on lampposts, even on newspaper boxes, the cells are roughly the size of a laptop. Therefore, the small cell base stations are set to play an important role in expanding the capacity of wireless networks [159]. The design of PC base stations has attracted the attention of the research and the industry communities as it has posed new challenges on making them small size, low power and low cost in comparison to the traditional Macrocell base

stations [160]. Typical coverage scenarios of Macrocell and PC base stations can be illustrated in Fig. 9.1.
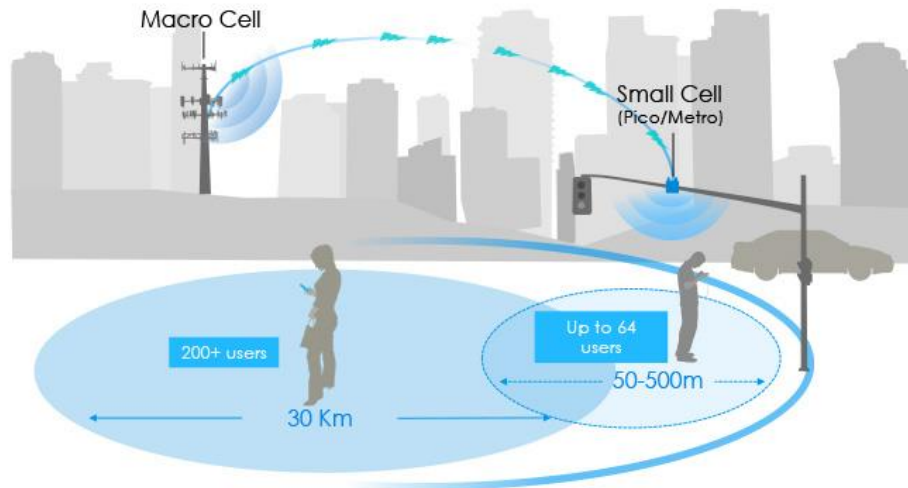
Fig. 9.1.   Macrocell and PC base stations coverage [160]

To respond to the public pressure of less conspicuous antenna systems, designers tend to produce camouflage base station antennas, which can be visually hidden [161]. Two main approaches can be utilized to achieve the concept of constructing camouflage antennas. The first approach is to install the base station antenna on a customized platform that looks like a part of the surrounding environment, like a palm tree in a garden or a cactus tree on the side of a highway road as shown in Fig. 9.2. This approach is quite costly because of the need for building a customized platform for each base station.

Fig. 9.2.   Base station antennas on camouflage platforms [161]

The second approach is to integrate the base station antenna with an already existing object in the surrounding environment such as the cross at the top of the cathedral shown in Fig. 9.3(a), which is nothing but a base station antenna array or being integrated to transparent window glass as shown in Fig. 9.3(b).

(a)   **(b)**
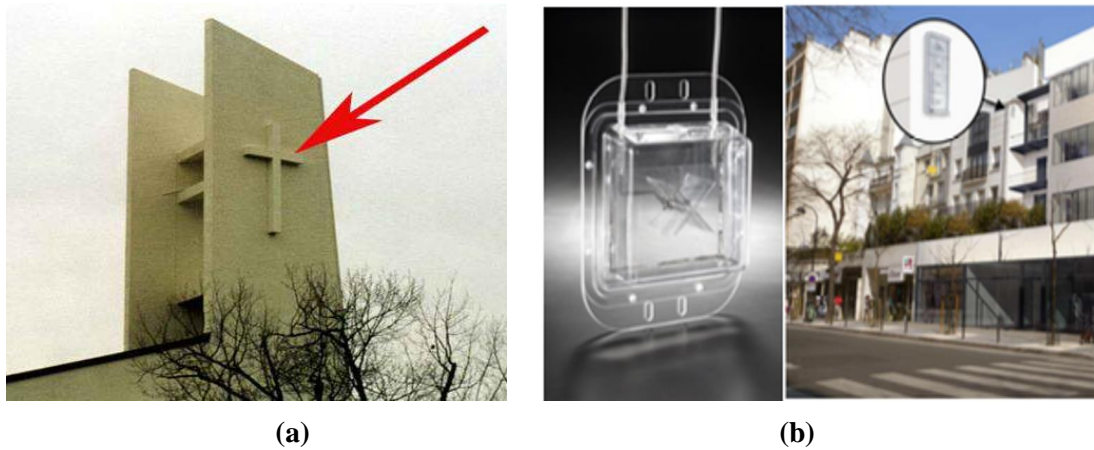
Fig. 9.3.   **A camouflage base station integrated to (a) cathedral cross (b) window glass**

The concept of using a camouflage antenna in wireless communication is nothing new. It has been adopted for both military [162] and civilian [163] applications. Furthermore, in [164], a transparent conductor printed on a glass substrate has been employed to form a transparent antenna, which is of low visibility and could be an attractive candidate for new PC base stations.

To make a transparent antenna, the selection of a suitable material is vital. Transparent conductive materials have been prepared with oxides of tin, indium, zinc and cadmium using magnetron sputtering [165]-[166]. These TCOs are employed in a wide spectrum of applications such as solar cells, electromagnetic shielding and touch-panel controls [167]. Notably, there has been little commercial application of TCOs in antenna design. Attempts have been made to create transparent patch antennas for automobile windshields and solar cells [168]-[172]. Many papers on this subject expressed the inability to achieve high gains (larger than 2 dBi) [171] due to the reduced efficiency of microstrip patch antennas with a ground plane compared with dipole antennas with no ground plane [170]. One of the problems is skin depth losses introduced by the requirement of thin TCO depositions for high optical transparency. Furthermore, ground effect losses present in patch antennas further aggravate the loss

due to skin effects. Both issues coupled with the relatively low conductivity of TCOs in comparison to copper [173], can cause significant increases in surface resistance of the microstrip patch and result in lower efficiency. Taking into consideration all of these effects, this work will also evaluate the necessary requirements of a transparent material for making such an antenna.

In this chapter, a novel transparent dual-polarized antenna array for sub-6 GHz 5G PC base stations is proposed. The antenna element has a transparent radiator printed on a transparent glass laminate, which gives the proposed design the advantage of being partially invisible. This low visibility allows the proposed antenna to be feasibly integrated with other daily suitable surrounding equipment to achieve visual camouflage. In this work, the street lamp is selected as an example of such surrounding equipment, which can be any other suitable one. A possible coverage scenario using the proposed PC base station is presented in Fig. 9.4.

Fig. 9.4. **The illustrative scenario of the 5G coverage area using the proposed PC base station**

The chapter is organized as follows: Section 9.2 describes the proposed antenna element design and its simulated and measured results; Section 9.3 discusses a 2×2 square antenna array configuration and its simulated and measured results; Section 9.4 illustrates the integration of the antenna array with a street lamp and its effects on the antenna performance; and finally, a summary is drawn in Section 9.5.

9.2. The Proposed Antenna Element

9.2.1. Antenna Element Design and Performance

In this section, the proposed antenna element is illustrated. Fig. 9.5 shows the exploded geometry of the proposed design. The antenna element shares the same features and working principles of the antenna element proposed in Chapter 8. However, a major difference between the two antennas is that the proposed antenna element in this chapter uses a transparent radiating layer.

The antenna consists of two layers separated by an air gap. Layer I (the feeding layer) is a Rogers RT5880 laminate with thickness $Hd1 = 1.6$ mm, relative permittivity $\varepsilon_{r1} = 2.2$ and a loss tangent of 0.0009. A square copper feeding patch is printed on the top of Layer I with two orthogonal 50 Ω microstrip feed lines for dual-polarization, which are excited by two feeding ports. A copper ground plane is printed on the bottom side of Layer I to provide unidirectional radiation. Layer II (the radiating layer) is a glass laminate with thickness $Hd2 = 2.2$ mm, relative permittivity $\varepsilon_{r2} = 2.3$ and loss tangent of 0.0054. A radiating square patch using a thin film of TCO is printed on the bottom side of Layer II with the same dimensions as the feeding patch. Indium tin oxide (ITO) film with a thickness of 0.3 μm and having a conductivity of 5.6×10^5 S/m is used as the TCO to achieve optical transparency of 88% for the radiating patch [174]. The material properties of the ITO will be explained in a later section.
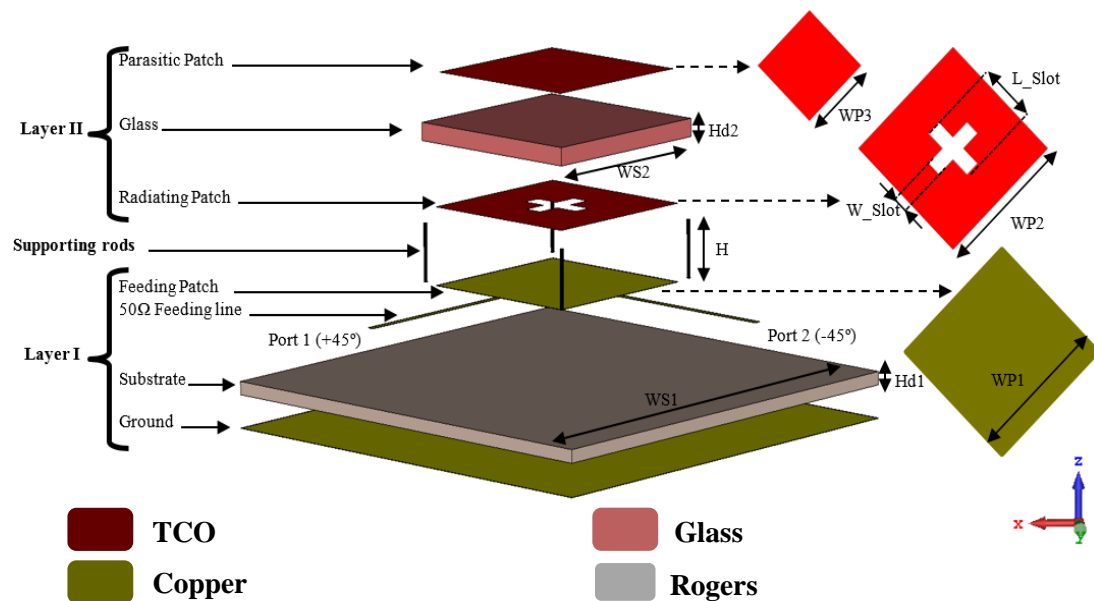
Fig. 9.5.   The geometry of the proposed antenna element

Two orthogonal symmetrical rectangular slots are cut in the radiating patch to improve the impedance matching and the transparency. A parasitic ITO patch is printed on the top side of the glass laminate to improve the impedance matching by adding a capacitive loading to the antenna input impedance. The two layers are separated by an air gap of a height of H. The radiating layer is fed by the electric field coupling from the feeding layer. The two layers are oriented in the XY plane. The two layers, the three patches (feeding, radiating and parasitic patches) and the slots are concentric. For ± 45° dual-polarization, the side lengths of the layers, patches, feed lines and slots form angles of ±45° with the X and Y-axes respectively. Four supporting rods are used to, mechanically, fix the radiating layer above the feeding layer at a height H. The optimized dimensions (in mm) are determined as $WP1 = WP2 = 27$, $WP3 = 20$, $WS1 = 71$, $WS2 = 30$, $L\_Slot = 9$, $W\_Slot = 3$ and H = 7.

To validate the design, a prototype was fabricated as shown in Fig. 9.6. In Fig. 9.6 (a), 20 stacked radiating layers are placed on a white paper to make the parasitic and radiating patches partially visible while Fig. 9.6 (b) shows a single radiating layer with an overall transparency of 77% (transparency for each patch is 88% while the transparency of the glass is around 99%).

(a)

(b)

(c)
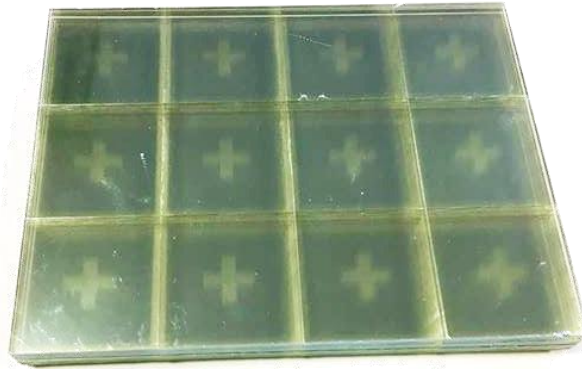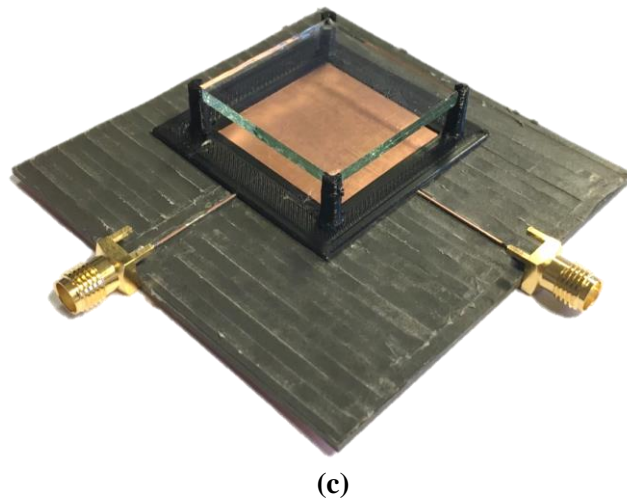
Fig. 9.6. **Prototypes of (a) 20 stacked radiating layers (b) a transparent single radiating layer (c) the proposed antenna element**

Fig. 9.7 shows a good agreement between the simulated and measured reflection coefficients, isolations between the ports and realized gains. A fractional BW of 14% is achieved (3.3-3.8 GHz) with a reflection coefficient less than -15 dB (VSWR $\leq$ 1.5) to meet the standard industrial requirement. The measured port-to-port isolation is better than 23 dB across the frequency band. It is also apparent that the proposed antenna has a stable realized gain of 7.3 dBi across the frequency band of interest.
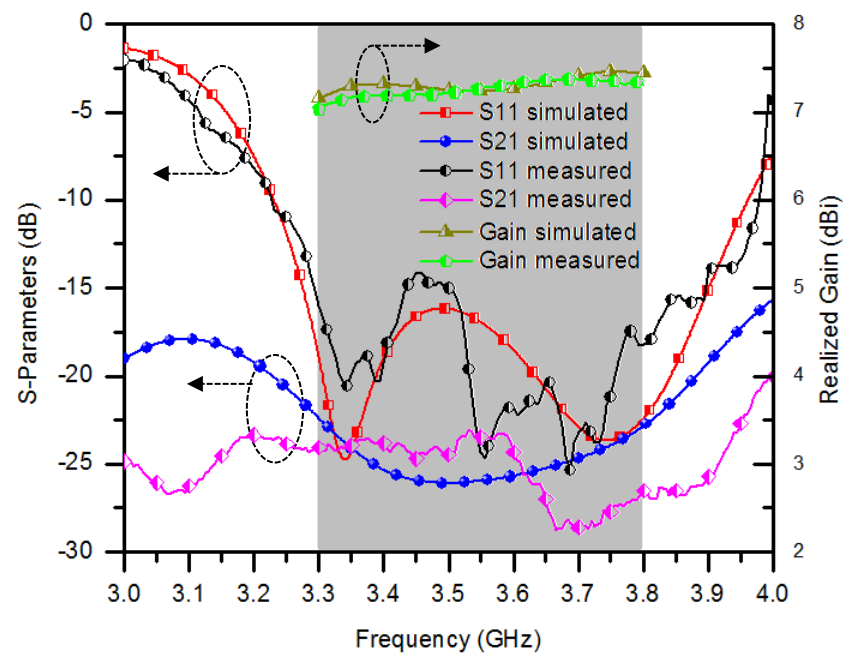
Fig. 9.7. **Simulated and measured reflection coefficients, isolation between the ports, and realized gains**

The measured co-and cross-polarized radiation patterns at the start, central and stop frequencies in H-plane (XZ plane) and V-plane (YZ plane) are shown in Fig. 9.8. Because the structure is almost symmetrical around the X and Y-axes, the HPBWs in H-plane and V-plane are about 75° across the frequency band. The XPD is better than 23 dB at boresight.
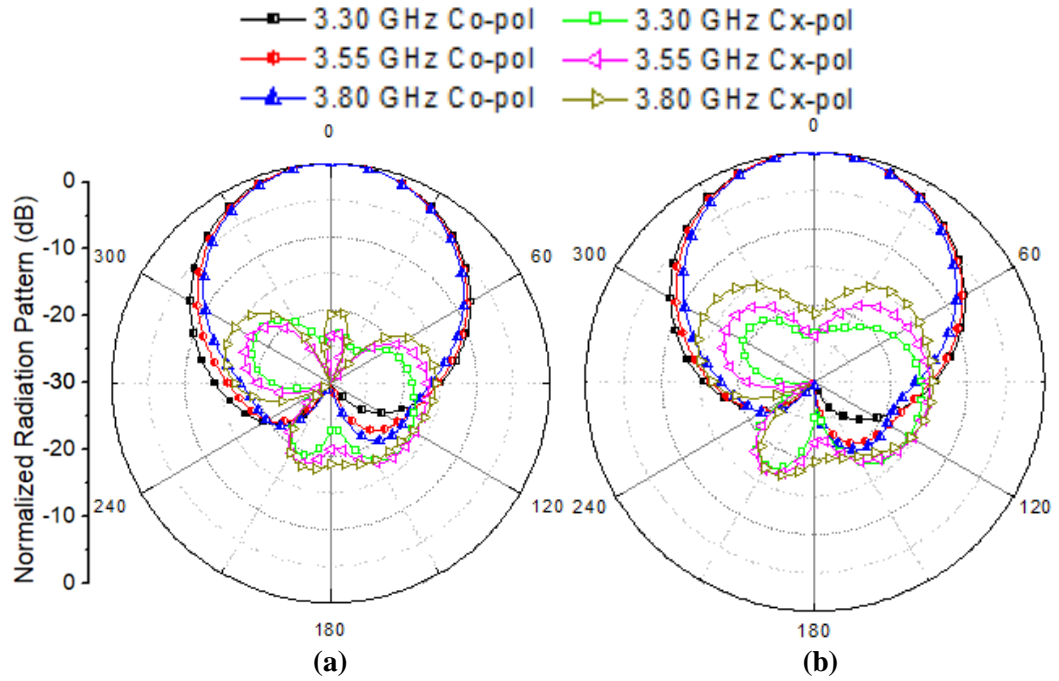
Fig. 9.8.   Measured radiation patterns of proposed antenna element across
(a) H-plane. (b) V- plane

A comparison between the state-of-the-art sub-6 GHz 5G antennas reported in the literature and the proposed antenna is tabulated in Table 9.1. It is apparent that the proposed antenna has a relatively wide BW and small size, with good isolation between its ports and a high XPD. The proposed antenna gain is slightly less than the gains of the other reported design as the efficiency of the proposed antenna is around 72% - 74% (~ -1.4 dB). This is due to using ITO as a conductor, which has less conductivity than the copper used in the reported designs.

The most important feature in the proposed antenna is its availability to be integrated with an object (such as a streetlamp in our case) for camouflage purposes because of its transparent radiating part.

Table 9.1.   Comparison of Reported Sub-6 GHz 5G Base Station Antennas to the
Proposed Antenna

Ref.	[175]	[176]	[177]	[178]	Proposed
Frequency Band (GHz)	3.65-3.81	3.3-3.6	3.5-5.1	3.45-3.55	3.3-3.8
Fractional BW	4.3%	8.7%	37.2%	2.9%	14.1%
Size (mm³)	86×81×3	72×72×18.8	60×60×17	74×74×1.5	71×71×11
Isolation (dB)	31	28.8	18	15	23
Gain (dBi)	10	8.2	8	8	7.3
Polarization	Dual	Dual	Dual	Single	Dual
XPD (dB)	23	24	NA	NA	23
Camouflage	NA	NA	NA	NA	Available

9.2.2. Transparent Material Properties

In this section, the various design parameters for the TCOs are discussed. Transparent oxides such as ITO, belong to the family of oxides (In_2O_3: Sn) that possess high optical transparency (> 80% at 550 nm wavelength) and good electrical conductivity at microwave frequencies (> 10^5 S/m) [173] [174]. These seemingly opposing characteristics of transparent and conducting oxides are possible through some of the laws of physics. In an effort to understand the duality of optical transparency and microwave conductivity of TCOs, a deeper understanding of TCO doping is required. In the case of ITO, simultaneous transparency and conductivity are possible due to the chemical doping of tin for indium or by the presence of oxygen impurities in indium oxides. With enough doping, it is possible to create a degenerate gas of free carrier absorption in far-infrared frequencies where the material is transparent at visible wavelengths. These free carriers produce, high electronic conductivity at microwave frequencies [173] [179]. Under this free electron model, created by conduction band doping, the optical and conductive properties may be simply described by using Drude's model [180]. With this model, it is possible to use Maxwell's equations to model the conductivity and permittivity of the TCO as a function of frequency. After a vigorous set of derivations, it has been found that in order to maximize the transmission of the whole visible electromagnetic spectrum

($\lambda_{visible}$ = 400 nm to 700 nm) through the TCO, the electron density N_e must satisfy the following relationship [181],

$$N_e < \frac{4\pi^2 \varepsilon_\infty m^*}{\mu_0 q^2 \lambda_{visible}^2} \qquad (9.1\ )$$

where μ_0 is the magnetic permeability of free space, ε_∞ is the high-frequency relative permittivity of the TCO and $m^* = 0.35\ m_e$ is the effective mass of the TCO. Equation (9.1) will serve as a guideline for the doping of free electrons in the TCO to control the transparency of the TCO [181].

The transmission coefficient is dependent on the amount of absorbed energy as it travels through the lossy dielectric slab TCO. The amount of absorbed energy is determined by the electromagnetic skin depth, which constrains the electromagnetic wave energy loss as it travels through a thickness t of the TCO. The transmission of light through a TCO is related to skin depth, δ, by:

$$T(t) \cong e^{\left(\frac{-2t}{\delta}\right)} \qquad (9.2\ )$$

The dual characteristic of light absorption and microwave energy conduction of the TCO yields two separate equations that determine the skin depth at frequencies where the TCO is a good conductor but not very transparent $\omega_P > \omega$, and where the TCO is transparent $\omega_P < \omega$, as illustrated below:

Case 1, where $\omega_P > \omega$, $\omega\tau << 1$:

$$\delta = \sqrt{\frac{2}{\omega\mu\sigma}} \qquad (9.3\ )$$

Case 2, where $\omega_P < \omega$, $\omega\tau >> 1$:

$$\delta = \frac{2m^*}{Z_\infty q^2} \frac{\omega^2 \tau}{N_e} \qquad (9.4\ )$$

where we assume that $\omega < E_g/h$, $Z_\infty = 377/(\varepsilon_\infty)^{0.5}$, and μ is the magnetic permeability of the TCO.

For the first case when the TCO is a good conductor, the skin depth is inversely

proportional to the square root of the frequency according to equation (9.3). It is well known that as the deposition thickness of TCO becomes thinner than the skin depth, the surface resistance dramatically increases as a function of thickness t. However, when using TCOs, thin film deposition is necessary to keep transparency high. At higher frequencies, the skin depth decreases and hence a thinner TCO deposition thickness can be used without increasing the surface resistance.

For the second case, the transparency, $T(t)$ increases with the skin depth δ according to equation (9.2) and hence proportional to the electron mobility $\mu_e = q\tau / m^*$ and inversely proportional to N_e. It is also important to observe that an increase in the free electron mass m^* will have the same effect according to equation (9.4). The relation between the conductivity and electron mobility is given by [180],

$$\sigma = qN_e\mu_e \qquad (9.5)$$

According to equation (9.5), an increase in N_e and μ_e will increase the conductivity of the TCO. Therefore, the choice of a TCO for antenna design is determined by the electron density N_e, free-electron mobility μ_e and free-electron mass m^* of the material. Upon choosing a specific TCO, by controlling the thickness of film deposition during the antenna fabrication, the transparency and the conductivity can be optimized.

$$Sheet\ resistance, R_S = \frac{1}{\sigma \times t} \qquad (9.6)$$

In this work, ITO is used as the TCO for designing the transparent patches. Typical values for ITO permittivity and effective electronic mass are $\varepsilon_\infty = 4$ and $m^* = 0.35m_e$ [173]. Electron mobility on high-quality ITO films can reach values of $\mu_e \approx 50 \times 10^{-4}$ $m^2\ V^{-1}\ s^{-1}$. Drude empirical approximations suggest that the electronic relaxation time is $\tau \approx 3.3 \times 10^{-15}s$. The variation of $T(t)$ with deposition thickness for various N_e is plotted in Fig. 9.9 using equations (9.2) and (9.4). As the thickness increases, transparency decreases. In addition, increasing N_e decreases transparency.

The frequency band for the proposed design is centred around 3.5 GHz. Upon the calculation using equation (9.3), the skin depth is comparable to the thickness of thin-film deposition. As seen in Fig. 9.9, excellent transparency > 88% can be obtained by using a thin ITO coating of thickness approximately 0.3 μm for $N_e = 0.7 \times 10^{27}\ m^{-3}$. The sheet resistance can be varied by controlling the film thickness, t as seen in Fig.

9.10 using equation (9.6). By choosing N_e, the transparency and conductivity of ITO can be set before the ITO sheet fabrication. The sheet resistance and transparency can be fixed during the antenna fabrication stage by choosing the required film thickness. The sheet resistance for ITO at a deposition thickness of 0.3 μm is approximately 6 Ω/sq for the conductivity of 5.6×10^5 S/m as seen in Fig. 9.10 and this deposition thickness is chosen during the antenna fabrication.
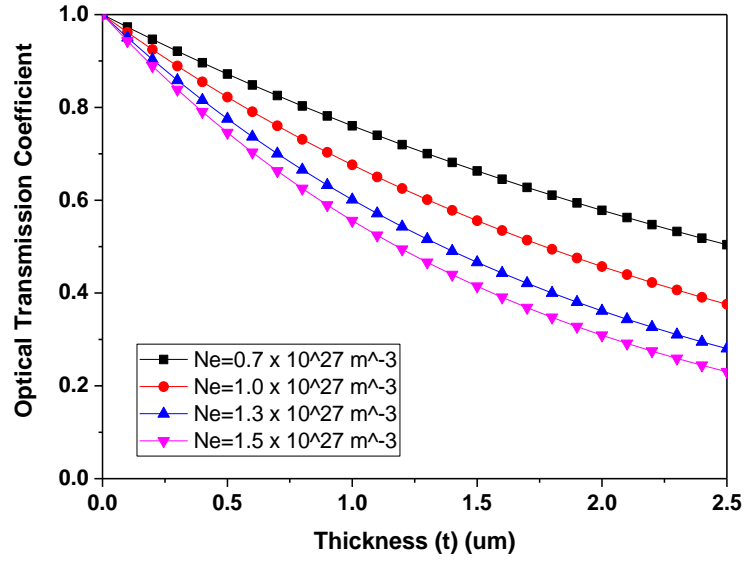
Fig. 9.9. **The optical transmission coefficient of ITO for λ_0 = 550 nm and electron mobility $\mu_e \approx 50 \times 10^{-4}$ $m^2V^{-1}s^{-1}$ for various electron densities**
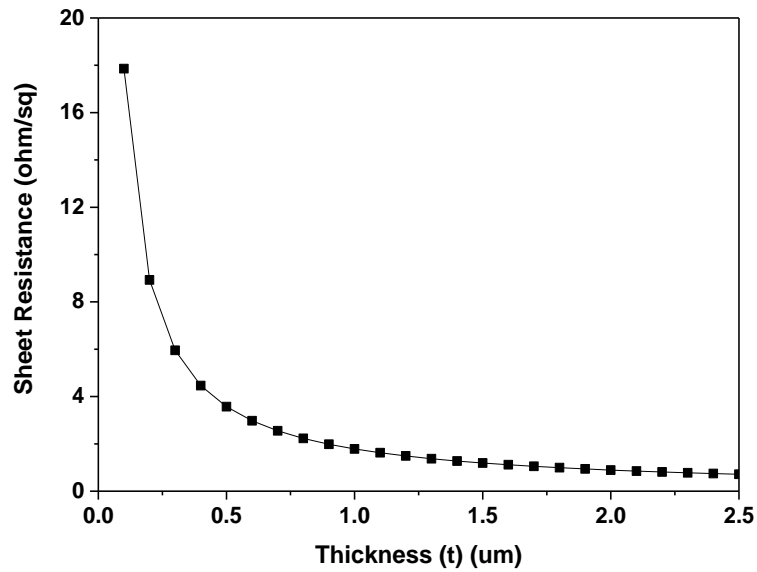
Fig. 9.10. **ITO sheet resistance for electron mobility $\mu_e \approx 50 \times 10^{-4}$ $m^2V^{-1}s^{-1}$ and ITO conductivity $\sigma \approx 5.6 \times 10^5$ S/m for $N_e = 0.7 \times 10^{27}$ m^{-3}**

9.3. A 2 × 2 Antenna Array

To increase the antenna gain, a square 2 × 2 antenna array is formed as shown in Fig. 9.11 (a) and a prototype has been fabricated as shown in Fig. 9.11 (b). The spacing between any two adjacent elements is set to 65 mm ($0.8\lambda_0$ where λ_0 is the free space wavelength at the central frequency 3.55 GHz).

(a)

(b)
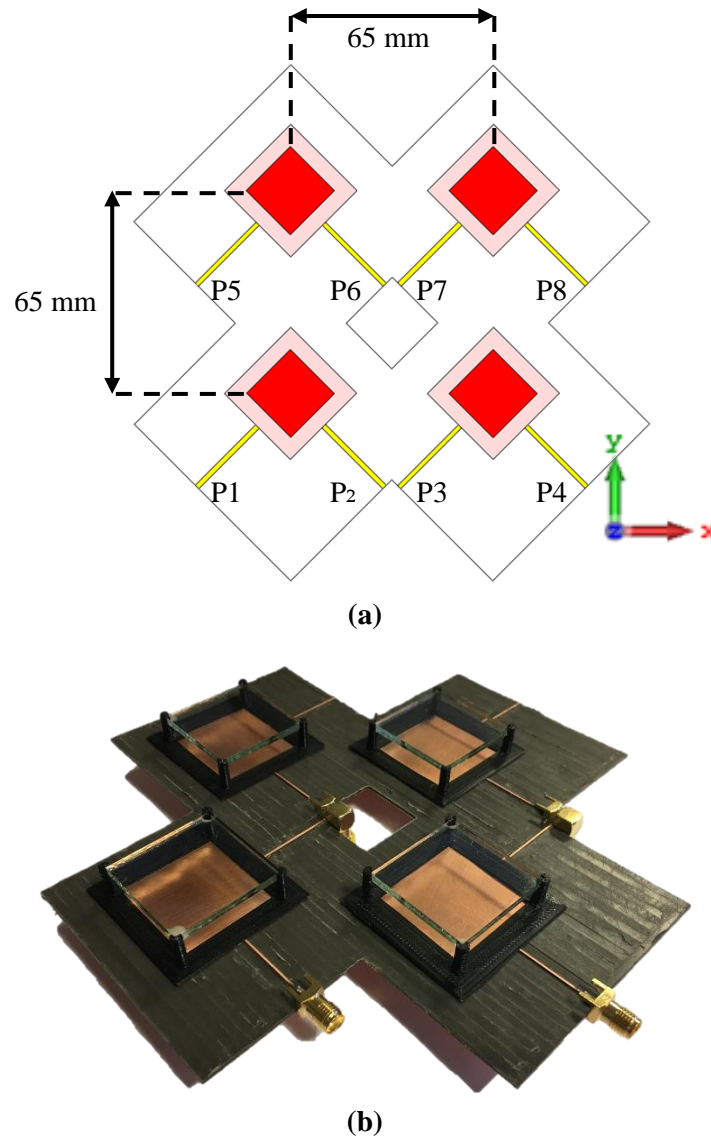
Fig. 9.11.   A 2 × 2 antenna array (a) layout (b) prototype

The reflection coefficient and the isolations between the ports (*P1*, *P2*… *P8*) for the antenna array are shown in Fig. 9.12. The results indicate a 15 dB return loss across

the desired BW from 3.3 to 3.8 GHz and worst-case isolation of 23 dB between any pair of ports. The average realized gain is 13.7 dBi as noticed from Fig. 9.12.
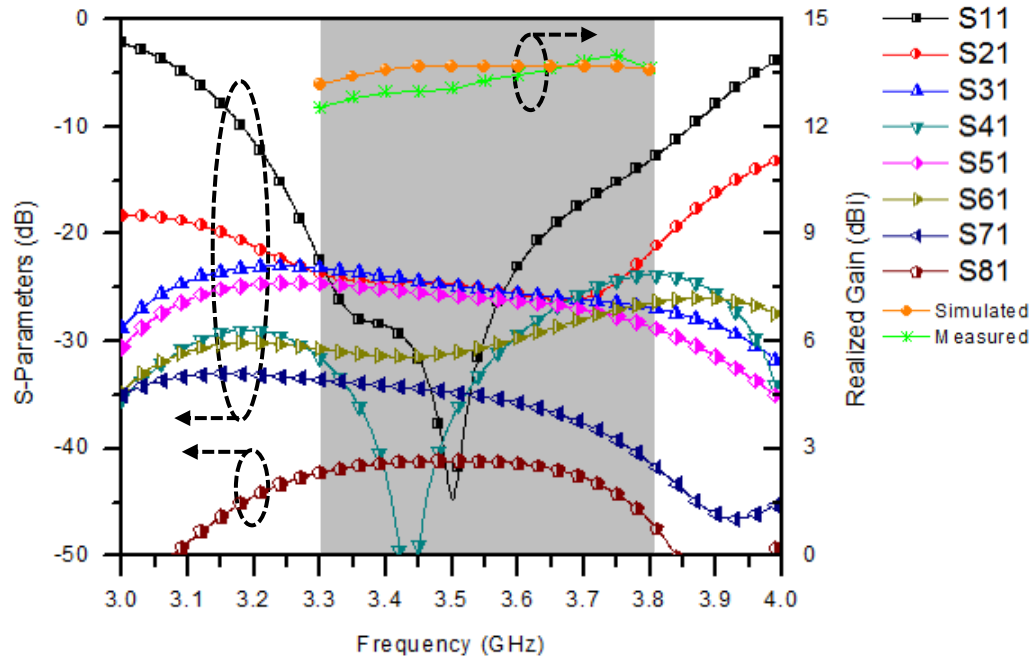
Fig. 9.12.   **Reflection coefficient, isolations between the ports and realized gains of the antenna array**

    The simulated and measured radiation patterns of the antenna array at the start, central and stop frequencies are shown in Fig. 9.13. The HPBW is 33° in both H and V planes.
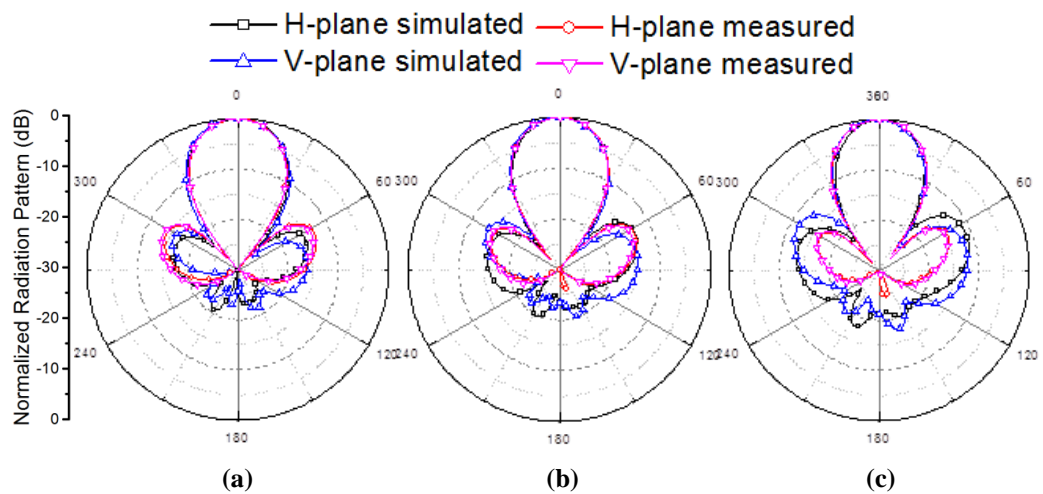
Fig. 9.13.   **The simulated and measured radiation patterns of the antenna array at (a) 3.3 GHz (b) 3.55 GHz (c) 3.8 GHz**

9.4. Integrated Antenna Array with a Street Lamp

To achieve camouflage, the proposed antenna array presented in section 9.3 is integrated with the head of a street lamp. The transparent radiating layer is integrated with the transparent glass cover of the head of the street lamp while the feeding layer is embedded inside the head as shown in Fig. 9.14. The two layers are separated by an air gap of a height H. Finally, a transparent thin protective silicon coating is placed on top of the radiating layer to provide protection to the antenna array.

(a)

(b)

(c)
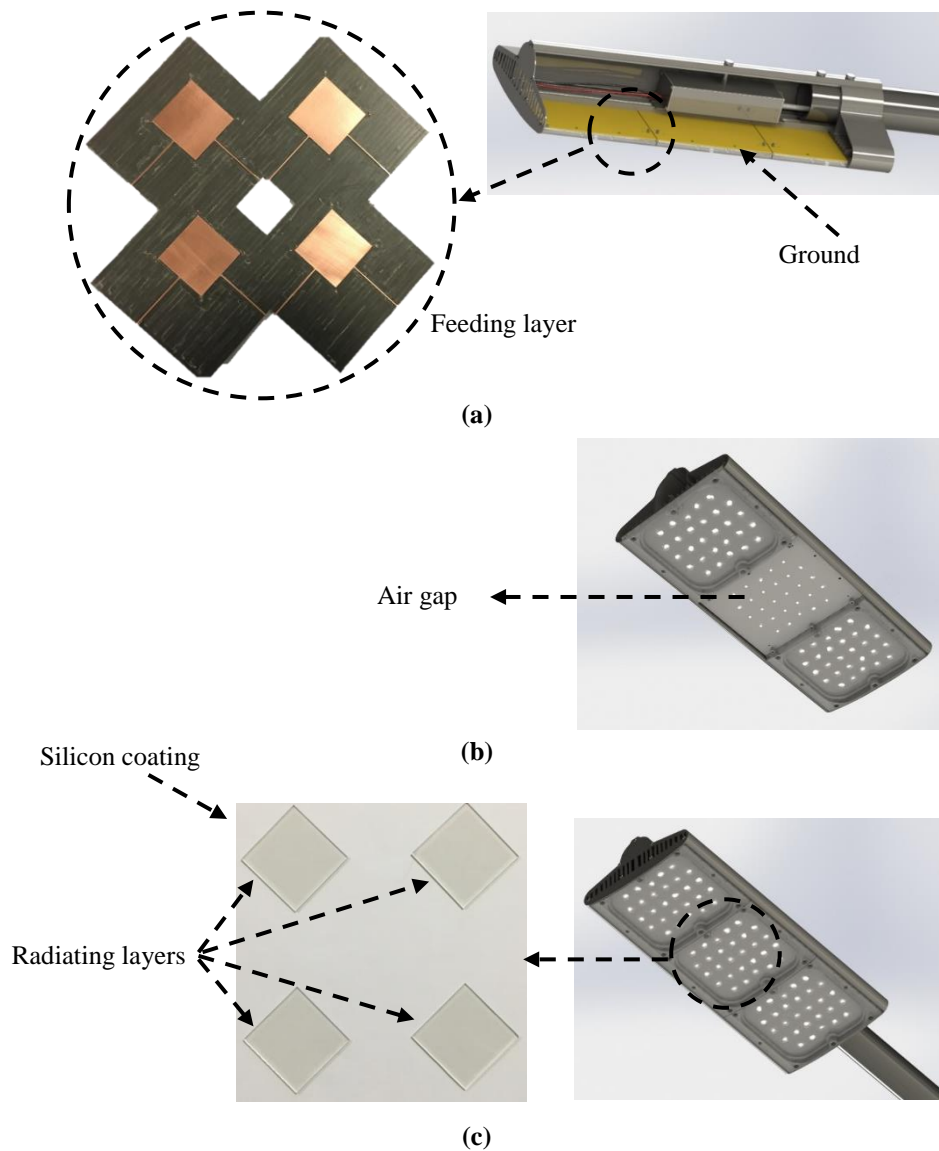
Fig. 9.14.   Integration of the proposed antenna array with a street lamp
(a) feeding layer (b) air gap (c) radiating layers

To study the effect of the street lamp on the antenna performance, the antenna array was re-simulated after integration with the head of the street lamp using CST Microwave studio. For more realistic study, the lamp feeding wires, light bulbs, fixing screws and nuts were all included in the simulation model. The simulated 3D radiation pattern is presented in Fig. 9.15. It is clear that the antenna realized gain has slightly decreased to be 13.2 dBi due to the effect of the large size of the head of the street lamp and the silicon coating.
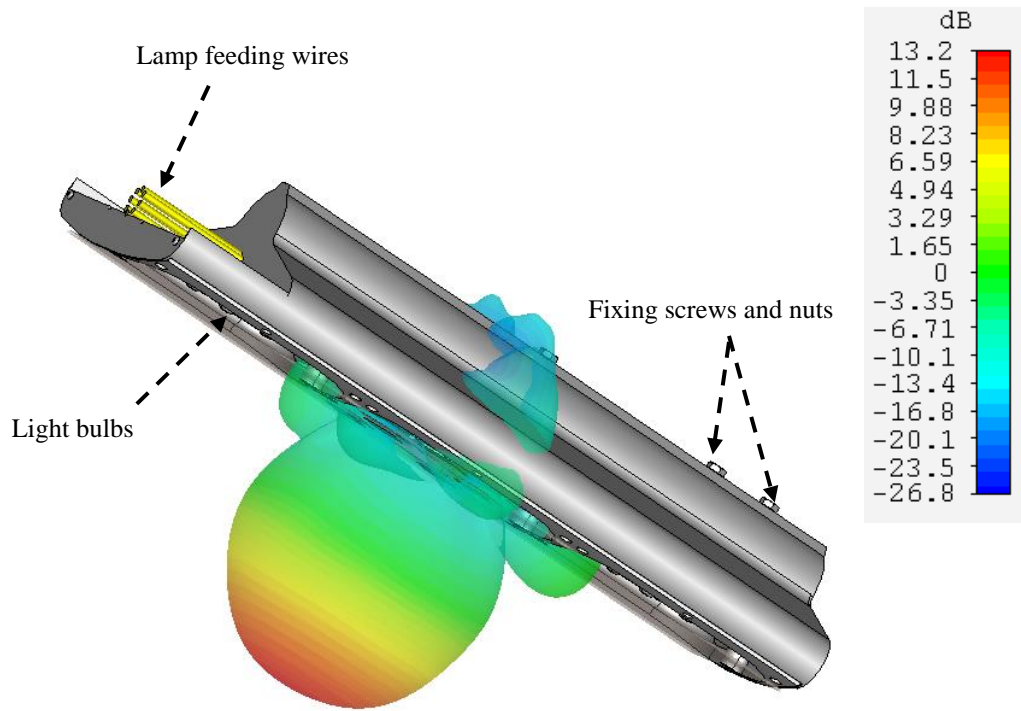
Fig. 9.15.   The simulated 3D radiation pattern of the proposed antenna array integrated with a street lamp.

9.5. Summary

A new transparent dual-polarized antenna array for PC base stations has been designed, fabricated and measured to serve the sub-6 GHz 5G applications. The antenna elements radiate through transparent patches formed using a thin film of a transparent ITO conductor printed on glass laminates achieving 77% of transparency. The proposed antenna array covers the frequency band from 3.3 GHz to 3.8 GHz with VSWR ≤ 1.5 to meet the impedance matching industrial standard and good isolations

between its ports. It also has a stable radiation pattern within the desired frequency band with a small size and low profile.

Being transparent, the antenna array has been successfully integrated to the head of a street lamp to achieve camouflage which makes the proposed design a special ideal antenna candidate for camouflage sub-6 GHz 5G PC base stations.

Chapter 10. Conclusions and Future Work

10.1. Conclusions

This thesis introduced many solutions for some challenges and problems that face the designers of base station antenna. These solutions have been presented as several base station antenna structures and mathematical formulas. These solutions can be divided into two main phases or themes:

In the first phase, MIMO antenna structures were introduced to put some solutions of the challenges in MIMO systems such as re-configurability and multi-band performance. The introduced solutions showed how a MIMO antenna system could maintain high diversity performance. In addition, phased-MIMO array technique has been moved from the theory to practice for the first time in this thesis.

In the second phase, some solutions for the challenges in the new 5G mobile network were presented for both indoor and outdoor scenarios. Several antenna designs were introduced to meet the requirements of the new 5G network. Moreover, an innovative design of transparent antenna was presented for Pico-cell base station.

Finally, it is worth mentioning that the performance parameters of all the proposed antenna solutions were obtained and evaluated based on both simulated and measured results. They are in very good agreements. Although some of the designs have some limitations, the idea and the knowledge gained should be useful for further design guidance.

In this chapter, the key contributions of this thesis to the development of novel base station antennas are summarized in section 10.2. Some suggestions for future work are discussed in section 10.3.

10.2. Key Contributions

In this thesis, six main contributions to base station antenna designs are investigated. These major contributions are detailed in the following sections:

10.2.1. A Reconfigurable Dual-Mode Base Station Antenna

In Chapter 4, a novel design of a dual-polarized oval-shaped cross-dipole antenna element was proposed to cover the frequency band from 1.7 to 2.7 GHz. This antenna element offers a good impedance matching, a stable radiation pattern, a high XPD and a small size. The design was verified by fabricating and measuring a prototype. Based on this antenna element, a design of a reconfigurable broadband dual-mode three-sector antenna was proposed. The reconfigurable antenna can operate as a sectoral (directive) or omnidirectional base station antenna whenever required. The selection of its role is determined by its excitation only. A prototype was fabricated and measured to validate the idea.

10.2.2. Optimum Partitioning of a Phased-MIMO Antenna Array

In Chapter 5, the concept of applying MIMO OLAS was adopted and optimized for multi-band base station antenna. A mathematical formula for optimum partitioning scheme of a phased-MIMO antenna array was derived to determine the optimum division of an array into subarrays and the number of the elements in each subarray.

10.2.3. Dual-Band Base Station Antenna Using Overlapped Subarrays

Chapter 6 proposed a novel design of a dual-band fylfot-shaped antenna to cover the frequency bands from 0.7 to 0.96 GHz and from 1.7 to 2.7 GHz simultaneously. Then, the optimized partitioning scheme mentioned above was applied to a linear antenna array that consists of two MIMO OLAS. The array has been found to have the same performance as a standard conventional base station antenna but with 25% fewer antenna elements, which leads to a smaller size and lower cost. Both the antenna element and the antenna array were fabricated and measured.

10.2.4. A Triple-Band Indoor Base Station Antenna

The fourth investigation of this work focused on indoor base station antennas. In Chapter 7, a novel design of an indoor triple-band dual-polarized base station antenna was proposed. The antenna covers the frequency bands from 0.7 to 0.96 GHz, 1.7 to

2.7 GHz and 3.3 to 3.8 GHz simultaneously to serve 2G, 3G, 4G and sub-6 GHz 5G networks. The antenna performs support MIMO system utilizing polarization diversity due to its co-located dual-polarized cross dipoles. To verify the design, a prototype was fabricated and measured.

10.2.5. A 5G MIMO Base Station Antenna for Broadcasting and Traffic Communications

Chapter 8 proposed a novel design of a dual-polarized antenna element for sub-6 GHz 5G base stations to cover the frequency band from 3.3 to 3.8 GHz. The design offers a good impedance matching, high isolation between its ports, a stable radiation pattern, and a low profile. A prototype was fabricated and measured to validate the design. Moreover, the antenna element was expanded to form a planar MIMO antenna array to either perform in a broadcast or traffic communication topology whenever required. In the broadcast communication topology, the proposed MIMO antenna array covers a sector of 65º in the horizontal plane as conventional base station antennas used for 2G, 3G and 4G. In traffic topology, the proposed MIMO antenna array can direct multiple beams to concurrent multiple users in P2MP communication based on a novel PIS. The novel PIS has been proved to be better than the other approaches which use frequency or pattern diversity as it possesses the advantage of the pattern diversity (by using a single frequency for multi-user coverage) and the advantages of the frequency diversity (by offering good steering capability and high directivity for each user). It is capable of radiating dynamic multiple beams with excellent flexibility and steering capabilities for real-time processing and outperforming other multi-beam antenna array methods.

10.2.6. A Camouflage Antenna for 5G Pico-Cell Base Stations

In Chapter 9, a novel transparent dual-polarized antenna array for sub-6 GHz 5G PC base station was proposed. The antenna element has a transparent radiator printed on a transparent glass laminate, which gives the proposed design the advantage of being partially invisible. This low visibility allows the proposed antenna to be feasibly integrated with other daily suitable surrounding equipment to achieve visual

camouflage. In this work, a street lamp was selected as an example of such surrounding equipment, which can be any other suitable one.

10.3. Future work

Based on the conclusion drawn and the limitations of the work presented, future work can be carried out in the following areas;

    (a) Dual-band MIMO 5G base station antenna should be designed to cover the sub-6 GHz frequency bands from 3.3 to 3.8 GHz and from 4.8 to 5 GHz. This may be a big challenge, as the designed antenna array should support not only the dual-band coverage with good performance but also the functionality of a MIMO system with effective executions.

    (b) Massive MIMO is a possible solution for 5G base station antennas to overcome the limitation introduced by the MIMO system and improve diversity performance.

    (c) For 5G base stations at mm-wave, the path loss is a big issue. Therefore, 5G base station antenna with a sufficiently high gain is a necessary requirement. In such a case, the high gain could not be achieved by increasing the number of antenna elements in the antenna array due to the high insertion loss within the feeding network at mm-wave bands. Moreover, the base station antenna at mm-wave should support good beam steering capabilities. This also may be a challenging issue due to the high power consumed within the active feeding network.

    (d) Decoupling techniques to improve the antenna array isolation needs to be explored for miniaturisation of antenna arrays.

The future work in base station antenna design, especially for 5G networks, is not limited to the works proposed in this thesis. According to different applications of this technology, developments are still taking place in many areas.

5G is one of the most sophisticated wireless technologies that have ever been developed. The socio-economic impact of 5G is yet to be analysed. However, it will make a significant impact on every area where wireless transmission is inevitable.

References

[1] Nokia, "Looking ahead to 5G", Espoo, Finland, 2014. [Online]. Available: *http: //networks.nokia.com/sites/default/files/document/5g _white_paper_0.pdf.*

[2] Cisco, Cisco visual networking index: Global mobile data traffic forecast update, 2014–2019, San Jose, CA, USA, 2015. [Online]. Available: *http://www.cisco.com/c/en/us/solutions/collateral/service-provider/   visual networking -index-vni/white_paper_c11-520862.pdf.*

[3] Ericsson, Ericsson mobility report – on the pulse of the networked society, Stockholm, Sweden, 2014. [Online]. Available: *http://www.ericsson.com/ res/docs/2014/ericsson-mobility-report-November-2014.pdf.*

[4] GSMA Intelligence. Definitive data and analysis for the mobile industry. Accessed: 25.3.2019, [Online]. Available: *https://www.gsmaintelligence.com/.*

[5] A. F. Molisch, "*Wireless Communications*", 2nd ed., John Wiley & Sons, Oxford, 827 pages, 2011.

[6] "ITU-R M.2134: Requirements related to technical performance for IMT Advanced radio interface(s)", ITU, Tech. Rep., 2008. [Online]. Available: *http: //www.itu.int/dms_pub/itu-r/opb/rep/R-REP-M.2134-2008-PDF-E.pdf.*

[7] Adrio Communications Ltd. LTE frequency bands & spectrum allocations. Accessed: 25.3.2019, [Online]. Available: *http://www.radio-electronics.com/ info/cellulartelecomms/lte- long- term- evolution/lte- frequencyspectrum.php.*

[8] S. Parkvall, E. Englund, A. Furuskär, E. Dahlman, T. Jönsson, and A. Paravati, "LTE evolution towards IMT-Advanced and commercial network performance", *Int. Conf. Commun. Systems*, pp. 151–155, 2010.

[9] T. Wheeler, "*The Future of Wireless: A Vision for U.S. Leadership in a 5G World*", Washington, D.C, Jun. 20, 2016.

[10] X. P. Mao and J. W. Mark, "On Polarization Diversity in Mobile Communications," *International Conference on Communication Technology*, Guilin, pp. 1-4, 2006.

[11] D. V. Thiel and S. Smith, "*Switched Parasitic Antennas for Cellular Communications*", Artech House, Inc., Norwood, MA, USA, 2001.

[12] J. Ilvonen, "Multiband and environment insensitive handset antennas", *PhD dissertation*, Aalto University, 100 pages, 2014.

[13] A. Sutton, "Base Station Antenna Systems" *The ITP (Institute of Telecommunications Professionals)*, Journal 12, no. 4: 35–39, 2018.

[14] S. R. Saunders and A. Aragón-Zavala, "*Antennas and Propagation for Wireless Communication Systems*", John Wiley & Sons, 2nd ed., Chichester, 524 pages, 2007.

[15] L. Godara, "*Handbook of Antennas in Wireless Communications*", CRC Press, Inc., Boca Raton, FL, USA, 2001.

[16] B. Sklar, "*Digital Communications: Fundamentals and Applications*". Vol. 2. Prentice Hall, Upper Saddle River, NJ, USA, 2001.

[17] G. V. Tsoulos, "*Adaptive antennas for wireless communications*", Wiley-IEEE Press, 2000.

[18] T. Chiou and K. Wong, "A compact dual-band dual-polarized patch antenna for 900/1800-MHz cellular systems," *IEEE Transactions on Antennas and Propagation*, vol. 51, no. 8, pp. 1936-1940, Aug. 2003.

[19] H. Huang, Y. Liu and S. Gong, "A Dual-Broadband, Dual-Polarized Base Station Antenna for 2G/3G/4G Applications," *IEEE Antennas and Wireless Propagation Letters*, vol. 16, pp. 1111-1114, 2017.

[20] K. Wong, "*Planar Antennas for Wireless Communications*." John Wiley & Sons. Hoboken, NJ, USA. 2003.

[21] Z. Chen, and K. Luk, "*Antennas for Base Stations in Wireless Communications*", US: McGraw-Hill Professional, 2009.

[22] Amphenol Antenna Solutions, Inc. Founded in 1979. [Online]. Available: *https://amphenol-antennas.com/datasheets/6890100.pdf*.

[23] C. A. Balanis, "*Antenna Theory: Analysis and design*", 3rd ed., John Wiley & Sons, New Jersey, USA, 2005.

[24] C. Beckman and B. Lindmark, "The Evolution of Base Station Antennas for Mobile Communications," *International Conference on Electromagnetics in Advanced Applications*, Torino, pp. 85-92, 2007.

[25] J. L. Volakis, "*Antenna Engineering Handbook*", McGraw-Hill, 4th ed., New York, 1872 pages, 2007.

[26] Z. N. Chen, "*Antennas for portable devices*", John Wiley & Sons, 2007.

[27] K. Fujimoto and J. R. James, "*Mobile antenna system handbook*", Artech House, 2nd Ed., Norwood USA, 2001.

[28] Y. Huang and K. Boyle, "*Antennas: from theory to practice*", John Wiley & Sons, 2008.

[29] C. Ding, H. Sun, R. W. Ziolkowski and Y. J. Guo, "Simplified Tightly-Coupled Cross-Dipole Arrangement for Base Station Applications," *IEEE Access*, vol. 5, pp. 27491-27503, 2017.

[30] Y. He, W. Tian and L. Zhang, "A Novel Dual-Broadband Dual-Polarized Electrical Downtilt Base Station Antenna for 2G/3G Applications," *IEEE Access*, vol. 5, pp. 15241-15249, 2017.

[31] D. Muirhead, M. A. Imran and K. Arshad, "A Survey of the Challenges, Opportunities and Use of Multiple Antennas in Current and Future 5G Small Cell Base Stations," *IEEE Access*, vol. 4, pp. 2952-2964, 2016.

[32] Z. Wu, B. Wu, Z. Su and X. Zhang, "Development challenges for 5G base station antennas," *International Workshop on Antenna Technology (iWAT)*, Nanjing, pp. 1-3, 2018.

[33] E. Dahlman, S. Parkvall, and J. Sköld, "*3G Evolution: HSPA and LTE for Mobile Broadband*", Academic Press, London, 2008.

[34] B. K. Lau, "*Multiple antenna terminals,*" in *MIMO: From Theory to Implementation*, USA: Academic, San Diego, CA, pp. 267–298, 2011.

[35] X. P. Mao and J. W. Mark, "On Polarization Diversity in Mobile Communications," *International Conference on Communication Technology*, Guilin, pp. 1-4, 2006.

[36] G. J. Foschini and M. J. Gans, "On limits of wireless communications in a fading environment when using multiple antennas", *Wireless personal communications*, vol. 6, no. 3, pp. 311–335, 1998.

[37] E. Telatar, "Capacity of multi-antenna gaussian channels", *Eur. Trans. on Telecommun.*, vol. 10, no. 6, pp. 585–595, 1999.

[38] J. Mietzner, R. Schober, L. Lampe, W. H. Gerstacker, and P. A. Hoeher, "Multiple antenna techniques for wireless communications-a comprehensive literature survey", *IEEE Commun. Surveys & tutorials*, vol. 11, no. 2, 2009.

[39] J. W. Wallace and M. A. Jensen, "Mutual coupling in MIMO wireless systems: A rigorous network theory analysis", *IEEE Trans. on Wireless Commun.*, vol. 3, no. 4, pp. 1317–1325, 2004.

[40] C. P. Domizioli and B. L. Hughes, "Front-end design for compact MIMO receivers: A communication theory perspective", *IEEE Trans. on Commun.*, vol. 60, no. 10, pp. 2938–2949, 2012.

[41] G. L. Stuber, J. R. Barry, S. W. Mclaughlin, Y. Li, M. A. Ingram, and T. G. Pratt, "Broadband MIMO-OFDM wireless communications", *Proc. IEEE*, vol. 92, no. 2, pp. 271–294, 2004.

[42] H. Bolcskei, "MIMO-OFDM wireless systems: basics, perspectives, and challenges", *IEEE Wireless Commun.*, vol. 13, no. 4, pp. 31–37, 2006.

[43] E. Biglieri, R. Calderbank, A. Constantinides, A. Goldsmith, A. Paulraj, and H. V. Poor, "*MIMO wireless communications*", Cambridge University Press, 2007.

[44] E. G. Larsson, O. Edfors, F. Tufvesson, and T. L. Marzetta, "Massive MIMO for next-generation wireless systems", *IEEE Communications. Magazine*, vol. 52, no. 2, pp. 186–195, 2014.

[45] W.C. Jakes, "*Microwave mobile communications*", IEEE Press, 1994.

[46] V. Pohl, V. Jungnickel, T. Haustein, and C. Von Helmolt, "Antenna spacing in MIMO indoor channels", *IEEE Veh. Technol. Conf.*, vol. 2, pp. $749 - 753$, 2002.

[47] D. Liang, C. Hosung, R. W. Heath Jr., and L. Hao, "Simulation of MIMO channel capacity with antenna polarization diversity", *IEEE Trans. on Wireless Commun.*, vol. 4, no. 4, pp. $1869 - 73$, 2005.

[48] J. Perez, J. Ibanez, L. Vielva, and I. Santamaria, "Capacity estimation of polarization diversity MIMO systems in urban microcellular environments", *Int. Sym. on Personal, Indoor and Mobile Radio Commun.*, vol. 4, pp. $2730 - 2734$, 2004.

[49] M.R. Andrews, P.P. Mitra, and R. DeCarvalho, "Tripling the capacity of wireless communications using electromagnetic polarization", *Nature*, pp. $316 - 318$, 2001.

[50] T. W. C. Brown, S. R. Saunders *et al*, "Characterisation of polarization diversity at the mobile", *IEEE Trans. Antennas Propag.*, vol. 56, no. 5, pp. 2440-2447, Sep. 2007.

[51] http://www.cst-korea.co.kr/Application/MIMO-Antenna-Simulation-CSTMWS.pdf.

[52] R. G. Vaughan, "Switched parasitic elements for antenna diversity", *IEEE Trans. Antennas Propag.*, vol. 47, no. 2, pp. 399-405, Feb. 1999.

[53] P. Mattheijssen, *et. al*, "Antenna-pattern diversity versus space diversity for use at handhelds", *IEEE Trans. Veh. Tech.,* vol. 53, no. 4, pp. 1035-1042, Jul. 2004.

[54] P. L. Penry, C. L. Holloway, "Angle and space diversity comparison in different mobile radio environments", *IEEE Trans. Antennas Propag.,* vol. 46, no. 6, pp. 764-775, Jun. 1998.

[55] R. G. Vaughan, "Pattern translation and rotation in uncorrelated source distributions for multiple beam antenna design", *IEEE Trans. Antennas Propag.,* vol. 46, no. 7, pp. 982-990, Jul. 1998.

[56] P. B. Fletcher, M. Dean and A. R. Nix, "Mutual coupling in multi-element array antennas and its influence on MIMO channel capacity", *Elec. Lett.,* vol. 39, no. 12, pp. 342-344, 2003.

[57] R. G. Vauchan and J. B Anderson, "Antenna diversity in mobile communications", *IEEE Trans. Veh. Technol.,* vol. 36, no. 4, pp. 149-172, Nov. 1987.

[58] S. C. K. Ko and R. D. Murch, "Compact Integrated diversity antenna for wireless communications", *IEEE Trans. Antennas Propag.,* vol. 49, no. 6, pp. 954-960, Jun. 2001.

[59] M. K. Ozdemir, E. Arvas *et al.*, "Dynamic of spatial correlation and implications on MIMO systems", *IEEE Commun. Mag.,* vol. 42, no. 6, pp. 514-519, Jun. 2004.

[60] S. Blanch, J. Romeu, and I. Corbella, "Exact representation of antenna system diversity performance from input parameter description", *Elec. Lett.*, vol. 39, no. 9, pp. 705-707, 2003.

[61] P. Hallbjorner, "The significance of radiation efficiencies when using S-parameters to calculate the received signal correlation from two antennas", *IEEE Antenna Wireless Propagation Letter*, vol. 4, pp. 97-100, 2005.

[62] T. C. Tang, K. H. Lin, "MIMO antenna design in thin-film integrated passive devices", *IEEE Trans. Components, Packaging and Manufac. Technol.*, vol. 4, no. 4, pp. 648-655, Apr. 2014.

[63] J. F. Li, Q. X. Chu *et al.*, "Compact dual band-notched UWB MIMO antenna with high isolation", *IEEE Transactions on Antennas and Propagation,* vol. 61, no. 9, pp. 4759-4766, Sep. 2013.

[64] R. Vaughan and J. Anderson, "Antenna diversity in mobile communications", *IEEE Trans. Veh. Technol.*, vol. VT-36, no. 4, pp. 149-172, Nov. 1987.

[65] V. Plicanic, "Antenna diversity studies and evaluation", *M.S. thesis*, Dept, of Electroscience, Lund University, May. 2004 [Online]. Available: htttp://www,es.lth.se/teorel/publications/TEAT-500-se-ries/TEAT-5064.pdf.

[66] J. Yang, S. Pivnenko, T. Laitinen, J. Carlsson, and X. Chen, "Measurements of diversity gain and radiation efficiency of the Eleven antenna by using different measurement techniques", *Eur. Conf. Antennas and Propag.*, pp. 1-5, 2010.

[67] R. Bhagavatula, A. Forenza, and R. W. Heath, Jr., "Impact of Antenna Array Configurations on Adaptive Switching in MIMO Channels," *Proc. of Int. Symp. on Wireless Pers. Mult. Comm.*, Sept. 2006.

[68] A. Forenza and R. W. Heath, Jr., "Benefit of Pattern Diversity Via 2-element Array of Circular Patch Antennas in Indoor Clustered MIMO Channels," *IEEE Trans. on Comm.*, vol. 54, no. 5, pp. 943 - 954, May 2006.

[69] K. L. Wong, *Compact, and Broadband Microstrip Antennas*, Hoboken, NJ, USA: Wiley, p. 10, 2002.

[70] Y. He, Z. Pan, X. Cheng, Y. He, J. Qiao and M. M. Tentzeris, "A Novel Dual-Band, Dual-Polarized, Miniaturized, and Low-Profile Base Station Antenna," *IEEE Transactions on Antennas and Propagation*, vol. 63, no. 12, pp. 5399-5408, Dec. 2015.

[71] I. Seo et al., "Design of dual polarized antenna for DCS, UMTS, WiBro base stations," *IEEE International Conference on Wireless Information Technology and Systems*, HI, pp. 1-4, 2010.

[72] N. Fhafhiem, P. Krachodnok, and R. Wangsan, "Design of a dual polarized resonator antenna for mobile communication system", *International Journal of Electrical, Computer, and Communication Engineering*, vol. 8, no. 7, 2014.

[73] Y. Jung, and S. Eom, "A compact multiband and dual-polarized mobile base-station antenna using optimal array structure," *International Journal of Antenna and Propagation*, vol. 2015, p. 11, 2015.

[74] Y. Luo, Q. X. Chu, and D. L. Wen, "A Plus/Minus 45 Degree Dual-Polarized Base-Station Antenna with Enhanced Cross-Polarization Discrimination via Addition of Four Parasitic Elements Placed in a Square Contour," *IEEE Transactions on Antennas and Propag.*, vol. 64, no. 4, pp. 1514-1519, April 2016.

[75] A. Kaddour, S. Bories, Anthony Bellion and Christophe Delaveaud, "3D printed compact dual-polarized wideband antenna," *11th European Conference on Antenna and Propagation (EUCAP)*. pp. 3452-3454, 2017.

[76] Y. Cui and R. Li," Analysis and design of a broadband dual-polarized planar antenna for2G/3G/4G base station," *11th European Conference on Antenna and Propagation*, pp. 2152-2156, 2017.

[77] D. H. Huang and Q. X. Chu, "Broadband dual-polarized oval-shaped antenna for base-station applications," *2016 IEEE International Symposium on Antennas and Propagation (APSURSI)*, Fajardo, pp. 1859-1860, 2016.

[78] Y. Gou, S. Yang, J. Li, and Z. Nie, "A Compact Dual-Polarized Printed Dipole Antenna with High Isolation for Wideband Base Station Applications," *IEEE Transactions on Ant. and Propag.*, vol. 62, no. 8, pp. 4392-4395, Aug. 2014.

[79] H. Huang, Y. Liu and S. Gong, "A Broadband Dual-Polarized Base Station Antenna with Sturdy Construction," *IEEE Antennas and Wireless Propagation Letters*, vol. 16, pp. 665-668, 2017.

[80] D. Z. Zheng and Q. X. Chu, "A Multimode Wideband ± 45° Dual-Polarized Antenna with Embedded Loops," *IEEE Antennas and Wireless Propagation Letters*, vol. 16, pp. 633-636, 2017.

[81] D. Z. Zheng; Q. X. Chu, "A Wideband Dual-Polarized Antenna with Two Independently Controllable Resonant Modes and Its Array for Base-Station Applications," *IEEE Antennas and Wireless Propagation Letters*, vol. 16, pp.2014-2017, 2017.

[82] Q. X. Chu, D. L. Wen, and Y. Luo, "A Broadband ±45° Dual-Polarized Antenna With Y-Shaped Feeding Lines," *IEEE Transactions on Antennas and Propagation*, vol. 63, no. 2, pp. 483-490, Feb. 2015.

[83] A. Ando, A. Kondo, and S. Kubota, "A Study of Radio Zone Length of Dual-Polarized Omnidirectional Antennas Mounted on Rooftop for Personal Handy-Phone System," *IEEE Transactions on Vehicular Technology*, vol. 57, no. 1, pp. 2-10, Jan. 2008.

[84] Y. Li, Z. J. Zhang, J. F. Zheng, and Z. H. Zheng, "Compact azimuthal omnidirectional dual-polarized antenna using highly isolated collocated slots," *IEEE Transactions on Antennas and Propagation*, vol. 60, no. 9, pp. 4037–4045, 2012.

[85] X. Quan, R. Li, Y. Fan and D. E. Anagnostou, "Analysis and Design of a 45° Slant-Polarized Omnidirectional Antenna," *IEEE Transactions on Antennas and Propagation*, vol. 62, no. 1, pp. 86-93, Jan. 2014.

[86] X. Quan and R. Li, "A Broadband Dual-Polarized Omnidirectional Antenna for Base Stations," *IEEE Transactions on Antennas and Propagation*, vol. 61, no. 2, pp. 943-947, Feb. 2013.

[87] Y. Yu, J. Xiong and R. Wang, "A Wideband Omnidirectional Antenna Array with Low Gain Variation," *IEEE Antennas and Wireless Propagation Letters*, vol. 15, pp. 386-389, Dec. 2016.

[88] F. Jolani, Y. Yu and Z. Chen, "A novel broadband omnidirectional dual-polarized MIMO antenna for 4G LTE applications," *IEEE International Wireless Symposium*, X'ian, pp. 1-4, 2014.

[89] Constantine A. Balanis, *Antenna Theory: Analysis and Design*, 3rd edition USA: Wiley, 2005.

[90] M. I. Skolnik, *Introduction to Radar Systems*, the 3rd edition. New York: McGraw-Hill, 2001.

[91] E. Fishler, A. Haimovich, R. Blum, D. Chizhik, L. Cimini, and R. Valenzuela, "MIMO radar: An idea whose time has come," *Proc. IEEE Radar Conf.*, Honolulu, HI, vol. 2, pp. 71–78, Apr. 2004.

[92] A. Haimovich, R. Blum, and L. Cimini, "MIMO radar with widely separated antennas," *IEEE Signal Process. Mag.*, vol. 25, pp. 116–129, Jan. 2008.

[93] J. Li and P. Stoica, "MIMO radar with collocated antennas," *IEEE Signal Process. Mag.*, vol. 24, no. 5, pp. 106–114, Sep. 2007.

[94] L. Xu and J. Li, "Iterative generalized-likelihood ratio test for MIMO radar," *IEEE Trans. Signal Process*, vol. 55, no. 6, pp. 2375–2385, Jun. 2007.

[95] J. Bergin, S. McNeil, L. Fomundam, and P. Zulch, "MIMO phased array for SMTI radar," *Proc. IEEE Aerospace Conf.*, Big Sky, MT, pp. 1–7, Mar. 2008.

[96] J. P. Browning, D. R. Fuhrmann, and M. Rangaswamy, "A hybrid MIMO phased-array concept for arbitrary spatial beam pattern synthesis," *Proc. IEEE Digital Signal Processing Signal Processing Education Workshop (DSP/SPE)*, Marco Island, FL, pp. 446–450, Jan. 2009.

[97] D. Fuhrmann, P. Browning, and M. Rangaswamy, "Constant-modulus partially correlated signal design for uniform linear and rectangular MIMO radar arrays," *Proc. Int. Conf. Waveform Diversity Design*, Orlando, FL, pp. 197–201, 2009.

[98] D. Fuhrmann, P. Browning, and M. Rangaswamy, "Signaling strategies for the hybrid MIMO phased-array radar," *IEEE J. Sel. Topics Signal Process,* vol. 4, no. 1, pp. 66–78, Feb. 2010.

[99] A. Hassanien and S. A. Vorobyov, "Phased-MIMO radar: A tradeoff between phased-array and MIMO radars," *IEEE Trans. Signal Process.*, vol. 58, no. 6, pp. 3137–3151, Jun. 2010.

[100] N. El-Din Ismail, S. H. Mahmoud, A. S. Hafez and T. Reda, "A New Phased MIMO Radar Partitioning Schemes," *IEEE Aerospace Conference*, Big Sky, MT, pp. 1-7. 2014.

[101] W. Khan, I. M. Qureshi, A. Basit and M. Zubair, "Hybrid Phased MIMO Radar with Unequal Subarrays," *IEEE Antennas and Wireless Propagation Letters*, vol. 14, pp. 1702-1705, 2015.

[102] K. L. Wong, *Compact, and Broadband Microstrip Antennas*, Hoboken, NJ, USA: Wiley, p. 10, 2002.

[103] X. P. Mao and J. W. Mark, "On Polarization Diversity in Mobile Communications," *International Conference on Communication Technology*, Guilin, pp. 1-4, 2006.

[104] Y. Luo, Q. X. Chu and D. L. Wen, "A Plus/Minus 45 Degree Dual-Polarized Base-Station Antenna with Enhanced Cross-Polarization Discrimination via Addition of Four Parasitic Elements Placed in a Square Contour," *IEEE Transactions on Ant, and Propag,* vol. 64, no. 4, pp. 1514-1519, April 2016.

[105] A. Sattar Kaddour, S. Bories, A. Bellion and C. Delaveaud, "3D printed compact dual-polarized wideband antenna," *11th European Conference on Antenna and Propagation (EUCAP).* pp. 3452-3454, 2017.

[106] Y. He and W. Tian, "A broadband dual-polarized base station antenna element for European Digital Dividend, CDMA800 and GSM900 applications," *13th International Wireless Communications and Mobile Computing Conference (IWCMC)*, Valencia, Spain, pp. 659-663, 2017.

[107]   Y. Cui, R. Li and P. Wang, "Novel Dual-Broadband Planar Antenna and Its Array for 2G/3G/LTE Base Stations," *IEEE Transactions on Antennas and Propagation*, vol. 61, no. 3, pp. 1132-1139, March 2013.

[108]   X. Liu, S. He, H. Zhou, J. Xie and H. Wang, "A novel low-profile, dual-band, dual-polarization broadband array antenna for the 2G/3G base station," *IET International Conference on Wireless, Mobile and Multimedia Networks*, Hangzhou, pp. 1-4, China, 2006.

[109]   Y. He, Z. Pan, X. Cheng, Y. He, J. Qiao and M. Tentzeris, "A Novel Dual-Band, Dual-Polarized, Miniaturized, and Low-Profile Base Station Antenna," *IEEE Transactions on Ant. and Propag.*, vol. 63, no. 12, pp. 5399-5408, Dec. 2015.

[110]   H. Huang, Y. Liu and S. Gong, "A Novel Dual-Broadband and Dual-Polarized Antenna for 2G/3G/LTE Base Stations," *IEEE Transactions on Ant. and Propag,* vol. 64, no. 9, pp. 4113-4118, Sept. 2016.

[111]   G. Cui, S.-G. Zhou, G. Zhao, and S.-X. Gong, "A compact dual-band dual-polarized antenna for base station application," *Prog. Electromagn. Res. C*, vol. 64, pp. 61-70, 2016.

[112]   Q. Chu, D. Zheng and R. Wu, "Multi-array multi-band base-station antennas," *International Workshop on Antenna Technology: Small Antennas, Innovative Structures, and Applications (iWAT)*, Athens, pp. 137-139, 2017.

[113]   Y. Jung, and S. Eom, "A compact multiband and dual-polarized mobile base-station antenna using optimal array structure," *International Journal of Antenna and Propagation*, vol. 2015.

[114]   Y. He, W. Tian and L. Zhang, "A Novel Dual-Broadband Dual-Polarized Electrical Downtilt Base Station Antenna for 2G/3G Applications," *IEEE Access*, vol. 5, pp. 15241-15249, 2017.

[115]   H. Huang, Y. Liu and S. Gong, "A Dual-Broadband, Dual-Polarized Base Station Antenna for 2G/3G/4G Applications," *IEEE Ant. and Wireless Propag. Letters*, vol. 16, pp. 1111-1114, 2017.

[116]   C. Beckman and B. Lindmark, "The Evolution of Base Station Antennas for Mobile Communications," *International Conference on Electromagnetics in Advanced Applications*, Torino, pp. 85-92, 2007.

[117]   Tzung-Wern Chiou and Kin-Lu Wong, "A compact dual-band dual-polarized patch antenna for 900/1800-MHz cellular systems," *IEEE Transactions on Antennas and Propagation*, vol. 51, no. 8, pp. 1936-1940, Aug. 2003.

[118]   S. Nikmehr and K. Moradi, "Design and simulation of triple band GSM900/DCS1800/UMTS2100 MHz microstrip antenna for a base station," *IEEE ICCS*, Singapore, pp. 113-116, 2010.

[119]   P. Li, K. M. Luk, and K. Lau, "A dual-feed dual-band L-probe patch antenna," *IEEE Transactions on Ant. and Propag.*, vol. 53, no. 7, pp. 2321-2323, July 2005.

[120]   W. X. An, H. Wong, K. L. Lau, S. F. Li and Q. Xue, "Design of Broadband Dual-Band Dipole for Base Station Antenna," *IEEE Transactions on Ant. and Propag.*, vol. 60, no. 3, pp. 1592-1595, March 2012.

[121]   https://alphaantennas.com/products/tri-sector/

[122]   C. A. Balanis, *Antenna Theory Analysis, and Design.*, NJ, USA: Wiley, 2005.

[123]   H. Huang, X. Li and Y. Liu, "5G MIMO Antenna Based on Vector Synthetic Mechanism," *IEEE Antennas and Wireless Propagation Letters*. 2018.

[124]   T. Chiou and K. Wong, "A compact dual-band dual-polarized patch antenna for 900/1800-MHz cellular systems," *IEEE Transactions on Antennas and Propagation*, vol. 51, no. 8, pp. 1936-1940, Aug. 2003.

[125]   P. Li, K. M. Luk and K. L. Lau, "A dual-feed dual-band L-probe patch antenna," *IEEE Transactions on Ant.s and Propag*, vol. 53, no. 7, pp. 2321-2323, July 2005.

[126]   W. X. An, H. Wong, K. L. Lau, S. F. Li and Q. Xue, "Design of Broadband Dual-Band Dipole for Base Station Antenna," *IEEE Transactions on Antennas and Propagation*, vol. 60, no. 3, pp. 1592-1595, March 2012.

[127]   Iswandi, A. K. D. Jaya and E. S. Rahayu, "Design of triple band printed dipole antenna for indoor small cell base station in LTE systems," *2nd International conferences on Information Technology, Information Systems and Electrical Engineering (ICITISEE)*, Yogyakarta, pp. 207-210, 2017.

[128]   A. Edalati and W. McCollough, "A novel dual-band beam-switching antenna based on active frequency selective surfaces," *IEEE International Symposium on Antennas and Propagation & USNC/URSI National Radio Science Meeting*, San Diego, CA, pp. 1985-1986, 2017.

[129] S. Nikmehr and K. Moradi, "Design and simulation of triple band GSM900/DCS1800/UMTS2100 MHz microstrip antenna for the base station," *IEEE International Conference on Communication Systems*, Singapore, pp. 113-116, 2010.

[130] Z. Wang, G. x. Zhang, Y. Yin and J. Wu, "Design of a Dual-Band High-Gain Antenna Array for WLAN and WiMAX Base Station," *IEEE Antennas and Wireless Propagation Letters*, vol. 13, pp. 1721-1724, 2014.

[131] A. Toktas and A. Akdagli, "Wideband MIMO antenna with enhanced isolation for LTE, WiMAX and WLAN mobile handsets," *Electronics Letters*, vol. 50, no. 10, pp. 723-724, May 2014.

[132] M. van Rooyen, J. W. Odendaal and J. Joubert, "High-Gain Directional Antenna for WLAN and WiMAX Applications," *IEEE Antennas and Wireless Propagation Letters*, vol. 16, pp. 286-289, 2017.

[133] K. Yu, Y. Li, X. Luo and X. Liu, "A modified E-shaped triple-band patch antenna for LTE communication applications," *IEEE International Symposium on Antennas and Propagation (APSURSI)*, Fajardo, pp. 295-296, 2016.

[134] A. Alieldin and Y. Huang, "Design of broadband dual-polarized oval-shaped base station antennas for mobile systems*," IEEE International Symposium on Antennas and Propagation & USNC/URSI National Radio Science Meeting*, San Diego, CA, USA, pp. 183-184, 2017.

[135] H. Huang, Y. Liu and S. Gong, "A Dual-Broadband, Dual-Polarized Base Station Antenna for 2G/3G/4G Applications," *IEEE Antennas and Wireless Propagation Letters*, vol. 16, pp. 1111-1114, 2017.

[136] Y. Gao, R. Ma, Y. Wang, Q. Zhang and C. Parini, "Stacked Patch Antenna With Dual-Polarization and Low Mutual Coupling for Massive MIMO," *IEEE Transactions on Ant. and Propag.*, vol. 64, no. 10, pp. 4544-4549, Oct. 2016.

[137] H. Huang, X. Li and Y. Liu, "5G MIMO Antenna Based on Vector Synthetic Mechanism," *IEEE Antennas and Wireless Propagation Letters*, vol. 17, no. 6, pp. 1052-1055, June 2018.

[138] Q. Wu, P. Liang, and X. Chen. "A Broadband ±45° Dual-Polarized Multiple-Input Multiple-Output Antenna for 5G Base Stations with Extra Decoupling Elements," *Journal of Communications and Information Networks*, Vol. 3, Issue 1, pp 31–37, March 2018.

[139] M. A. Al-Tarifi, M. S. Sharawi and A. Shamim, "Massive MIMO antenna system for 5G base stations with directive ports and switched beam steering capabilities," *IET Microwaves, Antennas & Propagation*, vol. 12, no. 10, pp. 1709-1718, 15 8 2018.

[140] M. Alibakhshi-Kenari, M. Naser-Moghadasi, R. A. Sadeghzadeh, B. S. Virdee and E. Limiti, "Periodic array of complementary artificial magnetic conductor metamaterials-based multiband antennas for broadband wireless transceivers," *IET Microwaves, Ant. & Propag.*, vol. 10, no. 15, pp. 1682-1691, 2016.

[141] M. Alibakhshikenari, B. S. Virdee, A. Ali and E. Limiti, "Miniaturised planar-patch antenna based on metamaterial L-shaped unit-cells for broadband portable microwave devices and multi-band wireless communication systems," *IET Microwaves, Antennas & Propagation*, vol. 12, no. 7, pp. 1080-1086, 2018.

[142] Z. Wu, B. Wu, Z. Su and X. Zhang, "Development challenges for 5G base station antennas," *International Workshop on Antenna Technology (iWAT)*, Nanjing, pp. 1-3, 2018.

[143] D. Muirhead, M. A. Imran and K. Arshad, "A Survey of the Challenges, Opportunities and Use of Multiple Antennas in Current and Future 5G Small Cell Base Stations," *IEEE Access*, vol. 4, pp. 2952-2964, 2016.

[144] E. Björnson, L. Van der Perre, S. Buzzi and E. G. Larsson, "Massive MIMO in Sub-6 GHz and mmWave: Physical, Practical, and Use-Case Differences" *arXiv*: 1803.11023v1, 29 Mar 2018.

[145] H. Hu, H. Gao, Z. Li and Y. Zhu, "A Sub 6GHz Massive MIMO System for 5G New Radio," *IEEE 85th Vehicular Technology Conference (VTC Spring)*, Sydney, NSW, pp. 1-5, 2017.

[146] H. T. Chou, "An Effective Design Procedure of Multibeam Phased Array Antennas for the Applications of Multi-satellite/Coverage Communications," *IEEE Transactions on Ant. and Propag*, vol. 64, no.10, pp. 4218-4227, Oct. 2016.

[147] Y. Cao, K. S. Chin, W. Che, W. Yang and E. S. Li, "A Compact 38 GHz Multibeam Antenna Array With Multifolded Butler Matrix for 5G Applications," *IEEE Antennas and Wireless Propagation Letters*, vol. 16, pp. 2996-2999, 2017.

[148] Q. Wu, J. Hirokawa, J. Yin, C. Yu, H. Wang and W. Hong, "Millimeter-Wave Multibeam Endfire Dual-Circularly Polarized Antenna Array for 5G Wireless Applications," *IEEE Transactions on Antennas and Propagation*, vol. 66, no. 9, pp. 4930-4935, Sept. 2018.

[149] J. Zhang, W. Wu and D. g. Fang, "360° scanning multi-beam antenna based on homogeneous ellipsoidal lens fed by circular array," *Electronics Letters*, vol. 47, no. 5, pp. 298-300, March 2011.

[150] A. S. Daryoush, "Digitally beamformed multibeam phased array antennas for future communication satellites," *IEEE Radio and Wireless Symposium*, Orlando, FL, pp. 831-834, 2008.

[151] S. Mondal, R. Singh, A. I. Hussein and J. Paramesh, "A 25–30 GHz Fully-Connected Hybrid Beamforming Receiver for MIMO Communication," *IEEE Journal of Solid-State Circuits*, vol. 53, no. 5, pp. 1275-1287, May 2018.

[152] M. A. Panduro and C. del Rio-Bocio, "Design of Beam-Forming Networks for Scannable Multi-Beam Antenna Arrays Using Corps," *Progress In Electromagnetics Research*, Vol. 84, 173-188, 2008.

[153] L. Manica, P. Rocca, G. Oliveri and A. Massa, "Synthesis of Multi-Beam Subarrayed Antennas Through an Excitation Matching Strategy," *IEEE Transactions on Ant. and Propag*, vol. 59, no. 2, pp. 482-492, Feb. 2011.

[154] J. Sheu, W. Sheen and T. Guo, "On the Design of Downlink Multiuser Transmission for a Beam-Group Division 5G System," *IEEE Transactions on Vehicular Technology*, vol. 67, no. 8, pp. 7191-7203, Aug. 2018.

[155] K. R. Mahmoud and A. M. Montaser, "Performance of Tri-Band Multi-Polarized Array Antenna for 5G Mobile Base Station Adopting Polarization and Directivity Control," *IEEE Access*, vol. 6, pp. 8682-8694, 2018.

[156] H. Chou and J. W. Liu, "Synthesis and Characteristic Evaluation of Convex Metallic Reflectarray Antennas to Radiate Relatively Orthogonal Multibeam," *IEEE Transactions on Antennas and Propagation*, vol. 66, no. 8, pp. 4008-4016, Aug. 2018.

[157] A. Smida, R. Ghayoula and A. Gharsallah, "Beamforming multibeam antenna array using Taguchi optimization method," *2nd World Symposium on Web Applications and Networking (WSWAN)*, pp. 1-4, Sousse, 2015.

[158] N. El-Din Ismail, S. Hanafy, A. Hamed, and A. Hafez, "Design and Analysis of Planar Phased MIMO Antenna for Radar Applications", *Progress In Electromagnetics Research Symposium PIERS*, Guangzhou, China, August 25-28, pp 1832-1838, 2014.

[159] R. Branson et al., "Creating a high efficiency, miniaturized power amplifier module for the emerging pico-cell base station market," *2014 IEEE Topical Conference on Power Amplifiers for Wireless and Radio Applications (PAWR)*, Newport Beach, CA, 2014, pp. 73-75.

[160] L. H. Trinh, F. Ferrero, R. Staraj and J. Ribero, "700–960MHz MIMO antenna for Pico cell applications," *IEEE Antennas and Propagation Society International Symposium*, Orlando, FL, pp. 366-367, 2013.

[161] Z. Chen, and K. Luk, *Antennas for Base Stations in Wireless Communications*, US: McGraw-Hill Professional, 2009.

[162] J. Lebaric and Ah-Tuan Tan, "Ultra-wideband conformal helmet antenna," *Asia-Pacific Microwave Conference. Proceedings*, Sydney, NSW, Australia, pp. 1477-1481, 2000.

[163] B. Sanz-Izquierdo, F. Huang and J. C. Batchelor, "Small size wearable button antenna," *First European Conference on Antennas and Propagation*, Nice, pp. 1-4, 2006.

[164] M. Stanley, Y. Huang, H. Wang, H. Zhou, A. Alieldin, and S. Joseph, "A Transparent Dual-Polarized Antenna Array for 5G Smartphone Applications" *IEEE International Symposium on Antennas and Propagation & USNC/URSI National Radio Science Meeting*, Boston, USA, 2018.

[165] N. Moghadasi and M. Koohestani, "A Simple UWB Microstrip-Fed Planar Rectangular Slot Monopole Antenna", *Loughborough Antenna & Propagation. Conf.*, Loughborough, pp1-3, Nov. 2011.

[166] P. Prajuabwan, S. Porntheeraphat, et. al, "ITO Thin Films prepared by Gas-Timing RF Magnetron Sputtering for Transparent Flexible Antenna", *Nano/Micro Engineered and Molecular Systems*, pp. 647 – 650, 2007.

[167] R. Gordon, "Criteria for choosing transparent conductors", *MRS Bulletin*, Aug. 2000.

[168] N. Guan, H. Furuya, D. Delaune and K. Ito, "Antennas made of transparent conductive films", *Propagation. In Electromagnetic. Research*, vol. 4, 2008.

[169] T. Turpin, and R. Baktur, "Integrated solar meshed patch antennas", *IEEE Antennas and Wireless Propagation Letter*, vol. 8, pp. 693-696, 2009.

[170] N. Outleb, J. Pinel, M. Drissi, and O. Bonnaud, "Microwave planar antenna with RF-sputtered indium tin oxide films", *Microwave and Optical. Technology. Lett.*, vol. 24, 2000.

[171] M. Bourry, et.al, "Novel ITO alloy for microwave and optical applications", *Midwest Sym. on Circuits and Systems*, 615-618, August 2015.

[172] H. J. Song, et. al, "A method for improving the efficiency of transparent film antennas", *IEEE Antennas and Wireless Propagation. Letter*. vol. 7, 2008.

[173] A. Porch, et. al, "Electromagnetic absorption in transparent conducting films" *Jour. of Applied Physics.*, vol. 95, no. 9, May 2004.

[174] K. Narasimha Rao, "Optical and electrical properties of indium tin oxide films", *Indian journal of pure and applied physics*, vol 42, March 2004.

[175] Y. Gao, R. Ma, Y. Wang, Q. Zhang and C. Parini, "Stacked Patch Antenna With Dual-Polarization and Low Mutual Coupling for Massive MIMO," *IEEE Transactions on Ant. and Propag.*, vol. 64, no. 10, pp. 4544-4549, Oct. 2016.

[176] H. Huang, X. Li and Y. Liu, "5G MIMO Antenna Based on Vector Synthetic Mechanism," *IEEE Antennas and Wireless Propagation Letters*, vol. 17, no. 6, pp. 1052-1055, June 2018.

[177] Y. Li, C. Wang, H. Yuan, N. Liu, H. Zhao and X. Li, "A 5G MIMO Antenna Manufactured by 3-D Printing Method," *IEEE Antennas and Wireless Propagation Letters*, vol. 16, pp. 657-660, 2017.

[178] M. A. Al-Tarifi, M. S. Sharawi and A. Shamim, "Massive MIMO antenna system for 5G base stations with directive ports and switched beam steering capabilities," *IET Microwaves, Antennas & Propagation*, vol. 12, no. 10, pp. 1709-1718, 2018.

[179] J. Saberin and C. Furse, "Challenges with Optically Transparent Patch Antennas", *IEEE Antennas and Propag. Mag.*, Vol. 54, No. 3, June 2012.

[180] B. Streetman and S. Banerjee, *Solid State Electronic Devices*, Pearson Prentice Hall, New Jersey, 2006.

[181] J. Saberin, "Optically Transparent Antennas for Small Satellites," *M.Sc. dissertation*, Dept. Electrical. Computer. Eng., Uni. of Utah, Utah, US, 2010.